Paleomagnetic studies of Jurassic and Cretaceous rocks in the Eastern Qiangtang Terrane, Tibetan Plateau, China

Qiang Fu

Utrecht Studies in Earth Sciences No. 278

ISBN: 978-90-6266-648-5

Cover image: Field work in Mangkang, Tibet, China, taken by Miaomiao Shen.
Circular images: (left to right) red beds in Qamdo, Tibet, China; limestone specimens of the Buqu Formation, Zaduo, Qinghai, China; paleomagnetic laboratory of the Institute of Tibetan Plateau Research, Chinese Academy of Sciences (ITPCAS), Beijing, China; in-house-developed robot at paleomagnetic laboratory - Fort Hoofddijk, Utrecht, the Netherlands, taken by Qiang Fu.
The cover is designed by Margot Stoete and Qiang Fu.

Printed by: Ipskamp Printing, Enschede, the Netherlands

Paleomagnetic studies of Jurassic and Cretaceous rocks in the Eastern Qiangtang Terrane, Tibetan Plateau, China

Paleomagnetische onderzoekingen aan gesteenten van Jura en Krijt ouderdom in het Oostelijk Qiangtang Terrein, Tibetaanse Plateau, China

(met een samenvatting in het Nederlands)

Proefschrift

ter verkrijging van de graad van doctor aan de Universiteit Utrecht op gezag van de rector magnificus, prof.dr. H.R.B.M. Kummeling, ingevolge het besluit van het college voor promoties in het openbaar te verdedigen op

woensdag 31 mei 2023 des middags te 12.15 uur

door

Qiang Fu

geboren op 13 september 1991
te Baoji, China

Promotor:
Prof. dr. W. Krijgsman

Copromotor:
Dr. M.J. Dekkers

Beoordelingscommissie:

Dr. Annique van der Boon
Prof. dr. Tilo von Dobeneck
Prof. dr. Stuart Gilder
Prof. dr. D. J. J. van Hinsbergen
Prof. dr. Agnes Kontny

CONTENTS

To my family, for their love and support, I dedicate this thesis.

P

PROLOGUE

The Tibetan Plateau is the highest and largest topographic feature in the world, known as the 'Roof of the World', the 'Asian Water Tower' or the 'Third Pole' of the Earth (e.g., Liu et al., 2008; Pandit et al., 2014; Ran et al., 2017; Yao et al., 2012, 2019). It is composed of multiple terranes including the Tethyan Himalaya, Lhasa, Qiangtang, Songpan-Ganzi, Kunlun-Qilian terranes from south to north (Fig. 1). Their amalgamation involved many significant events, including various kinds of geodynamic processes, e.g., continental drift, intra-continental collisions, and evolution of the Tethyan oceans (Yin & Harrison, 2000; Kapp et al., 2003a, 2003b; Royden et al., 2008; Zhu et al., 2013; Ding et al., 2014; Yan et al., 2016), enrichment of mineral resources (e.g., Hou et al., 2007; Liang et al., 2009; Zheng et al., 2011; Ding et al., 2013), and impacted regional and global climate change (e.g., Ruddiman & Kutzbach, 1989; Fang et al., 2016). Thus, the Tibetan Plateau is regarded as an ideal natural laboratory for geoscientists. The Qiangtang Terrane, the target terrane of this thesis, is one of the major tectonic components of the Tibetan Plateau. It is bounded by the Bangong-Nujiang suture zone (BNSZ) to the south from the Lhasa Terrane, and by the Jinshajiang suture zone (JSSZ) to the north from the Songpan-ganzi Terrane (Dewey et al., 1988; Yin & Harrison, 2000; Kapp et al., 2007; Zhu et al., 2011; Xu et al., 2012; Yan et al., 2016).

The tectonic evolution of the Qiangtang Terrane

Previous investigations of the Qiangtang Terrane (ophiolite obduction, metamorphism, peripheral foreland basin, faunal migration, paleomagnetism, etc.) have provided extensive information about the origin of the Qiangtang Terrane (Kapp et al., 2003b; Pan et al., 2004a, 2004b; Zhao et al., 2014), the closure of the Paleo-Tethys Ocean, i.e. the collision between the Qiangtang and the northern terranes, such as the Songpan-Ganzi Terrane and Tarim Basin (e.g., Yin & Harrison, 2000; Kapp et al., 2003b; Pan et al., 2004a; Pullen et al., 2008; Li et al., 2009a; Gehrels et al., 2011; Zhu et al., 2013; Song et al., 2015, 2017, 2020; Guan et al., 2021; Yu et al., 2022a), the closure of the Meso-Tethys-Bangong-Nujiang Ocean, i.e. the Lhasa Qiangtang collision (e.g., Metcalfe et al., 2006; Zhu et al., 2011; Zhang et al., 2012; Ding et al., 2013; Fan et al., 2014; Yan et al., 2016; Chen et al., 2017b, 2020), and the crustal shortening and widespread lateral extrusion of lithospheric blocks after the

India-Eurasia collision (e.g., Tapponnier et al., 1982; Otofuji et al., 1990; Huang et al., 1992; Tong et al., 2015, 2017, 2022; Li et al., 2020b; Zhang et al., 2020a).

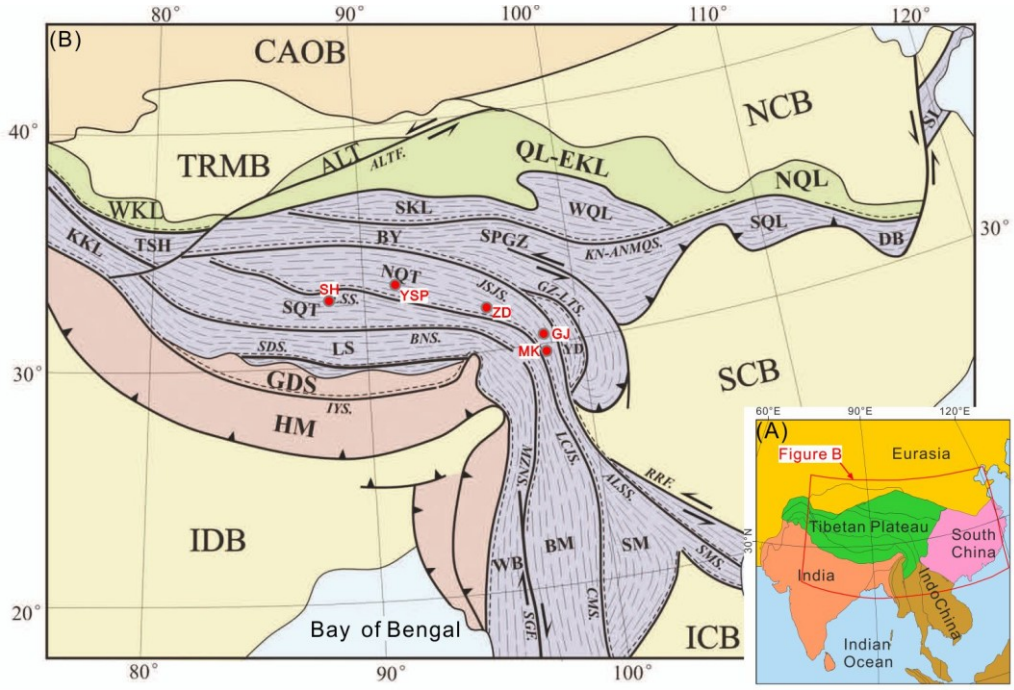

Figure 1. *(A and B) Simplified tectonic map of the Tibetan Plateau and its adjacent areas. (A) modified after Van Hinsbergen et al. (2012). (B) modified after Xu et al. (2012). The abbreviations of the tectonic units are CAOB: Central Asian orogenic belt; TRMB: Tarim block; WKL: Western Kunlun terrane; TSH: Tianshuihai terrane; KKL: Kalakunlun terrane; ALTF: Altyn Tagh fault; QL-EKL:Qilian-Eastern Kunlun terrane; NQL: North Qinling terrane; SKL: Southern Kunlun terrane; WQL: Western Qinling terrane; BY: Bayabhar terrane; SPGZ: Songpan-Ganzi terrane; KN-ANMQS:Kunnan-Animaqin suture; SQL: Southern Qinling terrane; DB: Dabie terrane; GZ-LTS: Ganzi-Litang suture; NQT: Northern Qiangtang terrane; SQT: Southern Qiangtang terrane; LT: Lhasa terrane; JSJS: Jinshajiang suture; LSS: Longmu Tso-Shuanghu suture; BNS: Bangong-Nujiang suture; GDS: Gangdese main subduction accessional orogenic zone; HM: Himalayan main collision orogenic zone; IYS: IndusYaluzangbu suture; IDB: India block; NCB:North China block; SCB:South China block; ICB: Indochina block; WB: Western Burma terrane; BM: Bisimasu terrane; SM: Simao terrane; RRF: Red River fault; ALSS: Ailaoshan suture; SH: Shuanghu; YSP: Yanshiping; ZD: Zaduo; GJ: Gongjue; MK: Mangkang.*

Origin of the Qiangtang Terrane

There are three general models on where and how the Qiangtang Terrane originated. The first model envisages that the Qiangtang Terrane originated from Laurasia, and

considers the Bangong-Nujiang Suture Zone as the northern margin of Gondwana. This model is supported by some geological and geophysical evidence (e.g., Pan et al., 2004a, 2004b; and references therein). The second model assumes that the Qiangtang Terrane was the northernmost part of Gondwana and hence originated from this supercontinent since the Late Carboniferous-Early Permian (e.g., Yin & Harrison, 2000; Kapp et al., 2003b; Metcalfe, 2006, Song et al., 2017). In both models, the Qiangtang Terrane is considered to have been a contiguous part. The subduction-related mélange with high-pressure rocks in the central Qiangtang Terrane was from the JSSZ (Fig. 1); the mélange was underplated below the Qiangtang Terrane and exhumed by detachment faulting (Kapp et al., 2000, 2003b; Pullen et al., 2011; Zhao et al., 2014). Yet another model, the third model, envisages that the Qiangtang Terrane consisted of the East and West Qiangtang terranes (sometimes referred to as North and South Qiangtang, respectively) that are separated by the Longmu Tso-Shuanghu Suture Zone (LSSZ). Both terranes have their respective evolution history (Li et al., 2006; Zhai et al., 2011). The Eastern Qiangtang Terrane originated from Laurasia (Li et al., 1987, 2009a), the Cathaysian continent (Zhu et al., 2013), or Gondwana (Song et al., 2015, 2017), while the Western Qiangtang Terrane separated from Gondwana during the Late Permian (Zhu et al., 2012). In this scenario, the northward subduction of the Paleo-Tethys along the Longmu Tso-Shuanghu Suture Zone (LSSZ) brought out the thrusting of the mélange over the Eastern Qiangtang Terrane (Li et al., 2006; Zhai et al., 2011; Zhao et al., 2014).

The Closure of the Paleo-Tethys Ocean

The Paleo-Tethys is the oldest in a series of Phanerozoic ocean basins that closed between Eurasia and Gondwana (Ding et al., 2013). A common first-order narrative envisions the Paleo-Tethys as a single, wedge-shaped basin that ultimately closed by the arrival of a ribbon-shaped string of Gondwana-derived microcontinents (the Cimmerian terranes) to the southern margin of Laurasia and proto-Asia in the Mesozoic (Guan et al., 2021; Yu et al., 2022a). More simply, it was the paleo-ocean between the Qiangtang Terrane and Tarim/Songpan-Ganzi terranes. As a matter of fact, the eastern part of the Paleo-Tethys Ocean had a more complicated history involving at least two oceanic basins, or 'branches' of the Paleo-Tethys. A northern branch, which is often called the Paleo-Jinshajiang, separated the Tarim, Qaidam, Central Qilian, Alxa (or Alex) and North China blocks in the north from the Eastern Qiangtang Terrane and the Indochina and South China blocks in the south. A southern branch, often called the Longmu Tso-Shuanghu Ocean, separated the Eastern Qiangtang Terrane and the Indochina-South China blocks from the northeast margin of Gondwana and the Sibumasu and Western Qiangtang-Lhasa terranes which were likely peripheral to it in late Paleozoic times (Jian et al., 2009a, 2009b; Li, 2008; Zhai et al., 2011; Zhao et al., 2018; Fig. 1). The collision between the Qiangtang Terrane and the Tarim/Songpan-Ganzi terranes can be regarded as the closure of the Paleo-Tethys Ocean (at least a key branch of it). The closure timing proposed is mutually exclusive; various ages are argued for such as the Late Permian

(Sha & Fürsich, 1999), the Early–Middle Triassic (Pullen et al., 2008; Zi et al., 2012), the Late Triassic (Li, 2008; Song et al., 2015; Yan et al., 2016), and the latest Triassic–Early Jurassic (Roger et al., 2010; Zhang et al., 2014; Liu, et al., 2019; Tan et al., 2020). The probable reason for this remarkable diversion is that continental collision is a complex process, and different approaches (e.g., paleontological, paleomagnetic, magmatic, sedimentologic, structural) represent different stages and/or upper/lower limits of the collision. Recent paleomagnetic studies show that it was during the Late Triassic when the Eastern Qiangtang Terrane collided with the Tarim/Songpan-Ganzi/Yidun terranes which thereby led to the closure of the Paleo-Jinshajiang Ocean (Guan et al., 2021; Yu et al., 2022a).

The Lhasa-Qiangtang collision and Closure of the Meso-Tethys Ocean

The Meso-Tethys Ocean, also referred to as Bangong-Nujiang Ocean in some literature, is represented mainly by the Bangong-Nujiang Suture Zone (e.g., Li et al., 2019a; Cao et al., 2019; Chen et al., 2020). It separated the Lhasa Terrane to the south from the Qiangtang Terrane to the north prior to the early Mesozoic. The Meso-Tethys Ocean closed ultimately after existing for approximately 100 Myr (Yin & Harrison, 2000; Liu et al., 2018). There is still considerable controversy surrounding when and how the Lhasa-Qiangtang collision occurred. For example, the age of the Lhasa-Qiangtang collision is argued to range from the Middle Jurassic (Xu et al., 1985; Ma et al., 2017), to the Late Jurassic-Early Cretaceous (Yin & Harrison, 2000; Kapp et al., 2003a, 2007; Zhu et al., 2013, 2016; Zhang et al., 2004; Yan et al., 2016; Li et al., 2018, 2019a, 2019b; Chen et al., 2020), and even the Late Cretaceous (Zhang et al., 2012; Li et al., 2014; Fan et al., 2018b). The collision of the Lhasa and Qiangtang terranes occurred either synchronously (e.g., Zhang et al., 2012; Chen et al., 2020) or diachronously younging to the west in a scissor-like fashion (e.g., Dewey et al., 1988, Yin & Harrison, 2000; Kapp et al., 2003a, 2003b; Pan et al., 2004c; Zhu et al., 2013; Yan et al., 2016).

The Cenozoic tectonic deformation of the Qiangtang Terrane

One of the most spectacular events of Earth's history is the Cenozoic India-Eurasia collision and the subsequent subduction of the Indian Plate underneath the Eurasian Plate (Yin & Harrison, 2000; Tapponnier et al., 2001; Ding et al., 2017), resulting in significant latitudinal crustal shortening of the Asian lithospheric crust (Tapponnier et al., 1982, 2001; Yin & Harrison, 2000; Van Hinsbergen et al., 2011; Tong et al., 2017; Zhang et al., 2018, 2020a). To accommodate the shortening, the Tibetan Plateau either has undergone a wide continuously distributed deformation that gave rise to the thickening of the plateau lithosphere (England & Houseman, 1989; Molnar et al., 1993), or the collages of the Tibetan Plateau have been squeezed out and extruded eastward/ southward along several lithospheric-scale strike-slip fault systems (Peltzer & Tapponnier, 1988; Burchfiel et al., 1989; Tapponnier et al., 1990, 2001; Wang & Burchfiel, 2000; Molnar & Dayem, 2010). The Qiangtang Terrane has an interesting shape: it is aligned approximately east-west in its western and central

segments, and gradually shifts to a nearly north-south orientation at the eastern ending (Fig. 1). This feature strongly suggests that it has been subjected to significant clockwise rotations during the subduction of the Indian Plate underneath the Eurasian Plate (Zhang et al., 2018, 2020a; Li et al., 2020b).

To summarize, the Jurassic and Cretaceous evolution of the Qiangtang Terrane can provide important clues to understand not only the Lhasa-Qiangtang collision (hence the closure of the Meso-Tethys-Bangong-Nujiang Ocean) but also the India-Eurasia collision (hence the closure of the Neo-Tethys Ocean) (Allégre et al., 1984; Dewey et al., 1988; Yin & Harrison, 2000; Zhang et al., 2012; Zhu et al., 2013; Yan et al., 2016; Cao et al., 2019). Motivated by this topic, this thesis aims to carry out a paleomagnetism-based investigation, expecting to contribute to our understanding of the evolution history of the Qiangtang Terrane, with implications for the Tibetan Plateau.

Post-Jurassic paleomagnetic data of the Qiangtang Terrane

Paleomagnetism is a powerful tool for quantitative paleogeographic reconstruction. Many studies have been carried out on the Mesozoic paleographic position of the Qiangtang Terrane (Lin & Watts, 1988; Otofuji et al., 1990; Dong et al., 1990,1991; Huang et al., 1992; Chen et al., 1993; Song et al., 2012; Cheng et al., 2012; Ren et al., 2013; Song et al., 2015, 2020; Tong et al., 2015; Yan et al., 2016; Chen et al., 2017b; Meng et al., 2018; Ran et al., 2017; Zhou et al., 2019; Cao et al., 2019, 2020; Song et al., 2020; Guan et al., 2021; Yu et al., 2022a). Here we focus on the Jurassic and Cretaceous data; after consideration of the 'Van der Voo criteria' and the recently established 'R-criteria' (Van der Voo, 1990; Meert et al., 2020), robust paleomagnetic data sets are still rather limited in number given the size of the terrane. Based on paleomagnetic studies from the same Middle-Upper Jurassic marine sedimentary rock unit (the Yanshiping Group), Cheng et al. (2012), Ren et al. (2013) and Yan et al. (2016) obtain paleolatitudes of 20–25◦N for the Yanshiping area (Fig. 1), while Ran et al. (2017) suggest a synfolding remagnetization acquired during the early stage of folding (about 20 per cent). In the Shuanghu area (~300 km west of the Yanshiping area), Cao et al. (2019) report a Jurassic paleolatitude of ~35◦N for their reference site. In contrast, six Cretaceous results from the Western Qiangtang Terrane (Chen et al., 1993; Meng et al., 2018; Chen et al., 2017b; Cao et al., 2020) and two from the Eastern Qiangtang Terrane (Huang et al., 1992; Tong et al., 2015) meet the Van der Voo/R criteria. These data reveal consistent paleolatitudes at ~30°N (Meng et al., 2018; Chen et al., 2017b; Cao et al., 2020) for the Western Qiangtang Terrane, while the clearly shallower inclination from the Cretaceous red sandstones (Chen et al., 1993) may be attributed to inclination shallowing or the relative movement between the different portions of the Qiangtang Terrane. The Eastern Qiangtang Terrane was relatively stable at ~32-36°N during the Cretaceous (Huang et al., 1992; Tong et al., 2015).

Pertaining to the studies of Cenozoic strata, differential rotations resulting from the

India-Eurasia collision are a key topic. Zhang et al. (2020a) suggest that the Nangqian Basin has experienced a counterclockwise rotation of 25.9° ± 7.2° during ~52–46 Ma, and an insignificant rotation during ~46–41 Ma, followed by a clockwise rotation of 24.4° ± 9.7° during ~41–35 Ma. Palaeomagnetic results of volcanic rocks dated ~49–51 Ma in the Xialaxiu Basin show a consistent declination as the nearby Nangqian Basin, which indicates similar rotation histories of these regions (Roperch et al., 2017). In the Gongjue Basin, a three-stage rotation history since ~53 Ma is recorded as well (Zhang et al., 2018; Li et al., 2020b).

Approach

This thesis aims at widening current knowledge of the Jurassic and Cretaceous tectonic evolution of the Qiangtang Terrane. To achieve this goal, we have applied state-of-the-art paleomagnetism to paleogeographic reconstructions. Specifically, we place much weight on the timing and mechanism of the remanence acquisition for the studied lithologies. To investigate textural relationships and diagenetic conditions of magnetic minerals of these rocks, we adopted microscopic observations for the polished thin sections. In addition, other geophysical techniques, specifically gravity data, are used for providing further information to the kinematic reconstructions.

Demagnetization

Both alternating field and thermal demagnetization are applied to isolate the characteristic remanent magnetization (ChRM). The ChRM directions were determined from at least four successive steps by principal component analysis (Kirschvink, 1980). Specimens with maximum angular deviation (MAD) >15° were rejected for further analysis. Site-mean directions were calculated using Fisher's statistics (Fisher, 1953). the E/I method of Tauxe & Kent (2004) is used to detect possible inclination shallowing bias.

Rock magnetism

To identify the type, concentration, domain state, and potential alteration during heating, we have used integrated rock magnetic analyses, including multiple thermomagnetic experiments (susceptibility vs. temperature and magnetization vs. temperature), hysteresis measurements (loops, acquisition curves of isothermal remanent magnetization & backfield curves, first order reversal curves), acquisition curves of anhysteretic remanent magnetization, component analysis of isothermal/anhysteretic remanent magnetization. End-member modeling of isothermal/anhysteretic remanent magnetization developed by Gong et al. (2009) has been used to diagnose potential remagnetization. Anisotropy of magnetic susceptibility has been applied to evaluate paleostress.

Petrography

Petrographic analysis is commonly used to characterize rock samples, providing an overview of the compositions of the rocks. It is of value to identify textural relationships and diagenetic conditions of magnetic minerals. Micrographs of the same area in a thin section can be obtained under plane-polarized light, cross-polarized light, and reflected light.

Geophysics (gravity)

Geophysics uses physics to examine the Earth's structure, climate, oceans, etc. As a branch of geophysics, for a given region a gravity survey reveals changes resulting from density differences of deep structures, thus providing more detailed information on the rock types' distribution within the lithosphere than otherwise possible (Blakely, 1996; Hinze et al., 2013). The wavelet transform decomposition method is adopted here to evaluate the gravity data (Mallat, 1989; Moreau et al., 1997, 1999; Fedi & Quarta, 1998; Gao et al., 2000; Yang et al., 2015; Xu et al., 2017, 2018).

S-EN

SUMMARY

This thesis presents new paleogeographic data from the Early Cretaceous granites and the Mid-Late Jurassic limestones in the Zaduo area (Eastern Qiangtang Terrane), Tibetan Plateau. The outcome of the granite study provides further insight into the Lhasa-Qiangtang collision (**chapter 1**). However, the limestones appear to be remagnetized. The remagnetization is shown to be related to the India-Eurasia collision, and the magnetic fabric of the remagnetized limestones documented the NNE-SSW oriented compression during the remagnetization (**chapter 2** and **chapter 4**). The combination of gravity and paleomagnetic data reveals a coupled lithosphere-scale oroclinal deformation of the eastern ending of the Qiangtang Terrane (**chapter 3**). Given the fact that the Jurassic and Carboniferous limestones are found to have been remagnetized, while the Triassic and Cretaceous volcanic rocks are not, we carried out a comparative study of the remagnetized and unremagnetized rocks, which mainly concentrates on their rock magnetic properties with the aim to further explore magnetic features of remagnetized and non-remagnetized rocks (**chapter 5**).

In **Chapter 1** entitled "The Early Cretaceous Zaduo granite, Eastern Qiangtang Terrane (China) – an attempt to constrain its paleolatitude and tectonic implications", we present a new paleomagnetic investigation on an Early Cretaceous granite (~126 Ma) in the Zaduo area, Eastern Qiangtang Terrane. Petrographic observations indicate crystallization from primary melts with only limited subsequent alteration (some chloritization of biotite). Magnetite appears to be the dominant carrier of the characteristic remanent magnetization (ChRM) based on stepwise progressive demagnetization of the natural remanent magnetization (NRM), supplemented by detailed rock magnetic measurements, including magnetization versus temperature, and acquisition curves of the isothermal and anhysteretic remanent magnetization. The inconsistent demagnetization behavior between alternating field (AF) demagnetization at high levels and thermal demagnetization was attributed to the development of gyroremanent magnetization in the AF demagnetization generated by fine-grained single domain magnetite. We compared the expected bedding attitudes ($Strike_{exp}$ = 43.1°, Dip_{exp} = 46.1°) derived from published data (Huang et al., 1992; Tong et al., 2015) with the average observed

bedding attitudes ($Strike_{obs}$ = 54°, Dip_{obs} = 32°) of the Middle-Upper Jurassic sandstones of the Yanshiping Group that was intruded by the Early Cretaceous granite. The discrepancy between the expected and measured bedding attitudes implies that the strata of the Yanshiping Group in the Zaduo area were already tilted prior to the intrusion of the ~126 Ma Zaduo granite, which was attributed to the Lhasa-Qiangtang collision and the closure of the Bangong-Nujiang Ocean. The tilting/folding of the strata was generally delayed by layer parallel shortening processes during the early stages of the deformation, thus suggesting an older Lhasa-Qiangtang collision (i.e., >126 Ma).

In **Chapter 2** entitled "Remagnetization of the Jurassic limestones in the Zaduo area, Eastern Qiangtang Terrane (Tibetan Plateau, China): implications for the India–Eurasia collision", we paleomagnetically investigate the Middle-Upper Jurassic limestones of the Yanshiping group in the Zaduo area (32.5°N, 95.2°E), in the eastern Qiangtang Terrane. Both thermal and AF demagnetizations were carried out to isolate the ChRM. Despite a positive reversals test, rock magnetic information points to a remagnetized ChRM. The ChRM is residing in stable single-domain magnetite grains with cogenetic superparamagnetic particles. The co-occurrence of stable single-domain and superparamagnetic magnetites generates distinct rock-magnetic properties often referred to as the "remagnetized fingerprint" in limestones. This remagnetization process is also manifested by the widespread occurrence of gypsum veinlets in the limestones. The site-mean direction of the 12 sites after tilt-correction is declination D_s = 30.6°, inclination I_s = 35.6°, concentration parameter κ_s = 182.9, and 95% confidence cone α_{95} = 3.2°, corresponding to a paleolatitude of ~19.7° ± 2.8° N for the study area. The corresponding paleopole (59.8° N, 202.7° E with 95% confidence cone A_{95} = 2.8°) points to an NRM acquired after the India-Eurasia collision. The original sediments were likely anoxic because of the high organic carbon fluxes that prevailed during their deposition. After the India-Eurasia collision, it is envisaged that conditions became more oxic, giving rise to the oxidation of iron sulfides to authigenic magnetite and the acquisition of a secondary chemical remanent magnetization (CRM). The Zaduo area in the Eastern Qiangtang Terrane has experienced ~15.7° ± 3.2° (~1740 ± 350 km) of latitudinal crustal shortening since the Eocene. In addition, the clockwise rotation responding to the India-Eurasia collision is also detected in the Zaduo area.

In **Chapter 3** named "Dynamic deformation of the SE Tibetan Plateau: Insights from the Cenozoic oroclinal bending in the Eastern Qiangtang Terrane", we quantified the arcuate shapes at the eastern ending of the Qiangtang Terrane paleomagnetically. It reveals a secondary orocline formed after the Late Eocene. The deep structures in this area were also investigated using gravity data. The gravity anomalies were separated into different layers, representing density variations from the shallow to the deep crust. The orocline as expressed at the Earth's surface and the gravity anomaly orientations in the deep crust appear to be consistent, thus favoring a

coupled lithosphere-scale oroclinal deformation. We provide a more dynamic scenario of the growth and deformation in the eastern Tibetan Plateau: the orocline bending of the eastern ending of the Qiangtang Terrane occurred after the Late Eocene, during which a channel for crustal flow was created. The large-scale crustal flow after the Miocene dominated in the later stage of the uplift and outward expansion of the Tibetan Plateau.

In **Chapter 4** "Inverse magnetic fabric of the remagnetized limestones in the Zaduo area, Eastern Qiangtang Terrane (China) – implications for the orocline", we specify the magnetic fabrics of the remagnetized limestones described in **Chapter 2**. Both bulk susceptibility (K_m) and remanences are carried by authigenic magnetite as unveiled by their comparison. Trends in K_m were compared to trends in two remanences: K_m versus the NRM and K_m versus saturation isothermal remanent magnetization. Also the relation between K_m and the saturation magnetization was evaluated. Most of the magnetite grains have axial ratios less than 1.3:1, giving rise to the inverse magnetic fabrics observed. Four groups are distinguished in our sample collection based on their magnetic fabrics and rock magnetic behavior. The data document the NNE-SSW oriented compression during the Eocene remagnetization, whereas the early Paleogene NE-SW compression in the Gongjue area was recorded. This inconsistency in compression is the early response to the India-Eurasia collision and results in different rotations surrounding the East Himalayan Syntaxis.

Chapter 5 is titled "Remagnetization of magnetite-bearing rocks in the Zaduo area, Eastern Qiangtang Terrane: mechanism and diagnosis". It discusses a catalog of rock magnetic differences between remagnetized and unremagnetized rocks of the Zaduo area which may serve as a template to recognize such rocks elsewhere. The Jurassic and Carboniferous limestones were deemed to have been remagnetized, while the Cretaceous and Permo-Triassic tuff/rhyolite have preserved a primary NRM. Magnetite is the dominant magnetic carrier in all these rocks. The results consistently suggest that the magnetic carriers of the CRM are authigenic magnetite of stable single domain to superparamagnetic size ranges, resulting in uncommon rock magnetic characteristics, such as low unblocking temperature, 'wasp-waisted' hysteresis loops, the 'remagnetization trend' on the Day plot, etc. In addition, quantitative analysis of the hysteresis loop shape for different lithologies indicates its validity in detecting remagnetization. The hysteresis behavior of the remagnetized and unremagnetized rocks is illustrated in the Day plot, Néel diagram, Borradaile diagram, and Fabian diagram. We provide our assessment of these diagrams on discriminating remagnetized rocks from unremagnetized rocks. Our research emphasizes that the rock magnetic properties can serve as tools to diagnose remagnetization in magnetite-dominated rocks.

S-NL

SAMENVATTING

In dit proefschrift worden nieuwe paleogeografische gegevens gepresenteerd voor het Zaduo-gebied (Oost Qiangtang Blok, Tibetaans Plateau, China): graniet gesteente van Vroeg Krijt ouderdom en een kalksteensequentie van Midden tot Laat Jura ouderdom. De uitkomst van de granietstudie geeft meer inzicht in de botsing tussen de Lhasa en Qiangtang blokken (**hoofdstuk 1**). De kalksteensequentie draagt echter geen oorspronkelijk Jura paleomagnetisch signaal meer: het is geremagnetiseerd. De remagnetisatie blijkt gerelateerd te zijn aan de botsing tussen India en Eurazië. De magnetische anisotropie van de geremagnetiseerde kalkstenen heeft de NNO-ZZW georiënteerde compressie tijdens de remagnetisatie vastgelegd (**hoofdstuk 2** en **hoofdstuk 4**). Het oostelijke uiteinde van het Qiangtang Blok is een zogeheten orocliene zoals blijkt uit analyse van de paleomagnetische gegevens. De combinatie van deze gegevens met zwaartekracht data laat zien dat de oroclinale buiging tot op een diepte van meer dan 40 km heeft plaatsgevonden, en is hier dus een process op lithosfeer-schaal (**hoofdstuk 3**). De kalkstenen uit de Jura en ook uit het Carboon zijn gemagnetiseerd, terwijl de vulkanische gesteentes uit het Trias en het Krijt dat niet zijn. Daarom hebben we de magnetische eigenschappen van deze geremagnetiseerde en niet-geremagnetiseerde gesteentes met elkaar vergeleken, met als overkoepelend doel om de magnetische kenmerken van geremagnetiseerde en niet-geremagnetiseerde gesteenten onafhankelijk te kunnen onderscheiden, dat wil zeggen zonder gebruik te maken van paleomagnetische richtingen (**hoofdstuk 5**).

In **hoofdstuk 1**, met als titel "De Vroeg-Krijt Zaduo Graniet, Oost Qiangtang Blok – een poging om de paleolatitude te reconstrueren met gerelateerde tektonische implicaties", wordt een nieuw paleomagnetisch onderzoek naar een Vroeg-Krijt graniet (~126 Ma) in het Zaduo-gebied, Oost Qiangtang Blok gepresenteerd. Petrografische waarnemingen duiden op kristallisatie uit een primaire smelt met slechts beperkte latere alteratie (enige chloritisatie van biotiet). Magnetiet blijkt de dominante drager van de karakteristieke remanente magnetisatie (ChRM) te zijn op basis van stapsgewijze progressieve demagnetisatie van de natuurlijke remanente magnetisatie (NRM), aangevuld met gedetailleerde gesteentemagnetische metingen, waaronder de magnetisatie tegen de temperatuur, en acquisitie curves van de

isothermale en anhysteretische remanente magnetisatie. Wisselveld demagnetisatie (AF) bij hoge piekwaardes en thermische demagnetisatie laten een verschillend gedrag zien, toegeschreven aan het optreden van gyroremanente magnetisatie in de fijnkorrelige magnetiet van één-domein grootte tijdens de wisselveld-demagnetisatie. We vergeleken de verwachte laagstand ($Strike_{exp}$ = 43,1°, Dip_{exp} = 46,1°) afgeleid uit gepubliceerde gegevens (Huang et al., 1992; Tong et al., 2015) met de gemiddeld waargenomen laagstand ($Strike_{obs}$ = 54°, Dip_{obs} = 32 °) van de Midden-Laat-Jura zandsteen van de Yanshiping Group die is geintrudeerd door de graniet uit het Vroeg Krijt. De discrepantie tussen de verwachte en gemeten laagstand impliceert dat de gesteentelagen van de Yanshiping Group in het Zaduo-gebied al scheefgesteld waren vóór de intrusie van de ~126 Ma Zaduo-Graniet. Dit is een consequentie van de botsing tussen de Lhasa en Qiangtang blokken en de sluiting van de Bangong-Nujiang Oceaan. Het scheefstellen / plooien van de lagen is over het algemeen vertraagd door parallelle verkorting van de strukturen ten tijde van de vroege stadia van de deformatie, wat duidt op een oudere Lhasa-Qiangtang botsing (d.w.z. > 126 Ma).

In **hoofdstuk 2** getiteld "Remagnetisatie van de Jura kalkstenen in het Zaduo gebied, Oost Qiangtang Blok (Tibetaans Plateau, China): implicaties voor de botsing tussen India en Eurazië", is een paleomagnetisch onderzoek beschreven van de Midden-Laat Jura kalksteen uit de Yanshiping-Groep in het Zaduo gebied (32,5° N, 95,2° E), in het Oost Qiangtang Blok. Zowel thermische als wisselveld demagnetisaties zijn uitgevoerd om de ChRM te bepalen. Ondanks een positieve omkeringstest wijst gesteentemagnetische informatie op een geremagnetiseerde ChRM. De ChRM wordt gedragen door stabiele magnetietkorrels met één magnetisch domein die samen voorkomen met kleinere superparamagnetische korrels van de dezelfde generatie (co-genetisch). Het gelijktijdig voorkomen van stabiele één-domein magnetiet-korrels en superparamagnetische magnetiet-korrels genereert een typische gesteentemagnetische expressie in kalksteen die vaak de "geremagnetiseerde vingerafdruk" wordt genoemd. Dit remagnetisatieproces komt ook tot uiting in het wijdverbreid voorkomen van gipsaders in de kalksteen. De gemiddelde richting van de 12 locaties na correctie voor de laagstand is declinatie D_s = 30,6°, inclinatie I_s = 35,6°, concentratieparameter κ_s = 182,9, en 95% betrouwbaarheidsinterval α_{95} = 3,2°, overeenkomend met een paleolatitude van ~19,7° ± 2,8° N voor het studiegebied. De overeenkomstige paleopool (59,8° N, 202,7° E met 95% betrouwbaarheidsinterval A_{95} = 2,8°) wijst op een NRM verkregen na de botsing tussen India en Eurazië. De oorspronkelijke sedimenten waren waarschijnlijk anoxisch vanwege de hoge organische koolstofconcentratie die typisch is voor hun afzettingsmilieu. Het ligt in de lijn der verwachting dat na de botsing tussen India en Eurazië de omstandigheden meer oxisch werden, wat resulteerde in de oxidatie van ijzersulfiden tot authigene magnetiet met de bijbehorende secundaire chemische remanente magnetisatie (CRM). Het Zaduo-gebied in het Oost Qiangtang Blok heeft sinds het Eoceen een breedtegraad-verkorting van ~15,7 ° ± 3,2 ° (~1740 ± 350 km) ondergaan. Verder wordt

de kloksgewijze rotatie als reactie op de botsing tussen India en Eurazië ook waargenomen in het Zaduo-gebied.

In **Hoofdstuk 3** genaamd "Dynamische deformatie van het ZO Tibetaanse Plateau: Inzichten uit de Cenozoïsche oroclinale buiging in het Oost Qiangtang Blok", wordt de oroclinale buiging aan het oostelijke uiteinde van het Qiangtang Blok paleomagnetisch gekwantificeerd. Het betreft een secundaire orocliene die gevormd is na het Laat Eoceen. Ook de diepe structuren in dit gebied zijn onderzocht met behulp van zwaartekrachtgegevens. De zwaartekrachtafwijkingen zijn opgedeeld in verschillende lagen, die variaties in dichtheid vertegenwoordigen van de ondiepe tot de diepe korst. De expressie van de orocliene aan het aardoppervlak en het zwaartekracht-anomalie-patroon in de diepe korst lijken consistent te zijn, hetgeen een gekoppelde oroclinale vervorming op lithosfeerschaal inhoudt. Dit resulteert in een meer dynamisch scenario voor de groei en de deformatie van het oostelijke Tibetaanse Plateau: de oroclinale buiging van het oostelijke uiteinde van het Qiangtang Blok vond plaats na het Laat Eoceen, waarbij een kanaal voor zogeheten korst-stroom werd gecreëerd. De grootschalige korst-stroom na het Mioceen domineerde in het latere stadium van de opheffing en laterale expansie van het Tibetaans Plateau.

In **hoofdstuk 4** "Inverse magnetische anisotropie van de geremagnetiseerde kalkstenen in the Zaduo gebied, Oost Qiangtang Blok (China) – implicaties voor de orocliene", specificeren we de magnetische anisotropie van de geremagnetiseerde kalksteen beschreven in hoofdstuk 2. Zowel de bulk-susceptibiliteit (K_m) als remanenties worden gedragen door authigene magnetiet, zoals blijkt uit hun vergelijking. Trends in K_m zijn vergeleken met trends in twee remanenties: K_m versus de NRM en K_m versus de verzadigings isothermale remanente magnetisatie. Ook is de relatie tussen K_m en de verzadigingsmagnetisatie geëvalueerd. De meeste magnetietkorrels hebben een axiale verhouding van minder dan 1,3:1, wat aanleiding geeft tot de waargenomen inverse magnetische maaksels. In onze monstercollectie onderscheiden we vier groepen op basis van hun magnetische maaksels en gesteentemagnetisch gedrag. De gegevens laten de NNO-ZZW-georiënteerde compressie tijdens de Eocene remagnetisatie zien, terwijl een Vroeg Paleogene NO-ZW compressie in het Gongjue-gebied is vastgesteld. Deze inconsistentie in compressie is de vroege reactie op de botsing tussen India en Eurazië en resulteert in verschillende rotaties rond de Oostelijke Himalaya Syntaxis.

Hoofdstuk 5 is getiteld "Remagnetisatie van magnetiet-dragende gesteenten in het Zaduo-gebied, Oost-Qiangtang Blok: mechanisme en diagnose". Een catalogus van verschillen in magnetische eigenschappen tussen opnieuw gemagnetiseerde (geremagnetiseerde) en niet-geremagnetiseerde gesteenten uit het Zaduo-gebied is opgesteld, en kan als een sjabloon dienen om soortgelijke gesteenten elders te herkennen. De kalksteen uit het Jura en het Carboon zijn geremagnetiseerd, terwijl

de graniet en de tuf/rhyoliet uit respectievelijk het Krijt en Perm-Trias een primaire NRM hebben behouden. Magnetiet is de dominante magnetische drager in al deze gesteentes. Alle resultaten suggereren dat de magnetische drager van de CRM authigene magnetiet is met een korrelgrootte variërend van stabiele ééndomein grootte tot het kleinere superparamagnetische bereik, Dit resulteert in opmerkelijke gesteentemagnetische eigenschappen, zoals een lage deblokkerings-temperatuur, hysterese lussen met een 'wespen-taille', met plot-posities op de 'remagnetisatie-trend' in het Day diagram, enz.. Een kwantitatieve analyse van de vorm van de hysterese lussen maakt herkenning van remagnetisatie voor de verschillende lithologieën mogelijk. Het hysterese gedrag van de geremagnetiseerde en niet-geremagnetiseerde gesteentes wordt geïllustreerd in het Day-diagram, het Néel-diagram, het Borradaile-diagram en het Fabian-diagram. We analyseren hoe geschikt deze plot-methodes zijn bij het onderscheiden van geremagnetiseerde gesteentes en niet-geremagnetiseerde gesteentes. Ons onderzoek benadrukt dat de magnetische eigenschappen van gesteentes een nuttig hulpmiddel kunnen zijn bij het herkennen van remagnetisatie in door magnetiet gedomineerde gesteentes.

1

THE EARLY CRETACEOUS ZADUO GRANITE, EASTERN QIANGTANG TERRANE (CHINA) – AN ATTEMPT TO CONSTRAIN ITS PALEOLATITUDE AND TECTONIC IMPLICATIONS

Abstract

The Eastern Qiangtang Terrane is an orogenic-like belt around the Eastern Himalayan syntaxis (EHS). The deformation history of this terrane must be known to understand how the EHS region responded to the Lhasa-Qiangtang collision and the closure of the Bangong-Nujiang Ocean (BNO). Here, we present a new paleomagnetic investigation on an Early Cretaceous granite (~126 Ma) in the Zaduo area, Eastern Qiangtang Terrane. Petrographic observations reflect crystallization from primary melts with only limited subsequent alteration (chloritization of biotite). Magnetite appears to be the dominant carrier of the characteristic remanent magnetization (ChRM) based on stepwise demagnetization of the natural remanent magnetization, supplemented by detailed rock magnetic measurements, including magnetization versus temperature, and acquisition curves of the isothermal and anhysteretic remanent magnetization. End-member modeling of those acquisition curves helped to constrain the paleomagnetic analysis. The inconsistent demagnetization behavior between alternating field (AF) demagnetization at high levels and thermal demagnetization was attributed to the development of gyroremanent magnetization in the AF demagnetization generated by fine-grained single domain magnetite. The ChRM directions from 92 granite samples in geographic coordinates yield an average of declination (D_g) of 2.6° and inclination (I_g) of 38.6° (precision parameter k =51.4, and 95% confidence cone α_{95} = 2.1°). The amount of tilting of the granite is poorly constrained which makes proper correction rather tedious. We compared the expected bedding attitudes ($Strike_{exp}$=43.1°, Dip_{exp} =46.1°) derived from published data (Huang et al., 1992; Tong et al., 2015) with the average observed bedding attitudes ($Strike_{obs}$=54°, Dip_{obs} =32°) of the Middle-Upper Jurassic sandstones of the Yanshiping Group that was intruded by the Early

Cretaceous granite. The discrepancy between the expected and measured bedding attitudes implies that the strata of the Yanshiping Group in the Zaduo area were already tilted prior to the intrusion of the ~126 Ma Zaduo granite, which was attributed to the Lhasa-Qiangtang collision and the closure of the BNO. The collision led to a series of geological events, such as the tilting of the strata, the ophiolite emplacement, the development of a peripheral foreland basin, and the magmatic activity gap. The tilting/folding of the strata was generally delayed by the layer parallel shortening processes during the early stages of the deformation, thus suggesting an older Lhasa-Qiangtang collision (i.e., >126 Ma).

1.1 Introduction

The present-day Tibetan Plateau is known as the "roof" of the world and the "third pole" of the Earth. It is a complex terrane collage that comprises the Tethyan Himalaya, Lhasa, Qiangtang, Songpan-Ganzi and Qaidam-Qilian terranes from south to north (Fig. 1.1). These continental terranes sequentially accreted to Eurasia and formed the "Proto-Tibet" since the Paleozoic (Yin & Harrison, 2000; Tapponnier et al., 2001; Kapp et al., 2005, 2007; Metcalfe, 2011). The Qiangtang and Lhasa Terranes are two major crustal fragments in the central Tibetan Plateau and play a key role in understanding the formation and evolution of the "Proto-Tibet" region. In general, they are considered to have been separated by the Bangong-Nujiang Ocean (BNO) since the Permian (Dewey et al., 1988; Zhu et al., 2013; Metcalfe, 2013; Chen et al., 2017a; Fan et al., 2018a). The timing of the Lhasa-Qiangtang collision that followed the BNO closure, however, remains controversial, ranging from the Middle or Late Jurassic (Xu et al., 1985; Dewey et al., 1988; Yan et al., 2016; Ma et al., 2017; Li et al., 2019a, 2019b) to the Early Cretaceous (Kapp et al., 2003a, 2007; Zhu et al., 2006, 2011, 2013, 2016; Bian et al., 2017; Meng et al., 2018; Chen et al., 2020), or even the Late Cretaceous (Zhang et al., 2012; Liu et al., 2014a; Fan et al., 2014, 2015, 2018a, 2018b). Thus, one of the significant targets in the "Proto-Tibet" study is to determine when the Qiangtang Terrane collided with the Lhasa Terrane.

Paleomagnetism is an effective approach for quantifying terrane drift history. Many studies have been carried out on the Mesozoic paleographic positions of the Qiangtang Terrane (Lin & Watts, 1988; Otofuji et al., 1990; Dong et al., 1990, 1991; Huang et al., 1992; Chen et al., 1993; Song et al., 2012; Cheng et al., 2012; Ren et al., 2013; Song et al., 2015, 2020; Tong et al., 2015; Yan et al., 2016; Chen et al., 2017b; Meng et al., 2018; Ran et al., 2017; Zhou et al., 2019; Cao et al., 2019, 2020; Guan et al., 2021; Fu et al., 2022a). These studies have provided extensive knowledge on the tectonic evolution of the Qiangtang Terrane. However, most of these data were obtained from the center and western parts of the Qiangtang Terrane. Only three studies (Otofuji et al., 1990; Huang et al., 1992; Tong et al., 2015) were from the eastern part and all concerned Cretaceous rocks. To date, the timing of the Lhasa-Qiangtang collision is still under debate.

The Qiangtang Terrane is divided into the Eastern and Western Qiangtang subterranes (EQT, and WQT, respectively) (also named the Northern and Southern Qiangtang subterranes) (cf. Fig. 1.1; Yin & Harrison, 2000; Pan et al., 2004c; QGSI, 2005; Yan et al., 2016). The Zaduo area is the bending (transitional) part of the Eastern Qiangtang Terrane, where the tectonic trend is east–west to its west and north-south to its east and south (Fig. 1.1). Therefore, the tectonic evolution of the Zaduo area during the Late Jurassic to Early Cretaceous likely provides key information to address questions as to when the Lhasa-Qiangtang collision occurred and how the region deformed in response to the India-Asia collision. Investigations on the Middle-Upper Jurassic limestones of the Yanshiping Group in this area

indicate that primary natural remanent magnetization (NRM) was overprinted by a chemical remanent magnetization (CRM) during the India–Eurasia collision (Fu et al., 2022a). Igneous rocks are less prone to remagnetization than limestones. Thus, it is a very reasonable idea that we target the Cretaceous Zaduo granite to obtain trustworthy paleolatitude constraints to find a solution, which motivated this study.

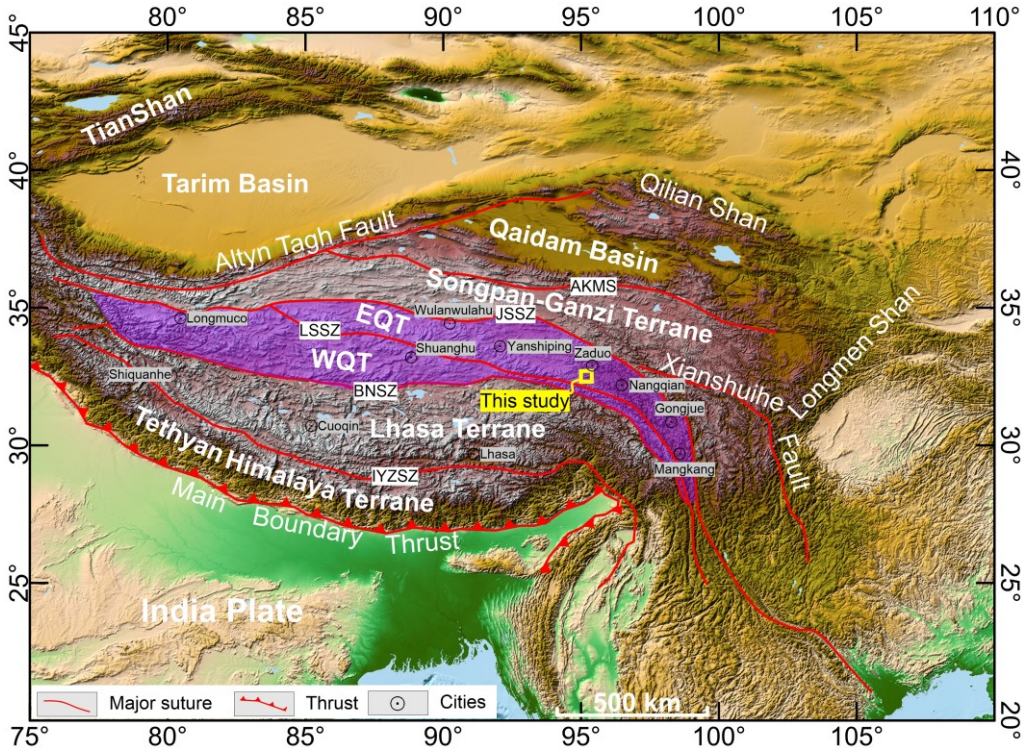

Figure 1.1. *Simplified tectonic map of the Tibetan Plateau and its adjacent regions. The abbreviations of the* tectonic *units are EQT: Eastern Qiangtang Terrane; WQT: Western Qiangtang Terrane; AKMS: Ayimaqing-Kunlun-Muztagh Suture Zone; JSSZ: Jinshajiang Suture Zone; LSSZ: Longmu Tso-Shuanghu Suture Zone; BNSZ: Bangong-Nujiang Suture Zone; IYZSZ: Indus-Yarlung Zangbo Suture Zone.*

In this paper, we report new paleomagnetic data of the ~126 Ma Cretaceous granite (QGSI, 2014) from the Zaduo area. The granite intruded into Middle-Upper Jurassic sandstones of the Yanshiping Group presently outcropping to the southeast of the granite and was overlain by the Paleogene-Neogene Tuotuohe Group (Et) presently outcropping to its northeast (Fig. 1.2, QGSI, 2014). Thermal and alternating field (AF) demagnetization yielded a set of characteristic remanent magnetization (ChRM) directions. Rock magnetic and petrographic studies were carried out to evaluate the reliability of the ChRM. Structural control of the granite and its adjacent formations was assessed as well. Overall, this sheds new light on the timing of the Lhasa-

Qiangtang collision, as well as the closure of the BNO.

1.2 Geological setting and sampling

The Qiangtang Terrane is one of the major units in the central Tibetan Plateau and is situated between the Bangong-Nujiang Suture Zone (BNSZ) to the south and the Jinshajiang Suture Zone (JSSZ) to the north (Fig. 1.1). It is aligned approximately east-west in the western and central parts with a maximum width of 400–500 km, but it is distinctly narrower (<150 km) in the eastern part where a gradual change to a north–south orientation is occurring (Yin & Harrison, 2000) (Fig. 1.1).

Our study transect (32.5°N, 95.3°E) is located in Zaduo County, the eastern part of the EQT (Fig. 1). The formations in this area are well exposed and mostly comprise Carboniferous, Jurassic and Cenozoic sedimentary rocks (Fig. 1.2A). The Cretaceous granite in this region intrudes Permo-Triassic volcanic rocks in the northwest and Middle-Upper Jurassic sandstones of the Yanshiping Group in the southeast. From base to top, the Paleogene to Neogene sedimentary rocks in this area consist of conformable contacts of the Tuotuohe (Et), Yaxicuo (Eny) and Wudaoliang (Ew) Formations, which conformably overlie each other (QGSI, 2005, 2014). The Jurassic Yanshiping Group consists of the Quemo Co (J_2q), Buqu ($J_{2-3}b$), Xiali (J_3x), Suowa (J_3s) and Xueshan (J_3x) Formations from base to top (QGSI 2005, 2014; Fang et al. 2016; Yan et al. 2016). The J_3s and J_3x Formations are absent in the study area (Fig. 1.2A). The granite intrusion is unconformably overlain by the Paleogene-Neogene Tuotuohe Group (Et) to its northeast (Fig. 1.2A, B). The Fenghuoshan Group which would normally be in between, is absent. The granite has an exposed surface of tens of square kilometers with pink to reddish color (Fig. 1.2C-E). The dominant lithologies of the granite intrusion include medium- to fine-grained monzogranite and syenogranite with feldspar phenocrysts ranging from 1 to 5 cm in size (QGSI, 2014). A previous geochemical study shows that the Zaduo granites have a moderately high alumina saturation index (ASI) >1.1, and a high SiO2 content (> ~70%). Thus, it is a typical peraluminous granite and classified as S-type (QGSI, 2005, 2014). Whole-rock and biotite K-Ar ages of ~126 Ma were reported for both monzogranite and syenogranite (QGSI, 2005, 2014). A total of 98 paleomagnetic core samples from 9 sites were collected from the Cretaceous granite intrusions; sites 1 to 4 are about 500 m away from sites 5 to 9. The lithology of the two locations is consistent, and no obvious weathering was observed. These core samples (2.5 cm diameter) were collected by using a portable gasoline-powered drill with a water cooling system. Each sample was oriented in the field using a solar and/or magnetic compass.

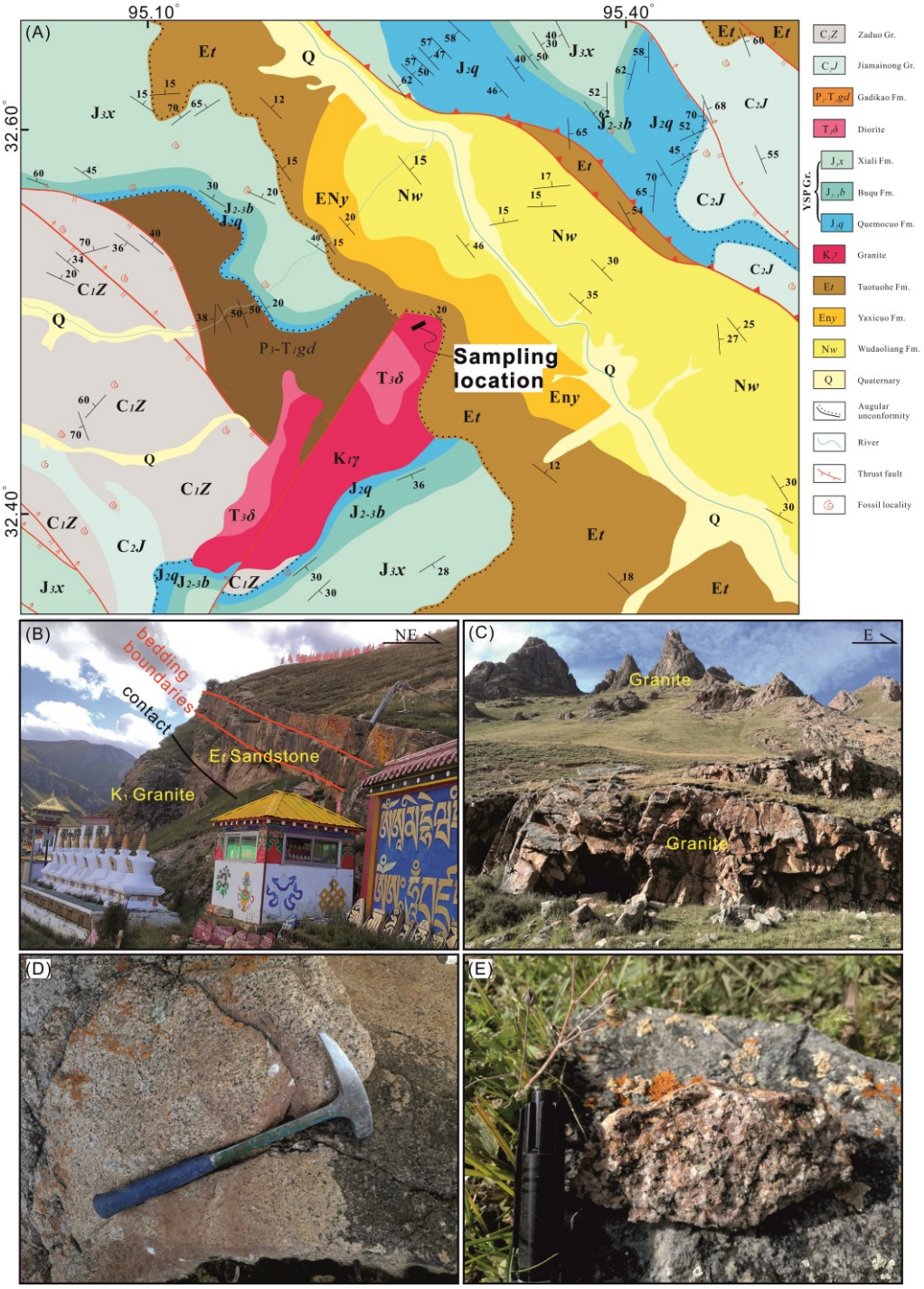
(A)
95.10°
95.40°
32.60°
32.40°
Et
Q
J3x
J2q
J2-3b
C2J
ENy
Nw
C1Z
P3-T1gd
T3δ
K1γ
Sampling location
Zaduo Gr.
Jiamainong Gr.
Gadikao Fm.
Diorite
Xiali Fm.
Buqu Fm.
Quemocuo Fm.
YSP Gr.
Granite
Tuotuohe Fm.
Yaxicuo Fm.
Wudaoliang Fm.
Quaternary
Augular unconformity
River
Thrust fault
Fossil locality
(B)
NE
bedding boundaries
contact
Et Sandstone
K1 Granite
(C)
E
Granite
Granite
(D)
(E)

Figure 1.2 (previous page). *(A) Geological map of the Zaduo area (modified from the 1:250 000 Zaduo County regional geological map [I46C004004] by the Qinghai Geological Survey Institute (QGSI) 2005). YSP: Yanshiping; Gr.:Group; Fm.: Formation. (B) Field photographs showing the contact between the Cretaceous granite and the sandstone of the Paleogene Tuotuohe Formation (Et). (C-E) Field photographs of representative outcrops and samples, hammer and marker for scale.*

1.3 Laboratory techniques

The cores were cut into specimens of 2.2 cm long and underwent stepwise AF demagnetization at the paleomagnetic laboratory of the Institute of Tibetan Plateau Research, Chinese Academy of Sciences, Beijing, China. In 20 steps, AF demagnetization was performed up to 140 mT with an ASC D2000/T demagnetizer. Six specimens were also progressively thermally demagnetized (TD) for comparison in 23 steps (80, 150, 200, 250, 300, 350, 400, 450, 475, 500, 530, 560, 570, 585, 610, 630, 650, 660, 665, 670, 675, 680, and 685 °C) in an ASC TD-48 oven with an internal residual field of less than 10 nT. The remaining NRM after each step was measured on a 2G Enterprises cryogenic magnetometer in a magnetically shielded room, which has an average field intensity of ~170 nT.

To investigate the mineralogical features of the granite, polished thin sections were prepared for microscopic observations with a polarizing microscope. Micrographs in plane-polarized light (PPL) and reflected light (RL) of the same area were obtained by means of a Leica DM750 optical microscope with a DMC5400 digital camera in the 'Fort Hoofddijk' paleomagnetic laboratory of Utrecht University, Netherlands.

Rock magnetic tests, including high-field thermomagnetic runs (magnetization versus temperature), acquisition curves of the isothermal remanent magnetization (IRM) and anhysteretic remanent magnetization (ARM), were conducted at the 'Fort Hoofddijk' Palaeomagnetic Laboratory. The high-field thermomagnetic runs were measured in air by an in-house-built horizontal translation type Curie balance with a sensitivity of ~5 × 10^{-9} Am^2 (Mullender et al., 1993). Approximately 60–80 mg of four representative samples were crushed to coarse powder (< 4 mm) with a conventional agate mortar and pestle, after which they were put into a quartz glass sample holder and held in place by quartz wool. The magnetic measurements were conducted with heating and cooling rates of 6 °C min^{-1} and 10 ℃ min^{-1}, respectively. The samples were first heated to 250 °C, cooled back to 150 °C, and then heated to 350 °C with cooling to 250 °C. The procedure was completed after performing several more of these heating-cooling cycles up to 700 °C followed by final cooling back to room temperature with an applied magnetic field of 100 mT to 300 mT. The successive peak temperatures of subsequent cycles were 250, 150, 350, 250, 450, 350, 520, 420, 620, 500 and 700 °C. The ARM acquisition curves of thirty-three representative samples were acquired in 19 steps up to a 150 mT peak AC field superimposed with a 40 μT direct field. Subsequently, IRM acquisition curves (43

field steps) were measured on those samples with a maximum applied field of 700 mT. Both ARMs and IRMs were measured by an in-house-developed robot (Mullender et al., 2016), which allowed the samples to pass through a 2G Enterprises SQUID magnetometer (noise level 10^{-12} Am^2) hosted in a magnetically shielded room (residual field <200 nT) at Utrecht University.

To quantitatively estimate the contributions of different magnetic carriers, IRM component analysis of Kruiver et al. (2001) was applied to the 33 samples of the two granite types. A parameter $B_{1/2}$ is defined as the field at which half of saturation isothermal remanent magnetization (SIRM) is reached, and another dispersion parameter DP is defined as the width of the distribution. For the paleomagnetic direction statistics, principal component analysis (Kirschvink, 1980) on at least five successive steps was performed to determine ChRMs, and directions with high maximum angular deviation (MAD) values (>15°) were systematically rejected from further analysis. Sample-mean ChRM directions were calculated using the statistical methods described by Fisher (1953). Because gyroremanent magnetization (GRM) occurred in so-called Type 2 granite samples, the directions towards the origin below 24mT were calculated for those samples. End-member modeling was used to illustrate the mechanism of remanence acquisition and to confirm a primary NRM; measurement and data analysis procedures are described in Aben et al. (2014), and the program used in this paper can be found online (http://people.rses.anu.edu.au/heslop_d/).

1.4 Petrography

Sampled outcrops of the Zaduo granite show a typical homogeneous texture and are barely weathered (Fig. 1.2D, E). Minerals in Type 2 samples are finer and cleaner than those in the Type 1 samples (Fig. 1.3). A classic granitic texture appears in thin section observations consisting of quartz, feldspar and biotite; opaque minerals include magnetite (Fig. 1.3). Quartz is one of the main constituents of the granite. It is in direct contact with other minerals and mostly > 1.0 mm in size. In addition, it is invariably clear and unaltered, being characterized by euhedral crystals (Fig. 1.3). Feldspar includes alkali feldspar and plagioclase feldspar, and shows euhedral or subhedral crystals; some feldspar crystals display clear and straight grain boundaries and slight alteration that is characterized by an uneven color (Fig. 1.3A-F). The brown–yellow pleochroic grains in PPL are biotite. In general, biotite is accompanied by magnetite and/or chlorite and has regular and sharp grain boundaries. Chlorite is commonly formed as the product of biotite chloritization, showing greenish-yellow pleochroism and irregular and indistinguishable boundaries with biotite (Fig. 1.3 E, F). Magnetite is observed in most samples, frequently occurring as interstitial crystals with irregular shapes. However, Type 2 granite samples show fewer and smaller magnetite crystals than Type 1 granite samples (Fig. 1.3).

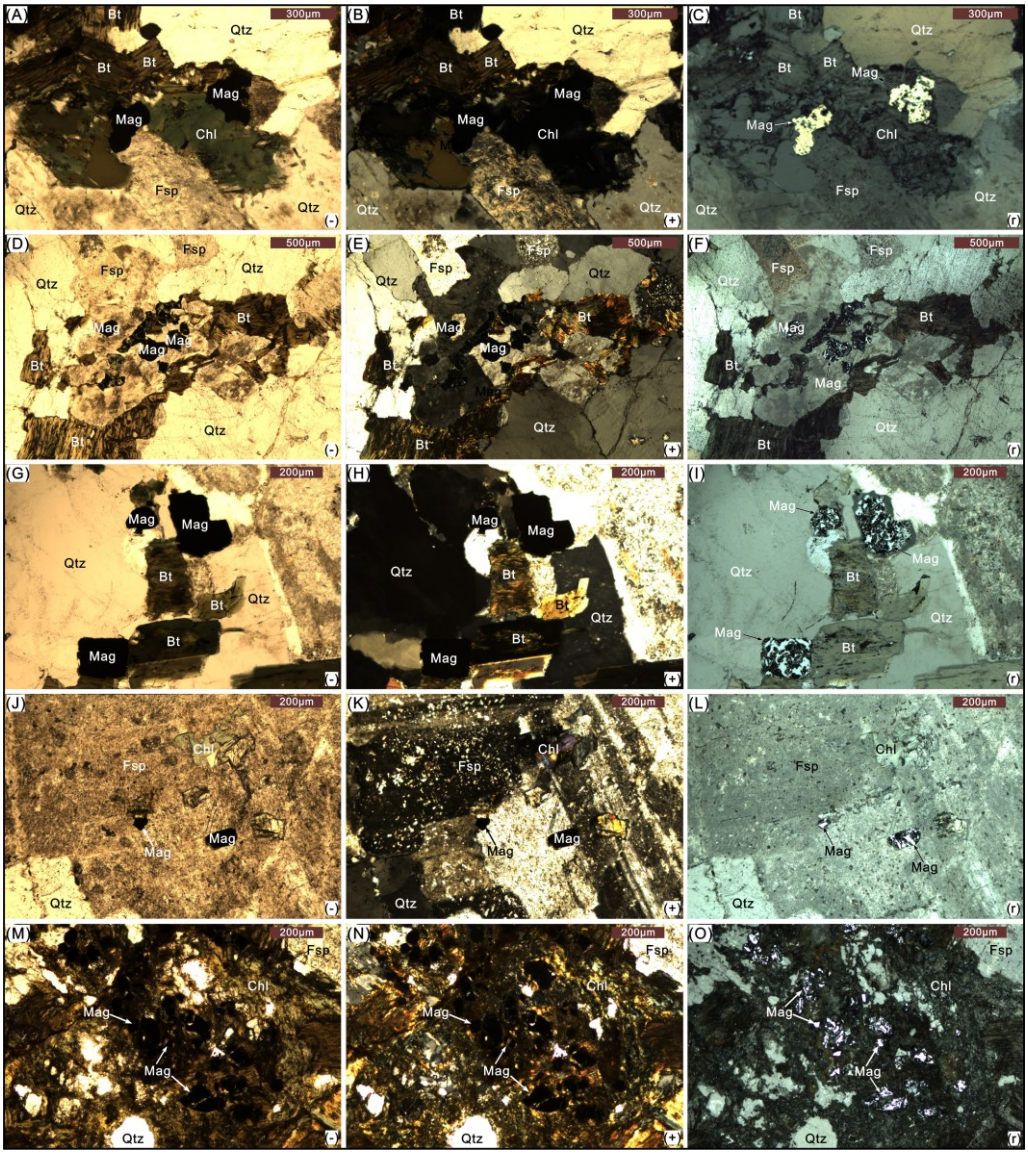

Figure 1.3. *Micrographs of Type 1 (A-I) and Type 2 (J-O) samples in plane-polarized light (-), cross-polarized light (+) and reflected light (r). Abbreviations of minerals in the images are Bt: biotite; Mag: magnetite; Fsp: feldspar; Qtz: quartz; Chl: chlorite.*

In the field, no massive veining or fluid motion was found in the granite. The outer surface of each sample was removed in the laboratory. Although chlorite is an alteration product, it is probably associated with the cooling of the granite, instead of being associated with later fluid motion due to intrusion of a new generation of granites. In addition, no ore bodies associated with the granite were reported. Magnetite formed during the cooling of the intrusion and the granite suffered minor

further hydrothermal alteration (some chloritization of biotite), thus probably reserving primary remanent magnetization.

1.5 Rock magnetism

1.5.1 *Magnetization versus temperature*

Stepwise high-field thermomagnetic runs of magnetization versus temperature were carried out for the Zaduo granite (Fig. 1.4). The initial magnetization intensity of most samples is fairly low (~5×10^{-3} to 5×10^{-2} Am^2/kg, Fig. 4A-C). Only ZD 9-10 has an initial magnetization intensity two orders of magnitude higher (~1.4 Am^2/kg, Fig. 1.4D). The thermomagnetic curves are characterized by a reversible decrease during heating to 700 °C and a steeper decrease in magnetization at ~500 °C – 580 °C, indicating magnetite. The descent of magnetization from ~580 °C to 700 °C is a very tiny and gradual process, which is thought to be the 'tail' of the magnetite or partially oxidized during heating instead of pointing to the presence of hematite. More importantly, we did not observe a distinct drop at ~680 °C, suggesting the absence of hematite. The final cooling curves from 700 °C to room temperature are slightly above the corresponding heating curves for most of the samples (Fig. 1.4A-C). These features likely indicate the alteration of a small quantity of Fe-bearing minerals to magnetite during heating (Dunlop & Özdemir, 1997; Li et al., 2016; Huang *et al.*, 2017a, 2017b). Only for the deviating sample ZD 9-10, it is below the heating curves.

Figure 1.4 (next page). *High-field thermomagnetic runs of representative samples from the Zaduo granite. Solid (dashed)* lines *indicate the heating (cooling) curves.*

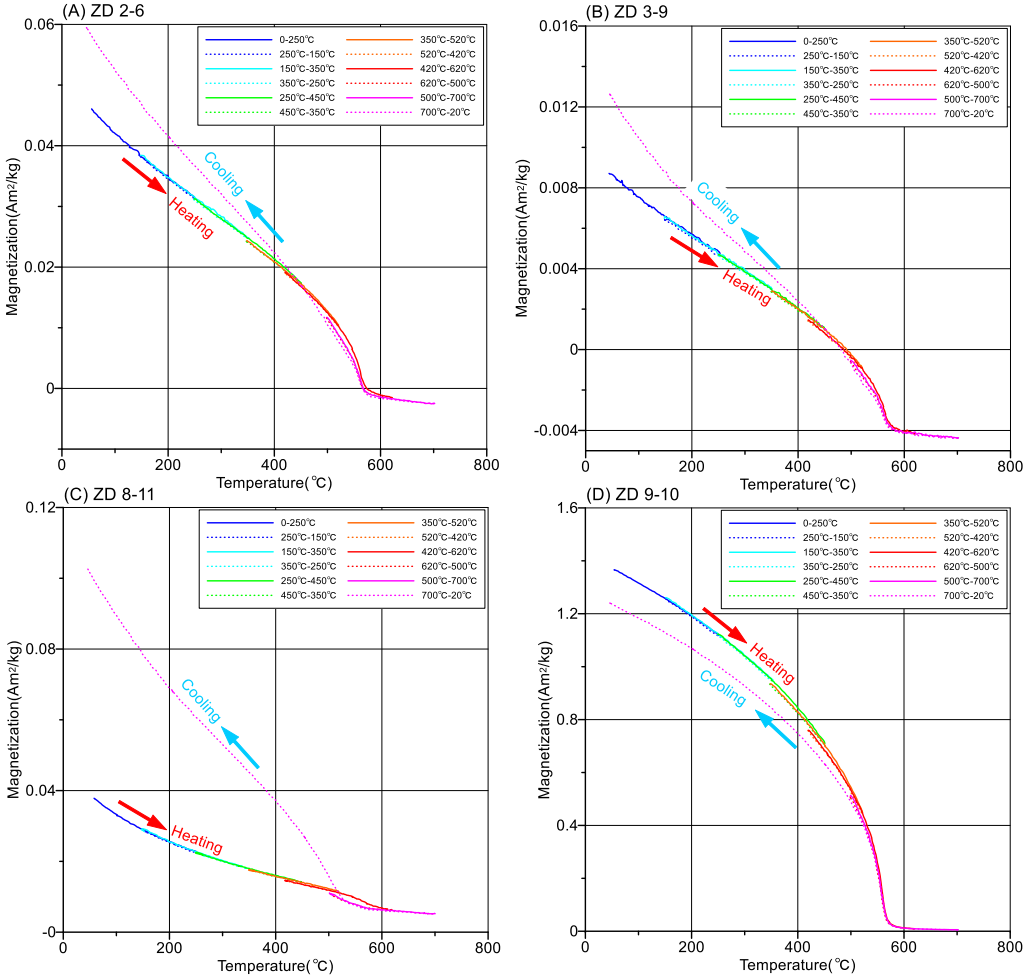

1.5.2 IRM acquisition curves and IRM component analysis

There are two types of granite samples classified by their rock magnetic and demagnetization characteristics. Type 1 comprises sites 1-4, as well as most of the samples of site 5, while Type 2 comprises the remainder. Thirty-three IRM acquisition curves show subtly different behavior between the two types. Type 1 includes seventeen samples and acquires 80-90% of its maximum IRM at 100 mT and is essentially saturated at 200 mT (Fig. 1.5A, B). These features indicate that low-coercivity magnetic components (e.g., magnetite sensu lato) are dominant. The saturation IRM values (IRM acquired in a field of 700 mT) range from ~1×10^{-3} to 3×10^{-3} Am²/kg (Fig. 1.5A, B; Supporting information Table S1.1, S1.4). Type 2 (16 samples)

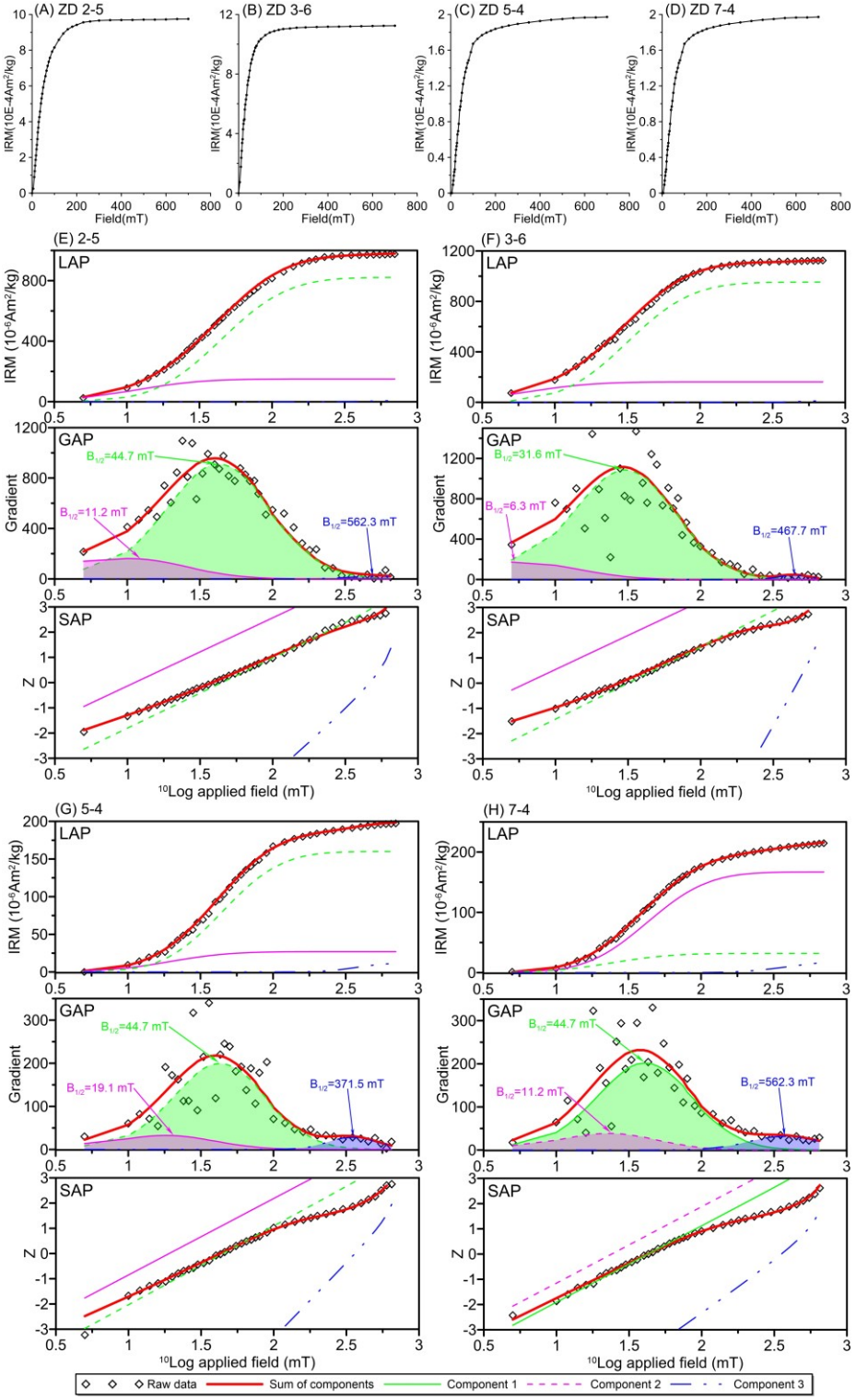
(A) ZD 2-5
(B) ZD 3-6
(C) ZD 5-4
(D) ZD 7-4
IRM(10E-4Am²/kg)
Field(mT)
(E) 2-5
(F) 3-6
(G) 5-4
(H) 7-4
LAP
GAP
SAP
IRM (10⁻⁶Am²/kg)
Gradient
Z
B1/2=44.7 mT
B1/2=11.2 mT
B1/2=562.3 mT
B1/2=31.6 mT
B1/2=6.3 mT
B1/2=467.7 mT
B1/2=19.1 mT
B1/2=371.5 mT
¹⁰Log applied field (mT)
Raw data
Sum of components
Component 1
Component 2
Component 3

Figure 1.5 (previous page). *(A-D) IRM acquisition curves of representative samples. (E-H) IRM component analysis* plots *(Kruiver et al., 2001) of representative samples. Squares are measured data points. The components are marked with different colored lines. $B_{1/2}$ and DP are in log_{10} mT. LAP: linear acquisition plot, GAP: gradient acquisition plot and SAP: standardised acquisition plot.*

behavior is also characterized by ~80-90% of the maximum IRM at 100 mT. However, the IRM acquisition curves show a gentle increase after 200 mT and seem to flatten off close to the maximum applied field of 700 mT. Thus, both typical magnetite and very fine-grained magnetite close to the SP threshold size (Gong et al., 2009) could be magnetic carriers in Type 2 granite. The saturation IRMs of Type 2 samples are much lower, below ~2×10^{-4} Am^2/kg (Fig. 1.5C, D; Supporting information Table S1.1, S1.4).

All of the IRM acquisition curves appear to be fit by up to three IRM components: component 1 with $B_{1/2}$ of ~10-20 mT, component 2 with $B_{1/2}$ of ~30-40 mT, and a harder component 3, with $B_{1/2}$ of ~400-600 mT (Fig. 1.5E-H, Supporting information Table S1.2). Component 1 has low coercivity and contributes ~15% to the SIRM. It is interpreted to be the result of thermally activated component 2 (Egli, 2004; Heslop et al., 2004; Huang et al., 2015a; Zhang et al., 2016b; Fu et al., 2022a) which results in a left-skewed distribution that must be fitted with an extra component in Kruiver et al. (2001) software that only considers symmetric log-Gaussian functions. Component 2 is the dominant magnetic carrier in the granite and contributes >80% to the SIRM; it is typically interpreted to be magnetite (e.g., Kruiver et al., 2001). Component 3 has a much higher coercivity and only contributes ~1-6% to the SIRM (Fig. 1.5E-H; Supporting information Table S1.2). This component can be interpreted along two lines: 1) hematite that has a typical $B_{1/2}$ value ranging from 300 to 800 mT (Kruiver & Passier, 2001); or 2) very fine-grained magnetite close to the SP threshold size, which may not be saturated at a fairly high field (Dekkers & Pietersen, 1992; Tauxe et al., 1996; Gong et al., 2009; Huang et al., 2015a). Here, we tend to favor the second option because hematite is not detected in the thermomagnetic runs. In addition, marginal oxidation of magnetite may result in a harder coercivity distribution. It is worth noting that Type 2 granite has a higher contribution to component 3 than Type 1 granite. Component 3 of Type 1 granite is only required to fit the 'tail' of the IRM acquisition curves (contributions < 1-2%). Thus, to some extent it is mineralogically less meaningful.

1.5.3 ARM acquisition curves analysis

ARM was imparted in a peak alternating field of 150 mT and a bias field of 40 μT (Supporting information Table S1.3). It is a sensitive probe of small variations in the domain state straddling the SD and pseudosingle domain (PSD) states (Hunt et al., 1995; Geiss et al., 2003). The ratio of ARM to IRM, as well as the shape of the acquisition curves of ARM are used as indicators of the domain state of the particles

(Egli & Lowrie, 2002). We used IRM acquired in a field of 100 mT (marked as IRM_{100mT}) and 700 mT (marked as IRM_{700mT}) to display the contribution of high-coercivity grains to the ratio of ARM/IRM. As shown in Fig. 1.6A, the ARM of Type 1 samples (~20 × 10^{-6} Am^2/kg) is distinctly higher than that of Type 2 samples (below ~20 × 10^{-6} Am^2/kg); similar characteristics can be observed in the SIRM (i.e., IRM_{700mT}, Fig. 1.6B; Supporting information Table S1.4). For Type 1 granite, the ratio of ARM/IRM_{100mT} is indistinguishable from the ratio of ARM/IRM_{700mT} (Fig. 1.6C), indicating that there is no obvious influence of high-coercivity grains. In contrast, the ratio of ARM/IRM_{100mT} is higher than the ratio of ARM/IRM_{700mT} for Type 2 granite (Fig. 1.6C), showing the influence of high-coercivity grains. A clear distribution of data points along a single line for Type 1 and 2 samples can be fitted with a linear trendline, whereas Type 1 samples have a larger coefficient of determination of the least-square fit (also reported in the Figure) than Type 2 samples (Fig. 1.6D). This testifies a finer but less uniform average magnetite grain size distribution in the Type 2 samples than in the Type 1 samples. These results are in line with the IRM component analyses.

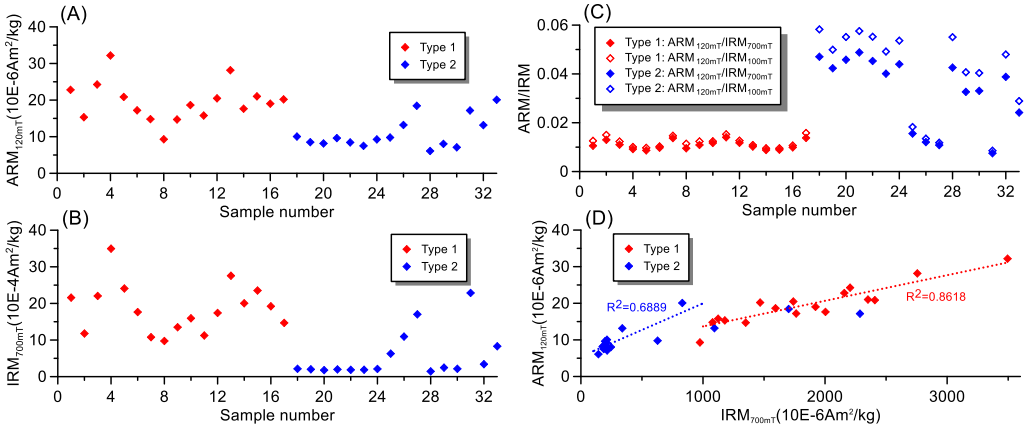

Figure 1.6. *(A-B) ARM and IRM acquired at 150 mT in a 40 T DC bias field and 700 mT respectively. (C) ARM* versus *IRM at sample level. (D) ARM versus IRM diagram confirming the uniformity in magnetic grain size for Types 1 and 2. The coefficient of determination of the least-square fitting is indicated for each data group.*

1.6 Demagnetization and chrm directional analyses

1.6.1 Demagnetization

The demagnetization characteristics are also different between Type 1 and Type 2 samples: 1) Type 1 with robust demagnetization behavior at a high field (temperature) that decays toward the origin, and 2) Type 2 with erratic demagnetization behavior at a high field level during AF demagnetization (>40 mT) but with a relatively stable demagnetization behavior of thermal demagnetization up to ~580 °C. More specifically, most of the Type 1 specimens exhibit a single NRM

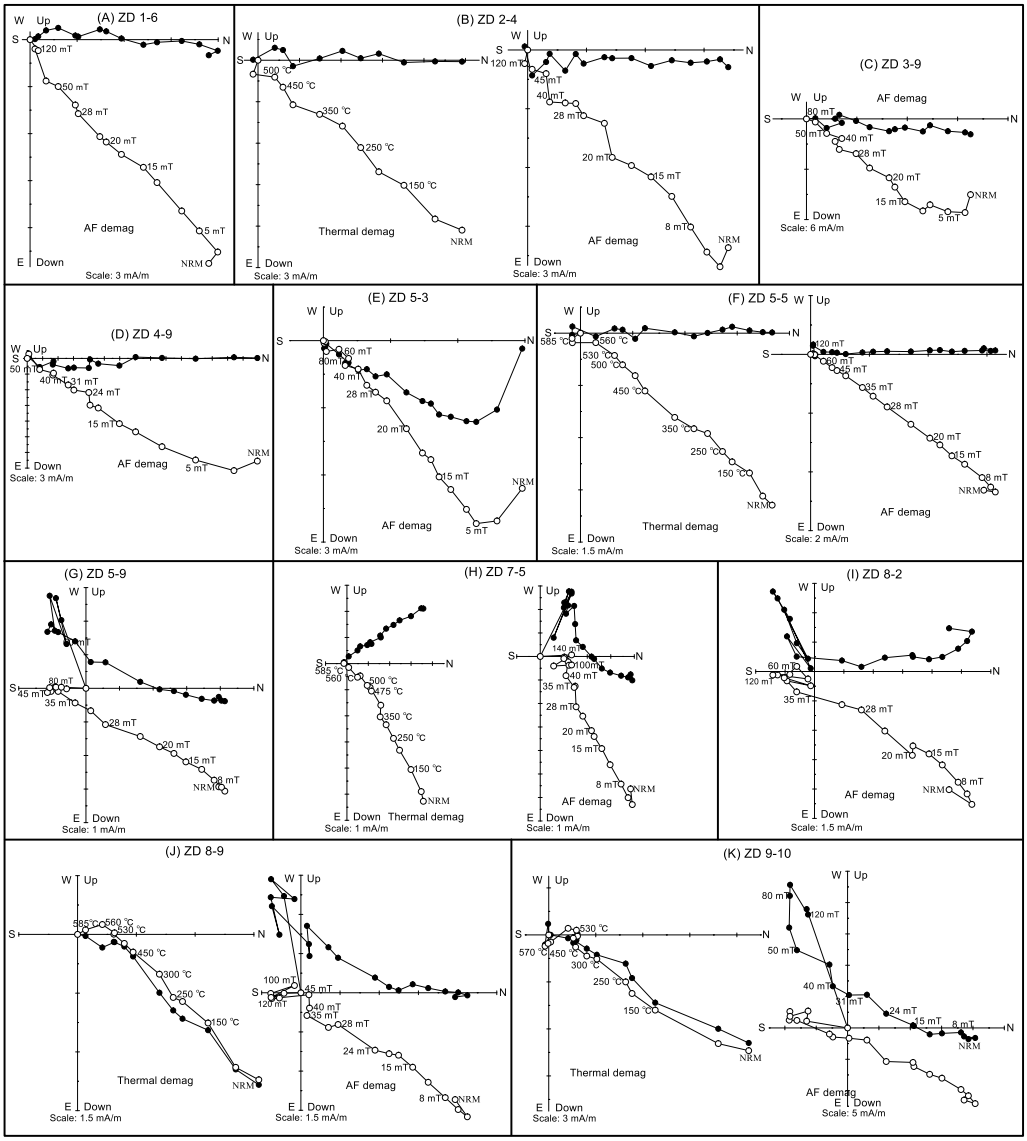

Figure 1.7. *Zijderveld diagrams (Zijderveld, 1967) of the representative granite samples (in geographic coordinates). Solid (open) symbols represent the projections of vector endpoints on the horizontal (vertical) plane. Numbers along the inclination represent the alternating field and thermal demagnetization steps in mT and °C, respectively.*

component, while the remainder shows two NRM components with the soft component removed at a fairly low field level (<15 mT) (Fig. 1.7B, C, E). The NRM decays to the origin down to 10-20% of the starting intensity at ~60 mT or 580 °C; it is thus considered as ChRM carried by magnetite (Fig. 1.7). Although the number of thermally demagnetized specimens is limited, the ChRM directions are similar in

both types of demagnetization, except for the specimen ZD 7-5 which has deviating ChRM directions. In most Type 2 samples, a demagnetization behavior similar to that presented in Type 1 occurred below ~24 to 28 mT. However, these specimens tend to bypass the origin after applying AF above 30 mT (Fig. 1.7G-K). A stable demagnetization direction towards the origin can be observed when conducting thermal demagnetization. It is worth noting that this direction is virtually identical to the direction identified below ~24 mT during AF demagnetization.

1.6.2 ChRM Directions

As the AF demagnetization yielded stable directions for Type 1 granite, we therefore calculated the ChRM directions from the AF demagnetization results. For Type 1 granites, 51 directions were obtained from 55 analyzed samples. The sample-mean direction of these 51 samples is D_g=2.8°, I_g=38.4°, κ =46.4, and α_{95} = 3.0°, n = 51 in geographic coordinates (Fig. 1.9A; Supporting information Table S1.7).

Gyroremanent magnetization (GRM) is a spurious magnetization that is rather frequently generated by procedures used in static 3-axis AF demagnetization of the NRM (Stephenson, 1980a, 1980b, 1993; Dankers & Zijderveld, 1981). Although greigite often acquires GRM during AF demagnetization (e.g., Snowball, 1997a, 1997b; Fu et al., 2008; Hu et al., 1998, 2002; Sagnotti & Winkler, 1999; Stephenson & Snowball, 2001; Duan et al., 2020), fine-grained (titano)magnetite has been reported to be able to acquire it (Roperch & Taylor, 1986; Stephenson, 1993). It seems plausible that GRM can account for the deviating demagnetization behavior at higher field levels during AF demagnetization (>40 mT).

To address this ambiguity, we analyzed the demagnetization directions of the sample collection as a function of AF levels (Fig. 1.8). The sample-mean directions of the Type 1 and 2 samples are basically identical at alternating fields below 24 mT, which agrees well with the demagnetization features shown on the orthogonal demagnetization diagrams (Fig. 1.7, 1.8). With the alternating field increasing from 28 to 50 mT, the sample-mean direction of the Type 2 samples shifts to the west with an increasingly shallower inclination, while the Type 1 samples maintain a stable direction albeit with a larger uncertainty (Fig. 1.8J-O). From 60 mT upward, Type 2 samples remain stable with a westerly direction while the Type 1 samples keep their original direction but with greater uncertainty (Fig. 1.8P-T). This difference can also be observed on the normalised decay curves (Fig. 1.8U). It is therefore likely that the high AF demagnetization behavior of Type 2 samples represents a GRM. To obtain a geologically meaningful direction we used the low AF steps (mostly < 28 mT) for principal component analysis (Kirschvink, 1980), and obtained the sample-mean direction from 41 Type 2 samples as D_g=2.8°, I_g=38.8°, κ =60.9, and α_{95} = 2.9°, n = 41 in geographic coordinates (Fig. 1.9B).

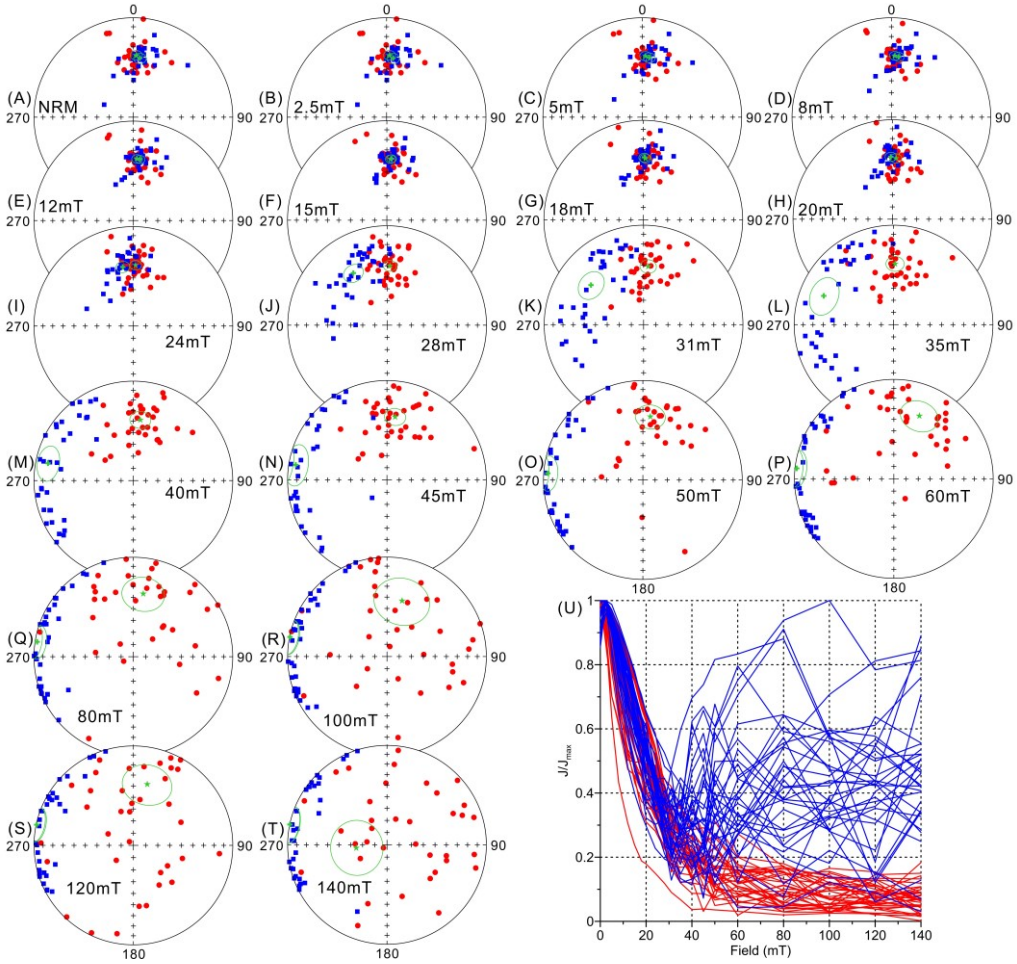

Figure 1.8. *(A-T) Equal-area projections of the AF demagnetization directions at each step. Red dots (blue squares) denote the samples of Type 1 and 2 samples. All diagrams are displayed in geographic coordinates. (U) Normalized remanence decay curves. Red (blue) lines denote the samples of Type 1 (Type 2) granite.*

The ChRM directions calculated from Type 1 samples are paleomagnetically well-behaved; the low field component of Type 2 samples, however, cannot be considered a ChRM without further ado. We note that the directions of the low field AF component are consistent with those of the high temperature segment during thermal demagnetization for Type 2 samples. In addition, the sample-mean direction obtained from 41 Type 2 samples (D_g=2.8°, I_g=38.8° and α_{95} = 2.9°) is statistically indistinguishable from the mean of 51 Type 1 samples (D_g=2.8°, I_g=38.4° and α_{95} = 3.0°). Thus, in the remainder the directions of Type 1 samples and low AF Type 2 samples are combined and yield D_g=2.6°, I_g=38.6° and α_{95} = 2.1°.

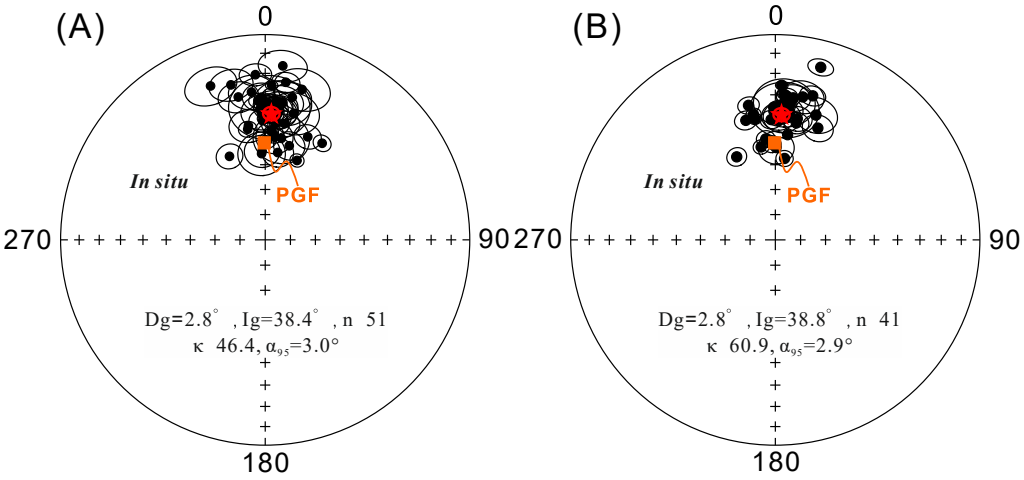

Figure 1.9. *Equal-area projections of the sample-mean directions of Type 1 (A) and Type 2 (B) granite based on principal component analysis (Kirschvink, 1980). The brown squares denote the direction of the present-day geomagnetic field (PGF, D = 359.5°, I = 51.1°) of the sampling location.*

1.7 End-member modeling of magnetic components

End-member modeling based on rock magnetic research has been a novel approach to detect potential remagnetization without a strong reliance on paleomagnetic field tests (i.e. the fold test, conglomerate test, reversals test, and baked contact test). It is based on the assumption that the measured data can be a linear mixture of a number of invariant constituent components referred to as end members. Several case studies have demonstrated the huge potential of the approach to evaluate the magnetic properties of remagnetized and non-remagnetized rocks (Gong et al., 2009; Van Hinsbergen et al., 2010; Meijers et al., 2011; Aben et al., 2014; Huang et al., 2015a). Magnetic particles were added to an existing particle suite in a chemically remagnetized rock, which resulted in distinct IRM acquisition curves and a collection of related end members. This approach was not only applied in sedimentary rock settings (Gong et al., 2009; Van Hinsbergen et al., 2010; Meijers et al., 2011; Aben et al., 2014; Huang et al., 2015a), but also used in volcanics (Huang et al., 2015a). IRM is considered to be a suitable rock magnetic property to define end-members (Gong et al., 2009; Dekkers, 2012; Aben et al., 2014). Typically, at least 30 IRM acquisition curves should be used as input to make use of the inherent variability within a data set. The only criterion is that the input curve must be monotonic (i.e., the derivatives of the input data should be ≥ 0) and contain the same number of data points at the same field steps (e.g., Heslop & Dilllon, 2007). The end-modeling algorithm used here is described in Aben et al. (2014). We interpolated the measured IRM acquisition curves onto a common field step grid via spline interpolation.

1.7.1 End-member modeling of acquisition curves of IRM

IRM acquisition curves of 33 specimens from the granite were used for the end-member model (Fig. 1.10A; Supporting information Table S1.5). The unmixing algorithm mathematically suggests four end-members as the optimal number of end-members, based on the break-in-slope in the coefficient of determination (r^2, ranging from 0 to 1) versus the number of an end-member graph (Fig. 1.10B). However, the end-member curves (called EM1, EM2, EM3 and EM4) become noisy, and two of them (EM2 and EM3) are essentially duplicating, suggesting overinterpretation of the data set (Fig. 1.10C-D). Thus, models from four end-members onward are not considered further. End-member solutions reveal that the three-end-member model has a convexity of -3.8872 (after 1000 iterations) and an r^2 value of 0.93, while the two-end-member model has a convexity of -3.3819 (after 1000 iterations) and an r^2 value of 0.89. Both of the r^2 values are higher than the lower limit of 0.8 and meet the requirements. The end-member curves of both the two and three end-member models show similar characteristics (Fig. 1.10E-I). The end-member curve 1 (EM1) is nearly identical in both models, whereas the end-member curve 2 (EM2) in the two end-member model is decomposed into two other end-member curves (EM2 and EM3) in the three end-member model. Plotted on a ternary plot, the three end-members show that all samples fall within the field with high contributions of EM1 and EM2, or EM2 and EM3, but without high contributions of EM2 and EM3 (Fig. 1.10F). There is no sample with a high contribution of EM1 or EM3 as shown in Fig. 1.10F. This appears to indicate that the three end-member model does not identify more than the two end-member model, but complicates the interpretation needlessly. Therefore, the two end-member model is considered the optimal model for the granite.

As shown in Fig. 1.10H, EM1 consists of ~80% of a soft component with a coercivity range below 100 mT while the remaining 20% is acquired with a broad coercivity fraction ranging up to 700 mT. EM2 presents a sharp increase in low fields and acquires >90% saturation below 100 mT, and can be considered to be saturated at 200 mT. We also applied IRM component analysis to these two end-members (EM1 and EM2 in the two end-member model) (Kruiver et al., 2001). EM1 can be fitted with three components (components C1, C2, and C3, increasing magnetically from soft to hard), while EM2 requires two components (components C1 and C2). Component C1 with $B_{1/2}$ < 20 mT is considered as thermally activated component C2 particles for both EM1 and EM2. Its contribution is approximately 10% to the SIRM (13% for EM1 and 9% for EM2) (Fig. 1.10J-K; Supporting information Table S1.2). Component C2 (with $B_{1/2}$ ~30 mT for EM2 and ~52 mT for EM1) is interpreted to be typical magnetite (Lowrie, 1990). It is the dominant *magnetic* component, contributing 81% and 91% to their respective SIRMs. Component C3 with a relatively high $B_{1/2}$ (~450 mT) contributes 6% to EM1, whereas it appears to be absent in EM2. As interpreted in section 5.2, we also regard it here as fine-grained magnetite or marginally oxidized magnetite. EM1 is dominant in Type 2 granite samples while EM2 dominates in Type

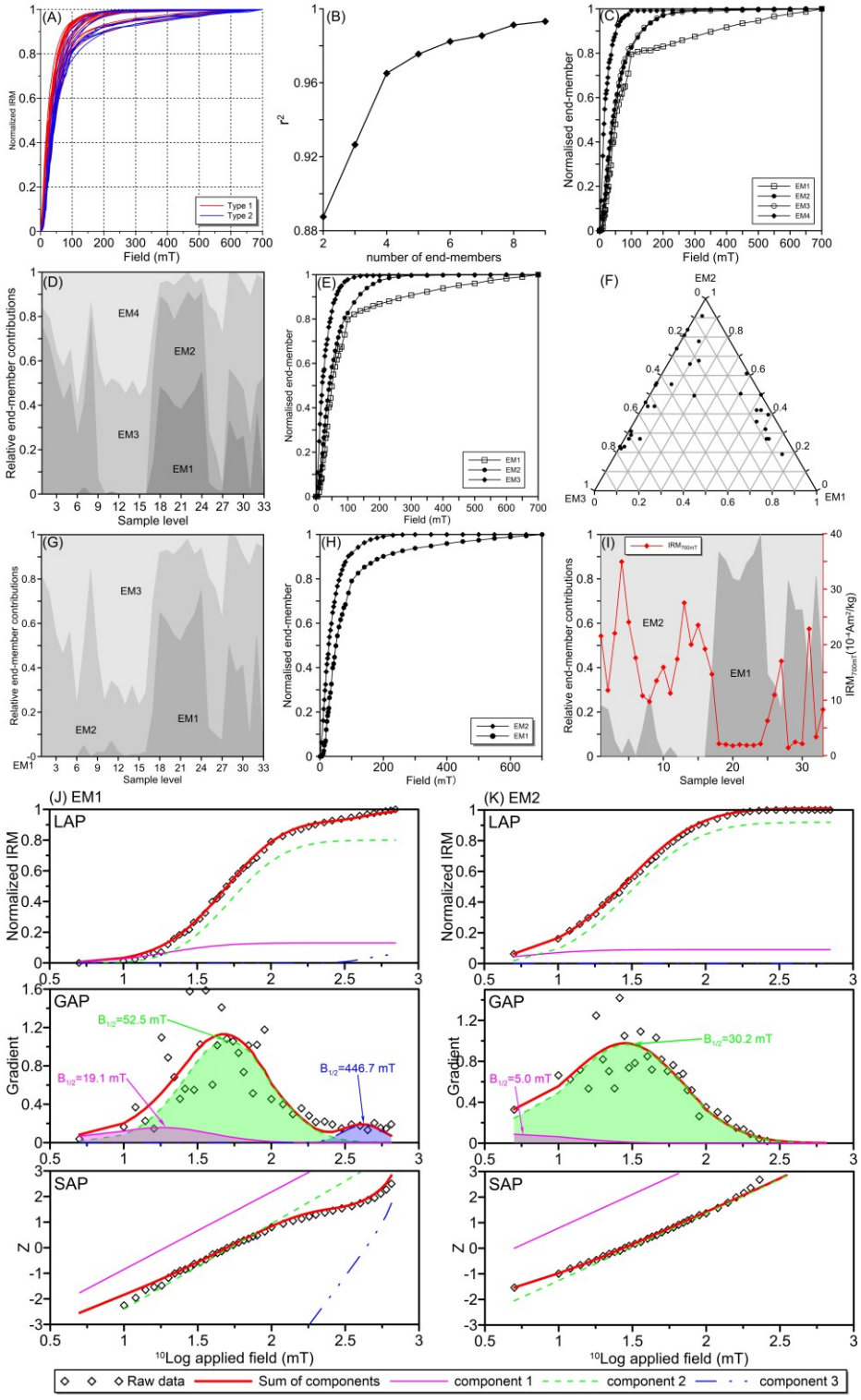
(A)
Normalized IRM
Field (mT)
Type 1
Type 2
(B)
r²
number of end-members
(C)
Normalised end-member
Field (mT)
EM1
EM2
EM3
EM4
(D)
Relative end-member contributions
Sample level
(E)
Normalised end-member
Field (mT)
(F)
EM2
EM3
EM1
(G)
Relative end-member contributions
Sample level
(H)
Normalised end-member
Field (mT)
(I)
Relative end-member contributions
Sample level
IRM700mT (10⁻³Am²/kg)
(J) EM1
LAP
Normalized IRM
GAP
Gradient
B1/2=52.5 mT
B1/2=19.1 mT
B1/2=446.7 mT
SAP
Z
10Log applied field (mT)
(K) EM2
LAP
Normalized IRM
GAP
Gradient
B1/2=30.2 mT
B1/2=5.0 mT
SAP
Z
10Log applied field (mT)
Raw data
Sum of components
component 1
component 2
component 3

Figure 1.10 (previous page). *IRM end-member modeling for the Cretaceous granite. (A) Normalized IRM acquisition curves for Type 1 and Type 2 samples. (B) Coefficient of determination versus the number of endmembers, there is a clear break-in-slope in the four end-member model. End-member modeling for the normalized IRM-acquisition curves with four (C-D), three (E-G) and two (H-I) end-members. (J-K) IRM component analysis (Kruiver et al., 2001) of the end-members in our favorable two end-member model; colors and symbols are the same as in Fig. 1.5.*

1 granite samples. IRM_{700mT} (Fig. 1.10I) also relates to the end-member allocation, where the EM2-dominated samples have a high IRM_{700mT} value. Several studies demonstrate that the end-members vary in remagnetized and non-remagnetized rocks (Gong et al., 2009; Van Hinsbergen et al., 2010; Meijers et al., 2011; Aben et al., 2014; Huang et al., 2015a).

1.7.2 End-member modeling of acquisition curves of ARM

Although ARM is not considered to be the most suitable rock magnetic property to define end-members, due to its bias towards magnetite (Gong et al., 2009; Aben et al., 2014), subtle differences can be expected when comparing end-member models of ARM and IRM data. We follow the end-member modeling procedures of IRM; the optimal end-member number remains obscure as no distinct break-in slope can be observed on the r^2 versus the number of end-members diagram. Based on the end-member models of the IRM acquisition curves, three and two end-member models are utilized in an attempt to satisfy the optimal number of end-members (Fig. 1.11A-G; Supporting information Table S1.6).

End-member solutions reveal that the three-end-member model has a convexity of -4.0807 (after 1000 iterations) and an r^2 value of 0.89, while the two-end-member model has a convexity of -6.1728 (after 1000 iterations) and an r^2 value of 0.87. EM1 in the two-end-member model seems to be the combination of EM1 and EM2 in the three-end-member model through the comparison of end-member contributions (Fig. 1.11C, F). In the ternary plot, most samples are mixtures of EM1 and EM2, or EM3 and EM2 (Fig. 1.11E). In addition, the three-end-member model is characterized by rather noisy end members, especially in high fields, which means that the dataset is overinterpreted. The general model selection criteria or rules follow the idea that the minimum number of components should be opted that still fit well to the input data (Burnham & Anderson, 2002; Heslop & Dillon, 2007). We therefore prefer the two-end-member model to interpret our ARM acquisition data.

The shape of the normalized ARM acquisition curve for each of the two end-members is shown in Fig. 1.11F. After being stable in the lowest AF steps, EM1 shows a rapid increase below 50 mT, followed by a gentle further rise. In contrast, EM2 has no stable zone at low AF levels and climbs much quicker than EM1 below 30 mT,

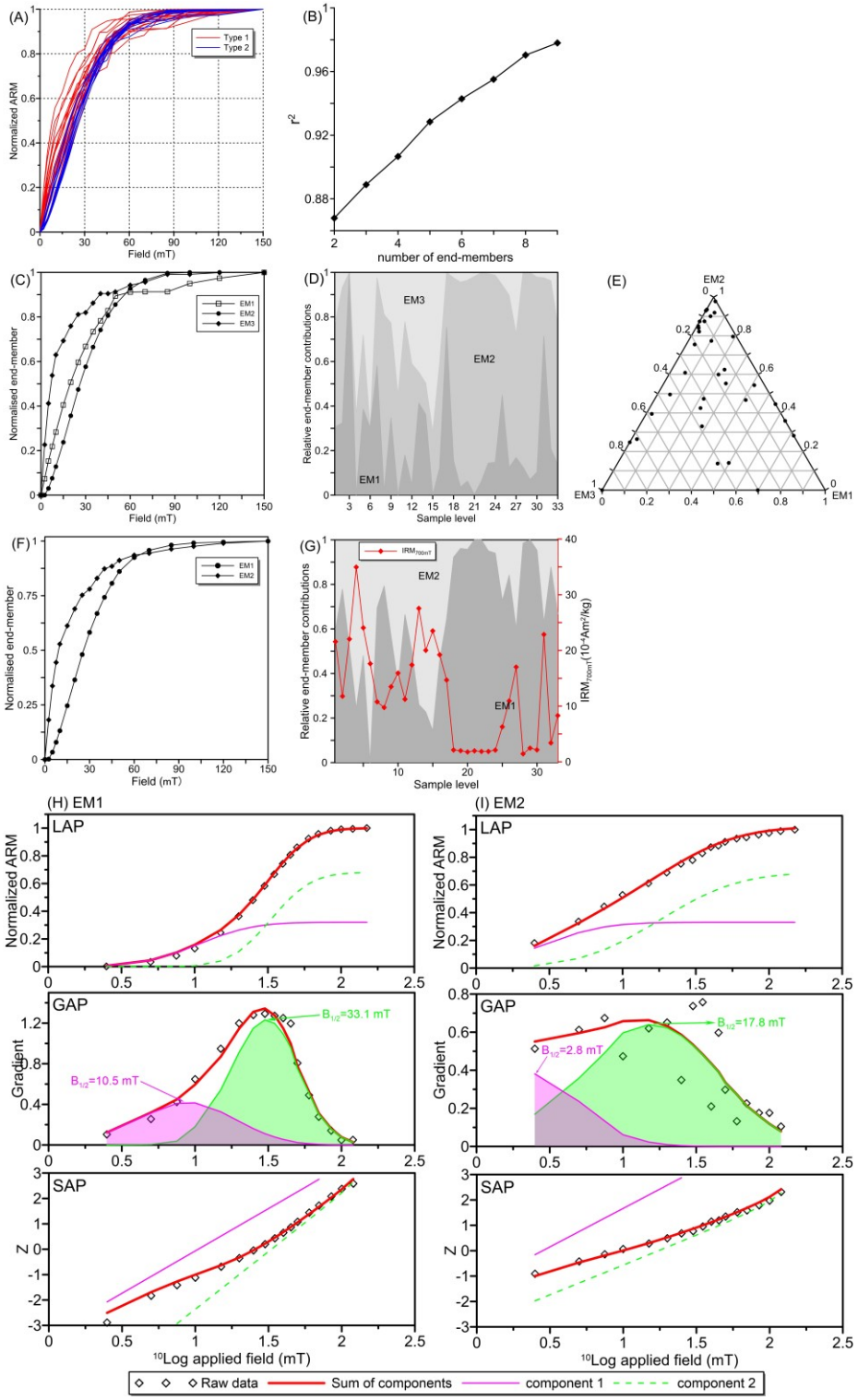
(A)
Type 1
Type 2
Normalized ARM
Field (mT)
(B)
r²
number of end-members
(C)
EM1
EM2
EM3
Normalised end-member
Field (mT)
(D)
EM3
EM2
EM1
Relative end-member contributions
Sample level
(E)
EM2
EM3
EM1
(F)
EM1
EM2
Normalised end-member
Field (mT)
(G)
IRM700mT
EM2
EM1
Relative end-member contributions
IRM700mT(10⁻³Am²/kg)
Sample level
(H) EM1
(I) EM2
LAP
GAP
SAP
Normalized ARM
Gradient
Z
B1/2=33.1 mT
B1/2=10.5 mT
B1/2=17.8 mT
B1/2=2.8 mT
10Log applied field (mT)
Raw data
Sum of components
component 1
component 2

Figure 1.11 (previous page). *ARM end-member modeling for the Cretaceous granite. (A) Normalized ARM acquisition curves for Type 1 and Type 2 granite. (B) Coefficient of determination versus the number of endmembers. End-member modeling for the normalized ARM acquisition curves with three (C-E) and two (F-G) end-members. (H-I) ARM component analysis (with the software of Kruiver et al., 2001) of the end-members in the two end-member model; colors and symbols are the same as in Fig. 1.5.*

followed by a gradual increase; both curves intersect at ~60 mT. We applied coercivity component analysis to these two end-members (Kruiver & Passier, 2001). Generally, both EM1 and EM2 can be fitted with two components (components C1 and C2, with C1 being the softer of the two). Component C1 has a very low $B_{1/2}$ and generally results from other thermally activated components (Egli, 2004; Heslop et al., 2004). Component C2 (with $B_{1/2}$ ~20-30 mT) represents typical SD magnetite (Lowrie, 1990), accounting for ~68% of both EM1 and EM2. The high coercivity component is absent in the end-members. For Type 1 granite, most samples are mixtures of EM1 and EM2 (Fig. 1.11F). The contributions of EM1 and EM2 vary considerably, yet an average of 50% for each. A great number of samples of Type 2 have the predominant EM1, indicating the sole contribution from EM1 (Fig. 1.11F). The end-member modeling of ARM acquisition curves resembles that of IRM acquisition curves. However, the EM1 contribution yielded from ARM is higher than that from IRM for all the samples, which coincides with those reported previously (Gong et al., 2009; Aben et al., 2014).

1.8 Discussion

1.8.1 Primary NRM in the early Cretaceous granites

The granites intruded into the early Carboniferous Zaduo Group, and the Permo-Triassic volcanic rocks outcropping to the northwest. Other rocks that were intruded are the Middle-Upper Jurassic sandstones of the Yanshiping Group outcropping to the southeast (Fig. 1.2A, B). Thus, the age of the granite is post Jurassic. This is confirmed by whole-rock and biotite K-Ar ages of ~126 Ma (QGSI, 2005, 2014). No younger igneous bodies are found near the studied location, and the nearby Permo-Triassic volcanic rocks retain primary magnetizations (Guan et al. 2021). Hence, it is less likely that thermoviscous resetting of existing magnetic minerals has occurred (Kent & Opdyke, 1985). The nearby Middle-Upper Jurassic limestones of the Yanshiping Group were reported to be remagnetized during the India–Eurasia collision process (Fu et al., 2022a). However, igneous rocks have a considerably lower porosity that grossly diminished the circulation of fluids. In addition, the absence of organic matter in igneous rocks could not drive oxidation/reduction reactions. Therefore, both the Permo-Triassic and Cretaceous igneous rocks escaped the remagnetization that affected the nearby Middle-Upper Jurassic limestones.

Rock magnetic analyses indicate that PSD-MD magnetite is the dominant magnetic

carrier of the granite. The presence of finer-grained magnetite in Type 2 granite samples yielded erratic demagnetization behavior at the highest field levels during AF demagnetization (Fig. 1.7, 1.8), GRM, a high contribution of EM1 (Fig. 1.10, 1.11) and deviating ARM/IRM values (Fig. 1.6C, D). Gong et al. (2009) reported that remagnetized limestones have a high percentage of end-member 1 that is close to saturation at approximately 700 mT, whereas non-remagnetized rocks have a high percentage of end-member 2 that saturates at ~300-400 mT. End-member 1 is interpreted to be very fine-grained magnetite, close to the SP threshold size. This is verified by other studies on both volcanic and sedimentary rocks (Van Hinsbergen et al., 2010; Meijers et al., 2011; Aben et al., 2014; Huang et al., 2015a). As shown in Fig. 1.10H, EM2 saturates at 200-300 mT while EM1 does not reach saturation until 700 mT. Most EM2-dominated samples belong to Type 1, indicating a primary remanent magnetization of Type 1 granite samples. Although EM1 that saturates at approximately 700 mT dominates in Type 2 granite samples, it is not considered as a remagnetized end-member because the sample-mean directions of the Type 1 and Type 2 samples are similar. We consider that EM1 is fine-grained magnetite, which can account for the GRM that occurred in Type 2 granite samples.

The granitic composition can be changed through mineral dissolution or recrystallization during post-magmatic hydrothermal/metasomatic alteration. Feldspars are generally vulnerable to alteration, and turbid feldspars are considered as a hint of hydrothermal alteration (e.g., Nédélec et al., 2015). Chlorite is formed after biotite; chloritization indicates medium- to high-temperature conditions (Bailey, 1984). Quartz formed during late crystallization and did not alter. As a whole, the studied granites display primary (magmatic) minerals in thin sections. Magnetite formed merely during the cooling of the igneous intrusion and underwent only slight hydrothermal alteration (some chloritization of biotite), thus probably retaining a primary remanent magnetization.

In summary, although we could not apply paleomagnetic field tests, it is very probable that the studied Cretaceous granite carries a (quasi) primary remanent magnetization acquired during its cooling. Our microscopic and rock magnetic results form the basis for this notion. The A_{95} of the pole (2.1°) falls within the theoretical range for a pole that has sufficiently averaged PSV (1.97–4.75° for N=92 samples) (Deenen et al., 2011, 2014), which is sufficiently long enough to average paleosecular variation.

1.8.2 Structural control of the granite and its implications for the Lhasa-Qiangtang collision

Structural control of granites is usually difficult due to poor constraints on the paleohorizontal. Intrusion need not occur in horizontal strata, so standard tilt correction of adjacent sediments with extrapolation to the granite cannot be performed here. The Late Cretaceous to early Cenozoic Fenghuoshan Group is

absent in this area, and the Eocene sedimentary rocks (Et) in the northeast unconformably overlie the Cretaceous granite (Fig. 1.2A, B). The bedding attitude of Et has an average strike/dip of 321°/20°. In the southeast, the Middle-Upper Jurassic sandstone of the Yanshiping Group has an average strike/dip of 54°/32°. Below we evaluate these constraints on the ChRM directions of the Zaduo granite.

The ChRM direction obtained from 92 granite specimens is D_g=2.6°, I_g=38.6°, κ =51.4, and α_{95} = 2.1° in geographic coordinates (Fig. 1.12A; Supporting information Table S1.7). First, we can assume that the studied granite had not been tilted prior to the deposition of the overlying Tuotuohe Formation, which was proposed to have been tilted during the late Himalayan period (~25 Ma) (STRGSQ, 1988; QGSI, 2005, 2014). In this scenario, it is reasonable to take the same tilting for the granite. After tilt-correction, the sample-mean direction of the 92 samples is D_s = 11.1°, I_s = 24.5°, κ_s = 51.4, α_{95} = 2.1°, corresponding to a paleopole at 67.1°N, 243.4°E with A_{95} = 2.1° and a paleolatitude at ~12.5 ± 2.9°N for the study area (Fig. 1.12B; Supporting information Table S1.7). This scenario yields an unrealistic paleolatitude as it is much lower than the predicted paleolatitude of over ~30°N for the Mangkang area in the Eastern Qiangtang Terrane (~500 km southeast of the Zaduo area) (i.e., paleolatitudes of 30.8° ± 10.9° during the Berriasian-Barremian and 33.3° ± 8.3° during the Aptian-Turonian by Huang et al., (1992); 36.2° ± 6.5° in the Late Cretaceous by Tong et al. (2015); 33.2° ± 2.5° in the Late Cretaceous in the center Qiangtang by Meng et al. (2018)). Therefore, it is improper to perform a granite tilt correction via the attitudes of the overlying sedimentary rocks of the Tuotuohe Formation. Thus, the target granite was (partially) tilted prior to Paleogene sediment deposition.

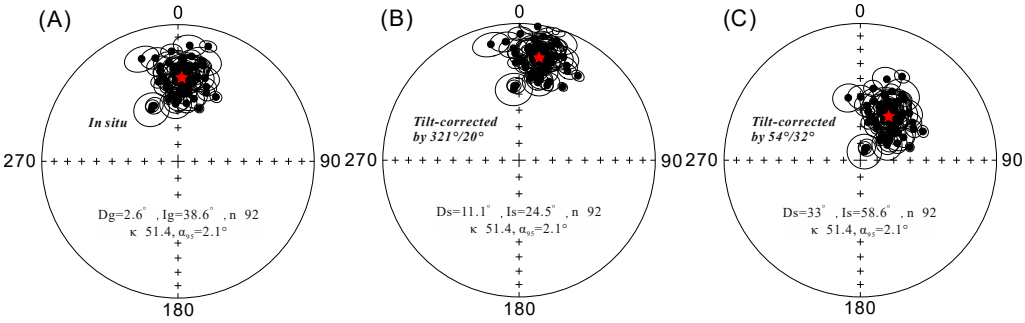

Figure 1.12. *Equal-area projections of the sample-mean directions from Type 1 and Type 2 granite before (A)* and *after bedding corrections with the bedding attitude (strike /dip) of Et (B) and Jq (C) sandstones.*

Table 1.1. *Paleomagnetic poles for the Eastern Qiangtang Terrane during the Cretaceous*

Sampling site			Lithology	n/N	In situ		Tilt-corrected		k	α_{95}	Pole location		
Site	Slat (°N)	Slon (°E)			Dec(°)	Inc(°)	Dec(°)	Inc(°)			Plat (°N)	Plon (°E)	A_{95} (°)
Lower Cretaceous strata of Huang et al., 1992													
A	29.7	98.4	Red beds	4/5	268.6	46.6	70.2	52.7	104.5	9	31.2	165.3	10.3
B	29.7	98.4	Red beds	4/5	279.2	42.1	78.6	53	73.1	9	24.7	162.4	10.4
D	29.7	98.4	Red beds	5/5	259.7	5.6	40.9	51.7	46.2	11.4	55	173.3	12.8
E	29.7	98.4	Red beds	5/5	265.4	5.8	38.1	45.3	198.9	5.4	56.5	183.9	5.5
G	29.7	98.4	Red beds	5/5	280.6	16.5	14.4	29.3	32.2	13.7	70.7	231.9	11.2
I	29.7	98.4	Red beds	5/5	276.1	23.7	46	31.6	95.1	7.9	46.2	194.5	6.6
J	29.7	98.4	Red beds	5/5	248.2	47.2	94.1	48.3	41	12.1	10.9	160.7	12.8
K	29.7	98.4	Red beds	5/5	250.9	55	86.8	39.5	29.1	14.1	13.5	170.3	13.4
A1	29.7	98.6	Red beds	3/5	64.3	-51.6	75.9	41.7	2272.3	2.6	23.3	173.3	2.5
B1	29.7	98.6	Red beds	4/5	76.2	-50.1	72.7	53.8	138.3	7.8	29.5	163.6	9.1
C1	29.7	98.6	Red beds	5/5	70.6	-33.9	47.4	61.7	152.7	6.2	50.2	156.1	8.4
D1	29.7	98.6	Red beds	5/5	67.9	-29.4	29.4	60.6	839.6	3.3	63.5	153.9	4.4
Upper Cretaceous strata of Tong et al., 2015													
MK2	29.7	98.6	Red beds	12/12	61.5	58.7	119.7	70	75.5	5	8.5	129.5	8
MK3	29.7	98.6	Red beds	13/14	226.5	18.5	224.8	-51.4	25.2	8.4	51.8	173.1	9.4
MK4	29.7	98.6	Red beds	12/12	221.4	15.6	218.2	-51.4	33.8	8	57.3	174.4	9
MK5	29.7	98.6	Red beds	11/13	216	29.9	214.6	-38.9	43.6	7.4	58	194.2	6.8
MK6	29.7	98.6	Red beds	12/12	75.9	5.5	71.1	59.2	119.9	3.8	32.3	157.5	4.9
MK7	29.7	98.6	Red beds	11/12	87.9	6.6	84.9	56.1	151.1	3.9	21	157.3	4.8
MK8	29.7	98.6	Red beds	8/11	107.4	49.9	56.2	55.5	132.7	5.8	43	165.3	7
MK9	29.7	98.6	Red beds	11/12	104.2	52.3	34.7	57.9	67.9	5.6	60.1	161.9	7.1

MK10	29.7	98.6	Red beds	11/12	62.5	4.6	47.6	62	66.2	6	50	155.4	8.2
MK11	29.7	98.6	Red beds	12/14	63.4	19.2	41.8	62.2	27	11.8	54.2	154.3	16.2
MK12	29.7	98.6	Red beds	13/14	62	23.4	33.2	56.9	116.5	4.8	61.4	163.9	5.9
MK13	29.7	98.6	Red beds	11/12	64.3	23.4	45.1	40.3	79.1	5.2	49.3	187.1	4.9
MK14	29.7	98.6	Red beds	9/13	1.8	39.1	40.5	44.5	111.9	4.9	54.2	184.2	4.9
MK15	29.7	98.6	Red beds	9/12	350.3	41.2	42.4	59.8	43	8.5	37.3	178.3	8.3
MK16	29.7	98.6	Red beds	10/12	348.9	37.6	46.5	69.6	49	10.1	49	139.8	16
MK17	29.7	98.6	Red beds	11/12	25.5	29.7	62.4	39.5	18.3	16.1	34.1	180.3	14.9
MK18	29.7	98.6	Red beds	10/12	10.1	39.6	70.6	53.7	104.5	5.9	31.2	164.2	6.9
Upper Cretaceous strata of Huang et al., 1992													
B	29.7	98.7	Red beds	5/5	45.7	-9.3	34.8	36.2	232.7	5	57.2	197.5	4.4
C	29.7	98.7	Red beds	5/5	21.5	2.6	3.9	57.5	93.6	8	91	118.8	10
D	29.7	98.7	Red beds	5/5	298.9	44.2	32.3	57.2	359.2	3.9	62.1	163.1	4.9
E	29.7	98.7	Red beds	5/5	9.8	38.7	49	39.3	433.6	3.7	45.7	186.3	3.4
F	29.7	98.7	Red beds	5/5	337.4	45.2	47.8	63.3	52.4	10.7	49.7	153	15
G	29.7	98.7	Red beds	5/5	5.5	28.7	43.4	55.1	66.3	9.5	53.3	167.7	11.4
H	29.7	98.7	Red beds	5/5	10.8	36.8	56.6	43.3	91.3	8.1	40.1	179.4	7.9
I	29.7	98.7	Red beds	5/5	151.2	-60.5	242.3	-51	1233.6	3.2	37.2	169.5	3.6
J	29.7	98.7	Red beds	5/5	325.2	49.7	44.1	45.8	513.4	3.4	51.4	181.1	3.5
K	29.7	98.7	Red beds	9/10	323.2	52.1	47.6	46.7	178.3	3.9	48.5	178.8	4
M	29.7	98.7	Red beds	5/5	44.6	32.1	357.6	55.9	102.3	7.6	50	165.9	9.2

Mean paleomagnetic pole during K_1: Plat. = 40.6°N, Plon. = 170.5°E, n=12, K = 12.2, A_{95} = 13.0° (Huang et al., 1992)

Mean paleomagnetic pole during K_2: Plat. = 48.9°N, Plon. = 168.1°E, n=28, K = 19.9, A_{95} = 6.3° (Huang et al., 1992 + Tong et al., 2015)

Mean paleomagnetic pole during K: Plat. = 46.5°N, Plon. = 168.9°E, n=40, K = 16.6, A_{95} = 5.7° (Huang et al., 1992 + Tong et al., 2015)

Note: *N and n are number of samples collected and used for paleomagnetic calculation, respectively. Dec. and Inc. are declination and inclination, respectively; k is the Fisherian precision parameter for samples (Fisher, 1953);* α_{95} *and* A_{95} *are the radius of cone at 95% confidence level about the mean direction. Slat. and Slon. are latitude and longitude of the sampling site. Plat. and Plon. are latitude and longitude of the paleomagnetic poles.*

Alternatively, if we assume that the sedimentary rocks of the Late Jurrasic Quemocuo Formation were not tilted prior to the granite intrusion, we can correct the granite tilt with the attitude of the adjacent Quemocuo Formation. The tilt-corrected paleomagnetic direction in this situation is $D_s = 33.0°$, $I_s = 58.6°$, with $\kappa_s = 51.4$ and $\alpha_{95} = 2.1°$, corresponding to a paleopole at 62.4°N, 161.9°E with $A_{95} = 2.1°$ and a paleolatitude of ~39.1° ± 3.8°N (Fig. 1.12C; Supporting information Table S1.7). In this scenario, the deduced paleolatitude remains improper as it is ~5-10° higher than previously published paleolatitude estimates (e.g., paleolatitudes of ~30-33° during K_1 by Huang et al. (1992); ~36° during K_2 by Tong et al. (2015); ~33° during K_2 by Meng et al., (2018)). This inconsistency suggests that the Quemocuo Formation was tilted before the intrusion of the granite, that is, ~126 Ma.

Although robust paleolatitudes cannot be obtained by the above two assumptions, we can estimate the tilt of the Middle-Upper Jurassic sandstones of the Yanshiping Group in the southeast at the time of intrusion. Two paleomagnetic studies on Cretaceous rocks in the Mangkang area provide forty mean paleopoles for the Eastern Qiangtang Terrane (Table 1.1). To constrain the reference paleopoles as precisely as possible, we calculated the average paleopoles using Fisher statistics: 40.6°N, 170.5°E, $A_{95} = 13°$ during the Early Cretaceous (Huang et al., 1992); 48.9°N, 168.1°E, $A_{95} = 6.3°$ during the Late Cretaceous (Huang et al., 1992; Tong et al., 2015); and 46.5°N, 168.9°E, $A_{95} = 5.7°$ during the Cretaceous (Huang et al., 1992; Tong et al., 2015). Another study from Otofuji et al. (1990) on Cretaceous strata was excluded because the number of samples is deemed insufficient. For completeness, it yields a similar mean paleopole of 48.5°N, 175.8°E, $A_{95} = 9.5°$ during the Barremian-Albian. The expected declination ($D_{s\text{-}exp} = 52.4°$) and inclination ($I_{s\text{-}exp} = 53.0°$) in stratigraphic coordinates can be obtained for our study area using the mean Cretaceous paleopoles, thus yielding an expected bedding attitude of $Strike_{exp} = 43.1°$ and $Dip_{exp} = 46.1°$ for the Middle-Upper Jurassic sandstones in the southeast of the granite. The observed bedding attitude of the Middle-Upper Jurassic sandstones is strike = 54° and dip = 32°. Thus, there is a discrepancy of ~10° between the expected and observed strike and ~14° between the expected and observed dip in the overlying Middle-Upper Jurassic sandstones of the Yanshiping Group.

The difference between the observed and expected bedding attitudes indicates that the strata of the Yanshiping Group in the Eastern Qiangtang (at least in the Zaduo area) were tilted during/prior to the intrusion of the granite. We provide two options here to interpret this discrepancy in attitudes. One is that the granite intrusion lifted the overlying Jurassic sedimentary strata and led to the SE dip. In this case, the S-type granite could be a result of orogenic building processes during the collision of the Lhasa and Qiangtang Terranes. The second option is that the Jurassic sedimentary strata were tilted before the granite intrusion, which was formed in a post-orogenic extensional regime after the Lhasa-Qaingtang collision. We tend to favor the second option, as there is roughly 40 Myr between the overlying Jurassic

sedimentary strata and the granite intrusion, during which the tilt could occur. In this case, the tilt of the Jurassic sedimentary strata was likely the response to the Lhasa-Qiangtang collision, as there was no other known significant tectonic activity from the late Jurassic to 126 Ma. Therefore, the age of the granite (~126 Ma) provides a minimum age constraint for the Lhasa-Qiangtang collision, or the closure of the Bangong-Nujiang Ocean. The NE-trending Jurassic sedimentary strata are distinguished from the SE-trending Cenozoic strata, which may signify a ~90° clockwise rotation before the Cenozoic. Another clockwise rotation may have occurred after the India-Eurasia collision, which formed the NE-trending Jurassic sedimentary strata. Given that layer parallel shortening (LPS) processes occurred widely during the early stages of deformation, which delayed the folding of the strata (Pueyo-Morer et al., 1997; Larrasoana et al., 2004; Weil and Yonkee, 2009; Rashid et al., 2015), the timing of the Lhasa-Qiangtang collision (the closure of the Bangong-Nujiang Ocean) could be even substantially earlier than ~126 Ma. Our results are in line with those published in several recent palaeomagnetic studies (Yan et al., 2016; Bian et al., 2017; Meng et al., 2018; Ma et al., 2018; Cao et al., 2019). Moreover, other lines of evidence support this scenario: (a) The Lagongtang Formation (starting at ~140 Ma) developed in a mature peripheral foreland basin in the Dingqing area. An abrupt transition in provenance and depositional environment is indicative of a response to the initial Lhasa-Qiangtang collision (Chen et al., 2020). (b) Angular unconformities and the accumulation of non-marine successions in the Bangong suture zone during the mid-Cretaceous are attributed to the Lhasa-Qiangtang collision (Zhu et al., 2016). (c) The 140–130 Ma magmatic activity gap in the Eastern Qiangtang Terrane suggests that the Lhasa-Qiangtang collision occurred during this period (Li et al., 2014; Zhu et al., 2016). (d) Studies on ophiolite, metamorphism, magmatism, lithostratigraphy and tectonism reveal that the closure of the Bangong-Nujiang Ocean terminated between the latest Jurassic and the Early Cretaceous (Li et al., 2019a, 2019b). S-type granites are generally considered to have formed in syn-collisional or post-collisional environments after the subduction of the oceanic crust, indicating a continental collision orogenic stage. Thus, the geological evolution in the Zaduo area can be outlined as follows: the Lhasa Terrane collided with the Qiangtang Terrane during the Late Jurassic to Early Cretaceous, followed by the closure of the Bangong-Nujiang Ocean. The strata of the Middle-Upper Jurassic Yanshiping Group tilted during the convergence of the Lhasa and Qiangtang Terranes. In response to the Lhasa-Qiangtang collision, the granite intruded into the Yanshiping Group at ~126 Ma and recorded a primary (or quasi-primary) magnetization during cooling; later, the region rotated clockwise in response to the India-Asia collision.

Conclusions

Granite plutons are widespread in Earth's upper crust in various geodynamic settings and can acquire a stable remanent magnetization during formation. However, granites are less paleomagnetically investigated due to poor constraints on the

paleohorizontal. We studied the Cretaceous granite that is outcropping in the Zaduo area, Eastern Qiangtang Terrane. Petrographic observations show that magnetite formed during the cooling of the intrusion and suffered minor further hydrothermal alteration, thus probably preserving a primary remanent magnetization. Rock magnetic analysis indicates magnetite as the main magnetic carrier. In particular, IRM-acquisition end-member modeling successfully assessed the veracity of the NRM residing in magnetite. EM1 does not reach saturation until 700 mT, which is interpreted as fine-grained magnetite and accounts for the GRM that occurred in some granite samples. EM2 saturates at 200-300 mT and dominates in other samples. The primary magnetization of the granite yields a ChRM direction in geographic coordinates: D_g = 2.6°, I_g = 38.6°, κ =51.4, α_{95} = 2.1° (n=92).

After tilt-correction via the bedding attitude of the Paleogene Tuotuohe Formation (Et), the sample-mean direction of the 92 samples is D_s = 12.1°, I_s = 35.6°, κ_s = 43.7, α_{95} = 3.7°, corresponding to a paleopole at 67.1°N, 243.4°E with A_{95}= 2.9° and a paleolatitude of ~12.5 ± 2.9°N. After tilt-correction via the bedding attitude of Middle-Upper Jurassic sandstones (Jq), the sample-mean direction of the 92 samples is D_s = 33.2°, I_s = 58.4°, with κ_s = 46.4 and α_{95} = 3.0°, corresponding to a paleopole at 62.4°N, 161.9°E with A_{95} = 3.8° and a paleolatitude of ~39.1° ± 3.8°N for the study area. Both assumptions appear to yield unrealistic paleolatitudes and are thus deemed improper, indicating that the target granite was tilted prior to the Paleogene deposition and/or the Jq sandstones were tilted to some degree before the intrusion of the granite. The expected declination ($D_{s\text{-}exp}$ = 52.4°) and inclination ($I_{s\text{-}exp}$ = 53.0°) in stratigraphic coordinates can be obtained for our study area using the published paleopoles, yielding an expected bedding attitude of $Strike_{exp}$ = 43.1° and Dip_{exp} = 46.1° for the Jq strata in the southeast of the granite. There is a discrepancy of ~20° between the expected and observed strike, and ~10° between the expected and observed dip in the overlying Jq sandstones, which justifies that the Jq sandstones in the study area had been tilted prior to the intrusion of the granite. Given the frequent LSP during the early stages of deformation, we infer that the Lhasa-Qiangtang collision occurred before ~126 Ma.

Acknowledgments

The authors thank Zhantao Feng, Ziqiang Mao for their assistance in the field and laboratory work. We sincerely thank Handling Editor Junsheng Nie, reviewers Tianshui Yang and Luis Manuel Alva Valdivia for their constructive comments and suggestions. This work was co-supported by the Natural Science Foundation of China (Grant 4197408o), the Basic Science Center for Tibetan Plateau Earth System (CTPES, Grant 41988101-01), the Natural Science Foundation of China (Grant 42164005), the Second Tibetan Plateau Scientific Expedition Program (Grant 2019QZKK0707), the Strategic Priority Research Program of Chinese Academy of Sciences (Grant XDA20070201), and the China Scholarship Council.

2

REMAGNETIZATION OF THE JURASSIC LIMESTONES IN THE ZADUO AREA, EASTERN QIANGTANG TERRANE (TIBETAN PLATEAU, CHINA): IMPLICATIONS FOR THE INDIA-EURASIA COLLISION

Abstract

A series of terranes were accreted to Eurasia in the region of what is now the Tibetan Plateau, including the Qaidam-Qilian, the Songpan-Ganzi, the Qiangtang, the Lhasa and the Tethyan Himalaya terranes. The drift history of the Qiangtang Terrane and the timing of the Lhasa-Qiangtang collision are controversial. To contribute to this topic, here, we paleomagnetically investigate the Middle-Upper Jurassic limestones of the Yanshiping Group in the Zaduo area (32.5°N, 95.2°E), in the Eastern Qiangtang Terrane. Twelve sites (133 samples) were processed. A major challenge in paleomagnetism is the possibility of remagnetization that interferes with paleogeographic reconstructions. Both thermal and alternating field demagnetizations were carried out to isolate the characteristic remanent magnetization (ChRM). Despite the positive reversals test, rock magnetic information points to a remagnetized ChRM. The ChRM is residing in stable single-domain (SSD) magnetite grains with cogenetic superparamagnetic (SP) particles. The co-occurrence of SSD and SP magnetites generates distinct rock-magnetic properties often refer to as the 'remagnetized fingerprint' in limestones. This remagnetization process is also manifested by the widespread occurrence of gypsum veinlets in the limestones. The site-mean direction of the 12 sites after tilt-correction is $D_s = 30.6°$, $I_s = 35.6°$, $\kappa_s = 182.9$, $\alpha_{95} = 3.2°$, corresponding to a paleolatitude of ~19.7°± 2.8°N for the study area. The corresponding paleopole (59.8°N, 202.7°E with A_{95} = 2.8°) points to an NRM acquired after the India-Eurasia collision. The original sediments were likely anoxic because of the high organic carbon fluxes that prevailed during their deposition. After the India-Eurasia collision, it is envisaged that conditions became more oxic, giving rise to the oxidation of iron sulphides to authigenic magnetite and the CRM acquisition. The Zaduo area in the Eastern

Qiangtang Terrane has experienced ~15.7° ± 3.2° (~1740 ± 350 km) of latitudinal crustal shortening since the Eocene. In addition, the clockwise rotation responding to the India-Eurasia collision is also detected in the Zaduo area.

2.1 Introduction

The Tibetan Plateau is composed of multiple accreted terranes, including (from south to north) the Tethyan Himalaya, the Lhasa, the Qiangtang, the Songpan-Ganzi and the Qaidam-Qilian terranes. (Fig. 2.1). These terranes originated from the super-continent of Gondwana, successively drifted northward and accreted to Eurasia from the Early Paleozoic to the Late Mesozoic (Dewey *et al*., 1988; Yin & Harrison, 2000; Tapponnier *et al*., 2001; Kapp *et al*., 2007). Afterwards, due to the persistent northward indentation of the Indian Plate with the Eurasian Plate and the related subduction, the Tibetan Plateau was established. The Qiangtang Terrane (QT), the target terrane of the present study, is a long and narrow major crustal fragment in the central Tibetan Plateau, generally thought to have separated from Gondwana in Late Paleozoic (Yin & Harrison, 2000; Metcalfe, 2013; Xu *et al*., 2015). It collided with the Songpan-Ganzi Terrane (SGT) during the Late Triassic to the Early Jurassic (Roger *et al*., 2010; Song *et al*., 2015; Yan *et al*., 2016; Guan *et al*., 2021). To the south, the Lhasa Terrane accreted with the Qiangtang terrane during the Middle or Late Jurassic (Xu *et al*., 1985; Dewey *et al*., 1988; Yan *et al*., 2016; Ma *et al*., 2017; Li *et al*., 2019a, 2019b), or the Early Cretaceous (Kapp et al., 2003a, 2007; Zhu *et al*., 2006, 2011, 2013, 2016; Bian *et al*., 2017; Meng *et al*., 2018; Chen *et al*., 2020), even the Late Cretaceous (Zhang *et al*., 2012; Liu *et al*., 2014a; Fan *et al*., 2014, 2015, 2018a, 2018b). The different methods used to constrain the collision age are likely the foremost reason for observed differences in timing (Ding *et al*., 2005; Chen *et al*., 2020). Methods include ophiolite obduction, faunal migration, peripheral foreland basin formation, and paleomagnetism. Each delivers the age of different stages in the collision history providing sometimes an upper or a lower limit (Ding *et al*., 2017).

To quantify the drift history of the Qiangtang Terrane, many paleomagnetic studies have been carried out on its Mesozoic strata that provided extensive knowledge on its tectonic history (Lin & Watts, 1988; Otofuji *et al*., 1990; Dong *et al*., 1990, 1991; Huang *et al*., 1992; Chen *et al*., 1993; Song *et al*., 2012; Cheng *et al*., 2012; Ren *et al*., 2013; Song *et al*., 2015, 2020; Tong *et al*., 2015; Yan *et al*., 2016; Chen et al., 2017b; Meng *et al*., 2018; Ran *et al*., 2017; Zhou *et al*., 2019; Cao *et al*., 2019, 2020; Song *et al*., 2020; Guan *et al*., 2021). However, despite this vast research effort, after consideration of the 'Van der Voo criteria' and the recently established 'R-criteria' (Van der Voo, 1990; Meert *et al*., 2020), robust paleomagnetic datasets are still rather limited in number given the size of the terrane. Based on paleomagnetic studies from the same Middle-Upper Jurassic marine sedimentary rock unit (the Yanshiping Group), Cheng *et al*. (2012), Ren *et al*. (2013) and Yan *et al*. (2016) obtain paleolatitudes of 20-25°N for the Yanshiping area (Fig. 2.1), while Ran *et al*. (2017) suggest a syn-folding remagnetization acquired during the early stage of folding (about 20%). In the Shuanghu area (~300 km west of the Yanshiping area), Cao *et al*. (2019) report a Jurassic paleolatitude of ~35°N for their reference site. Because of this paleolatitudinal discrepancy for the same Yanshiping Group, we investigate here the Middle-Upper Jurassic limestones of that group in the Zaduo area (~300 km east of

the Yanshiping area), in the Eastern Qiangtang Terrane.

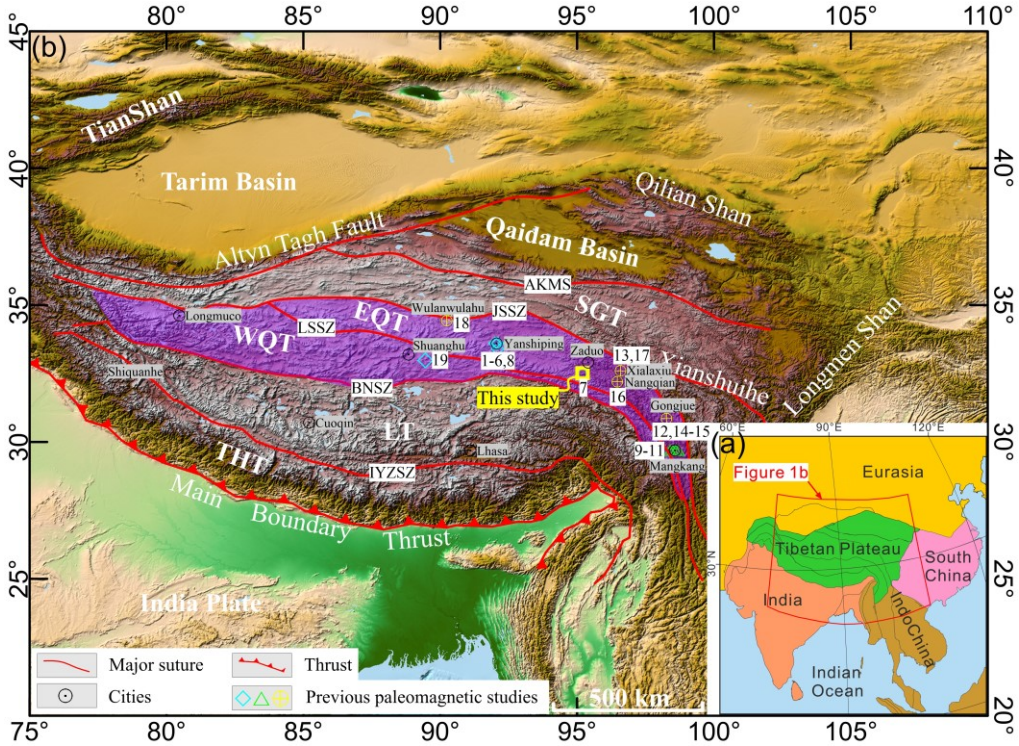

Figure 2.1. *(a and b) Simplified tectonic map of the Tibetan Plateau and its adjacent regions (a) modified after Van Hinsbergen et al., (2012). The abbreviations of the tectonic units are SGT: Songpan-Ganzi Terrane; EQT: Eastern Qiangtang Terrane; WQT: Western Qiangtang Terrane; LT: Lhasa Terrane; THT: Tethyan Himalaya Terrane; AKMS: Ayimaqing-Kunlun-Muztagh Suture Zone; JSSZ: Jinshajiang Suture Zone; LSSZ: Longmu Tso-Shuanghu Suture Zone;* BNSZ*: Bangong-Nujiang Suture Zone; IYZSZ: Indus-Yarlung Zangbo Suture Zone; The numbers show the locations of previous paleomagnetic studies: 1-Dong et al., 1991; 2-Dong et al., 1990; 3-Ran et al., 2017; 4-Yan et al., 2016; 5-Ren et al., 2013; 6-Cheng et al., 2012; 7-This study; 8-Lin & Watts, 1988; 9-Huang et al., 1992; 10-Otofuji et al., 1990; 11-Tong et al., 2015; 12-Li et al., 2020b; 13-Roperch et al., 2017; 14-Tong et al., 2017; 15-Zhang et al., 2018; 16-Zhang et al., 2020a; 17-Cogné et al., 1999; 18-Lippert et al., 2011; 19-Cao et al., 2019 (see also supporting information Table S2.1). The cyan, green and yellow symbols represent the previous paleomagnetic studies of the Jurassic, Cretaceous and Paleogene, respectively.*

A major challenge in paleomagnetism studies is that remagnetization can interfere with paleogeographic reconstructions, as is increasingly recognized (Van der Voo & Torsvik, 2012). It occurs unpredictably either pre-folding (e.g., Perroud & Van der Voo, 1984; Huang *et al.*, 2015a; Gao *et al.*, 2018), syn-folding (e.g., Kent & Opdyke 1985; Huang *et al.*, 2017a, 2017b; Ran *et al.*, 2017), or post-folding (e.g., Liebke *et al.*,

2013; Huang and Opdyke, 2015) rather than being restricted to a certain period in certain regions. Carbonate rocks are particularly notorious for being prone to remagnetization (Jackson & Swanson-Hysell, 2012). For instance, widespread remagnetization has been reported in the orogenic belts in America and Europe (Zegers *et al.*, 2003; Zwing *et al.*, 2009; Elmore *et al.*, 2012; Jackson & Swanson-Hysell, 2012; Van der Voo and Torsvik, 2012). Certain studies reveal carbonate remagnetization in the South China Block (Liu *et al.*, 2013; Huang and Opdyke, 2015; Zhang *et al.*, 2020b) and the Tibetan Plateau (Appel *et al.*, 2012; Liebke *et al.*, 2013; Huang et al., 2015a, 2017a, 2017b, 2019a; Ran *et al.*, 2017; Li *et al.*, 2017b). It is clear that improper conclusions will be reached when using remagnetized rocks for classic palaeogeographic reconstruction.

In this paper, we present a palaeomagnetic study on Middle-Upper Jurassic limestones from the Zaduo region. Their characteristic remanent magnetization was isolated using both thermal and alternating field (AF) demagnetization. Field tests and inclination shallowing correction were carried out. Specifically, we use detailed rock magnetism experiments and microscope observation to determine whether or not the rocks had suffered remagnetization. After confirming the remagnetization, we analyze its timing along with its geological implications. Finally, we discuss possible acquisition mechanisms of remagnetization that may have been operating in this particular setting.

2.2 Geological setting and sampling

The Qiangtang Terrane is located in the central Tibetan Plateau, bounded by the Bangong-Nujiang Suture Zone (BNSZ) to the south with the Lhasa Terrane and by the Jinshajiang Suture Zone (JSSZ) to the north with the Songpan-Ganzi Terrane (Fig. 2.1b). The Triassic Longmo Co-Shuanghu suture zone (LSSZ) subdivides the terrane into the Eastern and Western Qiangtang subterranes (EQT, and WQT, respectively), also known as the Northern and Southern Qiangtang subterranes (cf. Fig. 2.1b; Yin & Harrison, 2000; Pan et al., 2004c; QGSI, 2005; Li *et al.*, 2009a; Metcalfe, 2013).

Our sampled section (32.5°N, 95.2°E) is located in the eastern portion of the EQT, *about* 30 km to the south of Zaduo County (Fig. 2.1b). In the Zaduo area rocks from Paleozoic to Cenozoic are exposed, and they are separated by several unconformities, from old to young: the Lower Carboniferous Zaduo Group, the Upper Carboniferous Jiamainong Group, the Permian Kaixinling Group and Gadikao Formation, the Middle Triassic Jielong Formation, the Upper Triassic Jieza Group, the Middle-Lower Jurassic Yanshiping Group, the Cretaceous Fenghuoshan Group, the Paleocene Tuotuohe and Luolika Groups, and the Eocene Wudaoliang Quguo Groups (Fig. 2.2a; QGSI, 2005, 2014; Guan *et al.*, 2021). There is an obvious sedimentary hiatus during the Early Cretaceous (QGSI, 2005, 2014). The Jurassic Yanshiping Group is formally defined in the Yanshiping area and consists of the Quemo Co (J_2q), Buqu (J_2b), Xiali ($J_{2\text{-}3}x$), Suowa (J_3s) and Xueshan (J_3x) Formations from base to top (QGSI, 2005, 2014;

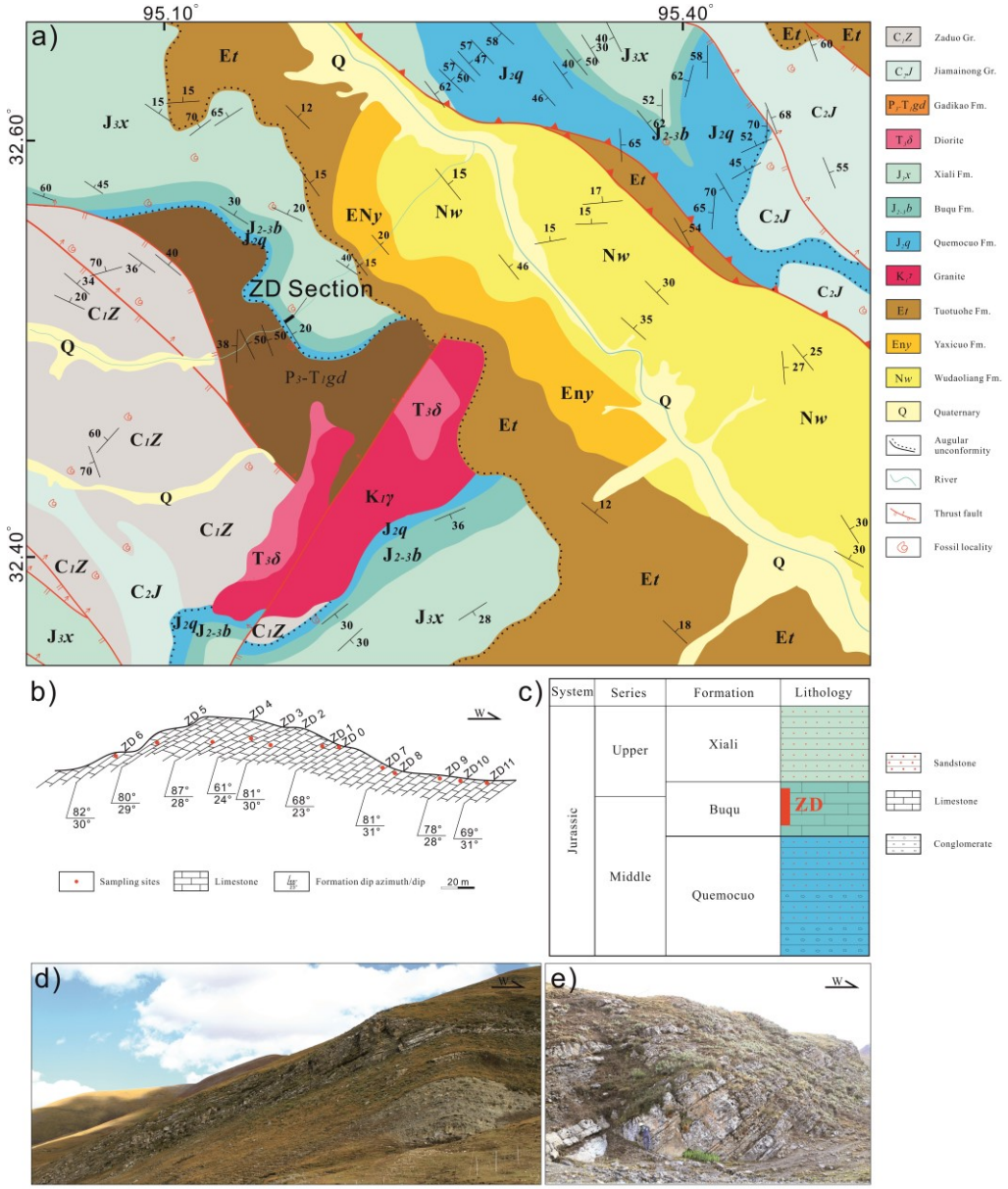

Figure 2.2. *a)* Geological *map of the Zaduo section (modified from the 1:250,000 Zaduo County regional geological map [I46C004004] by the Qinghai Geological Survey Institute (QGSI), 2005). b) Profile of the sampled section. c) Lithostratigraphy of the Buqu Formation with the sampling localities indicated. d-e) field photographs of the Buqu Formation.*

Yan *et al.*, 2016; Fang *et al.*, 2016). The Group is characterized by rhythmic alternations of sandstone and limestone sequences with an overall coarsening upward pattern (QGSI, 2005, 2014; Yan *et al.*, 2016; Fang *et al.*, 2016). All formation contacts are conformable. However, only the Quemo Co, Buqu, and Xiali Formations are exposed in the Zaduo area, our study target (Fig. 2.2a and c; QGSI, 2005, 2014; Yan *et al.*, 2016; Fang *et al.*, 2016; Song et al., 2016). The Quemo Co Formation consists of alternating purple-red sandstones to mudstones with a conglomerate layer at the bottom. The Buqu Formation is mainly white-grayish to dark-grayish oolitic and bioclastic limestone deposited in shallow littoral sea. The appearance of massive biolimestones indicates a warm climate at that time, which was conducive to the growth of organisms, while its bioclastic nature reflects the shallow sea depositional conditions (QGSI, 2005, 2014). Many bivalve fossils are identified in the Buqu Formation in the study area, including *Camptonectes* (*Camptochlamys*), *yanshipingensis* Wen, *Camptonectes* (*Camptonectes*) *rugosus* Wen, *Camptonectes* (*Camptonectes*) cf. *lens* (Sowerby), *Camptonectes concentrica* (Sowerby) and *Pholadomya socialis qinghaiensis* Wen, index fossils of the Bajocian and Bathonian Stages of the Jurassic Epoch (QGSI, 2005, 2014), which are similar to those observed in the Yanshiping region that were magnetostratigraphically dated to be 165.5-163.3 Ma (Fang *et al.*, 2016). The Xiali Formation consists of purple-red and yellow-green sandstones, siltstones, and multicolored (dark red, gray, grayish and light yellow) mudstones (QGSI, 2005, 2014; Fang *et al.*, 2016).

A total of 133 samples from 12 sites were collected from the Buqu Formation using a portable water-cooled petrol-powered drill. They were oriented with a magnetic compass and a sun compass when the weather allowed. All of the sites are located along a monoclinal section where bedding attitudes only have a slight variation with a NE dip direction and dips of 23°- 31° (Fig. 2.2b, d and e). Remarkably, veins are widespread in the Buqu limestones. Most of the samples were collected from fresh rock away from cracks and veins.

2.3 Petrography

Veins are very common in the Buqu limestones (Fig. 2.3a-c). To better understand their mineral composition, texture, and potential changes during burial, we microscopically analyzed thin sections of 10 representative samples. Although we collected fresh samples away from cracks and veins, small gypsum veins can be observed on the samples (Fig. 2.3d-h). Two different microtextures are present in these samples (Fig. 2.3i-p). The first type is characterized by a bioclastic structure, with micritic and/or sparry calcite as the dominant groundmass. Bioclastics account for 60% of the detrital component, and interstitial material for the remaining 40%. Extensive cementation, dissolution, replacement and recrystallization features are recognized. The bioclastics (e.g., crinoids, algae, crustaceans, and foraminifera) are almost completely altered by calcite. The dissolution pores are filled and cemented with calcite (Fig. 2.3i-l). The rocks were thus not immune to diagenetic features. The

other type is mainly micritic and/or has a microcrystalline structure. Calcite is the dominant mineral with a content of about 95%; bioclastics, terrigenous clastic quartz, and certain opaque minerals account for the remaining 5%. In addition, gypsum veinlets are visible under the microscope in most of the samples investigated (Fig. 2.3m-p). These veinlets vary in size, with a thickness ranging from a few to hundreds of micrometers. In short, the microscopic observations show widespread recrystallization and the epigenetic formation of gypsum veinlets. These features suggest hydrothermal activity with the likelihood of remagnetization (Parnell *et al*, 2000; Elmore *et al.*, 2012; Ran *et al.*, 2017; Huang *et al.*, 2017a).

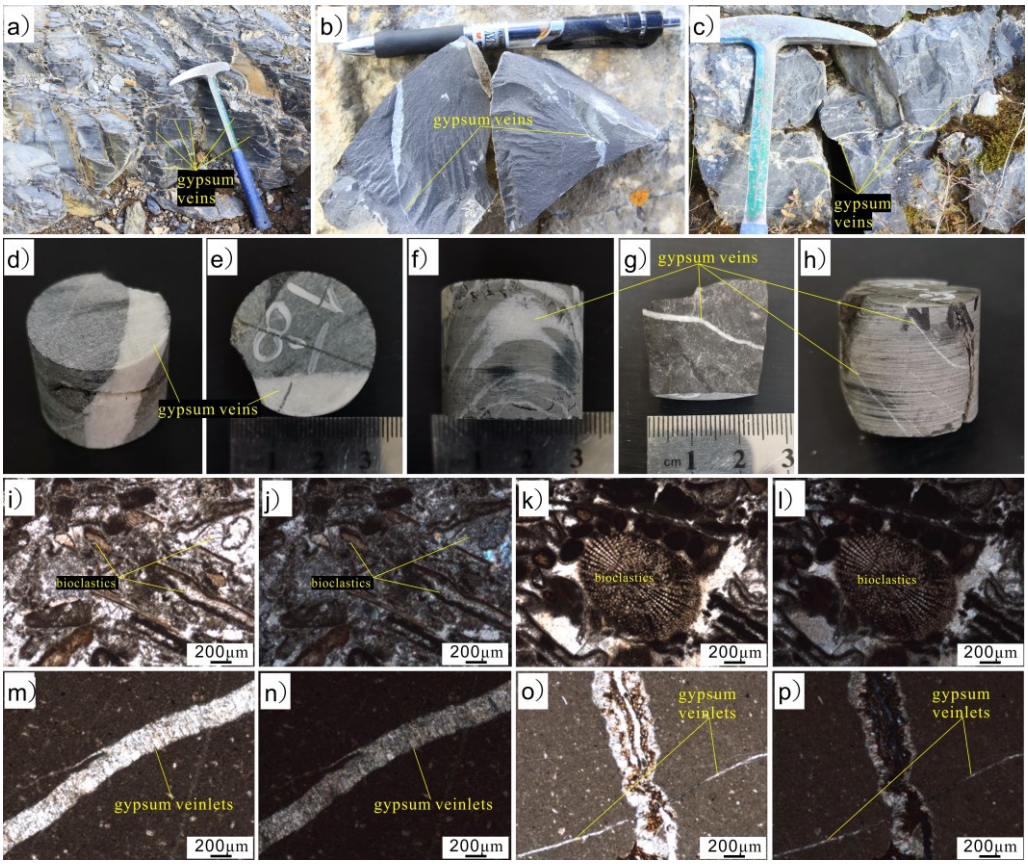

Figure 2.3. *Results of petrographic analysis of representative samples from the Buqu Formation limestones. a-c) widespread veins in thefield outcrops; d-h) macroscopic gypsum veins on the surface of the samples; i-j, k-l, m-n and o-p) micrographs in plane-polarized light and cross-polarized light.*

2.4 Paleomagnetism

Two specimens (diameter 2.5 cm, length 2.2 cm) were obtained from most of the paleomagnetic oriented core samples, one for stepwise alternating field (AF)

demagnetization and the other for stepwise thermal demagnetization to isolate the ChRM. Remnant measurements were conducted by a superconducting quantum interference device (SQUID) magnetometer (2G Enterprises) hosted in a magnetically shielded room (<170 nT). The AF demagnetization was conducted for 133 specimens up to an alternating field of 140 mT with intervals of 2 to 20 mT by a 2G degausser attached to the SQUID magnetometer. 25 sister specimens were progressively thermally demagnetized in 15 steps (100°C, 150°C, 200°C, 300°C, 350°C, 400°C, 425°C, 450°C, 475°C, 500°C, 525°C, 550°C, 570°C, 580°C, and 590°C) in an ASC TD-48 oven. All of the experiments above were conducted in the paleomagnetic laboratory of the Institute of Tibetan Plateau Research, Chinese Academy of Sciences (ITPCAS, Beijing, China).

2.4.1 Demagnetization

For the Buqu limestones, AF and thermal demagnetization data of sister specimens show similar ChRM directions (Fig. 2.4a-d). The ChRM directions were determined from at least four successive steps by principal component analysis (Kirschvink, 1980). Specimens with maximum angular deviation (MAD) >15° were rejected for further analysis. Site-mean directions were calculated using Fisher's statistics (Fisher, 1953). Given that the thermal demagnetization results were sometimes more erratic and yielded higher MAD values than the AF demagnetization, we used the latter to calculate the ChRM directions. Most of the specimens (from 10 out of 12 sites) exhibit a single component that is decaying toward the origin (Fig. 2.4b-d, f-h). This component was often isolated below ~140 mT or ~450-500 °C. The specimens' magnetic intensity usually drops to 20% of the starting value below 40 mT or 350 °C (Fig. 2.4). The other specimens show two components (Fig. 2.4a and e): a viscous low-field (temperature) component (LFC) which is removed below 20 mT or 300-350 °C and a high-field (temperature) component (HFC) which is isolated between 25 and 140 mT or ~300-500 °C. These specimens have a reverse ChRM, and their magnetic intensity increased as the alternating field increased to 20 mT or the temperature rose to ~350 °C (Fig. 2.4).

Figure 2.4 (next page). *Representative demagnetization diagrams for specimens from the Buqu limestones. All diagrams are displayed after bedding tilt correction. Solid (open) symbols represent the* projections *of vector endpoints on the horizontal (vertical) plane; In stereo plots, solid (open) symbols represent positive (negative) inclination. NRM: natural remanent magnetization.*

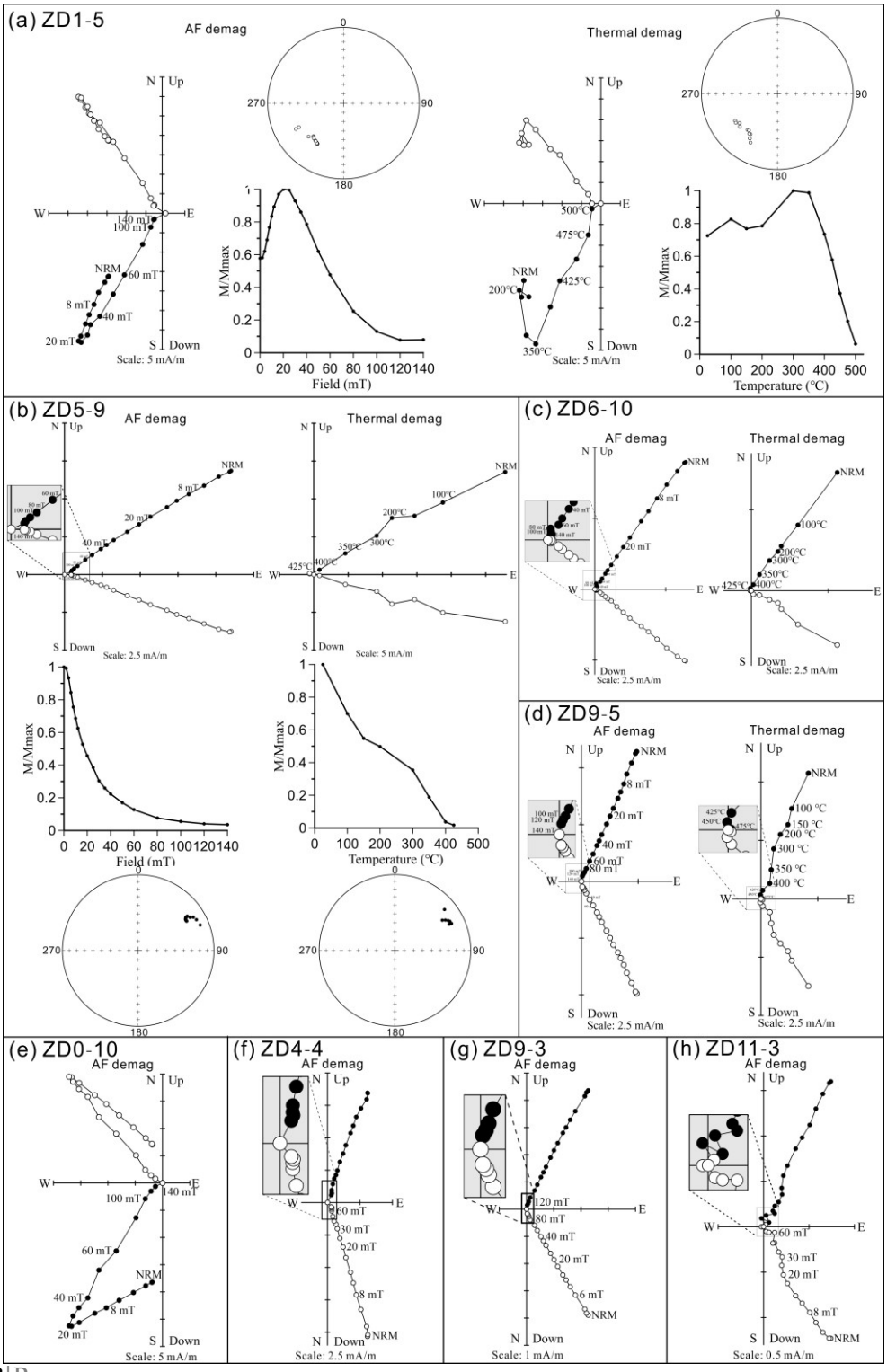
(a) ZD1-5
AF demag
Thermal demag
N Up
S Down
W
E
NRM
20 mT
8 mT
40 mT
60 mT
100 mT
140 mT
200°C
350°C
425°C
475°C
500°C
Scale: 5 mA/m
M/Mmax
Field (mT)
Temperature (°C)
(b) ZD5-9
Scale: 2.5 mA/m
Scale: 5 mA/m
(c) ZD6-10
Scale: 2.5 mA/m
(d) ZD9-5
100 °C
150 °C
200 °C
300 °C
350 °C
400 °C
(e) ZD0-10
Scale: 5 mA/m
(f) ZD4-4
Scale: 2.5 mA/m
(g) ZD9-3
120 mT
6 mT
Scale: 1 mA/m
(h) ZD11-3
30 mT
Scale: 0.5 mA/m

2.4.2 ChRM directions

The mean direction of the LFCs is D_g=16.4°, I_g=45.0°, κ =19, and α_{95} = 7.1°, n = 22 in geographic coordinates and D_s=29.1°, I_s=28.1°, κ =17.9, and α_{95} = 7.4°, n = 22 in stratigraphic coordinates (Fig. 2.5a). The LFCs are not clustered around the present-day geomagnetic field (PGF) direction (D = 359.5°, I = 51.1°) in this region. This component is not assigned geological significance, we thus will not speculate on its origin.

Table 2.1. *High-Field component (HFC) directions of the Middle Jurassic limestones in the Zaduo area, Eastern Qiangtang Terrane, Tibetan Plateau.*

Sites	*n/N*	D_g (°)	I_g (°)	D_s (°)	I_s (°)	κ_{95}	α_{95} (°)
Zaduo Section (32.5°N, 95.2°E)							
ZD 0	11/12	198.1	-52.1	213.8	-37.8	177.1	3.4
ZD 1	12/12	197.2	-52.1	212.4	-37.7	945.8	1.5
ZD 2	10/10	9.5	43.9	26.2	31.5	72.7	5.7
ZD 3	7/10	19.4	43.8	29.9	27.3	50.6	7.9
ZD 4	8/11	13.9	42.7	34.4	32.7	42.1	8.6
ZD 5	9/9	10.5	51.9	39.8	35.9	102.3	5.5
ZD 6	12/12	14.2	45.7	35.7	29.7	211.3	3
ZD 7	10/11	1.8	45.6	29.5	33.4	57.1	6.4
ZD 8	11/11	359.7	50.1	28.5	41.1	316	2.6
ZD 9	12/12	357.6	49.2	26.1	41.1	481.3	2
ZD10	11/11	355.8	46.4	23.5	39.5	551.6	1.9
ZD11	10/12	359.8	53	26.2	38.8	208.8	3.4

Note: *n/N = number of samples used to calculate mean and measured; D_g, I_g, D_s, I_s = declination and inclination in geographic and stratigraphic coordinates, respectively; κ_{95} = the best estimate of the precision parameter; α_{95} = the radius that the mean direction lies within 95% confidence.*

Only a single specimen from each core was paleomagnetically processed and therefore named a sample (Butler, 1992). A total of 123 out of 133 specimens/samples yield consistent high AF ChRM directions that provide 12 site-mean directions containing ten normal and two reverse polarity sites (Fig. 2.5b; Table 2.1, S2.2). Although the two reverse sites are grouped together stratigraphically and may not be sufficient in number, reversals test results (McFadden & McElhinny, 1990) are positive at the 95% confidence limit with a classification A (average g = 2.2 < Critical g = 3.7) for sample-mean directions and a classification B (average g = 3.6 < Critical g = 9.0) for site-mean directions. A fold test could not be conducted due to too slight variation of the bedding attitudes. Inclination shallowing is common in the ChRM directions derived from sedimentary rocks, and it is thought to be due to

depositional processes and/or compaction during burial (Tan *et al.*, 2003; Tauxe & Kent, 2004; Yan *et al.*, 2005, Ren *et al.*, 2013). However, unlike redbeds and other clastic rocks, it is commonly believed that limestone has little inclination shallowing, as it barely compacts, typically 10 times less than redbeds (Cheng *et al.*, 2012). To check whether there is indeed no inclination shallowing in the present sample collection, we applied the E/I method of Tauxe & Kent (2004) on the obtained 123 directions. The corresponding flattening factor (f=0.936) provides a mean inclination of 37.4° (Fig. 2.5d and e) with 95% confidence limit bounds of 35°- 44°, which is a little larger than both of the sample-mean inclination (36.3°) and the site-mean inclination (35.6°), but still well within the confidence limit. Therefore no inclination bias is present in the Buqu limestones in the Zaduo area. The site-mean direction of the 12 sites is D_g = 8.2°, I_g = 48.3°, κ_g = 138.3, α_{95} = 3.7° in situ, and D_s = 30.6°, I_s = 35.6°, κ_s = 182.9, α_{95} = 3.2° after tilt-correction, corresponding to a paleopole at 59.8°N, 202.7°E with A_{95} = 2.8° and a paleolatitude of ~19.7°± 2.8°N for the study area (Fig. 2.5c; Table 2.2).

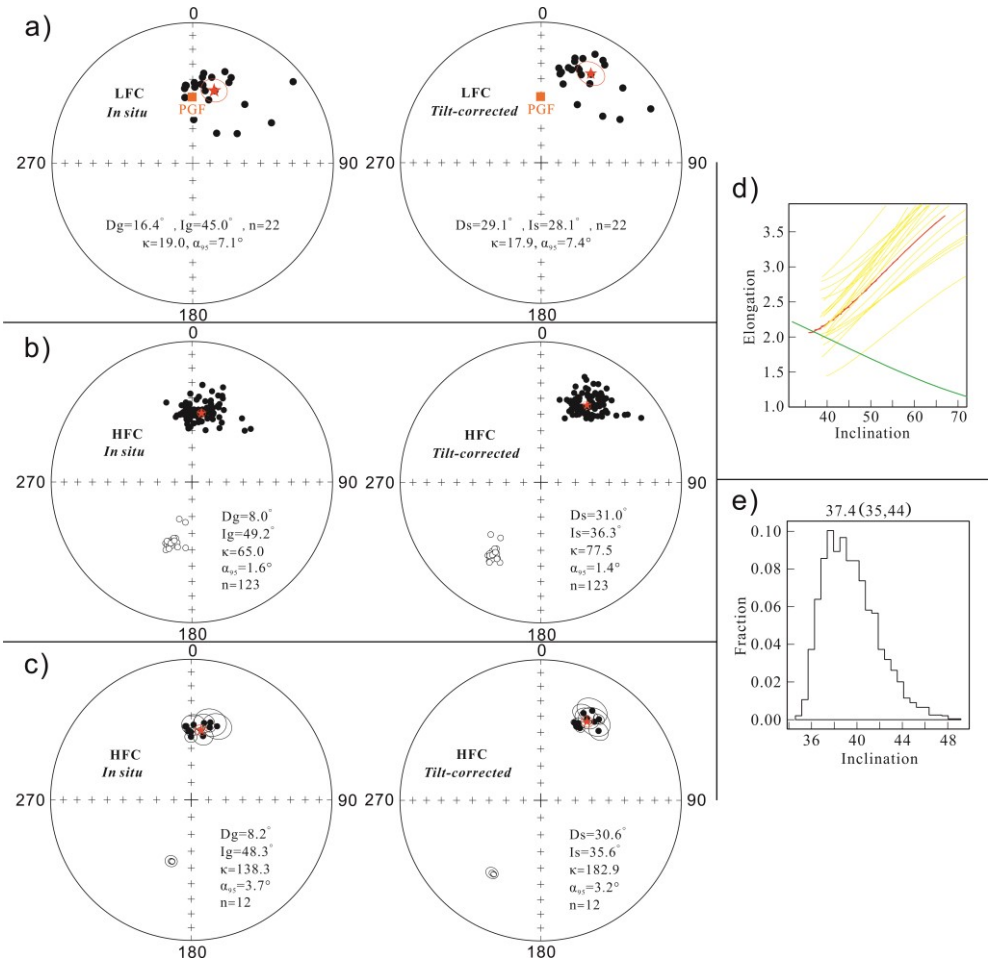

Figure 2.5 (previous page). *a-b) Equal-area projections of the sample-mean directions for LFCs/HFCs before and after tilt correction, respectively; c) Equal-area projections of the site-mean directions for HFCs before and after tilt correction; d) Plot of elongation versus inclination derived from the TK03. GAD model, the intersection point indicates the inclination/elongation pairs most consistent with the TK03.GAD model; e) Histogram of 1000 boot-straps, the most frequent inclination is 37.4°, and the 95% confidence limits are 35°-44°. Red stars and circles around them in panels a), b) and c) denote the overall mean direction and the 95% confidence limit. The brown squares in panels a) and b) denote the present-day geomagnetic field (PGF) direction of the sampling location. Solid and open symbols denote the lower and upper hemispheres projections before and after tilt correction, respectively.*

2.5 Rock magnetism

At least one representative sample from each site was selected for rock magnetic experiments. The low-field magnetic susceptibility as a function of temperature (κ-T) was measured with a MFK1-FA Kappabridge instrument with a CS-4 high-temperature furnace (AGICO, Czech Republic) in an argon atmosphere at a flow rate of 100 ml/min. The successive peak temperatures were 250, 350, 400 (partially), 450, 550, 620 and 700 ℃, respectively. These samples were first heated to 250 °C and cooled back to room temperature with an applied magnetic field of 200 A/m at a frequency of 976 Hz, then heated to 350 °C and cooled back to room temperature. The procedure was completed after repeating this cycle to 700 °C. Isothermal remanent magnetization (IRM) acquisition curves, direct current back field remagnetization curves, hysteresis loops, and first-order reversal curves (FORCs) were measured with a Lakeshore 8600 Vibrating Sample Magnetometer (VSM). Stepwise thermal demagnetization of IRM was conducted with a TD-48 oven and a minispin magnetometer.

2.5.1 Thermomagnetic runs of magnetic susceptibility

Stepwise thermomagnetic runs of magnetic susceptibility were carried out for the Buqu limestones (Fig. 2.6). The samples show a prominent increase in magnetic susceptibility at ~ 330 °C or 350 °C except for site ZD2 (Fig. 2.6a, c and d), which can be attributed to magnetite formed as high temperature product of iron sulfide alteration (i.e. pyrite, pyrrhotite and greigite) (Huang *et al*., 2019a). All of the 250 °C and some of the 350 °C heating-cooling cycles are reversible. The cooling curve is above the heating curve for all the 450 °C cycles. When it comes to the higher temperature interval (i.e., the 620 °C and 700 °C runs), some of the heating-cooling cycles are quasi-reversible. All of the samples show a decrease in susceptibility at ~580 °C, which is typical for magnetite. A distinct increase at ~400-500 °C of high temperature interval is likely the Hopkinson peak, suggesting fine grain size magnetite with a rather narrow grain size range as expected for magnetite formed

during the experiment itself (Fig. 2.6c and d).

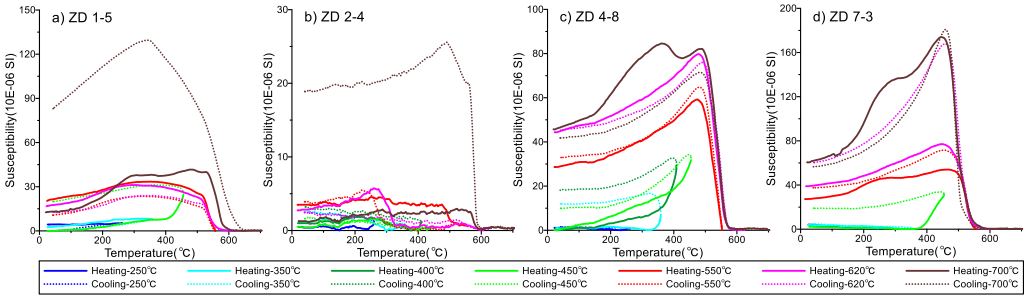

Figure 2.6. *Multicycle high-temperature magnetic susceptibility curves (κ-T) of the representative samples.*

2.5.2 IRM acquisition and back-field curves, thermal demagnetization of IRM, and IRM component analysis

The IRM acquisition curves of the representative samples show similar characteristics (Fig. 2.7a, c, and d). They present a sharp increase below 100 mT and acquire ~80-90% saturation at that step, with the remanent acquisition coercive force < 50 mT, suggesting that low-coercivity magnetic components (i.e., magnetite sensu lato) are dominant. Samples from site ZD 2 (Fig. 2.7b, note the unit of the vertical axis) are very noisy because of their weak IRM. In addition, two perpendicular IRMs with fields of 2.5 T and 120 mT were imparted in single samples and subjected to stepwise thermal demagnetization along the lines of Lowrie (1990). The soft and hard components in most of the samples exhibit a maximum unblocking temperature at ~500 °C (Fig. 2.7e, g, and h). This is too low for the typical SD magnetite, but compatible with the fine-grained quasi-superparamagnetic magnetite. For the samples from site ZD 2, the soft component exhibits the same features as in the others, but the hard component drops to essentially zero at ~640 °C, which is interpreted to indicate probably fine-grained hematite as a carrier (Fig. 2.7f).

To estimate the magnetic contributions of different magnetic minerals, we applied IRM component analysis to a sample of each site except the reverse polarity sites (Kruiver *et al.*, 2001). Four IRM components are used to fit the IRM acquisition curves: component 1 with $B_{1/2}$ (the field at which half of saturation isothermal remanent magnetization (SIRM) is reached) of ~5 mT and dispersion parameter DP (width of the distribution) of ~0.20-0.30 (log units); component 2 with $B_{1/2}$ of ~10-20 mT and DP of ~0.20-0.30; a harder component 3 with $B_{1/2}$ of ~50-70 mT and DP of ~0.30; and a much harder component 4 with $B_{1/2}$ of >300 mT and DP of <~0.20. In general, components 1 and 2 contribute ~10-20 % to the SIRM and might be the result of thermally activated component 3 (Egli, 2004; Heslop *et al.*, 2004; Huang et al.,

2015a; Zhang *et al.*, 2018). Component 3 is the dominant magnetic carrier in the Buqu limestone and contributes >70% to the SIRM, which is typically interpreted to be magnetite (Kruiver *et al.*, 2001). Component 4 has a distinctly $B_{1/2}$ value and contributes ~4% to the SIRM, which presumably represents very fine-grained magnetite close to the SP threshold size, or residual iron sulfide that remained after oxidation to authigenic magnetite.

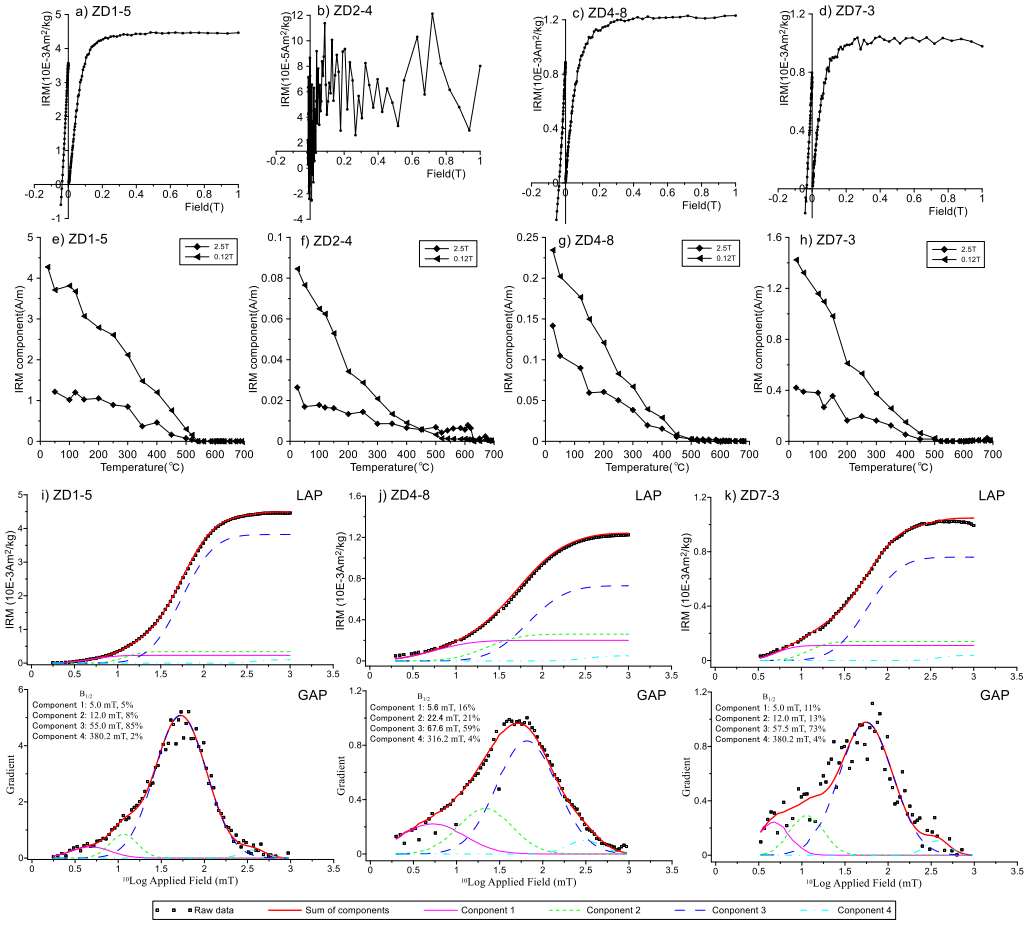

Figure 2.7. *a-d) IRM acquisition curves for representative samples; e-h) Thermal demagnetization of two perpendicular IRMs; i-k) IRM component analysis (Kruiver et al., 2001) of representative samples with ~80 data points acquired. Squares are measured data points. The components are marked with different colored lines. Log₁₀ ($B_{1/2}$) and DP are in log₁₀ mT. LAP: linear acquisition plot and GAP: gradient acquisition plot.*

2.5.3 Hysteresis Loops, Day-plot and FORC Diagrams

Hysteresis loops of the Buqu limestone samples can be divided into two types. Type one is from sampling site ZD 2 and shows 'pot-bellied' features (Fig. 2.8b). Type two samples are all from most of the sampling sites and are characterized by 'wasp-waisted' loops (Fig. 2.8a, c, and d). 'Wasp-waisted' hysteresis loops are indicative of discrete low-coercivity and high-coercivity phases in a single sample (e.g., Roberts *et al.*, 1995; Tauxe *et al.*, 1996; Jackson & Swanson-Hysell, 2012; Ge et al., 2017; Shen et al., 2020). This hysteresis behaviour results from multiple mineralogies or discrete fractions of ferrimagnetic grains in a largely mono-mineralic population (Jackson & Swanson-Hysell, 2012). The FORC diagrams for type one samples are characterized by closed concentric contours with a substantial vertical spread of the FORC distribution, indicating an assemblage of interacting SD particles (Roberts *et al.*, 2006, 2014). For type two samples (of normal polarity), FORC diagrams have a FORC density (ρ) peak (mixed second derivative of the magnetization data) with closed counters around B_c <20 mT and a vertically asymmetrical distribution of about ~-30-

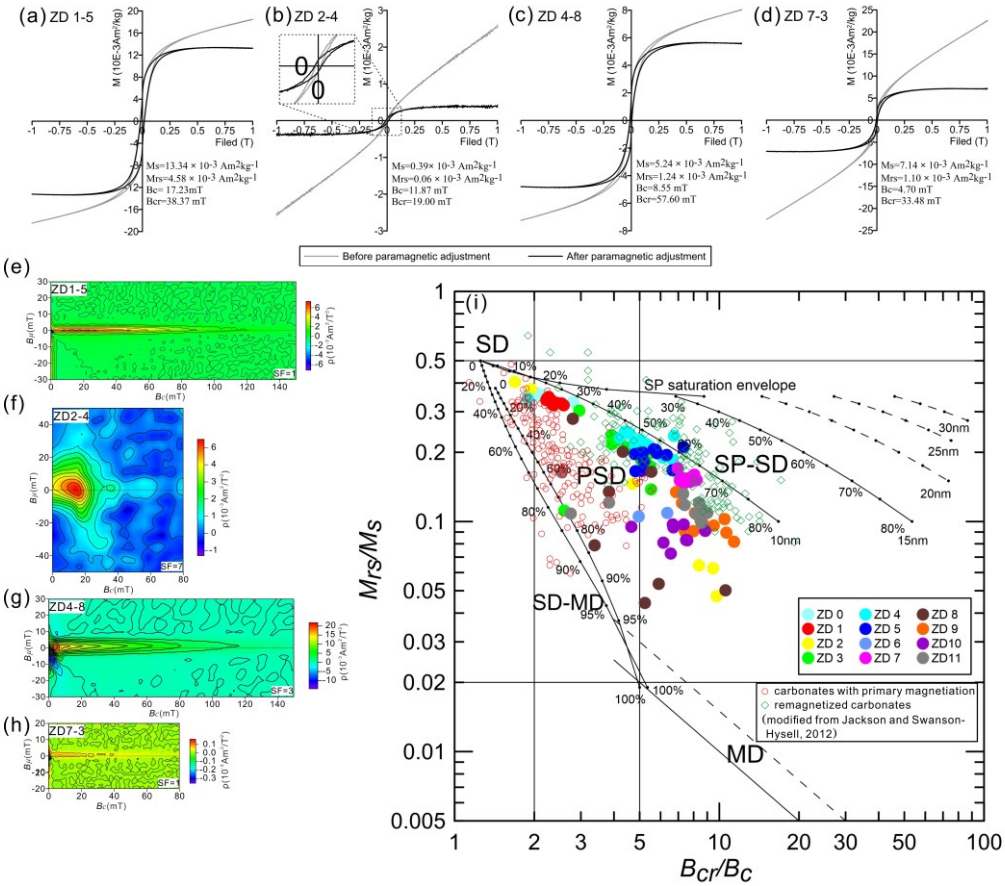

Figure 2.8 (previous page). *a-d) Hysteresis loops of representative samples; the grey and black loops are before and after correcting for the paramagnetic contribution, respectively; e-h) FORC diagrams for representative samples; i) Day plot (Dunlop, 2002) of 114 limestone samples. Also plotted are Day-plot of published hysteresis parameters for remagnetized and non-remagnetized carbonate rocks summarized by Jackson & Swanson-Hysell (2012). Solid dots denote different sampling sites from the ZD section, green diamonds and red circles denote remagnetized and non-remagnetized carbonate rocks from Jackson & Swanson-Hysell (2012), respectively.*

5 mT along the B_c = ~0-5 mT line. These characteristics resemble those of SP ferrimagnetic grain assemblies (Pike *et al.*, 2001; Roberts *et al.*, 2006, 2014). All the samples fall within the pseudosingle domain (PSD) field on the Day plot (Dunlop, 2002), with B_{cr}/B_c ratios ranging from 2 to 8 and M_{rs}/M_s ratios ranging from 0.1 to 0.4 (Fig. 2.8i). However, it should be noted that most natural sediment samples fall within the PSD domain, which makes interpretation rather complicated (e.g., Qin *et al.*, 2008; Li *et al.*, 2017a; Cao *et al.*, 2019; Guan *et al.*, 2021). Despite skepticism some people have pertaining to the Day-plot, remagnetization may be diagnosed with it (Roberts *et al.*, 2018).

2.6 Discussion

2.6.1 Does the Buqu Formation in the Zaduo area carry a primary NRM?

The limestones of the Buqu Formation in the Yanshiping area were dated to the Bajocian-Callovian stages based on biostratigraphic age constraints (QGSI, 2005, 2014; Fang *et al.*, 2016; Yan *et al.*, 2016). In the present study all of the samples, cq. sites, are from a monoclinal section with only a slightly varying bedding attitude. This precludes usage of the classic fold test to constrain the timing of their NRM. While the reversals test is positive which yields some support for a primary origin of the NRM, we should not exclude protracted remagnetization which may yield dual polarities (Meijers *et al.*, 2011; Huang & Opdyke, 2015; Huang *et al.*, 2019a). In addition to the classic geometric palaeomagnetic field tests (i.e., the fold test, conglomerate test, reversals test, and baked contact test), rock magnetic characterization and microscopic observation provide valuable information to evaluate the origin and significance of NRM components.

Authigenic magnetite, dominantly in the SP and SSD size range, is rather commonly used as a 'fingerprint' of remagnetization (McCabe & Channell, 1994; Jackson & Swanson-Hysell, 2012). Our rock magnetic results show that magnetite is the dominant magnetic carrier in the Buqu limestones. Magnetic properties differ widely with increasing size within the SP range and across the SP-SSD threshold: large SP particles more often saturate in low applied fields, while small SP particles may not saturate at all even in 2 T fields (e.g., Dekkers & Pietersen, 1992; Tauxe *et al.*, 1996; Gong *et al.*, 2009). In such cases, the 'wasp-waisted' hysteresis behavior can be

attributed to SP and SSD grain sizes of magnetite. SP particles are also indicated by the FORC features and low unblocking temperatures (400-500 ℃). Although the SP particles play no role in carrying a geologically stable NRM at room temperature, they are considered to have a similar origin as the cogenetic SSD particles that do carry the paleomagnetic information in many remagnetized carbonate rocks (e.g., Jackson & Swanson-Hysell, 2012; Huang *et al*., 2019b). Coercivity (B_{cr}/B_c) and remanence (M_{rs}/M_s) ratios for our Jurassic limestones are close to the 'remagnetization trend' on a Day-plot (Fig. 2.8i), previously interpreted to be characteristic of chemical remagnetization (e.g., Jackson, 1990; McCabe & Channel 1994; Jackson & Swanson-Hysell, 2012). This trend is distinct from the regions occupied by most other rocks, sediments and synthetic materials and arguably the biggest success of the Day plot (Fig. 2.8i, Roberts *et al*., 2018). The uncommon magnetic properties of remagnetized carbonates display an empirically derived equation of $M_{rs}/_{Ms}\approx0.89(B_{cr}/B_c)^{-0.6}$ (Jackson, 1990; Jackson et al., 1993). Our data show a trendline similar to this equation, except that the M_{rs}/M_s values of our samples are lower than those in Jackson's (1990) study, which can be attributed to partial oxidation of magnetite, particle shape, or uncertain mixtures of magnetic mineral components (Roberts *et al*., 2018). Our data will fit well if we would change the trendline equation to $M_{rs}/M_s\approx0.89(B_{cr}/B_c)^{-1}$ or $M_{rs}/M_s\approx0.5(B_{cr}/B_c)^{-0.6}$ as proposed by Jackson et al., (1993); the best-fit equation of our data is $M_{rs}/M_s\approx0.61(B_{cr}/B_c)^{-0.8}$ (Fig. 2.9).

In the study area, veins are widespread in the Buqu Formation limestones. Evidently, we focused on fresh rocks away from cracks and veins to collect samples. However, veins of a few to a dozen millimeters wide can be clearly observed on the surface of some core samples (Fig. 2.3). For those core samples whose veins are invisible by observation with the naked eye, a few to tens of microns wide veins can be observed under the microscope (Fig. 2.3). These veins are mainly composed of gypsum, commonly taken as being indicative of diagenetic fluid migration (Gustavson et al., 1994; Phillip, 2008; Bons *et al*., 2012; Gale *et al*., 2014), so, quite reasonably associated with remagnetization of the Buqu Formation limestones in the study area. Therefore, rock magnetic tests and thin section observations lead us to conclude that the studied Jurassic limestones of the Buqu Formation in the Zaduo area were remagnetized. Authigenic magnetite grains, dominantly of SSD size, but with cogenetic fine-grained SP size particles, are responsible for the secondary magnetizations.

Figure 2.9 (next page). *Hysteresis parameters for the Jurassic limestones in the Zaduo section and empirically derived equation of remagnetized carbonates. The red line represents the equation from Jackson (1990) and Jackson et al. (1993); the magenta short dashed and pink long dashed lines represent the modified equations Jackson et al., (1993); the blue dash-dotted line represents the best fit equation of our data.*

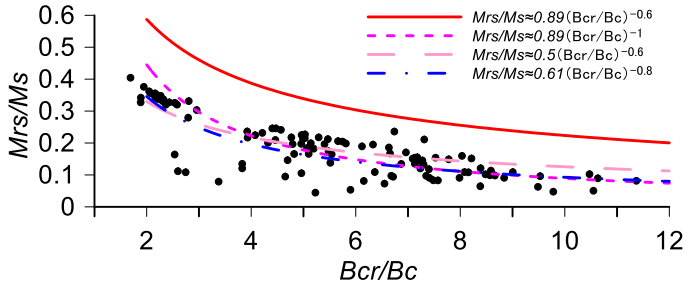

2.6.2 Timing of the remagnetization and tectonic implications

Remagnetization can occur in principle any time during geological history, yet it is generally tied to certain geological events (e.g., diagenesis, orogenies, metamorphism, or thermoviscous resetting by volcanism). Two major events have occurred in the Tibetan Plateau region after the middle Jurassic: one is the collision between the Lhasa and Qiangtang Terranes, and the other is the India-Eurasia collision. The shortest distance from a remagnetization paleopole to the reference apparent polar wander path (APWP) can be used to estimate the age of the remagnetization event despite the rather low precision of this approach (Van der Voo & Torsvik, 2012). Here we compare the paleopole from the present study with those from the Eastern Qiangtang Terrane. The Jurassic to Paleogene paleopoles of the Eastern Qiangtang Terrane were selected for consideration following the restrictive criteria for high-quality paleomagnetic data (Fig. 2.10a and Table 2.2). As shown in Fig. 2.10a and Table 2.2, the Jurassic paleopoles (Cheng *et al.*, 2012; Ren *et al.*, 2013; Yan *et al.*, 2016) are consistent. However, the Cretaceous and Paleogene paleopoles are more scattered, which is interpreted as local rotation after the Lhasa-Qiangtang and India-Eurasia collisions (Tong *et al.*, 2015; Chen et al., 2017b). Even in the presence of different coeval paleopoles, the paleopole of the present study (59.8°N, 202.7°E, A_{95}=2.8°) is fairly close to the sparsely available Paleogene poles (see the supporting information text and Table S2.1; Fig. 2.10a; Van der Voo, 1990; Meert *et al.*, 2020). We also calculated the mean inclinations of the Jurassic, Cretaceous and Paleogene, our inclination (35.6° ± 4.2°) is similar to the Jurassic (34.7° ± 5.2°) and the Paleogene (39.7° ± 7.3°) inclinations, but smaller than the Cretaceous inclination (52.8° ± 6.1°).

Alternatively, the timing of remagnetization can be estimated by comparison of the measured declination, inclination, and paleolatitude with the expected ones for different ages in the Qiangtang Terrane. All the paleomagnetic directions were converted to our study site (32.5°N, 95.2°E), the new declinations and paleolatitudes were then recalculated and are shown in Fig. 2.10c and d. Paleomagnetic declinations indicate that the Qiangtang Terrane relative to Eurasia experienced ~20° counterclockwise rotation since the Middle-Late Jurassic, ~30°-40° clockwise rotation since the Cretaceous (Huang *et al.*, 1992; Tong *et al.*, 2015), and ~10°-30°

clockwise rotation since the Paleogene (Lippert *et al*., 2011; Tong *et al*., 2017; Zhang *et al*., 2018, 2020a; Li et al., 2020b). The fold in our study area was formed during the late Himalayan period (QGSI, 2014). The ChRM directions after tilt-correction (κ_s = 182.9) are more clustered than in geographic coordinates (κ_g = 138.3) (Fig. 2.5b and c). It is likely that the remagnetization occurred prior to the folding. The declination after correction for the bedding attitude in this study is ~30°, which is comparable with either the Cretaceous or the Paleogene declination. Notably, the Early Cretaceous intrusive rock body nearby has an age of ~126 Ma (QGSI, 2014) which is plausible to account for the remagnetization, considering that ~126 Ma is fairly close to a N/R polarity transition (in the time scale of Gale *et al*., 2020, there is a normal-polarity zone from ~127.6 Ma to ~126.5 Ma and a reversed-polarity zone from ~126.5 Ma to ~124.7 Ma) which could account for the dual polarities found in this study. However, upon further analysis, this scenario seems unlikely (see section 2.6.3). Furthermore, dual-polarity makes it not likely that the remagnetization has occurred during the Cretaceous Normal Superchron (CNS), even though a very recent study suggests several reverse-polarity events or clusters of events within the CNS (Zhang *et al*., 2021). Inclination matching and paleolatitude matching were used to determine the remagnetization age. The paleolatitude of ~31°-36°N obtained from the Mangkang area is about ~10° -15° higher than that of this study (~20°N), but with large uncertainty in their studies (± 6.5°~ ± 10.9°) (Huang *et al*., 1992; Tong *et al*., 2015). In contrast, the 38.6 ± 0.5 Ma paleomagnetic data from the Wulanwulahu area indicate that the Eastern Qiangtang Terrane was at a paleolatitude of ~25°N at that time (Lippert *et al*., 2011). This is consistent with the inclination-shallowing-corrected result of ~24°N during the interval from 56.0-43.2 Ma by Tong *et al*. (2017). In addition, these paleolatitudes are similar to the predicted paleolatitude of the Eastern Qiangtang Terrane of ~24°-30°N, a prediction based on magnetostratigraphic data of the sedimentary sequences in the Nangqian and Gongjue basins (Zhang et al., 2020a; Li et al., 2020b). We therefore interpret that the episode of remagnetization studied here more likely occurred during the Eocene rather than the Cretaceous.

The collision between India and Eurasia during the Paleocene induced significant latitudinal crustal shortening across southern Eurasia (Dewey *et al*., 1989; Yin & Harrison, 2000; Dupont-Nivet *et al*., 2010a, 2010b; Lippert *et al*., 2011; Van Hinsbergen *et al*., 2012; Li *et al*., 2017c; Tong *et al*., 2017). The expected paleolatitude of the reference point (32.5°N, 95.2°E) calculated from the Eocene reference poles for Eurasia is ~35°N, indicating that the Zaduo area of the Eastern Qiangtang Terrane has experienced ~15.7° ± 3.2° (~1740 ± 350 km) of latitudinal crustal shortening since the Eocene. The large difference in latitudinal crustal shortening between the Zaduo and Mangkang areas would likely be accommodated by strike-slip faulting. However, strike-slip faulting is non-existent in the Eastern Qiangtang Terrane, either due to paleomagnetic data uncertainty, or alternatively due to clockwise rotations of the Mangkang area that would yield southward movements of the region, which indeed

have been documented by some studies (e.g., Huang *et al*., 1992; Tong *et al*., 2015). Also, a combination of both options is possible. Given that the paleomagnetic data generally come with statistical uncertainties>4°, sometimes even >10°, in our view, it is less relevant to discuss possible north/south movements of the Qiangtang Terrane for the period involved, because the data uncertainty is not really justifying that. Our estimates coincide with latitudinal shortening estimates across Tibet and stable Eurasia in a number of paleomagnetic studies (Dupont-Nivet *et al*., 2010a, 2010b; Tang *et al*., 2013; Ma *et al*., 2014; Li *et al*., 2017c; Tong *et al*., 2017). In response to the India-Eurasia collision, the southeastern part of the Tibetan Plateau underwent a clockwise rotation (Tapponnier *et al*., 1982). The Zaduo area, Nangqian, Xialaxiu, Gongjue, and Mangkang basins are all located in the transition zone where the overall structural trend turns from east-west-oriented in the central Tibetan Plateau to north-south-oriented in the southeastern edge of the Tibetan Plateau (Fig. 2.1). Zhang *et al*. (2020a) suggest that the Nangqian Basin has experienced a counterclockwise rotation of 25.9 ± 7.2° during ~52-46 Ma, and an insignificant rotation during ~46-41 Ma, followed by a clockwise rotation of 24.4 ± 9.7° during ~41-35 Ma. Paleomagnetic results of the Xialaxiu Basin volcanic rocks aged ~49-51 Ma show a consistent declination as the nearby Nangqian Basin, which indicates similar rotation histories of these regions (Roperch *et al*., 2017). In the Gongjue Basin, a three-stage rotation history since ~53 Ma is recorded as well (Zhang *et al*., 2018; Li et al., 2020b). The Mangkang Basin underwent a clockwise rotation of ~40° since the Cretaceous (Otofuji *et al*., 1990; Tong *et al*., 2015). Although the rotations vary with age, they are all clockwise which is noteworthy. Therefore, we believe that the ~30° clockwise rotation of the Zaduo area is most likely due to the large-scale tectonic deformation of the eastern Tibetan Plateau after the India-Eurasia collision rather than a local deformation feature.

Figure 2.10 (next page). *a) Equal-area projection of the reliable Jurassic, Cretaceous and Cenozoic paleopoles obtained from the Eastern Qiangtang terrane; b) The mean inclinations calculated from the Jurassic, Cretaceous and Cenozoic paleopoles, respectively; (c and d) Plots of the mean ChRM directions of previous paleomagnetic studies (declination and paleolatitude, respectively). The solid black line represents the expected declination and paleolatitude determined from the APWP curve of Eurasia (Besse & Courtillot., 2002, 2003). All these results have been converted to the reference point (32.5°N, 95.2°E). The red dashed box represents possible timing of the remagnetization. The orange dashed box represents the time interval of the Cretaceous Normal Superchron (CNS).*

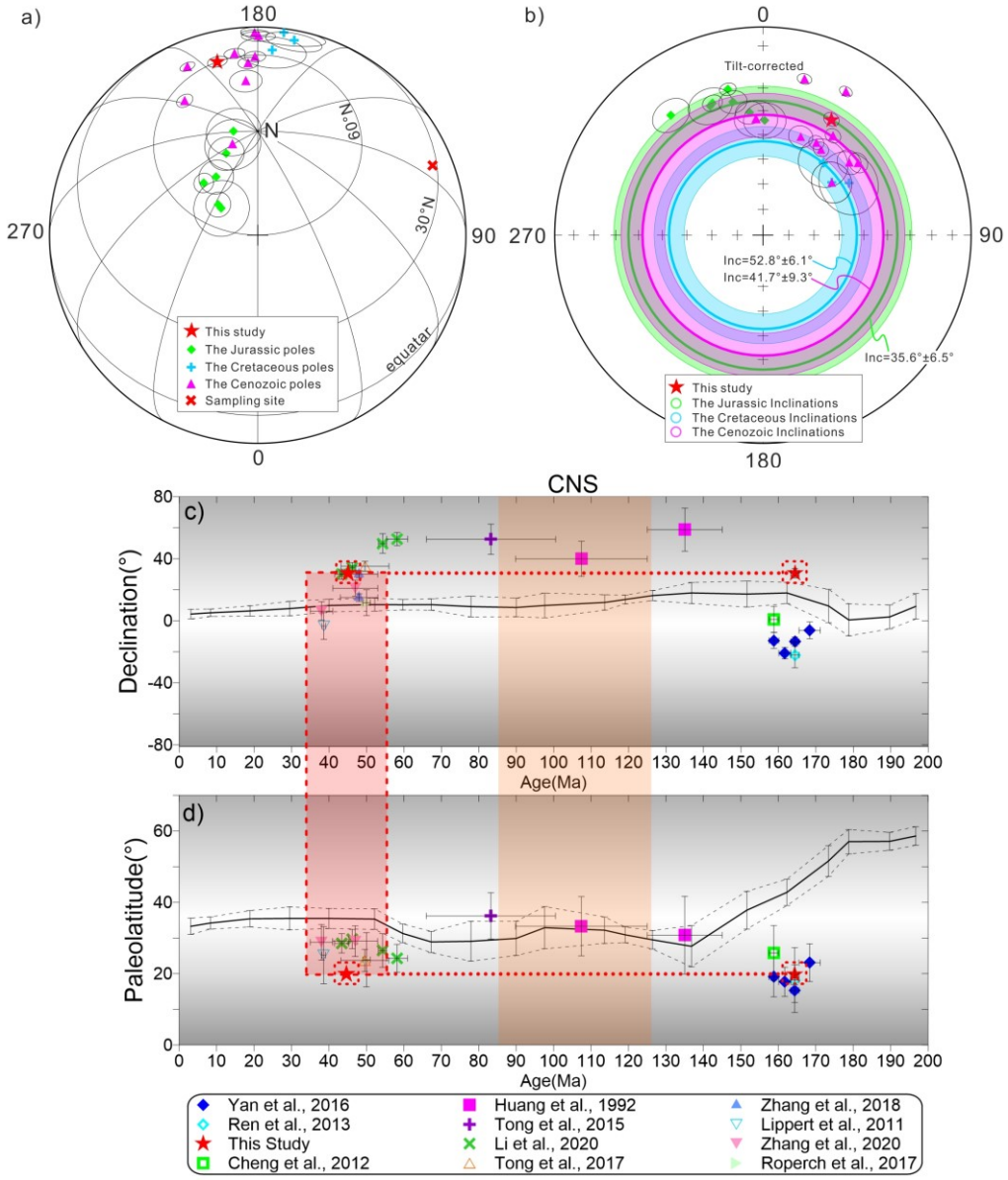
a)
180
270
90
0
N
60°N
30°N
equator
This study
The Jurassic poles
The Cretaceous poles
The Cenozoic poles
Sampling site
b)
0
Tilt-corrected
270
90
180
Inc=52.8°±6.1°
Inc=41.7°±9.3°
Inc=35.6°±6.5°
This study
The Jurassic Inclinations
The Cretaceous Inclinations
The Cenozoic Inclinations
CNS
c)
Declination(°)
Age(Ma)
d)
Paleolatitude(°)
Age(Ma)
Yan et al., 2016
Ren et al., 2013
This Study
Cheng et al., 2012
Huang et al., 1992
Tong et al., 2015
Li et al., 2020
Tong et al., 2017
Zhang et al., 2018
Lippert et al., 2011
Zhang et al., 2020
Roperch et al., 2017

Table 2.2. *Paleomagnetic poles for the Eastern Qiangtang Terrane*

Sampling site						Pole location			At Reference Position (32.5°N, 95.2°E)						
location	Slat (°N)	Slon (°E)	Lithology	Age (Ma)	N(n)	Plat (°N)	Plon (°E)	A_{95} (°)	Paleolat(°)	Dec(°)	ΔDec(°)	Inc(°)	ΔInc(°)	Criteria (Q)	References
Eastern Qiangtang Terrane															
Yanshiping	33.6	92.1	Clastic	165.5-171.2	25(182)	79.1	306.9	5	23.1±5.3	-6.2	5.4	40	6.8	123□5R7(6)	Yan et al. (2016)
Yanshiping	33.6	92.1	Limestone	163.3-165.5	27(245)	68.9	313.8	2.8	15.3±3.4	-14	2.9	29	4.6	123F5R7(7)	Yan et al. (2016)
Yanshiping	33.6	92	Limestone	163.3-165.5	30(171)	65.5	335	7.8	18.2±9.1	-22	8.2	33	12.1	123□5□7(5)	Ren et al. (2013)
Zaduo	32.5	95.2	Limestone	163.3-165.5	12(123)	59.8	202.7	2.8	19.7±2.8	31	3	36	4.2	123□5R7(6)	This study
Yanshiping	33.6	92.1	Sandstone	160.1-163.3	24(224)	66.1	332.1	3.5	17.7±4.1	-21	3.7	33	5.5	123F5R7(7)	Yan et al. (2016)
Yanshiping	33.6	92.1	Shale	157.5-160.1	20(191)	72.4	318.6	4.9	19.1±5.6	-13	5.2	35	7.4	123F5R7(7)	Yan et al. (2016)
Yanshiping	33.6	92.1	Limestone	157.5-160.1	6(59)	83.3	268.3	7.6	25.8±7.7	0.9	8.4	44	9.7	123 F5□7(6)	Cheng et al. (2012)
Mangkang	29.7	98.4	Red beds	Berriasian-Barremian	12(68)	40.6	170.5	12	30.8±10.9	59	13.9	50	13.3	123F5D7(7)	huang et al. (1992)
Mangkang	29.7	98.7	Red beds	Aptian-Turonian	11(79)	56.7	172.7	9.5	33.3±8.3	40	11.4	53	10	123F5□7(6)	huang et al. (1992)
Mangkang	29.7	98.5	Red beds	K_2	17(186)	47	165.1	7.9	36.2±6.5	53	9.8	56	7.7	□23F5R7(6)	Tong et al. (2015)
Gongjue	30.9	98.3	Sandstone	55.4-61	-(104)	43.4	181.2	3.8	24.3±3.9	53	4.2	42	5	123F5R7(7)	Li et al. (2020b)
Gongjue	30.9	98.3	Sandstone	53.2-55.4	-(68)	46.6	179.7	4.7	26.5±4.7	50	6.3	45	5.9	123F5R7(7)	Li et al. (2020b)
Xialaxiu	32.6	96.6	Volcanic rocks	49-51	21(-)	76.4	223.2	7.6	23.9±7.6	12	8.3	41	10.3	123□5□□(4)	Roperch et al. (2017)
Gongjue	31	98.2	Red beds	43.2-56	43(-)	57.9	192.1	2.9	23.7±3.1	35	3.2	41	3.9	123F5R7(7)	Tong et al. (2017)
Gongjue	31	98.2	Red beds	43-53	28(150)	55.1	216.2	2.2	11.1±2.9	30	2.2	21	4	123F5R7(7)	Zhang et al. (2018)
Gongjue	31	98.2	Red beds	43-53	33(178)	65.5	237.8	2.4	12.2±3.1	15	2.5	23	4.2	123F5R7(7)	Zhang et al. (2018)
Nangqian	32.2	96.6	Sandstone & Marlite	41-53	-(300)	71.7	190.5	4.5	29.1±4.3	21	5.1	48	5.3	123□5R7(6)	Zhang et al. (2020a)
Gongjue	30.9	98.3	Sandstone	45.3-47.1	-(162)	60.8	181.5	2.9	29.7±2.7	34	3.3	49	3.3	123F5R7(7)	Li et al. (2020b)

Gongjue	30.9	98.3	Sandstone	41.5-45.3	-(196)	63.9	186	2.8	28.5±2.7	30	3.2	47	3.3	123F5R7(7)	Li et al. (2020b)
Wulanwula hu	34.5	90.2	Volcanic rocks	38.6±0.5	7(53)	82.1	298.4	7.8	25.2±8.0	-3.4	8.6	43	10.1	123F5□7(6)	Lippert et al. (2011)
Nangqian	32.2	96.6	Mudstone	35-41	-(267)	83.4	217.9	5.3	28.8±5.0	6.3	6	48	6.3	123□5R7(6)	Zhang et al. (2020a)

Notes: *Slat and Slon, latitude and longitude of the sampling site; Age (Ma), age of the rock units; N(n), number of sites (samples) used to calculate Fisherian mean; Plat. and Plon., latitude and longitude of the pole; A_{95}, radius of the 95% confidence circle; Paleolat, paleolatitude calculated in respect to the reference site at 32.5°N, 95.2°E; Dec, ΔDec, Inc and ΔInc, declination and Inclination with their error converted to the reference site at 32.5°N, 95.2°E; Criteria (Q) = data quality criteria (number of criteria met) modified from Van der Voo (1990): 1, well-determined rock age; 2, sufficient number of samples (N≥6 and n≥36); 3, stepwise demagnetization; 4, robust field tests, F means positive fold test; 5, structural control and tectonic coherence with the craton or terrane discussed; 6, presence of reversal, R means positive reversal test and D means dual-polarity ChRM direction; 7, no resemblance to paleopole of younger age (by more than a period); "□" in the criterion column fails to fulfill this criterion; Gray data are those failed to fulfill the criteria mentioned in the text.*

2.6.3 Mechanisms for the Remagnetization of the Jurassic Limestones

Thermoviscous resetting of existing magnetic minerals (Kent *et al*., 1985) and chemical remanent magnetization (CRM) through magnetic mineral growth associated with orogenic fluids (e.g., Jackson, 1990; Elmore *et al*., 2006, 2012; Huang et al., 2015a, 2017a, 2017b) currently are the most common mechanisms to explain remagnetization. The maximum burial temperature of the Buqu Formation was below 150°C (Sun *et al*., 2020; Wu *et al*., 2020). However, the unblocking temperatures of the Jurrasic limestones in the study area are around 400°C - 500°C, giving a burial temperature of 150°C - 350°C based on the relaxation time-blocking temperature relationship for magnetite of Pullaiah *et al*. (1975). A lower burial temperature of below ~200°C would be obtained based on Kent's (1985). The remagnetization therefore could not be attributed to mere heating during burial. In addition, no Cenozoic igneous bodies are found near the section, but just Early Cretaceous intrusive rocks. Thermoviscous resetting is deemed a less likely mechanism for the remagnetization: it is hard to envisage that the intrusive rocks would have thermally reset the Jurassic limestones, but not nearby Permo-Triassic volcanic rocks (Guan *et al*., 2021). In fact, the rocks perhaps have not been heated for a sufficient amount of time at a sufficiently elevated temperature to make the thermal resetting feasible.

SSD magnetite with cogenetic SP particles is the dominant magnetic carrier in the studied rocks. This authigenic magnetite may well be responsible for chemical remagnetization of many carbonate rocks (Suk *et al*., 1990a, 1990b; Morris & Robertson, 1993; Jackson & Swanson-Hysell, 2012; Huang et al., 2015a, 2017a, 2017b; Ran *et al*., 2017; Zhang *et al*., 2020b). Authigenic magnetite can be an oxidation product of iron sulfides (i.e., pyrite, pyrrhotite, or greigite) under the influence of orogenic fluids (Suk *et al*., 1990a; Reynolds 1990; Roberts *et al*. 2011; Huang et al., 2015a). To better understand this process, we recapitulate how organic matter diagenesis affects the formation of magnetic minerals that are typically preserved in carbonates.

Diagenesis involving degradation of organic matter after deposition is an essential process in the preservation of magnetic minerals in sedimentary environments. Microbes derive energy through uptake of oxygen and release of CO_2 from the organic matter. In general, consumption of the organic matter and accompanying respiration processes (in parentheses) are: oxic (aerobic respiration), nitrogenous (nitrate reduction), manganous (manganese reduction), ferruginous (iron reduction), sulphidic (sulphate reduction), and methanic (methanogenesis) (Froelich *et al*., 1979; Roberts *et al*., 2013; Roberts, 2015; Huang *et al*., 2019a). When one oxidant is used up, the next one will be used, until either all oxidants or all organic matter is consumed. This process is accompanied by the increase of dissolved Mn^{2+}, Fe^{2+}, and HS^-. The Buqu limestones were deposited in a littoral and shallow

sea carbonate environment (Li *et al.*, 2002; Tan *et al.*, 2004; QGSI, 2014; Yan *et al.*, 2016; Cao *et al.*, 2019). The appearance of massive bioclastic layers indicates that the climate was warm at that time, which was conducive to biological growth (QGSI, 2014). Under those circumstances, organic carbon fluxes were high, and anoxic sulphidic diagenetic environments were typically formed, in which paramagnetic pyrite would replace originally present detrital magnetite and hematite. If the Fe^{2+} supply rate is higher than the HS^- production, intermediate iron sulphides would be preserved (Kao *et al.*, 2004; Roberts *et al.*, 2013; Roberts, 2015). In brief, the deposited sediments tend to undergo anoxic diagenesis and iron sulphides appear to be mainly formed during burial and diagenesis. After the India-Eurasia collision, the Nangqian, Gongjue, and Mangkang basins have been uplifted to a fairly high elevation during Paleogene (Xu *et al.*, 2013; Su *et al.*, 2019; Xiong *et al.*, 2020). The diagenetic environment therefore turned from anoxic to suboxic and/or oxic, giving rise to oxidation of iron sulphide to authigenic magnetite and the acquisition of CRM (Brothers *et al.*, 1996). This was likely mediated by the migration of orogenic fluids, fully endorsed by the occurrence of widespread gypsum veins in the Buqu limestones (Gustavson, 1994; Phillip, 2008; Bons *et al.*, 2012; Gale *et al.*, 2014). Two peaks of hydrocarbon generation occurred during the Early Cretaceous and Paleogene, respectively (Wu *et al.*, 2020). Fluids associated with hydrocarbon generation could be another trigger of remagnetization (e.g., Elmore *et al.*, 2006, 2012), however, both phenomena probably worked in tandem (they operated at the same time). The nearby Permo-Triassic volcanic rocks as described in Guan *et al.* (2021) have a substantially lower porosity than the limestones, which avoids the circulation of orogenic fluids amid. In addition, the absence of organic matter in volcanic rocks does not drive reactions. Thus, the primary NRM has been retained in those rocks.

2.7 Conclusions

We report new paleomagnetic results from limestones of the Middle to Late Callovian Buqu Formation in the Zaduo area, located in the eastern part of the Qiangtang Terrane. The primary NRM was overprinted by a CRM after the India-Eurasia collision. Rather uncommon in remagnetized strata, the secondary NRM dating from the Eocene has a 'false positive' reversals test. Due to the high organic carbon fluxes since the deposition of the Jurassic limestones, the oxygen was used up and the deposited sediments tend to be anoxic, thus iron sulphides appear to be mainly formed during burial and diagenesis. When the limestones were uplifted after the India-Eurasia collision, the diagenetic environment turned from anoxic to suboxic and/or oxic, giving rise to the oxidation of the pre-existing iron sulphides to authigenic magnetite and the acquisition of CRM. Like in many remagnetized limestones, the authigenic magnetite grains range from the superparamagnetic up to stable single-domain size, leading to distinctive rock-magnetic properties. The remagnetization process is also manifested by the widespread occurrence of gypsum veins in the limestones. The secondary remanence reveals that the Zaduo area of the Eastern Qiangtang Terrane has experienced ~15.7° ± 3.2° (~1740 ± 350 km) of

latitudinal crustal shortening since the Eocene. Besides, the ~20° clockwise rotation of the Zaduo area relative to Eurasia coincides with the rotation pattern in the eastern part of the Qiangtang Terrane, indicating that the clockwise rotation accommodating the India-Eurasia collision was also prevailing in the Zaduo area.

2.8 Acknowledgments

This work was co-supported by the Second Tibetan Plateau Scientific Expedition Program (Grant 2019QZKK0707), the Strategic Priority Research Program of the Chinese Academy of Sciences (Grant XDA20070201), the Natural Science Foundation of China (Grants 41974080 and 41804065), the Basic Science Center for Tibetan Plateau Earth System (CTPES, Grant 41988101-01), and China Scholarship Council. The authors thank Weilin Zhang, Jinbo Zan, Tao Zhang, Yi Chen, Zengguang Guo, Mengqi Tan, Liye Yang, Yaofei Chen, and Zhongyu Xiong for their assistance in the laboratory work. We sincerely thank Editor Eduard Petrovsky, Assistant Editor Fern Storey, Professor Richard Elmore and another anonymous reviewer for their insightful comments and suggestions that greatly improved this paper.

3

DYNAMIC DEFORMATION OF THE SE TIBETAN PLATEAU: INSIGHTS FROM THE CENOZOIC OROCLINAL BENDING IN THE EASTERN QIANGTANG TERRANE

Abstract

The crustal thickening, uplift, and outward expansion of the Tibetan Plateau have been the topic of many studies. The eastern Tibetan Plateau is regarded as a 'window' from which crustal fragments can 'escape'. Two mainstream but competing models are continuous crustal deformation and lateral extrusion of rigid blocks. To date, the plan-view curvature in orogens around the Eastern Himalayan Syntaxis was rarely studied quantitatively. Here, we quantified the arcuate shapes at the eastern ending of the Qiangtang Terrane paleomagnetically, revealing that secondary oroclines formed after the Late Eocene. In addition, multi-scale wavelet analysis and spectral analysis were employed to unravel the gravity anomalies in this area, providing information on density variations from the shallow to the deep crust. The orocline expression at the Earth's surface and the gravity anomaly orientations deeper in the lithosphere appear to be consistent, implying a coupled lithosphere-scale oroclinal deformation. We therefore picture a more dynamic scenario of the growth and deformation with time in the eastern Tibetan Plateau: the orocline of the eastern ending of the Qiangtang Terrane formed after the Late Eocene, this process likely created a channel for later crustal flow. After the Miocene, large-scale crustal flow occurred and caused the uplift and outward expansion of the plateau.

3.1 Introduction

The Cenozoic India-Eurasia collision was one of planet Earth's most major happenings in Earth's history (Yin & Harrison, 2000; Tapponnier et al., 2001; Ding et al., 2017). It induced various geodynamic processes including crustal thickening, uplift, and outward expansion of the Tibetan Plateau (e.g., Molnar & Tapponnier, 1975; Tapponnier et al., 1982, 2001; Royden et al., 1997; Clark & Royden, 2000; Clark et al., 2004; Schoenbohm et al., 2006; Bai et al., 2010; Wang et al., 2012; Li et al., 2015; Huang et al., 2015c; Zhang et al., 2022b; Yuan et al., 2022). Two main classes of models were proposed to describe the deformation and evolution in the eastern Tibetan Plateau: one class emphasizes the lateral extrusion of rigid blocks along major strike-slip faults and stepwise plateau growth (e.g., Molnar & Tapponnier, 1975; Tapponnier et al., 1982, 2001; Peltzer & Tapponnier, 1988), while the other class underlines the crustal continuous deformation (Royden et al., 1997; Clark & Royden, 2000; Schoenbohm et al., 2006; Bai et al., 2010). For both scenarios, however, the southeastern Tibetan Plateau holds the key in allowing the crustal units to escape from the Tibetan Plateau (Bai et al., 2010; Zhang et al., 2017; Feng et al., 2022).

Many previous studies have revealed various tectonic features and processes. Geodetic observations provided constraints on the present-day clockwise rotation of the eastern Tibetan Plateau (Shen et al., 2005; Wang & Shen, 2020; Wang et al., 2021). Evidence from paleomagnetism revealed the clockwise rotation and lateral extrusion since the Cenozoic (Yang et al., 2001b; Kondo et al., 2012; Tong et al., 2017, 2022). Geophysical investigations reported on various features of the region including low-velocity and high-conductivity zones with high Poisson's ratios (Wang et al., 2007; Bai et al., 2010; Liu et al., 2014b; Bao et al., 2015). According to these authors it implies the presence of partial melt and reduced viscosity in the mid-lower crust, attributed to mobile mid-lower crustal flow. However, some other studies cast doubt on such a model: 3-D thermo-mechanical modeling suggests coupled deformation of the lower crust and underlying lithospheric mantle, without crustal flow (Chen & Gerya, 2016). Geochemical and isotopic studies into Cenozoic igneous rocks from the eastern margin of the Tibetan Plateau indicate that the mid-lower crust was locally derived rather than stemming from the Eastern Qiangtang Terrane (Hu et al., 2022). Rather surprisingly, the plan-view curvature in the orogens around the Eastern Himalayan Syntaxis (EHS) is rarely studied to date. Worldwide, such remarkable curved topographic geometries were also observed on the American continents and elsewhere in Eurasia (e.g., Weil & Sussman, 2004; Weil et al., 2010; Pastor-Galán et al., 2011, 2015, 2017; Kondo et al., 2012; Shaw et al., 2012a, 2012b; Johnston et al., 2013; Meijers et al., 2010, 2017). The mechanisms proposed to interpret these bendings involved either upper crustal units close to the Earth's surface or units distributed across (almost) the whole lithosphere (Marshak, 2004; Gutiérrez-Alonso et al., 2004; Pastor-Galán et al., 2017). Therefore, constraints on the depth of the kinematic bending process are expected to shed light on the lithospheric scale of the deformation and evolution of the eastern Tibetan Plateau.

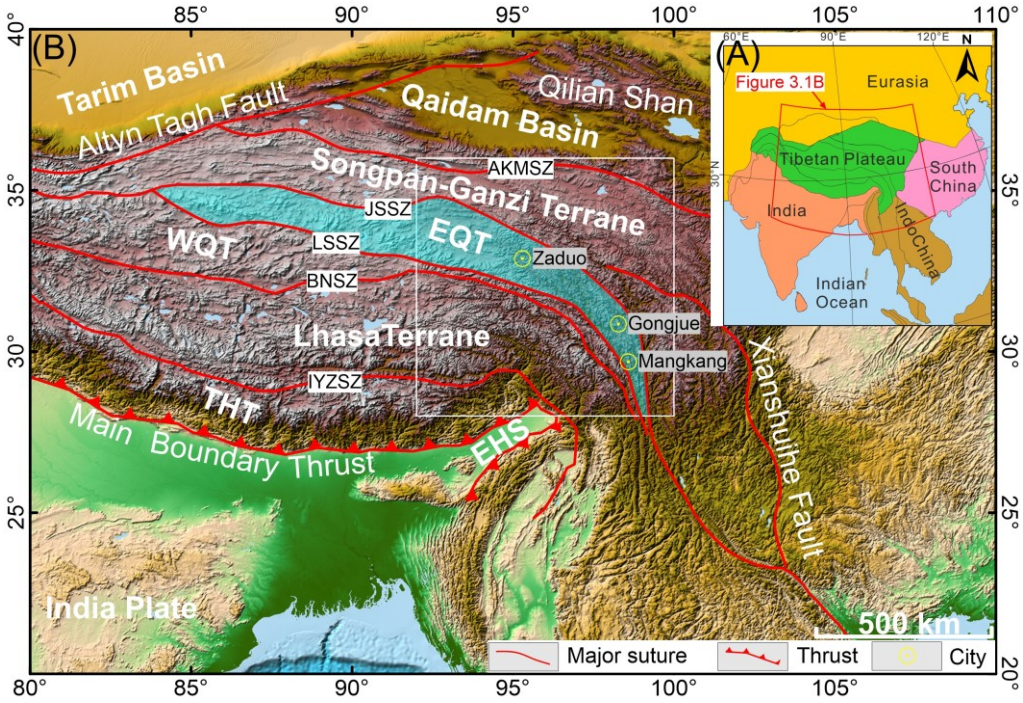

Figure 3.1. *(A) and (B) Simplified tectonic map of the Tibetan Plateau and its adjacent regions. (A) modified after Van Hinsbergen et al. (2012). (B) The white rectangle includes the curved topographic geometries of EQT, and shows our gravity study area. The abbreviations of the tectonic units are EQT: Eastern Qiangtang Terrane; WQT: Western Qiangtang Terrane; THT: Tethyan Himalaya Terrane; AKMSZ: Ayimaqing-Kunlun-Muztagh Suture Zone; JSSZ: Jinshajiang Suture Zone; LSSZ: Longmu Tso-Shuanghu Suture Zone; BNSZ: Bangong-Nujiang Suture Zone; IYZSZ: Indus-Yarlung Zangbo Suture Zone; EHS: Eastern Himalayan Syntaxis.*

In addition to the geodynamic reconstructions based on exposed rocks at the Earth's surface, a link with the deep structures may offer further clues to the geodynamic evolution of the eastern Tibetan Plateau. A gravity survey is one of the few approaches that can trace density variations of rock units deeper within the lithosphere. Thus, in this study, we selected the eastern ending of the Qiangtang Terrane, where there is a significant curvature around the EHS (Fig. 3.1), to investigate its kinematic evolution at both shallow and deep scales. Orocline tests (Schwartz & Van der Voo, 1983; Eldredge et al. 1985; Weil & Sussman, 2004; Pastor-Galán et al., 2017) were applied to quantify the kinematic evolution of this region. Furthermore, multi-scale wavelet analysis and spectral analysis were employed to evaluate the gravity anomalies. The combination of these results enables us to present an integrated interpretation of the deformation and evolution in the eastern Tibetan Plateau.

3.2 Geological setting

From north to south, three major suture zones, including the Jinshajiang Suture Zone (JSSZ), the Bangong-Nujiang Suture Zone (BNSZ), and the Indus-Yarlung Zangbo Suture Zone (IYZSZ) separate four main components of the Tibetan Plateau, that include the Songpan-Ganzi, Qiangtang, Lhasa, and Tethyan Himalaya Terranes (Fig. 3.1). The Qiangtang Terrane is subdivided into the Eastern and Western Qiangtang Terrane (EQT and WQT, respectively) (also known as the Northern and Southern Qiangtang Terrane) by the Longmo Co-Shuanghu Suture Zone (LSSZ) (Fig. 3.1; Yin & Harrison, 2000; Pan et al., 2004c; Li et al., 2009a; Metcalfe, 2013). The Qiangtang Terrane began to collide with the Songpan-Ganzi Terrane during the Late Triassic (Guan et al., 2021; Yu et al., 2022a). Later, the Lhasa Terrane amalgamated with the Qiangtang Terrane between the Late Jurrasic and the Early Cretaceous (Kapp et al., 2007; Zhu et al., 2013; Yan et al., 2016; Chen et al., 2020). Finally, the northward indentation and subsequent subduction of the Indian Plate underneath Eurasia led to the uplift and growth of the Tibetan Plateau (Yin & Harrison, 2000; Tapponnier et al., 2001; Ding et al., 2017).

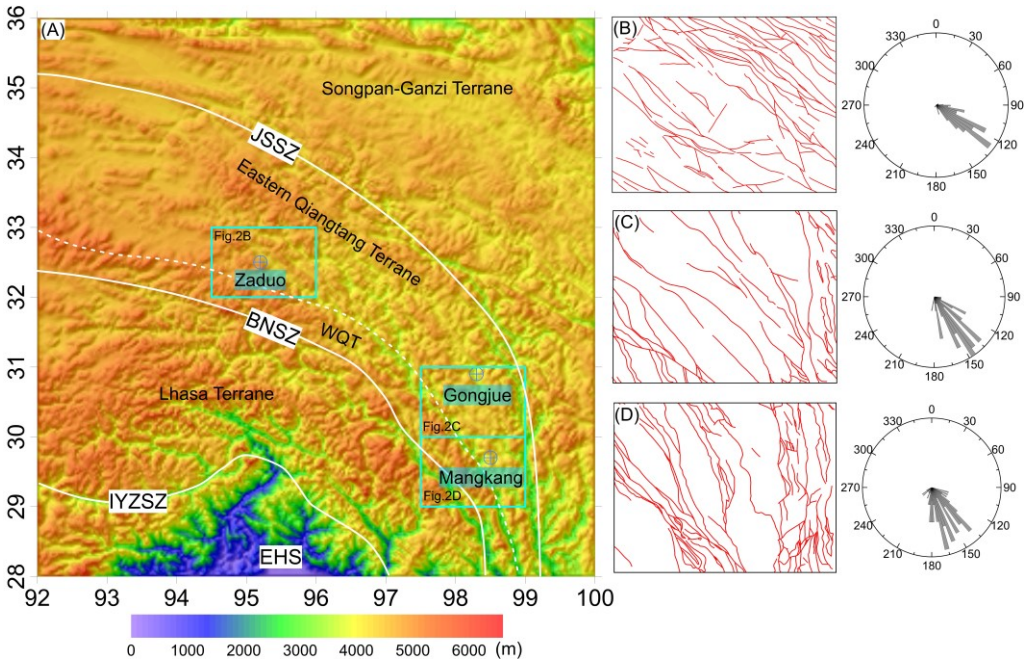

Figure 3.2. *(A) Digital Elevation Model (DEM) showing the topographic relief in this area delineated by the white rectangle in figure 3.1B (available for use from Bureau Gravimétrique International). (B)-(D) major faults and their strikes in the Zaduo, Gongjue and Mangkang areas, respectively. Refer to figure 3.1 for abbreviations.*

The southeastern Tibetan Plateau is characterized by an outward gradually decreasing elevation, widely distributed faults at various scales, and a plan-view

curvature of mountain belts around the EHS (Fig. 3.1 & 3.2A; Clark & Royden, 2000; Schoenbohm et al., 2006; Zhang et al., 2016a, 2017). The geometry of the Qiangtang Terrane changes in its eastern segment, showing a transformation from being west-east-oriented in the west to quasi-north-south-oriented in the east. The Zaduo, Gongjue and Mangkang areas, of prime interest in this study, are distributed from the northwest to the southeast along this bending (Fig. 3.2A). The regional faults in the three areas also display an approximate northwest-southeast trend albeit with variable values (Fig. 3.2B-D), which is in line with the general geometry of the Qiangtang Terrane in the east.

3.3 Data and applied techniques

The paleomagnetic data collection of this study comes from several publications on the Eastern Qiangtang Terrane (Huang et al., 1992; Tong et al., 2015; Li et al., 2020b; Xiao et al., 2021; Fu et al., 2022a). Our previous study from the Zaduo area demonstrates that the Middle-Late Jurassic limestones obtained a secondary remanence during the Eocene, revealing a clockwise rotation after that period (Fu et al., 2022a). To the southeast, the magnetostratigraphic investigations in the Gongjue area indicate more complex rotation patterns between ~69 Ma and ~41.5 Ma (Li et al., 2020b) or between ~69 Ma and ~50 Ma (Xiao et al., 2021). Further to the southeast, studies on Cretaceous rocks also reveal that the Mangkang area underwent a clockwise rotation after the Late Cretaceous (Huang et al., 1992; Tong et al., 2015). Site-mean directions were evaluated with Fisher statistics (Fisher, 1953). To judge kinematic models of oroclinal formation, the so-called orocline test (Schwartz & Van der Voo, 1983; Eldredge et al. 1985; Weil & Sussman, 2004; Yonkee & Weil, 2010; Pastor-Galán et al., 2017) is applied. This test can provide a constraint on the connection between variations in the regional structural trend and a given geologic fabric element denoting vertical-axis rotations.

Both the ordinary least squares (OLS) and total least squares (TLS) regressions were used as an orocline test to evaluate the relationship between deviations of declination (D-Do) and (S-So) (the tests are available on www.paleomagnetism.org; Koymans et al., 2016, 2020). Do is the reference declination, which stands for the average declination of the dataset in this study. Similarly, So is the reference regional geological strike (e.g., fault, bedding), representing the average strike in the area where the dataset was collected. The strikes were assigned a fixed 5° uncertainty. Bootstrapping was used to derive estimates of standard deviations (σ) and confidence intervals (Pastor-Galán et al., 2017). In general, two categories are recognized for such curved belts, that is, a primary arcuate shape of a mountain belt and a secondary orocline (Weil & Sussman, 2004; Weil et al., 2010; Pastor-Galán et al., 2011, 2017; Kondo et al., 2012; Johnston et al., 2013; Meijers et al., 2017). An intermediate status also exists, which is known as a progressive orocline (Weil & Sussman, 2004; Pastor-Galán et al., 2012; Meijers et al., 2017). A primary bend is formed during an initial deformation event and did not undergo a subsequent

vertical axis rotation. Alternatively, in the scenario of a secondary orocline, large-scale vertical-axis rotation occurs during a subsequent deformation phase (Weil & Sussman, 2004; Kondo et al., 2012; Meijers et al., 2017).

Gravity data used in this study (Free-air and Bouguer gravity anomalies) were collected from the Bureau Gravimétrique International (BGI) (Balmino et al., 2012; Bonvalot et al., 2012). These data were derived from the Earth Geopotential Model EGM2008/Technical University of Denmark DTU10 gravity field (Pavlis et al., 2008; Andersen, 2010) and were computed at the Earth's surface with a 1′ × 1′ resolution. The reference density of the Earth's crust is 2670 kg/m^3, and other density values used for calculations are 3270 kg/m^3 for mantle rock, 1000 kg/m^3 for fresh water, 1027 kg/m^3 for ocean water, and 917 kg/m^3 for ice (Balmino et al., 2012; Bonvalot et al., 2012).

To decompose the gravity anomalies and reveal three-dimensional density structures which may be interpreted as being related to tectonic patterns, the multi-scale wavelet analysis and spectral analysis of potential fields were employed by the software MAGS4.0 (developed by the School of Geophysics and Geomatics, China University of Geosciences) in this study as detailed next. In general, gravity anomalies produced by shallow and small-scale field sources are distinct from those by deep and large-scale sources: the former decrease faster than the latter with distance (Blakely, 1996; Yang et al., 2015). Multi-scale wavelet analysis can be used to analyze potential fields and to locate their causative sources (Moreau et al., 1997, 1999). It is considered a foremost approach to separate potential data into a wavelet approximation of the low-frequency component representing deep-seated and large structures, and the sum of the wavelet details of the high-frequency component which represents more shallow and local structures (Mallat, 1989; Moreau et al., 1997, 1999; Fedi & Quarta, 1998; Gao et al., 2000; Yang et al., 2015; Xu et al., 2017, 2018), as shown in the following equation:

$$\Delta g = A_j + \sum_{j=1}^{J} D_j \quad (j = 1, 2, \cdots, J) \tag{3.1}$$

where Δg denotes the gravity anomalies, A_j denotes the wavelet approximation generally representing regional anomalies produced by deep and large-scale geological mass, D_j denotes the wavelet detail mainly revealing local anomalies caused by shallow and small-scale field sources. The average depth of the decomposed gravity anomalies can be estimated by power spectrum analysis (Spector and Grant, 1970; Yang et al., 2015; Xu et al., 2017, 2018; Pinto & Vidotti, 2019; Wu & Gao, 2019; Özkaptan, 2019; Mazur et al., 2020). In addition, the directional derivative of the gravity anomalies may also be used to enhance the orientation of the topographic relief and the gravity anomalies.

3.4 Results

3.4.1 Paleomagnetic results

Paleomagnetic data from three localities along the eastern ending of the Qiangtang Terrane were used to evaluate the formation of arcuate belts, including the Zaduo, Gongjue, and Mangkang areas (Fig. 3.3). In the Zaduo area, we recognized a secondary magnetization with a tilt-corrected mean declination/inclination = 30.6°/35.6° and pole position of 59.8° N, 202.7° E (Fig. 3.3). This magnetization was determined to have been acquired during the Eocene (Fu et al., 2022a). In the Gongjue area, two investigations of high-resolution magnetostratigraphy constrained sedimentation in the central Gongjue basin to early Cenozoic (Li et al., 2020b; Xiao et al., 2021). In Li et al. (2020b), a total of 1096 successful specimens collected from a ~3.5 km thick sedimentary sequence were assigned to 66 thickness intervals; each interval is 50 m thick and consists of an average of ~16 specimens. Their data reveal a 69-41.5 Ma age range for the sedimentary succession. Two sections (a total thickness of ~2.3 km) published by Xiao et al. (2021) constrained sedimentation in the Gongjue area between 69 and 50 Ma; for our analysis we divided these 728 specimens into 56 sites based on their polarity and the strata thickness intervals, each interval is ~40 m thick and contains an average of ~13 specimens. Thus, a total of 122 sites compiled from Li et al. (2020b) and Xiao et al. (2021) in the Gongjue area yield an early Cenozoic paleopole of 48.7° N, 200.4° E (Fig. 3.3; see Supplementary Table S3.1 for more information). In the Mangkang area where the regional orientation trend is nearly NNW-SSE, three Cretaceous results were published (Otofuji et al., 1990; Huang et al., 1992; Tong et al., 2015). Data from Otofuji et al. (1990) was not considered here because of an insufficient number of specimens. Thus, a total of 28 sites from the upper Cretaceous strata yield a paleopole of 50.7° N, 168.3° E (Huang et al., 1992; Tong et al., 2015; Fig. 3.3), while 12 sites from the lower Cretaceous strata gave a paleopole of 56.1° N, 174.0° E (Fig. 3.3; Huang et al., 1992).

To quantify the kinematic evolution of orocline formation, orocline tests are applied. As shown in Fig. 3.4, deviations of the paleomagnetic declinations (D-Do) are plotted against deviations of the bedding strike (S-So) at the site level. We performed a two-step strike test for the dataset based on the localities and their ages. The first step includes the rocks that acquired the NRM presumably during the Cenozoic; these rocks are all from the Zaduo and Gongjue areas (Li et al., 2020b; Xiao et al., 2021; Fu et al., 2022a). The dataset from the Mangkang area was covered in the second step, which involves rocks that acquired their NRM during the Cretaceous (Huang et al., 1992; Tong et al., 2015). As shown in Fig. 3.4, sites of the Zaduo mainly distribute in the third quadrant, but sites of the Gongjue present a more scattered distribution, which falls within four quadrants. For the orocline test at the site level, inconsistencies exist between the OLS and TLS version (Fig. 3.4A). In the scenario with the Mangkang area involved, however, the orocline tests exhibit more similarity between the OLS and TLS version (Fig. 3.4B). The enlarged dataset makes the test more reliable and geologically meaningful.

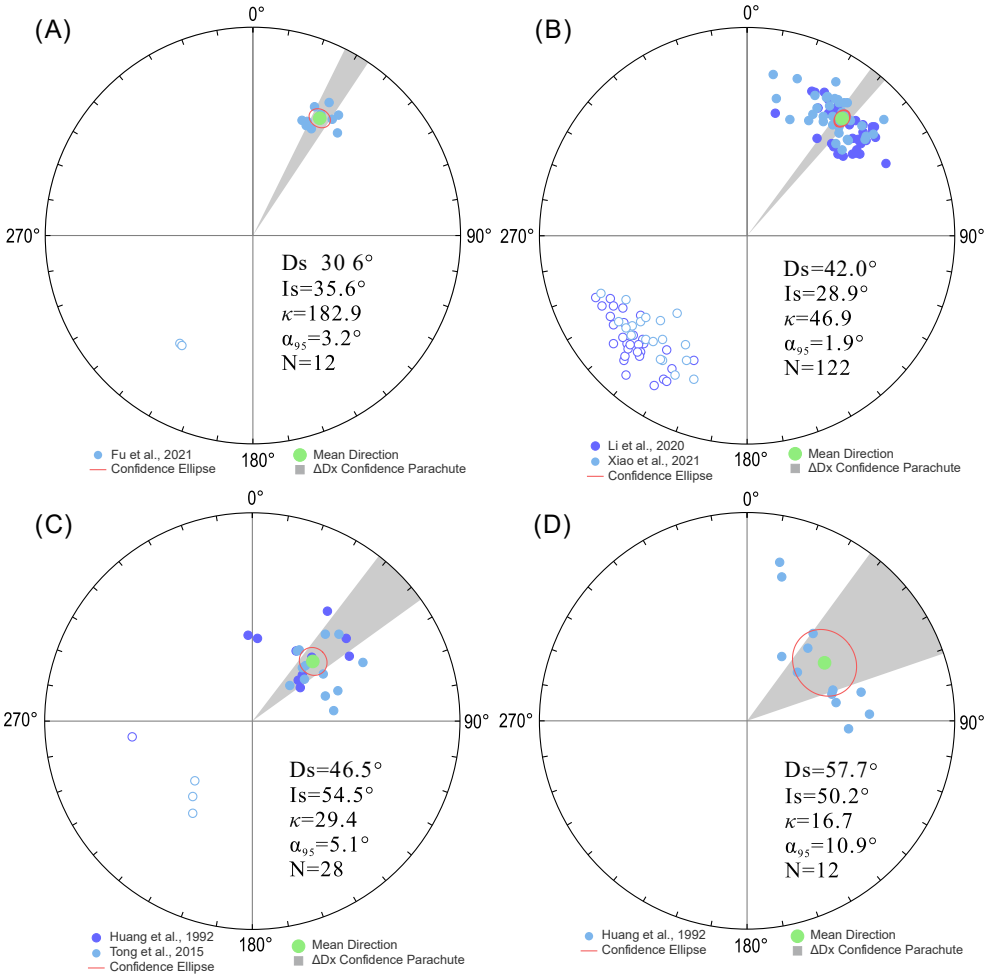

Figure 3.3. *Equal-area projections of the site mean directions for (A) the Zaduo area in the Eocene (Fu et al., 2022a), (B) the Gongjue area during the Paleocene and Eocene (Li et al., 2020b; Xiao et al., 2021), the Mangkang area in the Late Cretaceous (C) (Huang et al., 1992; Tong et al., 2015) and Early Cretaceous (D) (Huang et al., 1992). Solid and open symbols are projections on the lower and upper hemispheres in stratigraphic coordinates. The mean direction is shown by a green symbol with a_{95} per cent red confidence circle and grey shadow.*

Table 3.1. *Regression information of the different orocline tests*

Type	TLS	BCI	OLS
Slope	1.000	0.522-1.830	0.923
Intercept	-3.349	-7.903	-3.148

Note: *TLS: total least squares; BCI: bootstrapped confidence intervals; OLS: ordinary least squares.*

In addition to the (D-Do) versus (S-So) plot at the site level, the amount of tectonic rotation was also plotted against the deviation of the average bedding strike at the locality-mean level, which is more geologically meaningful than the test at the site level. The dataset of the Late Cretaceous and the Cenozoic exhibits a linear distribution (Fig. 3.4B). We note, however, that the Early Cretaceous results in the Mangkang area presented a clear deviation (Fig. 3.4C), which was therefore excluded from further analysis. Both the OLS and TLS were employed for the orocline test, and they provided similar results. The OLS yields a relation of the two parameters, that is, (D-Do) = 0.923 × (S-So) – 3.148 (Fig. 3.4C and Table 3.1). A slope of 0.923 together with a correlation coefficient (r) larger than 0.92 (r^2 = 0.853; r = 0.9235) indicates a reliable result (Fig. 3.4C and Table 3.1). The TLS regression is suggested to have better performance even in cases of dissimilar variances in (D-Do) and (S-So). It avoids the situation where certain unidentified outliers produce largely deviating parameter estimates (Pastor-Galán et al., 2017). TLS regression yields (D-Do) = 1.000 × (S-So) – 3.349 (r^2 = 0.853) (Fig. 3.4C and Table 3.1). Thus, both approaches point to a meaningful orocline test. The slope of m = 1 means a 100% positive orocline test while m = 0 represents a negative orocline test (Koç et al., 2016; Pastor-Galán et al., 2017). The orocline test in this study suggests that the eastern ending of the Qiangtang Terrane falls within the field of secondary oroclines. Thus, despite the limitation in the number of datasets: per time interval, as well as with regard to geographical coverage, a remarkable linear correlation emerged from the orocline test (Fig. 3.4C).

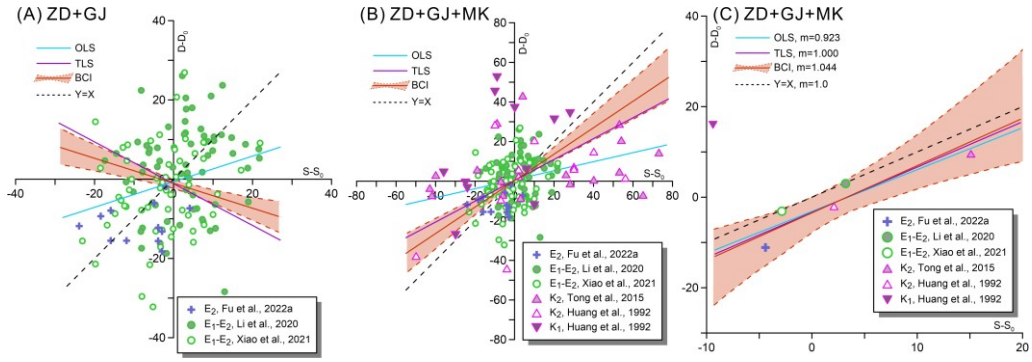

Figure 3.4. *Paleomagnetic orocline tests for data from the EQT orocline for sampling sites from (A) the Zaduo and Gongjue areas (including the Paleocene and Eocene sites); (B) the Zaduo, Gongjue and Mangkang areas (including the Late Cretaceous, Paleocene and Eocene sites); (C) sampling localities (including the Late Cretaceous, Paleocene and Eocene sites). OLS: ordinary least squares; TLS: total least squares; BCI: bootstrapped confidence intervals.*

3.4.2 Gravity anomalies and their decomposition

Free-air and Bouguer gravity anomalies are based on the theoretical model that

considers the effects of Earth's rotation, latitudinal change, and the topography of the Earth and the related effect of the atmosphere (Blakely, 1996; Hinze et al., 2013; Pasteka et al., 2017). The free-air anomalies contain the gravitational effect of uncompensated topographic masses, which can therefore reflect features of the topographic relief (Hinze et al., 2013; Özkaptan, 2019). As the most widely used gravity anomalies, the Bouguer gravity anomalies are generally free of local topography effects unless these features correlate with structural or stratigraphic variations resulting in density variations below the datum level (Blakely, 1996; Hinze et al., 2013; Xiao & Wang, 2017; Pasteka et al., 2017).

The free-air gravity anomaly map of the study area is given in Fig. 3.6A, showing that the gravity anomaly values range approximately between -200 and +200 mGal. The zero-gravity and mild anomalies ranging from roughly -50 mGal to +50 mGal mainly occur in the northern part of the study region. However, the southern part of the study region is characterized by significant gravity highs and lows, which reflects the dramatic topographic relief (Fig. 3.6). In addition, the EHS and the suture zones show clear gravity lows in the free-air gravity anomaly map.

The Bouguer gravity data from the study area are all negative ranging from approximately -520 mGal to -40 mGal and they display several remarkable high and low gravity anomalies (Fig. 3.6B). Specifically, a distinct relative high gravity anomaly occurs to the south of the IYZSZ and around the EHS, with gravity values ranging approximately between -250 mGal and -40 mGal. In contrast, a widely distributed gravity anomaly low mainly lies in the western segments of the Qiangtang and Lhasa terranes of the study area, where the gravity values are frequently below ~ -400 mGal. Intermediate gravity values are mainly occurring in the east, ranging from ~ -400 mGal to -300 mGal. Overall, a negative correlation exists between the gravity anomalies and the topographic elevation, that is, the gravity highs correspond to the topographic elevation lows (i.e., the EHS), whereas the gravity lows correspond to the topographic elevation highs (i.e., the Zaduo area and more western regions).

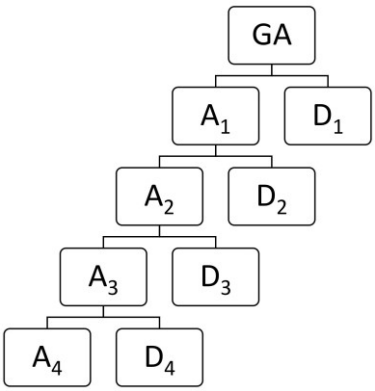

Figure 3.5. *Schematic diagram showing the gravitational decomposition of multi-scale wavelet analysis, an order of four was selected here. GA: gravity anomalies.*

The Bouguer gravity anomalies comprise the integrated effects of heterogeneous materials sourced from different scales and depths within Earth's interior (Blakely, 1996; Hinze et al., 2013; Yang et al., 2015; Xu et al., 2017, 2018). It is therefore pertinent to unmix the anomalies and determine their geological meaning. The order of the anomaly decomposition can be determined when the obtained wavelet approximation is smooth or when the wavelet details show regional features (Yang et al., 2001a; Wu & Gao, 2019). After comparing the decomposed results, the 5th-order wavelet detail diagram shows large-scale anomalies while the 6th-order wavelet detail diagram shows similarity with the 4th-order wavelet approximation of the Bouguer gravity anomalies (Fig. S3.1). The 5th-order wavelet data are discussible but the 6th is over-decomposed. Thus, an order of four is selected in this study and thus the expression of the gravitational decomposition is shown in Fig. 3.5 and Eq. 3.2:

$$\Delta g = A_4 + D_1 + D_2 + D_3 + D_4 \qquad (3.2)$$

where A_4 represents the 4th-order wavelet approximation of the Bouguer gravity anomalies (Fig. 3.6C), and D_1 to D_4 represent the wavelet details of the Bouguer gravity anomalies from the 1st- to the 4th-order (Fig. 3.6D-H).

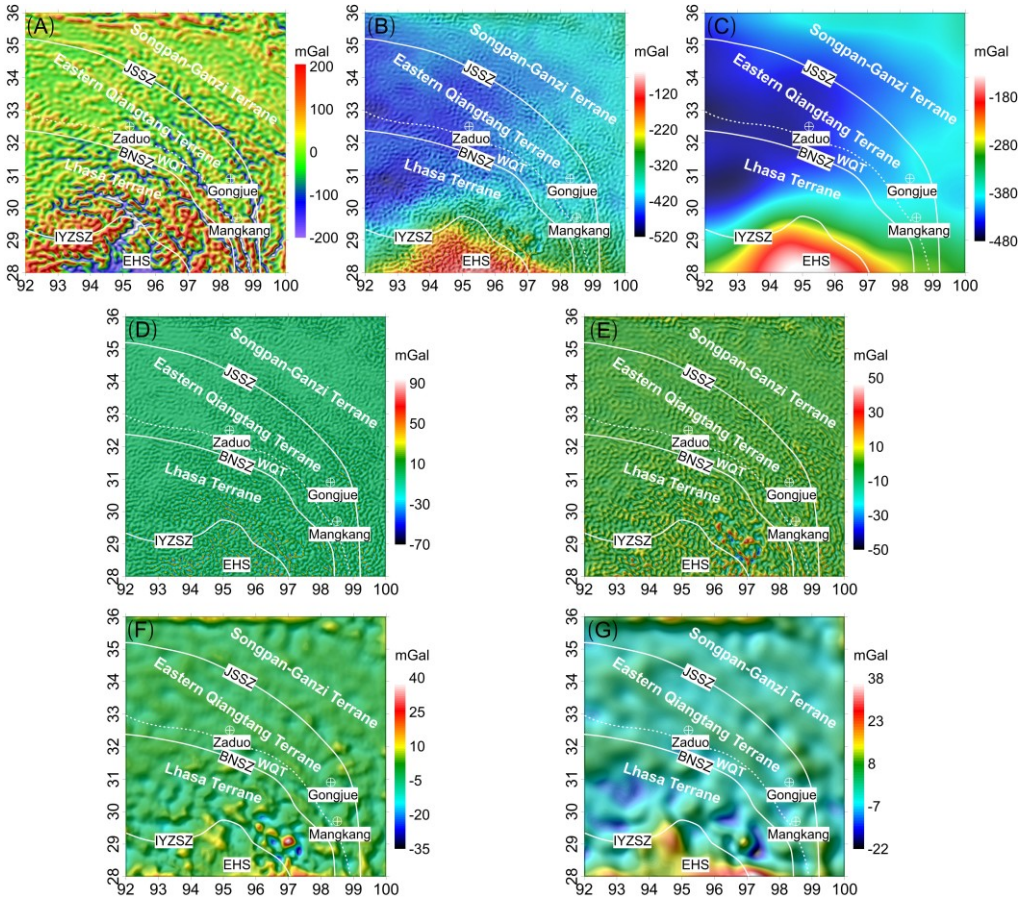

Figure 3.6 (previous page). *Gravity anomalies and their decomposition in the study area marked with a white rectangle in figure 3.1. (A) Free-air gravity anomalies; (B) Bouguer gravity anomalies; (C) the 4th-order wavelet approximation of the Bouguer gravity anomalies; (D)-(G) the 1st- to 4th-order wavelet detail of the Bouguer gravity anomalies. Refer to figure 3.1 for abbreviations.*

The 4th-order wavelet approximation shows features similar to the Bouguer gravity anomalies but is smoother (compare Fig. 3.6B and Fig. 3.6C). The values of the wavelet approximation are only slightly lower than those of the Bouguer gravity anomalies, implying that large- and regional-scale field sources dominate the Bouguer gravity anomalies. The 1st-order wavelet detail diagram is characterized by many bean-shaped small-scale anomalies. A small number of high anomaly values occur along suture zones and EHS (Fig. 3.6D). According to the power spectrum analysis, one or more depths can be obtained. For low-order wavelet details, a depth estimated from a high-frequency signal is meaningful; for high-order wavelet details, it is the other way around. The buried depth of the field source of the 1st-order wavelet detail is approximately 5.0 km (Fig. 3.7A), which mainly represents the density distribution near the surface (Yang et al., 2015; Xu et al., 2017, 2018). The 2nd-order wavelet detail shows similar bean-shaped anomalies but with a larger size, and more gravity highs emerge in the southern part of the region (Fig. 3.6E). It has an estimated field source depth of 13.2 km (Fig. 3.7B), likely reflecting the upper crust density. In the 3rd-order wavelet details, some large-scale gravity anomalies occur in the diagram, and linear distributions of gravity anomalies emerge

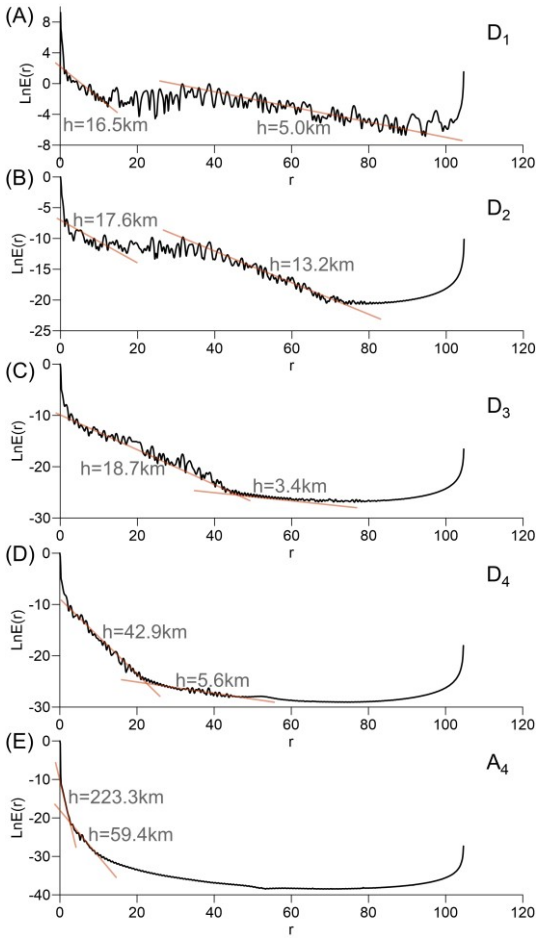

Figure 3.7. *Power spectrum depth estimation of the Bouguer gravity anomalies. (A)-(D) 1st- to the 4th-order wavelet details, and (E) the 4th-order wavelet approximation.*

along the JSSZ, the BNSZ, and the central Qiangtang Terrane (Fig. 3.6F). The power spectrum analysis of the 3rd-order wavelet details yields an approximate depth of 18.7 km (Fig. 3.7C), presenting an image of the deeper crust. Large-scale anomalies are presented in the 4th-order wavelet detail (Fig. 3.6G), indicating deep gravity sources. Anomaly highs and lows primarily lie in the EHS and Lhasa Terrane (Fig. 3.6G). Similarly, the power spectrum analysis was applied and provided an estimated depth of 42.9 km (Fig. 3.7D), indicating the density distribution in the lower crust. An approximate depth (~70 km) of the 5th-order wavelet detail was also estimated for completeness (Fig. S3.2). This depth is roughly consistent with the Moho discontinuity of the Qiangtang Terrane (Gao et al., 2009; Wang et al., 2014).

3.5 Discussion

3.5.1 Oroclinal bending of the eastern ending of the Qiangtang Terrane

The eastern ending of the Qiangtang Terrane presents a remarkable curvature of orogens and/or thrust belts in plan-view (Fig. 3.1 & 3.2A). Paleomagnetic declinations convincingly demonstrate that regional clockwise rotations occurred in the eastern segment of the Qiangtang Terrane (Huang et al., 1992; Tong et al., 2015; Zhang et al., 2020a; Li et al., 2020b; Xiao et al., 2021; Fu et al., 2022a). The secondary nature of the orocline here reveals that such curvature did not exist prior to those vertical-axis rotations.

In addition to the orocline test based on the bedding strike and the paleomagnetic declination, two other markers for highlighting variations in the regional structural trend were used to provide additional constraints, that is, fault strike and the directional derivative of the digital elevation model (DEM). For the Zaduo area, a total of 166 faults were considered: an average strike of 122.4° and a median strike of 124.0° were obtained. For the Gongjue area, the two corresponding values are respectively 143.7° and 144.6° (calculated from 79 faults), while for the Mangkang area, 135 faults produced an average/median strike of 159.4°/157.9°. The spatial change in fault orientation in the three localities broadly concurs with the variation in the amount of rotation (Fig. 3.8B), which further supports the secondary nature of the orocline. The directional derivative of the topography represents the gradient in a certain direction, which can be used to highlight the topographic relief. Note that the overall regional structural trend of the eastern ending of the Qiangtang Terrane is oriented SE-NW, so we consider a NE DEM gradient analysis that is normal to the regional structural trend (Fig. 3.8A). Thus, regional strikes of the three localities were estimated from a straight line parallel to their major derivative trend. We measured the orientations of the black arrows in Fig. 3.8A, they are 132°, 138° and 146°, respectively. The average value of the three localities is 138.7° (i.e., reference regional strike estimated from a NE DEM gradient), and the differences between the measured orientations and their reference regional strike are -6.7°, -0.7° and 7.3°, respectively. As shown in Fig. 3.8B, the variations of the DEM derivative also

correspond with the other parameters.

The orocline tests and correlation of related structural and topographic trends suggest that most of the curvature of the eastern ending of the Qiangtang Terrane was acquired after the deposition of the sediments in Gongjue area or the remagnetization of the limestones in the Zaduo area, i.e. roughly the Eocene (Li et al., 2020b; Xiao et al., 2021; Fu et al., 2022a). Because the orocline tests involved not only the Cenozoic data in the Zaduo and Gongjue areas but also the Late Cretaceous data from the Mangkang area, it indicates that the orocline formation in the Mangkang area also occurred after the Late Eocene.

Table 3.2. *Geological orientations and paleomagnetic declinations.*

Locality	DEM_Der (°)	FS (°)	BS (°)	Ds (°)
ZD	132	124	171.4	30.6
GJ	138	145	179.7	42.1
MK	146	158	167.1	46.5
Mean	138.7	142.3	172.7	39.7

Note: *ZD: Zaduo; GJ: Gongjue; MK: Mangkang; DEM_Der: NE derivative of the DEM; FS: fault strike; BS: bedding strike; Ds: declination.*

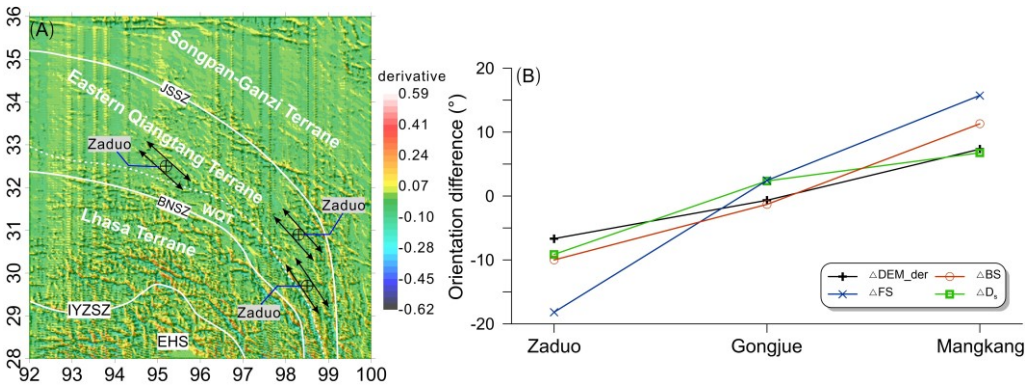

Figure 3.8. *Plots showing Earth's surface geological trend deviations in the Zaduo, Gongjue and Mangkang areas. (A) NE derivative of the DEM and the estimated regional strike, the black arrows define the estimated orientations of the Zaduo, Gongjue and Mangkang areas; (B) Deviation of each regional geological orientation element is calculated from their respective reference direction, data are from Table 3.2. DEM_Der: NE derivative of the DEM; FS: fault strike; BS: bedding strike; Ds: declination.*

3.5.2 Orocline: from shallow to deep

Most of the peculiar curved topographic geometries of active and ancient mountain

belts worldwide are apparent at Earth's surface (e.g., the Alaskan and Bolivian oroclines in the North and South American continents, respectively (Weil & Sussman, 2004; Kondo et al., 2012), Eastern Pontides and Lesser Caucasus oroclines (Meijers et al., 2010, 2017), Carpathian–Balkan oroclines (Shaw et al., 2012a), Iberian Variscan oroclines (Shaw et al., 2012b; Pastor-Galán et al., 2020), oroclinal bending in the central Taurides (Koç et al., 2016), etc.). Here, the bending of the eastern ending of the Qiangtang Terrane is shown to be a secondary orocline. However, tracing deeper structures and their possible relation to oroclinal bending can provide additional clues to understanding a range of deformation processes, including crustal thickening, and large-scale motion and deformation of deep units (Bai et al., 2010; Özkaptan, 2019; Mazur et al., 2020). Gravity anomaly evaluation is a useful method to obtain information about the structures of the upper and lower crust and upper mantle (Blakely, 1996; Hinze et al., 2013; Yang et al., 2015).

Although free-air gravity anomalies are unsuitable for most terrestrial geological problems because of their strong link with terrain elevation (Hinze et al., 2013), they can serve as another parameter in addition to the geological structure arguments above. To bolster the orientations in the gravity anomaly pattern, the NE derivative of the free-air gravity anomalies was calculated (Fig. 3.9). The long linear stripy anomalies oriented N-S throughout the figure (e.g., at ~92.5-93°E) are spurious signals generated during the computation. As anticipated, the orientations of the significant anomalies on this diagram and the bending of the regional geological structures appear to coincide. Subsequently, the directions along the most conspicuous anomalies around the Zaduo, Gongjue and Mangkang areas were measured, which show similar variation as the DEM results (Fig. 3.9 and Table 3.3).

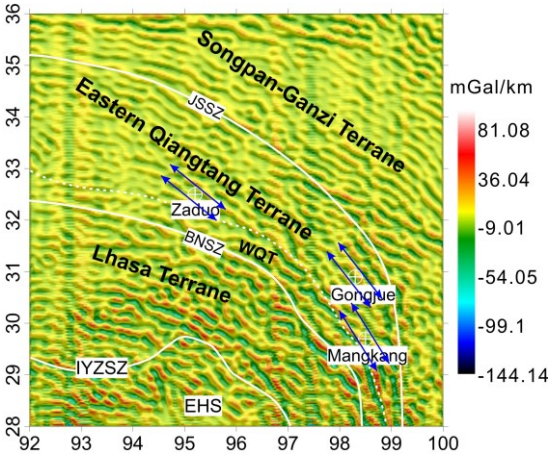

Figure 3.9. *Derivative diagram of the free-air gravity anomalies. The blue arrows define the estimated orientations of prominent anomalies in the Zaduo, Gongjue and Mangkang areas.*

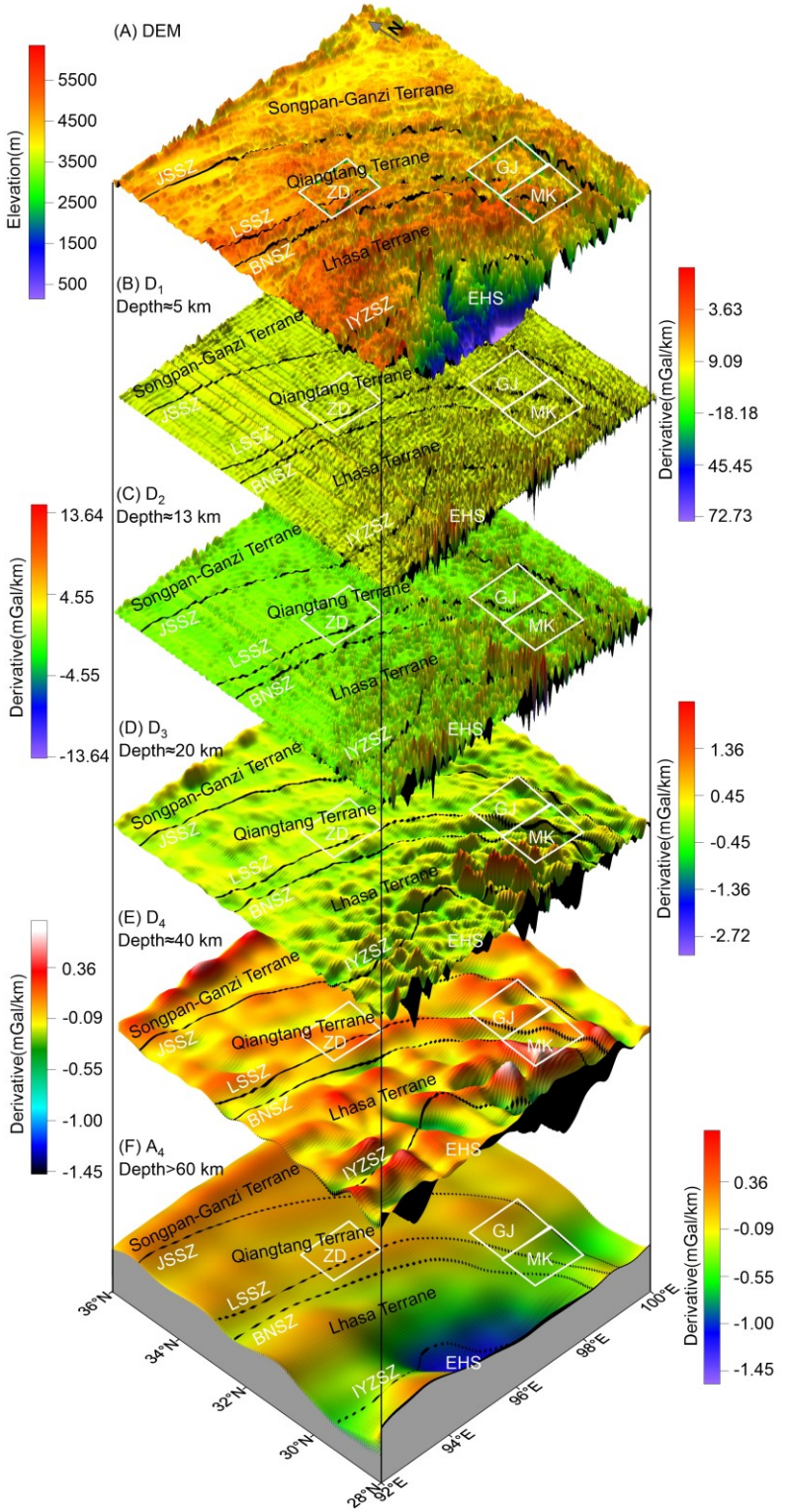
(A) DEM
Elevation(m)
5500
4500
3500
2500
1500
500
N
Songpan-Ganzi Terrane
Qiangtang Terrane
Lhasa Terrane
JSSZ
LSSZ
BNSZ
IYZSZ
ZD
GJ
MK
EHS
(B) D1
Depth≈5 km
(C) D2
Depth≈13 km
(D) D3
Depth≈20 km
(E) D4
Depth≈40 km
(F) A4
Depth>60 km
Derivative(mGal/km)
3.63
9.09
-18.18
45.45
72.73
13.64
4.55
-4.55
-13.64
1.36
0.45
-0.45
-1.36
-2.72
0.36
-0.09
-0.55
-1.00
-1.45
36°N
34°N
32°N
30°N
28°N
92°E
94°E
96°E
98°E
100°E

Figure 3.10 (previous page). *Derivative map of the decompositions of the Bouguer gravity anomalies. (A) DEM showing the topographic relief; NE derivative map of (B)-(E) the 1st- to the 4th-order wavelet detail (D_1 to D_4) and (F) the 4th-order wavelet approximation (A_4) of the Bouguer gravity anomalies. Refer to figure 3.1 for abbreviations.*

We follow the same procedure to obtain the major directions on the NE derivative map of the Bouguer gravity anomaly composition (Fig. 3.10). Thus, a total of nine orientations were obtained in this study: declination, bedding strike, fault strike, and six NE derivatives including that of the DEM, free-air gravity anomalies, and the 1st- to the 4th-order wavelet detail (Fig. 3.11 and Table 3.3). Although spurious signals were also generated in the 1st- and 2nd-order diagrams (long straight stripy anomalies oriented N-S in figure Fig. 3.10B, C), density distribution changes in the upper crustal portion (depth < ~15 km, Royden et al., 1997) can be evaluated (Fig. 3.10B, C). The 2nd-order diagram displays a similar regional orientation as the orocline on the Earth's surface. This similarity is more significant for the deeper layers representing the middle-lower crust with a depth of 20 to 40 km (Fig. 3.10D, E). The derivative diagram of the 4th-order approximation of the Bouguer gravity anomalies shows a clear difference between the EHS and other areas (Fig. 3.10F). When taken together, the orocline bend on the surface seems to be consistent with the density distribution at depth (Fig. 3.11 and Table 3.3).

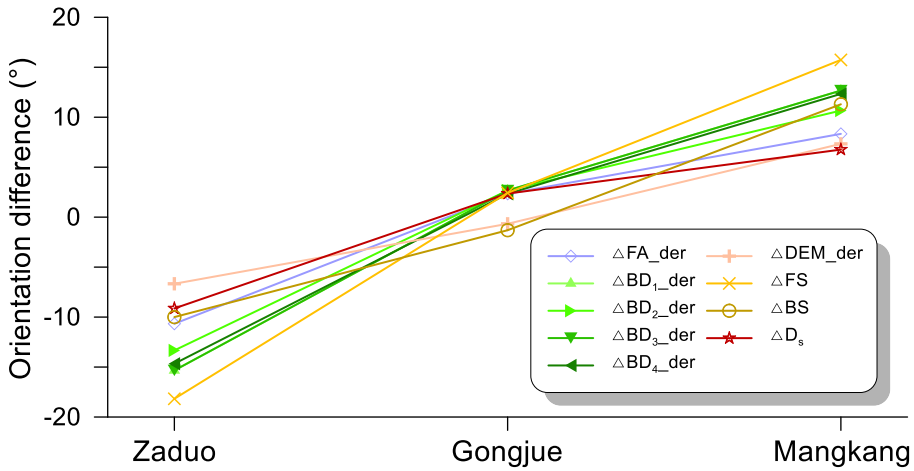

Figure 3.11. *Plots of geological trend deviations in the Zaduo, Gongjue and Mangkang areas, data are from Table 3.2 and 3.3. The deviation of each regional geological orientation element is calculated from their respective reference direction. FA_Der: NE derivative of the free-air gravity anomalies; BD1_Der to BD4_Der: NE derivative of the 1st- to the 4th-order wavelet detail of the Bouguer gravity anomalies. Refer to figure 3.7B for other abbreviations.*

Table 3.3. *Regional orientations of the gravity anomalies.*

Locality	FA_Der(°)	BD_1_Der(°)	BD_2_Der(°)	BD_3_Der(°)	BD_4_Der(°)
ZD	129	120	123	123	125
GJ	142	138	139	141	142
MK	148	148	147	151	152
Mean	139.7	135.3	136.3	138.3	139.7

Note: *FA_Der: NE derivative of the free-air gravity anomalies; BD_1_Der to BD_4_Der: NE derivative of the 1st- to the 4th-order wavelet detail of the Bouguer gravity anomalies.*

The correlation between the surficial geological structures and the deeper crust as determined here favors a coupled lithosphere-scale oroclinal deformation (Fig. 3.11), which implies the existence of a strong layer in the deep crust so that the stress can be transmitted effectively. However, both laboratory experiments and numerical modeling predict that the middle or lower crust would behave as a fluid on geological timescales because of the special stress/temperature conditions (e.g., Goetze & Evans 1979; Brace & Kohlstedt 1980; Kirby 1983; Kruse et al., 1991; MacCready et al., 1997; McKenzie et al., 2000; Copley & McKenzie, 2007; Whittington et al., 2009; Li & Zhang, 2013; Searle et al., 2016). The crustal flow is even possible when temperatures are low, i.e., above 400°C–500°C (MacCready et al., 1997; McKenzie et al., 2000); if temperatures are higher, i.e. > 700°C, larger-scale crustal flow could exist (Kruse et al., 1991). Thus, the surface deformation may be decoupled from the motion of the deep crust (Chen & Molnar, 1983; Royden, 1996; Royden et al., 1997; Clark & Royden, 2000; Roy & Royden, 2000). The mutually exclusive scenario can be reconciled by proposing an asynchronous deformation.

The orocline in the eastern ending of the Qiangtang Terrane was formed after the Late Eocene. However, the initiation of the large-scale motion of lower crustal material flowing into the SE Tibetan Plateau is later, probably after the Miocene (Clark & Royden, 2000; Schoenbohm et al., 2006). The Cenozoic mountain building probably occurred prior to the formation of a weak lower crust (Wang et al., 2012). The earlier oroclinal bending is likely to be the response to the lateral extrusion of the rigid blocks along major strike-slip faults (Molnar & Tapponnier, 1975; Tapponnier et al., 1982, 2001). This scenario perhaps built a channel for the later crustal flow. This deep structure was also observed by magnetotelluric imaging (Bai et al., 2010). In the eastern segments of the Qiangtang and Lhasa terranes, two major zones or channels of high electrical conductivity at a depth of 20-40 km were also discovered: one extends eastward from the Lhasa Terrane along the IYZSZ and turns southward around the EHS, while the other one extends eastward from the Qiangtang Terrane along the JSSZ and Xianshuihe Faults, and turns southward at the western margin of the Sichuan Basin (Bai et al., 2010). The electrical properties of such channels were interpreted as a combination of aqueous fluids and/or partial melt, which coincides with the weak flow (Bai et al., 2010). Subsequently, large-scale

crustal flow occurred, which is supported by a line of evidence: the thermal models of exhumation-driven cooling in the Sichuan Basin indicate a sustained exhumation since 10-15 Ma, which was driven by an underlying tectonic event (Wang et al., 2012). In addition, along the southeast margin of the Tibetan Plateau, the rapid passive surface uplift that occurred during the Late Miocene to Pliocene was suggested to be linked with the large-scale crustal flow (Clark & Royden, 2000; Beaumont et al., 2004; Clark et al., 2005; Schoenbohm et al., 2006; Medvedev & Beaumont, 2006; Wang et al., 2012; Zhang et al., 2016a; Zhang et al., 2017). To summarize, our study provides a picture depicting that continental deformation is a more dynamic process: first, the orocline occurred at the eastern ending of the Qiangtang Terrane after the Late Eocene, and this process set the stage for channelized crustal flow, which occurred later: large-scale crustal flow occurred after the Miocene.

3.6 Conclusions

In this paper, we quantified the plan-view curvature in the orogen at the eastern ending of the Qiangtang Terrane. The deep structures in this area were also investigated using gravity data. The Late Cretaceous to Cenozoic orocline test in the Zaduo, Gongjue and Mangkang areas yielded a slope m = 1.000 (by Total Least Squares) or m = 0.923 (by Ordinary Least Squares) and r^2 = 0.853, indicating a secondary orocline in the eastern ending of the Qiangtang Terrane. The gravity anomalies were separated into different layers, representing density variations from the shallow to the deep crust. The expression of the orocline at the Earth's surface and the anomaly orientations in the lower crust are consistent, and thus favor a coupled lithosphere-scale oroclinal deformation. We provide a more dynamic scenario of the growth and deformation in the eastern Tibetan Plateau: the orocline of the eastern ending of the Qiangtang Terrane occurred after the Late Eocene, whereas the large-scale crustal flow dominated in the later stage of the uplift and outward expansion of the plateau.

3.7 Acknowledgments

This work was co-supported by the Natural Science Foundation of China (Grant 41974080), the Basic Science Center for Tibetan Plateau Earth System (CTPES, Grant 41988101-01), the Natural Science Foundation of China (Grant 42164005), the Second Tibetan Plateau Scientific Expedition Program (Grant 2019QZKK0707), the Strategic Priority Research Program of Chinese Academy of Sciences (Grant XDA20070201).






4

INVERSE MAGNETIC FABRIC OF THE REMAGNETIZED LIMESTONES IN THE ZADUO AREA, EASTERN QIANGTANG TERRANE (CHINA) – IMPLICATIONS FOR THE OROCLINE

Abstract

Magnetic fabric analysis is a common technique to assess the stress regime during mountain building processes. Here, we use this approach to evaluate the tectonic evolution of the Tibetan Plateau and the Eastern Himalayan Syntaxis by analyzing the limestones of the Jurassic Buqu Formation in the Zaduo area, Eastern Qiangtang Terrane (China). However, these limestones were chemically remagnetized during the Cenozoic. For a proper assessment, it is relevant to understand how the mineralogy of the remagnetized limestones affects their magnetic fabric and how the magnetic fabric can further our understanding of the tectonic strain and regional deformation. The role of the authigenic magnetite in the development of the magnetic fabric should thus be explored. Comparison of the bulk susceptibility (K_m) with various natural and laboratory rock magnetic properties (K_m versus natural remanent magnetization, K_m versus saturation isothermal remanent magnetization, and K_m versus saturation magnetization) indicates that susceptibility and remanences are both carried by authigenic magnetite. Most of the magnetite grains show axial ratios less than 1.3 : 1 according to the Néel diagram, giving rise to the inverse magnetic fabrics observed. Twelve sites (120 specimens) are divided into four groups based on the magnetic fabrics and rock magnetic behavior. The data document the NNE-SSW oriented compression during remagnetization. Widespread clockwise rotation of the southeast Tibetan Plateau has occurred even later, likely since the late Eocene.

4.1 Introduction

The India-Eurasia collision is a critical player in the uplift and growth of the Tibetan Plateau (Molnar & Tapponnier, 1975; Burchfiel et al., 1989; England & Houseman, 1989; Beck et al., 1995; Yin & Harrison, 2000; Tapponnier et al., 2001; Garzanti et al., 2005; Wang et al., 2014; Ding et al., 2017; Zhang et al., 2020a). Directly related issues include the distribution of mineral resources (Hou et al., 2007; Hou & Zhang, 2015), and regional and global climate change (e.g., Ruddiman & Kutzbach, 1989; Raymo & Ruddiman, 1992; Fang et al., 2016). Hence, the Tibetan Plateau is commonly seen as a key natural laboratory for studying and geodynamic processes and the paleoclimate changes associated with the interaction between the atmosphere, biosphere, hydrosphere and lithosphere (Molnar & Tapponnier, 1975; Royden et al., 2008; Nábělek et al., 2009; van Hinsbergen et al., 2012; Yan et al., 2016; Su et al., 2019; Jadoon et al., 2021). As the prime driver of uplift and growth of the Tibetan Plateau, the northward indentation and subsequent subduction of the Indian Plate underneath the Eurasian Plate has brought about vast lithospheric crustal shortening and extrusion in Asia (Molnar & Tapponnier, 1975; Burchfiel et al., 1989; Yang & Besse, 1993; Chen et al., 1995; Beck et al., 1995; Yin & Harrison, 2000; Replumaz & Tapponnier, 2003; Van Hinsbergen et al., 2011; Chen et al., 2015), and clockwise rotation around the Eastern Himalayan Syntaxis (EHS) in the southeastern Tibetan plateau (Yang et al., 2001b; Sato et al., 2007; Tanaka et al., 2008; Kondo et al., 2012; Tong et al., 2013; Kornfeld et al., 2014; Gao et al., 2015; Li et al., 2017b; Tong et al., 2017). In general, the widespread rotation and southeastward extrusion of the southeastern Tibetan Plateau are believed to be related to lithospheric-scale strike-slip faults systems (Gao et al., 2015; Leloup et al., 1995; Li et al., 2017b; Sato et al., 2007; Tapponnier et al., 1990; Tong et al., 2013), and/or uplift of southeastern Tibet (Hoke et al., 2014; Li et al., 2019c; Su et al., 2019; Tang et al., 2017; Xiong et al., 2020).

The Tibetan Plateau consists of the Songpan-Ganzi, Qiangtang, Lhasa, and Tethyan Himalaya terranes from north to south. The Qiangtang Terrane is situated in the central Tibetan Plateau (Fig. 4.1A). It is separated geologically from the Songpan-Ganzi Terrane by the Jinsha suture zone to the north and from the Lhasa Terrane by the Bangong-Nujiang suture zone to the south. The Qiangtang Terrane is further divided into the Eastern (also referred to as Northern) Qiangtang Terrane (EQT) and the Western (or Southern) Qiangtang Terrane (WQT) by the Longmu Co-Shuanghu suture zone (Fig. 4.1A; Li, 1987; Huang et al., 1992; Yin & Harrison, 2000; Pan et al., 2004c; Li et al., 2009a; Metcalfe, 2013; Zhu et al., 2013, 2016; Yan et al., 2016). The easternmost part of the Qiangtang Terrane is a transition area that is adjacent to southeastern Tibet. Therefore, knowledge on the post-collisional tectonic evolution and deformation history of the EQT will enhance our understanding of the start of the rotation and southeastward extrusion in the southeastern Tibetan Plateau. Several paleomagnetic studies have been carried out on Cenozoic strata in the eastern Qiangtang Terrane to constrain its paleolatitude and quantify vertical axis rotations (Lippert et al., 2011; Roperch et al., 2017; Tong et al., 2017; Zhang et al., 2018;

2020a; Li et al., 2020b). This provides solid tectonic evidence for various deformation and uplift scenarios. However, magnetic fabric is less used in this region, somewhat surprisingly because the approach is a powerful tool for tectonic strain analysis in structural geology.

In the past few decades, many studies have demonstrated that anisotropy of magnetic susceptibility (AMS, also termed magnetic fabric), a comparatively rapid tool, has delivered crucial information on basin evolution (e.g., Mattei et al., 1997; Cifelli et al., 2005; Oliva-Urcia et al., 2010, 2011, 2013; Yu et al., 2014; Tang et al., 2015; Li et al., 2020a, 2020c, 2021; Jiang et al., 2022; Zhang et al., 2022a), emplacement of igneous bodies (e.g., Hrouda, 1982; Bascou et al., 2005; Antolín-Tomás et al., 2009; Cañón-Tapia and Mendoza-Borunda, 2014; Yan et al., 2019), fold/fault deformation (e.g., Aubourg et al., 1999; Saint-Bezar et al., 2002; Evans et al., 2003; Luo et al., 2009; García-Lasanta et al., 2015), and paleocurrent directions (e.g., Tarling and Hrouda, 1993; Pueyo Anchuela et al., 2013; Ejembi et al., 2020; Bilardello, 2021). A fundamental step prior to interpreting AMS data is to ascertain what minerals give rise to the magnetic fabric. Recently, a paleomagnetic study with detailed rock magnetic experiments was conducted on the Jurassic limestones from the Eastern Qiangtang Terrane, where authigenic magnetite was responsible for the secondary remanent magnetization acquired during the Cenozoic (Fu et al., 2022a, thesis chapter 2). This provides a good opportunity to explore how the characteristic mineralogy of remagnetized limestones that contain large amounts of superparamagnetic (SP) and stable single domain (SSD) magnetite affects the AMS, and how this magnetic fabric can shed light on the tectonic strain and regional deformation. Thus, on the one hand (i) the relation between AMS and various remanences including natural remanent magnetization (NRM), saturation isothermal remanent magnetization (SIRM), and saturation magnetization (M_s) are compared, and on the other hand, (ii) we propose that inverse AMS occurs in these remagnetized limestones. The results obtained are of interest for the compression and deformation history of the east central Tibetan plateau in response to the early India-Eurasia collision.

4.2 Geological setting

Our study area has an average elevation of ~4,700 m (Fig. 4.1C) and lies in a transitional region of the Eastern Qiangtang Terrane where a gradual change in orientation from east-west trending to north-south trending structures is present (Fig. 4.1A). The tectonic lineaments (e.g., faults, thrusts, and fold axes) in the Zaduo area are NW-SE oriented (Fig. 4.1B), in accordance with the regional trending of the east central Qiangtang Terrane (Fig. 4.1A, QGSI, 2014). These tectonic features are mostly related to the significant Cenozoic shortening and strike-slip faulting in response to the India-Eurasia collision (Horton et al., 2002; Kapp et al., 2005).

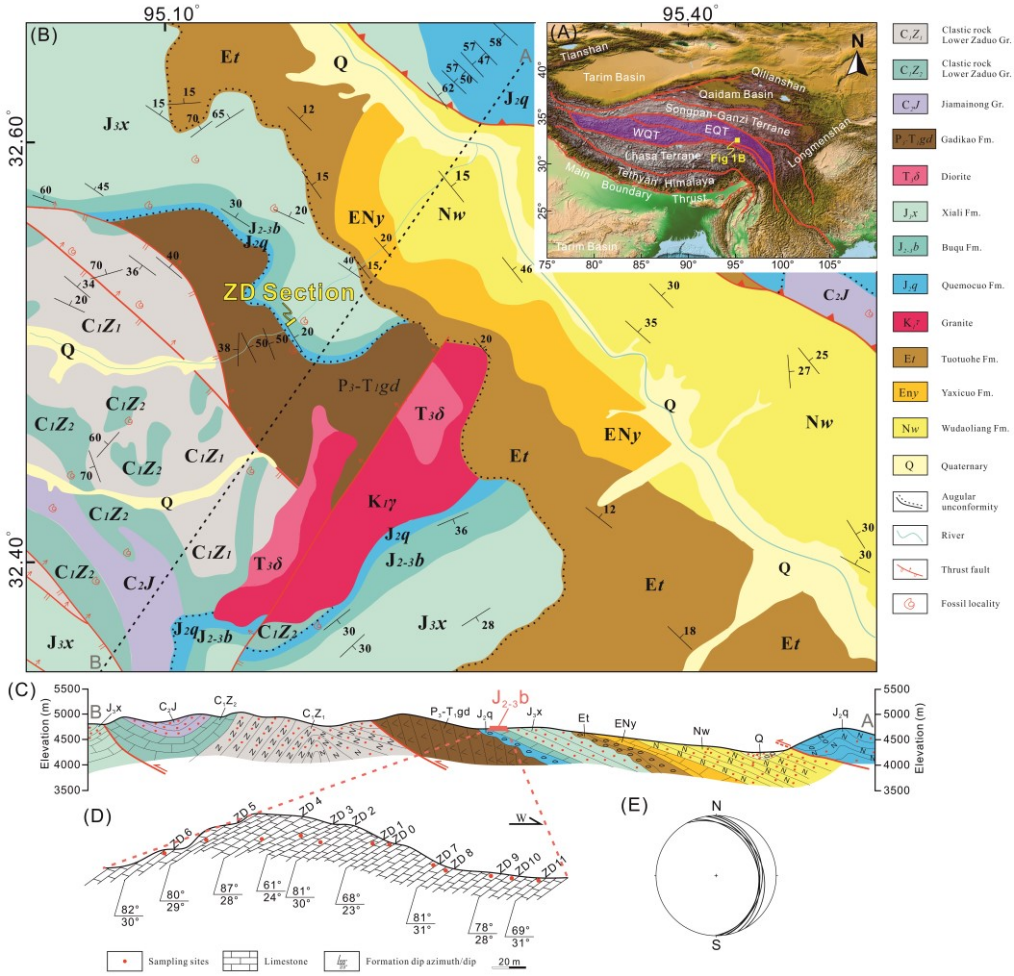

Figure 4.1. *(A) Topographic map of the Tibetan Plateau and surrounding areas; the red lines outline the major suture zones. The abbreviations of the tectonic units are EQT: Eastern Qiangtang Terrane; WQT: Western Qiangtang Terrane. (B) Geological map of the Zaduo area showing the location of the sampling section, black dashed line AB represents the cross-section of the Zaduo area (QGSI, 2014) displayed in (C). (C) Cross-section AB showing the exposed sedimentary succession. (D) Cross-section showing the sampling sites; Note: the sampling section is not on the Cross-section AB, but it shows the same stratigraphic position as marked in pink in (C). (E) Equal-area lower-hemisphere stereographic projection of the bedding attitudes. (B) and (D) are modified from Fu et al., (2022a).*

Rocks from the Paleozoic to the Cenozoic are exposed in the Zaduo area (Fig. 4.1B, refer to Fu et al. (2022a, thesis chapter 2) for more detailed descriptions). Our target rocks, the limestones of the Middle-Upper Jurassic Buqu Formation were collected

from a monoclinal section. Previous high-resolution magnetostratigraphic studies were conducted in the Yanshiping area (~300 km to the west of the Zaduo area) and constrained the Buqu Formation to be ~165.5-163.3 Ma (Fang et al., 2016; Yan et al., 2016). The AMS sites studied in this contribution were paleomagnetically investigated before and deemed to be remagnetized (Fu et al., 2022a, chapter 2). The oxidation of the existing iron sulfides to authigenic magnetite was argued to be a major magnetization mechanism. Moreover, from the analysis of the declination, inclination and calculated paleopole, the acquisition of the secondary NRM was dated to the Paleogene, more likely to the Eocene (Fu et al., 2022a, chapter 2).

4.3 Applied techniques

The AMS is a second-rank symmetrical tensor that can be graphically displayed by an ellipsoid with orthogonal principal axes that represent the three principal magnetic susceptibilities namely: K_1 (maximum), K_2 (intermediate), and K_3 (minimum) (e.g., Tarling and Hrouda, 1993). The magnetic lineation L (K_1/K_2) and foliation F (K_2/K_3) are often used to characterize the magnetic ellipsoids. Other AMS parameters, such as the mean magnetic susceptibility (K_m), the corrected degree of anisotropy (P_j) and shape parameter (T) can be defined as follows:

$$K_m = \frac{K_1 + K_2 + K_3}{3},$$

$$P_j = exp\sqrt{2\left[\left(\eta_1 - \eta_m\right)^2 + \left(\eta_2 - \eta_m\right)^2 + \left(\eta_3 - \eta_m\right)^2\right]},$$

$$T = \left[\frac{2ln\left(K_2/K_3\right)}{ln\left(K_1/K_3\right)}\right] - 1,$$

where $\eta_1 = \ln K_1$, $\eta_2 = \ln K_2$, $\eta_3 = \ln K_3$, and $\eta_m = (\eta_1 + \eta_2 + \eta_3)/3$ (Jelínek, 1977, 1981; Jelínek and Kropáček, 1978). P_j can be linked to lithostratigraphic variations and strain (Hrouda, 1982) and normally does not exceed 1.1 for sedimentary rocks (Tarling and Hrouda, 1993); A negative T ($-1 < T < 0$) is indicative of a prolate ellipsoid, whereas a positive T ($0 < T < 1$) corresponds to an oblate ellipsoid.

Magnetic susceptibility measurements were performed with a KLY-3S Kappabridge susceptibility meter (AGICO Inc., Brno, Czech Republic) at room temperature with an applied magnetic field of 300 A/m and frequency of 875 Hz, at the paleomagnetic laboratory of the State Key Laboratory of Tibetan Plateau Earth System, Resources and Environment (TPESRE), Institute of Tibetan Plateau Research, Chinese Academy of Sciences (ITPCAS, Beijing, China). The AMS data were processed using the Anisoft 4.2 and Anisoft 5.0 software packages (Chadima & Jelinek, 2009) and plotted by Stereonet11 software (Allmendinger et al., 2011; Cardozo & Allmendinger, 2013). The previous rock magnetic study on these samples has revealed that SP and SSD magnetite are the dominant magnetic carriers and that calcite accounts for 95%

of the total rock in most of the samples (Fu et al., 2022a, chapter 2). Additional measurements of magnetization versus temperature were carried out with an in-house built horizontal translation type Curie balance with a sensitivity of ~5 × 10^{-9} Am^2 (Mullender et al., 1993) in the 'Fort Hoofddijk' paleomagnetic laboratory of Utrecht University (Utrecht, The Netherlands). To determine the relative content of the paramagnetic and ferromagnetic fraction of the samples, we analyzed the high-field and low-field slopes of the 'induced hysteretic' magnetization, which is defined by the mean value of the descending and ascending branch for a hysteresis loop (Fig. 4.2, Fabian, 1997).

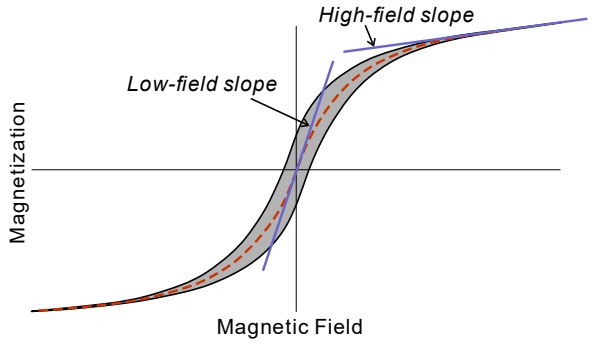

Figure 4.2. *Hysteresis loop of a sample consists of a descending branch and an ascending branch, showing high-field and low-field slopes of the 'induced hysteretic' magnetization.*

4.4 Results

Through the detailed comparison of different fabrics and rock magnetic behavior (e.g., K_m, NRM, SIRM or paramagnetic percentage), the twelve sites (120 specimens) are divided into four different groups. Sites 0, 1 and 7 are included in group I; sites 3, 4, 5 and 11 are classified into group II; group III consists of sites 6, 8, 9 and 10; the remaining site 2 shows different features and therefore constitutes group IV. Although most of the parameters allow separating these four groups, overlap of the different indicators is observed among the defined groups.

4.4.1 Rock Magnetism

Previous rock magnetic studies have revealed that authigenic magnetite mainly of SP and SSD size range is the dominant magnetic NRM carrier (see Fu et al., 2022a, chapter 2 for more details, the site numbers here are the same as in that study). This authigenic magnetite formed as an oxidation product of iron sulfides. Groups I, II, and III show similar characteristics in routine rock magnetic experiments, including 'wasp-waisted' hysteresis loops, SP-dominated first-order-reversal-curve (FORC) diagrams and soft-style IRM acquisition curves (Fu et al., 2022a, chapter 2). Group IV specimens show noisy IRM acquisition and interacting SD- or PSD-like FORC diagrams (Fu et al., 2022a, chapter 2).

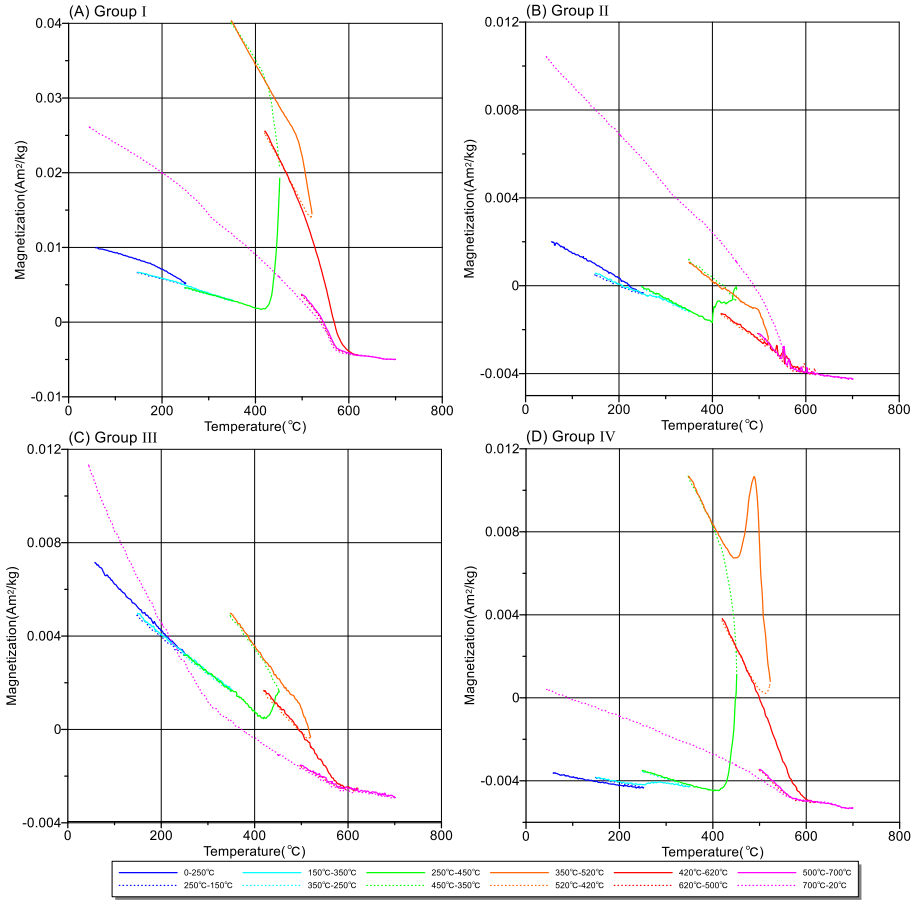

Figure 4.3. *High-field thermomagnetic runs of representative specimens of each group. Solid (dashed) lines indicate the heating (cooling) curves.*

Stepwise high-field thermomagnetic runs of magnetization versus temperature were conducted for four specimens to detect the alteration of iron sulfides during heating (Fig. 4.3). In general, specimens of each group show clear reversibility during heating/cooling below 350 °C. Irreversibility for cycles is noted at higher temperatures starting at ~420 °C. An abrupt increase of magnetization occurs at ~410-420 °C during heating, likely indicating the alteration from pyrite to magnetite (Passier et al., 2001; Li et al., 2005; Wang et al., 2008). The magnetic behavior of pyrite during thermal treatment seems to be complicated. Pyrite can be altered to stable pyrrhotite in an argon atmosphere at temperatures above 560 °C or in air above 600 °C, and to magnetite at low temperature (~350-500°C) (Li et al., 2005). The newly formed magnetite can be reduced to monoclinic pyrrhotite by the unreacted pyrite (Wang et al., 2008). The minute discontinuity at 320 °C in the final cooling curve could be due to the presence of pyrrhotite (Fig. 4.3A-C). The the 'hump' present in the heating curve of 350-520 °C of the group IV specimen may be due to oxidation of

organic matter and formation of magnetite (Fig. 4.3D).

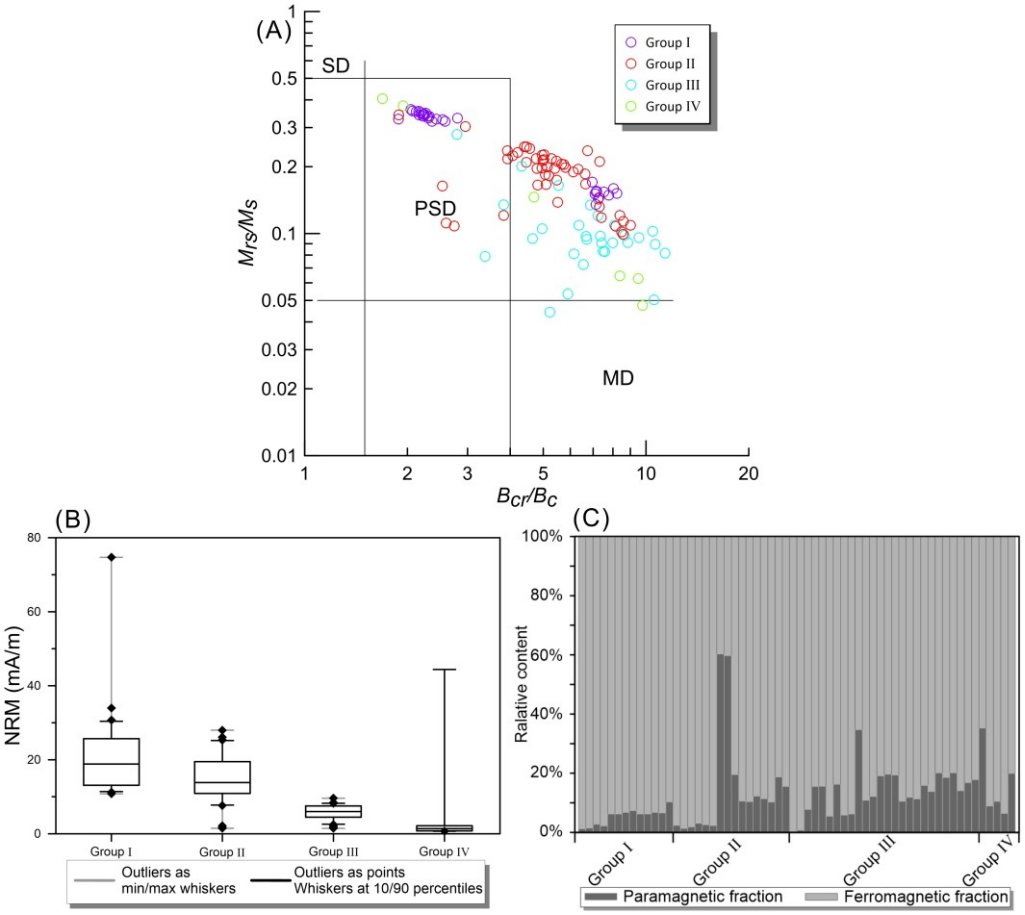

Figure 4.4. *(A) Day plot (Day et al., 1977; Dunlop, 2002) of representative samples for the four groups. (B) starting NRM values of each group. (C) Paramagnetic and ferromagnetic fractions for representative samples of each group.*

Plotted on the Day diagram, the overall data (from group I to group IV) lie mainly in the PSD field displaying high values of M_{rs}/M_s and low values of B_{cr}/B_c. Samples to the right of the PSD field feature low values of M_{rs}/M_s and high values of B_{cr}/B_c (Fig. 4.4A). Some exceptions exist, for example, group I has two clear subgroups; two specimens of group IV lie in the PSD field (Fig. 4.4A). Compared with classical carbonates, the NRM of the present limestone is rather strong, which seems to support the *in situ* growth of a significant population of SP–SSD particles (Jackson & Swanson-Hysell, 2012). The NRM decreases from group I to group IV, and group I has an average NRM about one order of magnitude greater than that of group IV (Fig. 4.4B). In addition, the paramagnetic and ferromagnetic fractions were

evaluated. Paramagnetic minerals appear to contribute less than 10% in group I, while it ranges 10-20 % in groups II-IV. Group III is most variable with notably high or low paramagnetic contribution samples; the paramagnetic fraction in this group is slightly higher than in groups II and IV (Fig. 4.4C). The negative correlation between NRM and the paramagnetic phase percentage reveals the variable SP–SSD magnetite concentration in these groups (Fig. S4.1); group I has the largest population of magnetite.

4.4.2 Anisotropy of Magnetic Susceptibility

One hundred and twenty specimens from 12 sites were measured and analyzed. The sampled section is monoclinal that the bedding attitudes change slightly with a dip direction of NE and dips of ~20-30° (Fig. 4.1D). Overall, stereonet projections show that the K_1 and K_3 axes are generally well grouped and oriented roughly along the NE-SW and NW-SE directions, respectively (Fig. 4.5A-B). The specimens show an average low-field susceptibility of 624×10^{-6} (all in SI units) ranging from 31×10^{-6} to 1527×10^{-6} (Fig. 4.5C, supporting information Table S4.1). The corrected anisotropy degree (P_j) ranges from 1.007 to 1.095, with an average value of 1.039 ± 0.018 (Fig. 4.5D). A poor linear correlation between K_m and P_j suggests that the P_j is independent of the lithology (Fig. 4.5D). The shape parameter T is variable, with an average value of -0.281 and a range of -0.922 and 0.878 (Fig. 4.5E), indicating a similar number of samples with oblate and prolate ellipsoids. The magnetic foliation (F) exhibits a relatively narrow range of distribution from $1.001 \leq F \leq 1.057$ ($F_{mean} = 1.018$), similar to the magnetic lineation (L) that ranges from 1.002 to 1.054, with an average value of 1.019. The F-L plot (Flinn diagram) shows the same oblate/prolate character of distributions (Fig. 4.5F). Comparison of these indicators among the four groups shows no/barely differences in the P_j-T and F-L diagrams (Fig. 4.5E-F). Although a negligible increase of P_j with larger spreading and a decrease of T from group I to group IV can be observed (Fig. 4.6 C-D), the interquartile ranges of the box and whisker plot are large so that this trend is deemed not significant.

Group I specimens have highest average susceptibility of ~1200×10^{-6} (SI) and the lowest paramagnetic mineral percentage (Fig. 4.6A, B, Table 4.1). Their stereonet projections are characterized by K_1 being grouped and oriented along a NE-SW girdle (~40-220°), and K_3 showing a NW-SE distribution (Fig. 4.7A). Group II specimens have lower average susceptibility of of ~700×10^{-6} (SI), and a contribution of paramagnetic minerals of ~10 % (Fig. 4.6A, B). Although the three principal axes of group II specimens are rather randomly distributed, the direction defined by the K_1 axis (~40°) is virtually identical to that of the group I specimens (Fig. 4.7A, B, Table 4.1). Group III and group IV specimens have similar AMS distributions but different rock properties (4.7C, D). The K_1 and K_2 axes are grouped roughly in the bedding plane, while the K_3 axis is clustered around the bedding pole and thus perpendicular to the bedding plane. However, the directions of these two groups defined by K_1 are different by ~20°: the K_1 axis of group III has a declination of ~50° and that of group

IV has a declination of ~30° (Fig. 4.7C, D, Table 4.1). In addition, group IV specimens have the lowest average susceptibility of ~100 × 10^{-6} (SI) and a high paramagnetic mineral percentage of ~15% (Fig. 4.6 A, B).

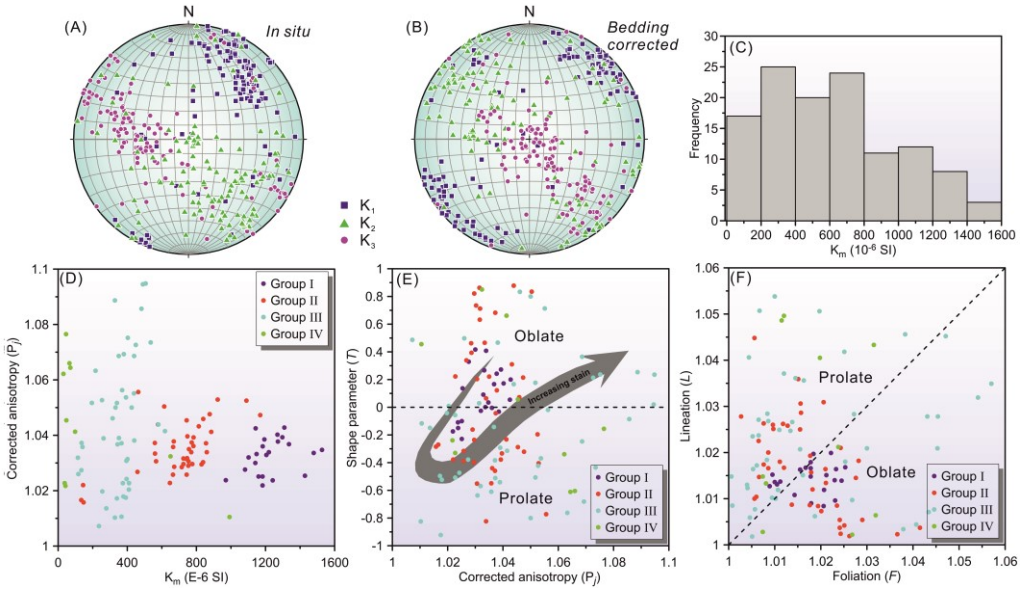

Figure 4.5. *Low field anisotropy of magnetic susceptibility results for the Jurassic limestones. In situ (A) and bedding-corrected (B) equal-area stereographic projections of the AMS principal axes (squares, triangles and circles show orientations of K_1, K_2 and K_3 axes, respectively). (C) Histogram for the total range of mean magnetic susceptibility (K_m) (N=120 specimens). (D) Mean magnetic susceptibility (K_m) versus corrected anisotropy degree (P_j) diagram. (E) P_j versus shape parameter (T) diagram (the grey arrow showing the path of the magnetic ellipsoid and its relation to strain, modified from McCarthy et al., 2015). (F) Foliation F (K_2/K_3) versus lineation L (K_1/K_2) diagram (Flinn diagram (Flinn, 1965)).*

Figure 4.6 (next page). *Box and whisker plots showing the median (horizontal lines in the boxes) and the quartiles of the different parameters measured in the specimens. (A) Bulk susceptibility (K_m) at room temperature. (B) Paramagnetic percentage contributions (%Para) to the total bulk magnetic susceptibility. (C) Corrected degree of anisotropy (P_j) of the AMS. (D) Shape parameter (T) of the AMS.*

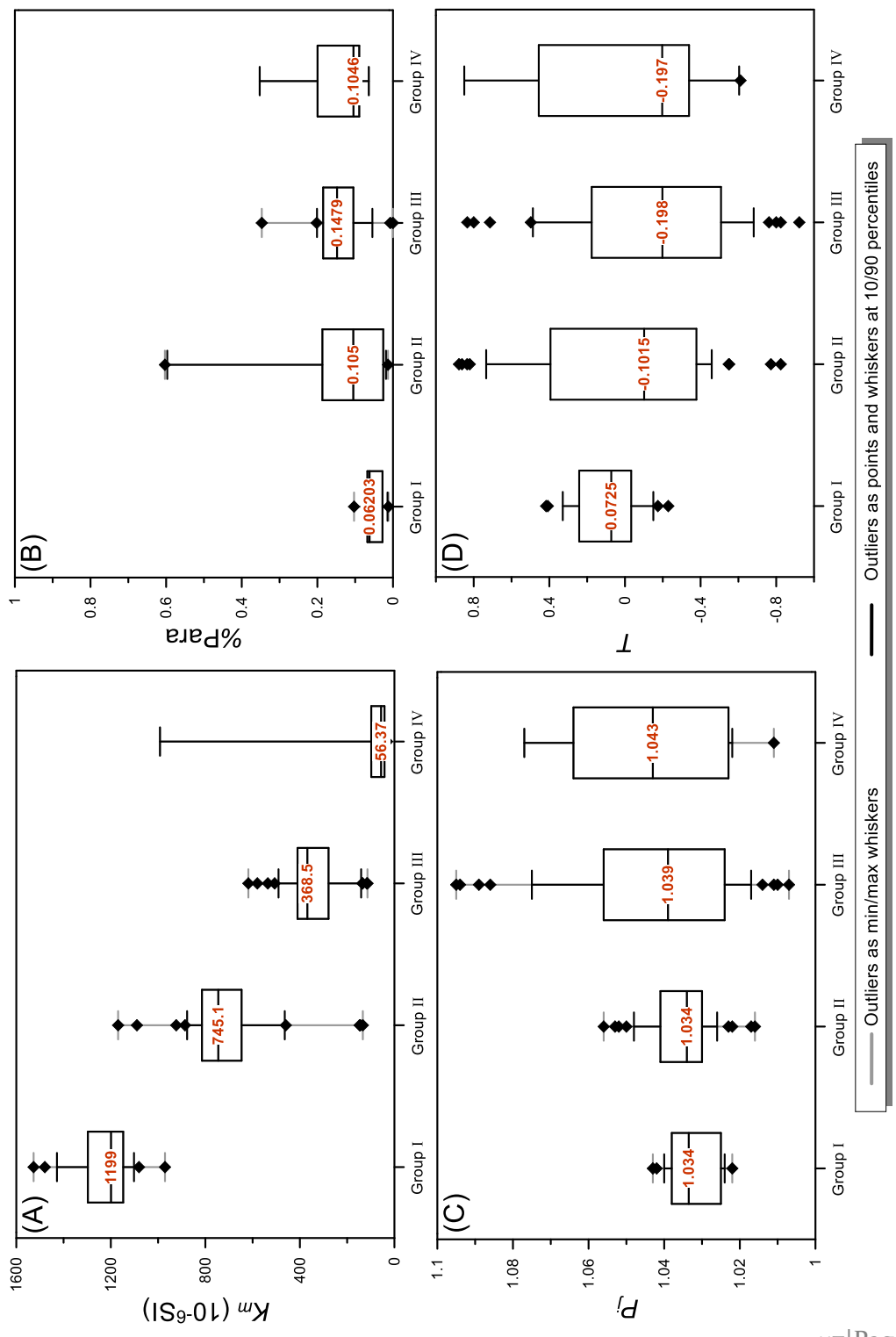
(A)
(B)
(C)
(D)
Km (10-6SI)
%Para
Pj
T
Group I
Group II
Group III
Group IV
1199
745.1
368.5
56.37
0.06203
0.105
0.1479
0.1046
1.034
1.034
1.039
1.043
0.0725
0.1015
0.198
0.197
Outliers as min/max whiskers
Outliers as points and whiskers at 10/90 percentiles

Table 4.1. *Scalar parameters of the AMS for the remagnetized limestones*

Site	n	K_m	L	F	P_j	T	K_1		K_2		K_3	
		(10^{-3}) SI					Dec	Inc	Dec	Inc	Dec	Inc
Group I												
Site 00	6	1.269	1.017	1.016	1.033	-0.025	57.1	8.4	147.7	3.8	261.7	80.7
Site 01	6	1.269	1.017	1.016	1.033	-0.025	49.3	14	147.2	29	296.6	57.2
Site 07	11	1.223	1.013	1.02	1.034	0.211	31.7	15.7	281	51.5	132.7	34.1
Mean	23	1.231	1.018	1.007	1.026	-0.453	40.5	10.5	302.8	36.1	144.2	51.9
Group II												
Site 03	10	0.713	1.011	1.014	1.024	0.135	329.5	15	63.2	13.5	193.5	69.6
Site 04	11	0.8463	1.007	1.011	1.018	0.185	37.6	5.9	292.1	68.8	129.8	20.3
Site 05	9	0.7361	1.023	1.007	1.031	-0.558	217.8	5.6	313	42.6	121.7	46.9
Site 11	12	0.5417	1.005	1.022	1.028	0.654	230.3	5	340.6	75.9	139.2	13.2
Mean	42	0.7039	1.009	1.009	1.018	-0.029	39.6	4.4	303.6	53.9	132.7	35.7
Group III												
Site 06	12	0.4425	1.028	1.038	1.067	0.145	36.3	3.6	305.1	18	137.2	71.6
Site 08	11	0.2509	1.023	1.011	1.034	-0.356	230.6	8.6	322	9.2	98.2	77.4
Site 09	12	0.3279	1.017	1.007	1.024	-0.426	58.2	2.4	328	3.6	181.5	85.7
Site 10	11	0.3823	1.017	1.002	1.021	-0.755	245.7	8.1	340.1	28.5	141.4	60.2
Mean	46	0.3524	1.019	1.015	1.035	-0.128	230.1	1.9	320.6	15.7	133.2	74.2
Group IV												
Site 02	10	0.208	1.02	1.017	1.037	-0.103	33.7	1.9	123.7	1.6	253.5	87.6

Note: *n: number of specimens used to calculate the AMS results; K_m: mean magnetic susceptibility for all specimens of each site/group; L: magnetic lineation; F: magnetic foliation; P_j: corrected anisotropy degree; T: shape parameter; Dec, Inc: declination (azimuth) and inclination (plunge), respectively, of the K_1, K_2, and K_3 axes after bedding correction.*

Figure 4.7 (next page). *Stereographic lower-hemisphere projections of the magnetic susceptibility axes (after bedding-correction). The contours of variable colors represent the distribution of percentage densities of the K_1 (blue) and K_3 (red) axes. Black arrows (K_1) represent the measured magnetic lineation.*

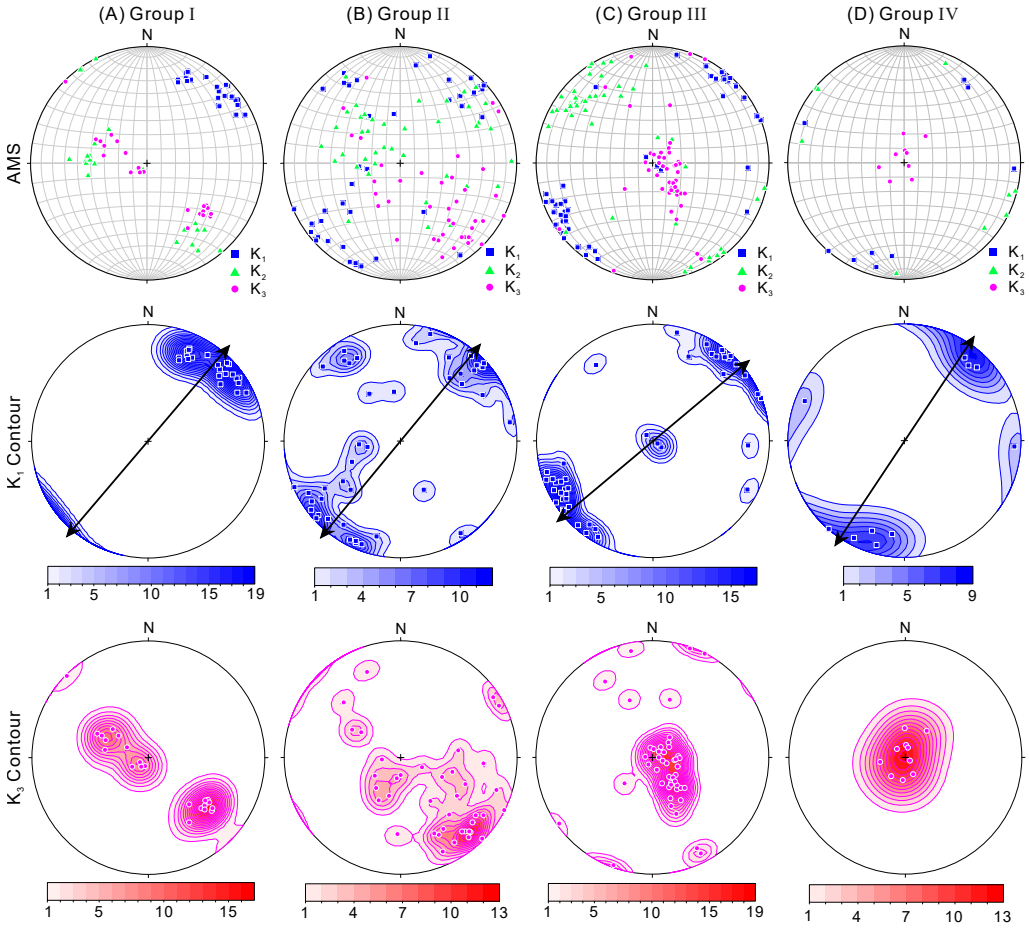

4.5 Discussion

4.5.1 Carriers of magnetic susceptibility

The total magnetic susceptibility of a rock represents a summation of the contributions from all mineral species present, including diamagnetic (most of the primary rock-forming minerals such as quartz, calcite, and many feldspars), paramagnetic (many important auxiliary minerals such as hornblende, biotite, and chlorite), antiferromagnetic (hematite, goethite), and ferromagnetic (sensu lato) minerals (e.g., magnetite, greigite, and pyrrhotite). The relative abundances and specific susceptibilities of the minerals determine the susceptibility. Different minerals have different origin and may have a variable response to deformation. Thus, identification of the mineralogical sources of AMS is of great significance in deciphering these susceptibilities (Rochette, 1987b; Rochette et al., 1992; Borradaile, 1988; Jackson, 1991; Borradaile & Jackson, 2010; García-Lasanta et al., 2018; Calvín et al. 2018a). Early investigations focused mostly on the ferromagnetic (sensu lato) minerals, which were deemed to be the major AMS carriers (Hargraves & Fischer,

1959; Fuller, 1963, 1969). Later, it is suggested that paramagnetic minerals might contribute to AMS significantly, as they normally act as the major rock-forming minerals with a much larger volume fraction than ferromagnetic minerals in rocks (e.g., Hounslow, 1985; Rochette, 1987b; Rochette et al., 1992; Lüneburg et al., 1999; Parés, 2004; Cifelli et al., 2004, 2005, 2009; Li et al., 2020a, 2020c, 2021; Cao et al., 2021). Our previous investigation has revealed that authigenic magnetite grains, dominantly in the SSD and SP size range, are responsible for the secondary magnetizations of the studied Jurassic limestones in the Zaduo area (Fu et al., 2022a, chapter 2). However, the carriers of the magnetic remanence are not necessarily same as those of the AMS. For example, while sedimentary rocks deposited during the Late Paleozoic Ice Age in the Paraná Basin of South America are shown to have been remagnetized during the Cretaceous, their AMS is not overprinted by the secondary magnetic overprints as the AMS is carried by paramagnetic minerals (Bilardello, 2021).

Many studies follow a rather simple criterion to estimate the contributions of ferromagnetic minerals and paramagnetic minerals, that is, susceptibilities exceeding 5000×10^{-6} indicate that the ferromagnetic minerals dominate the signal, whereas susceptibilities lower than 500×10^{-6} imply that the paramagnetic minerals are the controlling factor, and that between 500 and 5000×10^{-6} indicate that fernmagnetic and paramagnetic fractions mix (Rochette, 1987a, 1987b; Borradaile, 1987; Hrouda & Jelinek, 1990; Tarling & Hrouda, 1993). However, the criterion is oversimplified and ambiguous, and thus more comprehensive investigations are required to reduce the ambiguity (García-Lasanta et al., 2015; Wang et al., 2017). In the present study, microscopic observations have shown that the diamagnetic rock-forming minerals calcite and quartz account for 98% of the rock in most of the samples (Fu et al., 2022a, chapter 2). It is worth noting that calcite is quickly paramagnetic when Fe and/or Mn substitution is present, so is quartz when it has a coating of ferrous/ferric iron (hydr) oxides. The magnetic susceptibility values of all samples range from 31×10^{-6} to 1527×10^{-6}, with a median of 572×10^{-6} and an average of 624×10^{-6} (SI), which is rather high for carbonates like those studied here (Jackson & Swanson-Hysell, 2012). Given that magnetite has a susceptibility of about 6 orders of magnitude greater than that of calcite (Jackson, 1991), a plausible interpretation for the difference is that our limestone samples have a fairly high concentration of authigenic magnetite grains.

On the other hand, magnetic remanence resides exclusively in ferromagnetic (sensu lato) minerals. The comparison between susceptibility and the intensity of a remanent magnetization (characteristic or/and anhysteretic remanent magnetization) has been used successfully by Lowrie & Heller (1982) to qualitatively verify whether it was the same mineral that carries susceptibility and remanence. Positive correlations between susceptibility and various remanences/magnetization (i.e., K_m versus NRM, K_m versus SIRM, and K_m versus M_s) are observed in our samples

(Fig. 4.8; supporting information Table S4.1), indicating that susceptibility and remanence are carried by the same mineral, that is, authigenic magnetite in our study (Fu et al., 2022a, chapter 2).

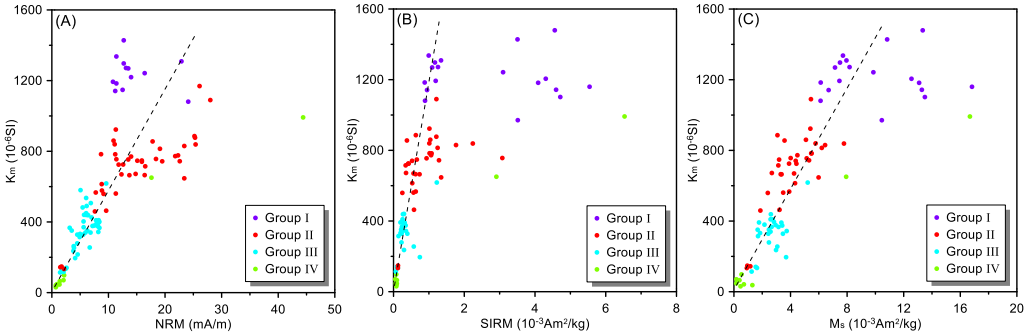

Figure 4.8. *Remagnetized limestones: Correlation between (A) mean magnetic susceptibility (K_m) and natural remanent magnetization (NRM); (B) K_m and saturation isothermal remanent magnetization (SIRM); (C) K_m and saturation magnetization (M_s).*

4.5.2 Diagnosis of the inverse magnetic fabric

A normal magnetic fabric is described as a type of anisotropy with the K_1 axis parallel to the long axis of the crystal (the easy direction of magnetization). Occasionally, the K_1 axis is normal to the long axis of the crystal, and this type of anisotropy is called an inverse magnetic fabric (Fig. 4.9, Rochette, 1988; Potter & Stephenson, 1988). Uniaxial SD magnetite possess an inverse magnetic susceptibility fabric. This is because SD particles are magnetically saturated. Thus, the easy direction of the magnetization corresponds to the hard direction of the susceptibility and K_1 is perpendicular to the long axis of elongate SD particles (Jackson, 1991).

Large quantities of uniaxial SD (USD) magnetite have been identified in remagnetized carbonates (e.g., Jackson & Swanson-Hysell, 2012; Calvín et al., 2018b). Plotted on a Day plot (Day et al., 1977), our data distribution falls along the SD+SP trend (Fig. 4.4A) as expected for remagnetized limestones (e.g., Channell & McCabe, 1994). On a Néel diagram (Néel, 1955; Tauxe et al., 2002), our data plot to the left of the line from the origin to USD particles with axial ratio of 1.3:1 (Fig. 4.10). The authigenic magnetite grains grew evenly and thus have small axial ratios. Because shape and grain size are major controlling factors for magnetite anisotropy, small deviations from equant grains already induce uniaxial magnetic anisotropy (Winklhofer et al., 1997; Evans et al., 2003; García-Lasanta et al., 2018). Indeed, the data plot between the cubic SD + SP trend line and USD + SP field (Fig. 4.10). Thus, the authigenic magnetite in the remagnetized limestones would give rise to an inverse magnetic fabric. It is noteworthy that the susceptibility inversely relates to the samples' paramagnetic percentage (Fig. 4.6A, B) and the anisotropy degree (P_j)

(Fig. 4.6A, C). A lower paramagnetic proportion equates with higher ferromagnetic (sensu lato) minerals, resulting in higher susceptibility. The negative correlation between susceptibility and anisotropy degree (P_j) can be attributed to the counteraction of anisotropy ellipsoids between SSD and SP magnetic grains: SSD magnetite has an inverse magnetic fabric while SP magnetite has a normal magnetic fabric, the mixing of the two magnetic fabrics results in intermediate fabrics (Ferré, 2002; Calvín et al., 2018a). When SSD particles prevail over SP particles, the total anisotropy will decrease while the orientation will remain unchanged.

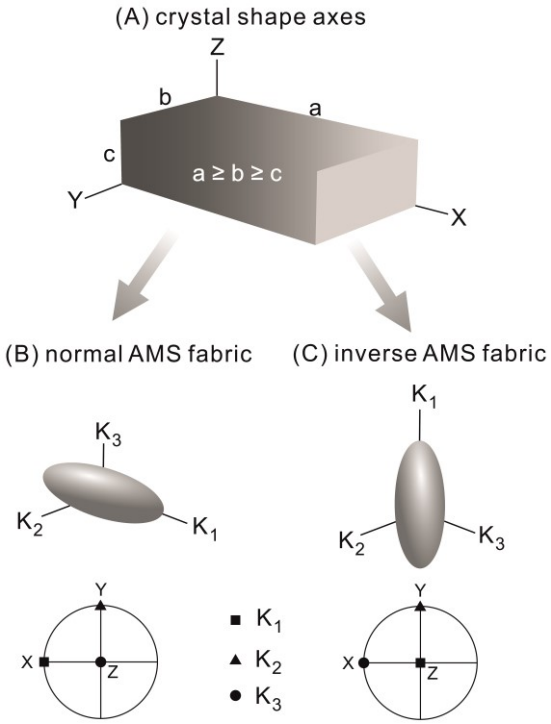

Figure 4.9 *Relationship between crystal shape axes and magnetic susceptibility principal axes modified from Ferré (2002). (A) Crystal shape axes. (B) Normal magnetic fabric. (C) Inverse magnetic fabric. The upper figure in (B) and (C) represents the magnetic susceptibility ellipsoid, the lower figure in (B) and (C) shows the orientation of the magnetic susceptibility axes (X, Y, and Z refer to the orientation of the crystal shape axes).*

Alternatively, from the geological setting point of view, the collision between India and Eurasia led to N-S shortening, which is obviously different from the direction perpendicular to the K_1 measured in the present study. Given the rotation of the Zaduo area after India-Eurasia collision (Fu et al., 2022a, chapter 2), the compression direction is more likely represented by the magnetic lineation, that is, an inverse magnetic fabric present.

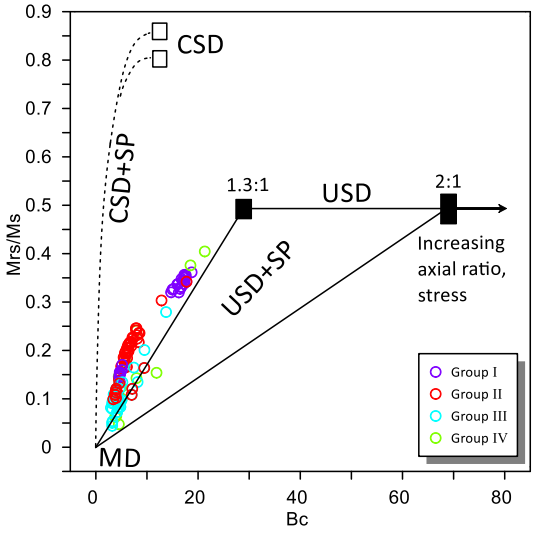

Figure 4.10. *Néel diagram (Néel, 1955) of representative samples from the four groups, with a slightly modified interpretive framework provided by Tauxe et al. (2002), USD = uniaxial single domain, CSD = cubic single domain.*

4.5.3 The behavior of the authigenic magnetite under deformation and its tectonic implications

The oxidation of iron sulfides to authigenic magnetite is interpreted to be the remagnetization mechanism in the studied carbonates (Fu et al., 2022a, chapter 2). It is conceivable that the authigenic magnetite could produce a new fabric recorded during the remagnetization, because the oxidation of iron sulfides to authigenic magnetite is not a topotactic reaction. All samples were collected from a monoclinal section, and the oblique extent of magnetic foliation with respect to bedding does not appear to be closely related to bedding variation, that is, an oblique magnetic lineation occurs. The magnetic fabric of each group is characterized by a variably oblique magnetic foliation with respect to bedding, which can be related with the sense of shear induced by flexural slip during folding (Saint-Bezar et al., 2002; Wang et al., 2017). Group IV is a typical intermediate fabric between a sedimentary fabric and tectonic fabric (Fig. 4.7D; Saint-Bezar et al., 2002; Jia et al., 2007; Wang et al., 2017; Cao et al., 2021), while groups I, II, and III imply an increasing strain from I to III. However, this feature does not follow the classic evolution from oblate ellipsoids (sedimentary fabric) to prolate (overlap of sedimentary and tectonic) and back to oblate ellipsoids (tectonic fabric) (Fig. 4.5E, Parés et al., 1999; Parés, 2015; Kanamatsu et al., 2001; McCarthy et al., 2015). Therefore, it is likely that the groups of magnetic fabric do not represent the development from sedimentary fabrics to deformation fabrics. In addition, two major events after the deposition of the Buqu formation are the Qiangtang-Lhasa collision and the India-Eurasia collision. The latter is deemed to be the most significant geological event over the last 500 million years (Yin & Harrison, 2000); any preexisting fabric record is likely to have been overprinted by the strong N-S compressional deformation.

On the other hand, studies on AMS of remagnetized carbonates indicate that the secondary remanence and the associated AMS were acquired synchronously (Sun et al., 1993; Calvín et al., 2018a). For pyrite, this process involves its isotropic microstructure and the growth of the authigenic magnetite. Small magnetite particles (nanoscale) residing in the pyrite grains (or at their cracks/surface) grew as external rims in remagnetized rocks (e.g., Suk et al., 1993; Blumstein et al., 2004; Oliva-Urcia et al., 2009; Kars et al., 2014; Calvín et al., 2018a, 2018b). Pyrite grains prevent the magnetite particles inside from being affected by the deformation. Thus, magnetite grains can form under infinitesimal strain (equivalent to the stress conditions), i.e., independentl of previous sedimentary or tectonic structures (Sun et al., 1993; Calvín et al., 2018a, 20118b). Following this rationale, the alteration of the precursor sulfides to authigenic magnetite during remagnetization is conditioned by contemporary dynamic factors, such as the compression field (Calvín et al., 2018a, 2018b). For other iron sulfides, their anisotropy should have allowed rotation by compression, and their oxidation to authigenic magnetite would accordingly record the compression field. In other words, the inverse magnetic fabric of the limestones of the Buqu Formation reflects the compression direction during remagnetization.

The accommodation of the India-Eurasia collision led to a ~20° clockwise rotation of the Zaduo area relative to Eurasia since the Paleogene (Fu et al., 2022a, chapter 2). Passive rotation of the magnetic fabric occurs during the host block rotation (Larrasoaña et al., 2004; Weil & Yonkee, 2009; Wang et al., 2017). The directions of the K_1 axis in all four groups range from ~33° to 50° and yields an overall average of 43.1° $\pm$ 6.2° (Fig. 4.7; Table 4.1). Thus, the paleo-compression direction can be restored to ~13° to 30°, with an average of 23.1° $\pm$ 6.2°, which is distinct from the present-day NEE-SWW shortening direction of ~70° from GPS data (Wang & Shen, 2020). In detail, the restored K_1 axis direction of group IV displays a nearly N-S compression (~13°), groups I and II show a ~20° compression direction, and group III shows an NNE-SSW compression direction of ~30°. This discrepancy is likely be related to measurement uncertainties and local structural 'noise'. Li et al. (2020c) provide AMS data of sediments with an age range between ~69 and 41 Ma in the central Gongjue Basin, while Xiao et al. (2021) suggest that the basin has an age between ~69 and 50 Ma. Despite disagreement on the age model in the two afore mentioned studies and the AMS interpretation for the Gongjue Basin, the overall orientation of K_1 axis is tightly clustered in NNW-SSE. The magnetic susceptibility is mainly carried by hematite, paramagnetic minerals and some magnetite, and shows a normal magnetic fabric. Their results reveal ENE-WSW tectonic compression that is normal to the K_1 axis (Li et al., 2020c; Xiao et al., 2021). There is a strong correlation between the paleomagnetic declinations and AMS K_1 declinations (Li et al., 2020c), indicating that the AMS orientation is controlled by the rotation of the Gongjue area. The magnetostratigraphic results from Li et al. (2020c) suggest a ~30°-40° clockwise rotation of the Gongjue area relative to Eurasia. The paleo-compression direction of the Gongjue area can be restored to ~35° to 45°, with an average of ~40° (Fig. 4.11B).

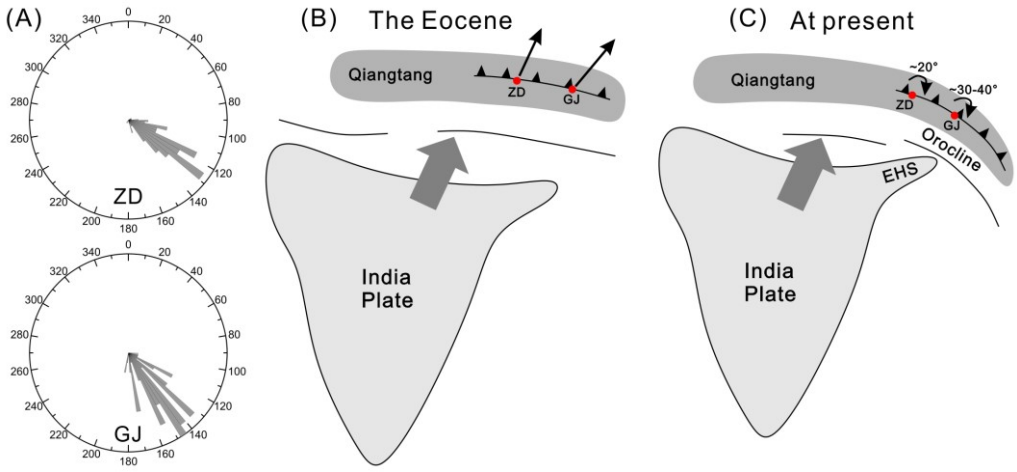

Figure 4.11 *(A) Rose diagrams of the fault strikes in the Zaduo (ZD) and Gongjue (GJ) areas. Schematic models illustrating (B) deformation of the Qiangtang Terrane in the Eocene and (C) evolution of the orocline after the late Eocene. The black arrows in (B) represent the compression directions in the Zaduo and Gongjue areas.*

The structural trend in the Zaduo and Gongjue areas can be quantified by averaging their respective regional fault strikes. 166 faults yield a structural trend of ~125° in the Zaduo area, and 79 faults produce a trend of ~145° in the Gongjue area (QGSI, 2005; XGS, 2007, Fig. 4.11A). Thus, the difference in structural trend of the two regions is ~20°, which is similar to their rotation difference (~10°-20°). However, the difference in compression direction (~30°-40°) is slightly larger. After restoration of the later rotation, an Eocene NNE-SSW compression is obtained in the Zaduo area and a NE-SW compression in the Gongjue area (Fig. 4.11B). These results likely indicate a secondary orocline around the EHS during the India-Eurasia collision. Our AMS data suggest that the India-Eurasia convergence was NNE-SSW instead of N-S, which is also in line with the moving trajectory of the Indian plate relative to fixed Eurasia (Van Hinsbergen et al., 2011; Todrani et al., 2022). The deceleration of the convergence implies a stronger resistance of Eurasia (Pusok & Stegman, 2020; Van Hinsbergen et al., 2011), which may result in regionally different compression directions (Fig. 4.11B). AMS is a very sensitive strain parameter. It may record a stress direction even when such stress has resulted in no/very limited regional rotation (Luo et al., 2013). In the north of the EHS, at least in the Qamdo region (Nangqian, Gongjue and Mangkang areas) and the Zaduo area, it is the northward compression rather than rotation that dominated the far field effect of India - Eurasia collision before the late Eocene (Xu et al., submitted). Afterwards, widespread clockwise rotation of the southeast Tibetan Plateau occurred after the late Eocene (e.g., Tong et al., 2017, 2022; Zhang et al., 2020a; Li et al., 2020b; 2020c; Todrani et al., 2022; Xu et al., submitted; Fig. 4.11C).

In summary, we have identified inverse magnetic fabrics in the Jurassic Buqu limestones that were remagnetized in the Eocene. The growth of authigenic magnetite generated both the secondary NRM and the associated AMS. Together with the AMS data from the Gongjue area, the inverse magnetic fabrics of our study provide a picture of how the orocline developed. The Eocene NNE-SSW compression in the Zaduo area and the NE-SW compression in the Gongjue area are early response to the India-Eurasia collision. This compression differentiation is likely the origin of the different rotations and structural trend surrounding the EHS.

4.6 Conclusions

The magnetic fabrics of the limestones that crop out in the Zaduo area, Eastern Qiangtang Terrane, are analyzed in 12 sites (120 specimens). The studied Jurassic rocks are reported to have been chemically remagnetized during the Cenozoic and gave rise to SSD and SP authigenic magnetite. Overall, an average low-field susceptibility of 624×10^{-6} (SI) is determined with a range between 31×10^{-6} (SI) and 1527×10^{-6} (SI). The Flinn and P_j-T diagrams show the same oblate/prolate character of the AMS principal axis distributions. Positive correlations between bulk susceptibility and remanences (i.e., K_m versus NRM, K_m versus SIRM, and K_m versus M_s) suggest that susceptibility and remanence are carried by the same mineral, that is, authigenic magnetite.

The Néel diagram reveals that the magnetite particles are likely have axial ratios less than 1.3:1, which is a controlling factor in magnetic anisotropy. The inverse magnetic fabrics are generated by these small authigenic magnetite grains, and therefore the K_1 axis is perpendicular to the long axis of the crystal. Four groups of magnetic fabrics have been differentiated according to the detailed comparison of fabrics and rock magnetic behaviors:

- Group I specimens have the highest average susceptibility of ~1200×10^{-6} (SI) and the lowest paramagnetic mineral percentage (with an average value of ~5 % and a median value of ~6 %). Their stereonet projections are characterized by K_1 being grouped and oriented NE-SW (~40°), and K_3 showing a girdle distribution.
- Group II specimens have lower average susceptibility of ~700×10^{-6} (SI), and a higher contribution of paramagnetic minerals (with an average value of ~15 % and a median value of ~11 %). The direction defined by K_1 axis (~40°) is virtually identical to that of the group I specimens but its distribution shows a wider spreading.
- Group III specimens have average susceptibility of ~400×10^{-6} (SI) and a paramagnetic mineral percentage of ~14-15 % (both the average and median values). K_1 axis of this group has a declination of ~50°, the K_3 axis is clustered around the bedding pole and perpendicular to the bedding plane.
- Group IV contains only site 2, it is characterized by the lowest average susceptibility of ~60×10^{-6} (SI) and high paramagnetic mineral percentage

(with an average of ~16 % and a median of ~11 %). The AMS principal axes coincide with those of group III but with K_1 oriented along ~33°.

Given the ~20° clockwise rotation of the study area relative to the Eurasia since the Paleogene, we interpret that the AMS documented the NNE-SSW oriented compression during remagnetization. However, an early Paleogene NE-SW compression in the Gongjue area was recorded. This inconsistency in compression is the early response to the India-Eurasia collision and results in different rotations surrounding the EHS.

Acknowledgments

This work was co-supported by the Natural Science Foundation of China (Grant 41974080), the Basic Science Center for Tibetan Plateau Earth System (CTPES, Grant 41988101-01), the Natural Science Foundation of China (Grant 42164005), the Second Tibetan Plateau Scientific Expedition Program (Grant 2019QZKK0707), the Strategic Priority Research Program of Chinese Academy of Sciences (Grant XDA20070201).

5

REMAGNETIZATION OF MAGNETITE-BEARING ROCKS IN THE ZADUO AREA, EASTERN QIANGTANG TERRANE: MECHANISM AND DIAGNOSIS

Abstract

Remagnetization is a common yet notorious phenomenon that interferes with paleogeographic reconstruction. Classical paleomagnetic field tests are helpful in detecting remagnetization but their diagnostic power is limited: remagnetization may occur before folding, the tilting age may be ambiguous, or protracted remagnetization may yield dual polarities. Rock magnetic information can provide other constraints on our understanding of the origin of natural remanent magnetization (NRM). Here we focus on the rock magnetic properties of acknowledged remagnetized limestones and unremagnetized rocks of the Zaduo area in the Eastern Qiangtang Terrane, Tibetan Plateau (China). Chemical remanent magnetization is suggested as a more frequent mechanism than the thermoviscous resetting of the NRM. Authigenic magnetite of stable single domain and superparamagnetic (SP) size forms during the acquisition of the secondary NRM. Both high-field and low-field thermomagnetic runs reveal the alteration of existing iron sulfides to magnetite in the remagnetized limestones. Remanence decay curves show that the maximum unblocking temperature of the remagnetized samples is significantly lower than that of the unremagnetized samples. Component analysis of acquisition curves of the isothermal remanent magnetization reveals a hard component that represents SP magnetite in remagnetized limestones. This component is absent in unremagnetized rocks. End-member modeling reveals a convex curve in the r^2 versus the number of end-members plot in the remagnetized limestones, while a near-linear shape occurs in the unremagnetized rocks. In addition, quantitative analysis of the hysteresis loop shape for different lithologies indicates its validity in detecting remagnetization. Furthermore, we show the differences in the hysteresis data distributions of the two rock types on the Day plot, the Néel diagram, the Borradaile diagram, and the Fabian diagram. Our research

emphasizes that rock magnetic properties can serve as tools to diagnose remagnetization in magnetite-dominated rocks. We recommend a comprehensive rock magnetic study to discriminate remagnetization, involving the Day plot, Fabian diagram, thermal demagnetization curves, IRM component analysis and end member modeling.

5.1 Introduction

A partial or complete remagnetization occurs when the natural remanent magnetization (NRM) is reset, that is, it represents a paleomagnetically younger age than the formation age of the rock under study. Resetting can occur at any time during the geological history, either pre-folding (e.g., Perroud & Van der Voo, 1984; Huang et al., 2015a; Gao et al., 2018), syn-folding (e.g., Kent & Opdyke, 1985; Huang et al., 2017a, 2017b; Ran et al., 2017) or post-folding (e.g., Stearns & Van der Voo, 1987; Liebke et al., 2013; Huang & Opdyke, 2015). Also, it can occur in any environment in which secondary magnetic minerals form, such as oxic (e.g., Van der Voo & Torsvik, 2012), sulfidic (e.g., Roberts & Weaver, 2005), or methanic environments (e.g., Weaver et al., 2002; Larrasoaña et al., 2007). The temperature range of the secondary magnetic mineral formation may vary as well from moderate to high temperatures (e.g., Kent & Opdyke, 1985, Aubourg & Pozzi, 2010; Kars et al., 2012, 2014; Appel et al., 2012; Abrajevitch et al., 2014; Meng et al., 2022). Remagnetization can seriously complicate classical paleomagnetic interpretation (Elmore et al., 2006, 2012; Jackson & Swanson-Hysell, 2012; Van der voo & Torsvik, 2012; Dekkers, 2012). Paleomagnetic studies in the Qiangtang Terrane, one of the major units in the central Tibetan Plateau (Fig. 5.1), have often yielded controversial geological interpretations. For example, the Jurassic paleolatitudes obtained from the Yanshiping Group ranges from 20-25 °N (Ren et al., 2013; Yan et al., 2016) to ~35 °N (Cao et al., 2019), or it is reported as a remagnetization for the same Group (Ran et al., 2017; Fu et al., 2022a (also chapter 2 of this thesis)). In other cases, although the position of the Qiangtang Terrane is deemed to remain quite stable during the Cenozoic, its reported paleolatitudes vary from ~ 10 °N to 30 °N (Lippert et al., 2011; Roperch et al., 2017; Zhang et al., 2018; Li et al., 2020b; Zhang et al., 2020a).

Traditional paleomagnetic field tests such as the conglomerate, reversals, baked contact, or fold test are classic techniques for diagnosing a remagnetization. However, they are not without problems: conglomerate tests are usually ambiguous; protracted remagnetization may yield dual polarity remagnetized strata (Meijers et al., 2011; Huang & Opdyke, 2015; Huang et al., 2019b; Fu et al., 2022a (chapter 2)); the exact time of folding is hard to determine in many cases and baked contacts associated with dike intrusions are not always available. In addition to the classic diagnosis of remagnetization via paleomagnetic field tests, another line of thought to identify remagnetization is associated with the mechanism of the secondary NRM acquisition. For instance, the concave shape of the thermal decay curves of the NRM and widely distributed S ratios (defined here as -IRM-0.3T/IRM1.8T with IRM standing for isothermal remanent magnetization) are used to indicate chemical remanent magnetization (CRM) in red beds (Liu et al., 2011; Jiang et al., 2015, 2017). Remagnetization in carbonates commonly raises 'wasp-waisted' hysteresis loops and the 'remagnetization trend' on the Day plot, which has been used as a fingerprint for recognition of remagnetized strata (Jackson, 1990; Channell & McCabe, 1994; McCabe & Channell, 1994; Elmore et al., 2012; Jackson & Swanson-Hysell, 2012; Van

der Voo & Torsvik, 2012). End-member modeling of IRM acquisition curves also shows great potential for detecting remagnetization (Gong et al., 2009; Van Hinsbergen et al., 2010; Meijers et al., 2011; Aben et al., 2014, Huang et al., 2015a; Fu et al., 2022b (chapter 1)).

In the Zaduo area of the Eastern Qiangtang Terrane, the Permo-Triassic tuff and rhyolite and the Cretaceous granites are reported to retain a primary NRM residing in magnetite (Guan et al., 2021; Fu et al., 2022b (chapter 1)), while the Carboniferous and the Jurassic limestones have a secondary remanence also residing in magnetite (Fu et al., 2022a (chapter 2); Yu et al., 2022b). The remagnetized characteristic remanent magnetization (ChRM) is residing in stable single domain (SD) and cogenetic superparamagnetic (SP) grains of authigenic magnetite, which is absent in the samples with a primary NRM. The difference provides a good opportunity to compare differences in the magnetic properties between remagnetized and unremagnetized rocks, in which magnetite dominates the magnetic carriers.

Here, we present the results of a detailed rock magnetic study. We test differences in unblocking temperature spectra and decay curves of AF demagnetization. The behavior of both low-field and high-field thermomagnetic runs of selected samples is also evaluated. In addition, IRM, component analysis of IRM, end-member modeling of IRM and first-order-reversal-curve (FORC) diagrams are used to depict the magnetic characteristics. We also quantitatively describe the hysteresis loop shape of representative samples. Next to the classic Day plot, alternative diagrams are used to illustrate the domain state, including the Néel diagram, the Borradaile diagram and the Fabian diagram. We evaluate the acquisition mechanisms of the CRM in carbonates, and the difference of hysteresis properties in various rock units. Finally, we summarize the magnetic characteristics of the remagnetized rocks and propose how to diagnose the CRM in these rocks. This paper aims to assess the feasibility of rock magnetic property-based approaches to unveil remagnetization; they can be used in conjunction with paleomagnetic field tests but also in a stand-alone fashion, i.e., without directional paleomagnetic information.

5.2 Geological setting, previous paleomagnetic investigations, and sampling

The Zaduo area is located in the Eastern Qiangtang Terrane (also known as Northern Qiangtang Terrane), which is bounded by the Longmu Tso-Shuanghu Suture Zone in the south and the Jinshajiang Suture Zone in the north (Fig. 5.1). It is a transitional area where the structural trend gradually deflects from an approximately E-W orientation more to the west to a N-S orientation in the southeast. The opening and closure of the Paleo-, Meso-, and Neo-Tethys Oceans were recorded by the sedimentary successions in this area (QGSI 2005, 2014; Guan et al., 2021; Fu et al., 2022a (chapter 2), 2022b (chapter 1)).

The sedimentary successions mainly consist of the Lower Carboniferous Zaduo Group (C_1Z), the Upper Carboniferous Jiamainong Group (C_2J), the Middle Permian Kaixinling Group, the Late Permian to Early Triassic Gadikao Formation (P_3-T_1gd), the Middle Triassic Jielong Formation (T_2j), the Upper Triassic Jiezha Group, the Middle-Upper Jurassic Yanshiping Group, the Upper Cretaceous Fenghuoshan Group, and several Cenozoic formations (QGSI 2005, 2014; Fig. 5.1). Detailed stratigraphic descriptions of each formation in these groups are provided in the supporting information. Four angular unconformities are present: 1) between T_2j and the Upper Triassic Jiapila Formation (T_3jp); 2) between the Upper Triassic Bolila Formation (T_3b) and the Middle Jurassic Quemocuo Formation (J_2q); 3) between the Late Jurassic Xiali Formation (J_3x) and the Cretaceous Cuojuri formation (Kc), and 4) between the Cretaceous Luolika formation (Kl) and the Paleogene Tuotuohe formation (Et) (QGSI 2005, 2014; Fig. 5.1).

Tuff and rhyolite samples of the Gadikao Formation straddling the Permo-Triassic boundary were processed as well. Zircon U-Pb geochronologic study constrains their age to ~254-248 Ma (Guan et al., 2021). Rock magnetic analyses suggest that SD to pseudo-single domain (PSD) magnetite is the main magnetic carrier, and the positive fold and reversals tests support a primary origin of the NRM (Guan et al., 2021). A second target is the ~126Ma Cretaceous Zaduo granite where microscopic and rock magnetic results support a primary remanent magnetization acquired during its cooling albeit without support of paleomagnetic field tests (Fu et al., 2022b (chapter 1)). In contrast, paleomagnetic results of the limestones of the Jurassic Buqu Formation show that their primary NRM was overprinted by a CRM during the Paleogene, although the samples pass the reversals test (Fu et al., 2022a (chapter 2)). Similarly, the Lower Carboniferous Zaduo Group limestones (C_1Z_2) were reported to be remagnetized after the India-Eurasia collision (Yu et al., 2022b). In the present study, we focus on rock magnetically discriminating the remagnetized limestone samples and unremagnetized volcanic samples that possess magnetite as the dominant magnetic carrier. The paleomagnetism is largely a reassessment of existing data for the required framework while the rock magnetism is novel data. At least one sample from each site was randomly picked representing all possible lithologies of a given formation. Then, these samples were subjected to rock magnetic experiments.

Figure 5.1 (next page). *(A) Simplified tectonic map of the Tibetan Plateau and its adjacent regions. The abbreviations of the tectonic units are EQT: Eastern Qiangtang Terrane; WQT: Western Qiangtang Terrane. (B) Geological map of the Zaduo area [modified from the 1:250 000 Zaduo County regional geological map (I46C004004) by the Qinghai Geological Survey Institute (QGSI) 2005]. The abbreviations of the tectonic units are Gr: Group; Fm: Formation.*

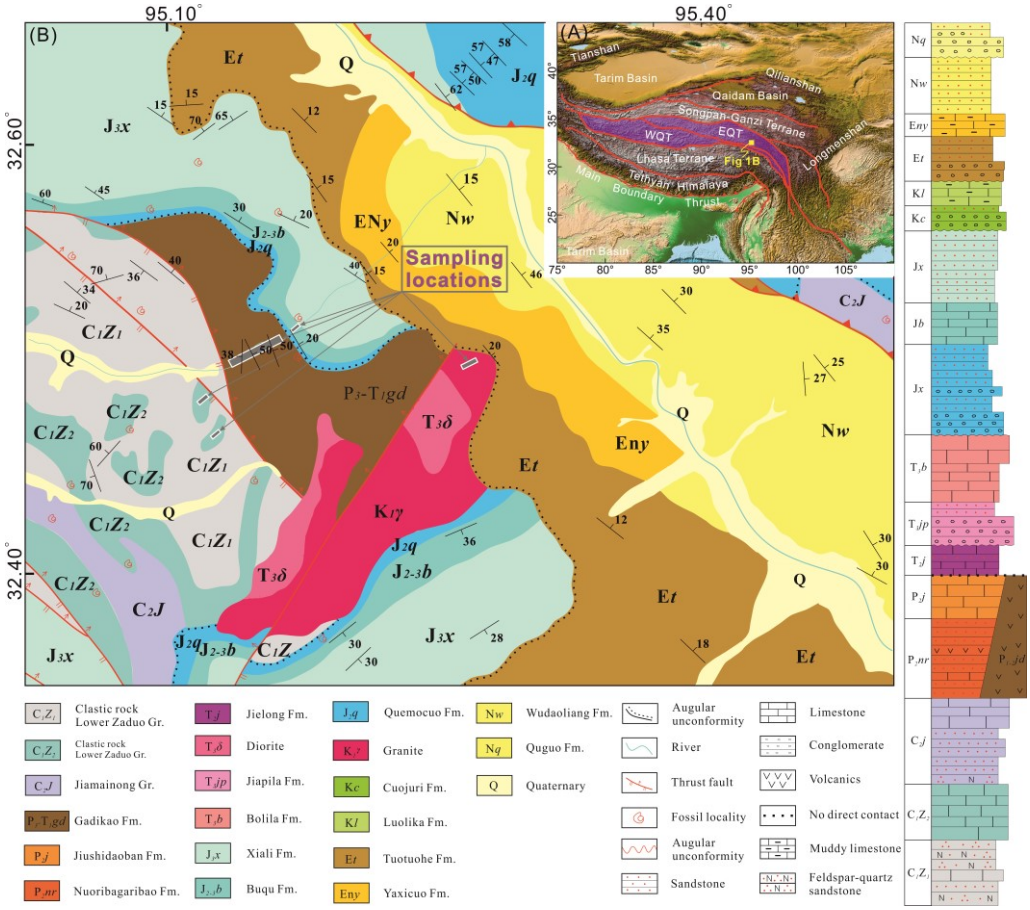

5.3 Demagnetization behavior of the NRM

Both AF and thermal demagnetization were performed to isolate the ChRM directions in each lithology; consistent directions were obtained (Guan et al., 2021; Fu et al., 2022a (chapter 2), 2022b (chapter 1); Yu et al., 2022b). For most of the remagnetized limestones, a stable single component decaying linearly to the origin below~140 mT or ~450-500 °C was obtained (Fig. 5.2). Only specimens of two Jurassic limestone sampling sites show two components, of which the high-field (temperature) component has a reverse ChRM. The remagnetized ChRM of the Jurassic limestones has a positive reversals test (Fu et al., 2022a (chapter 2)). All of the Carboniferous limestones have a single component that fails to pass the fold test (Yu et al., 2022b).

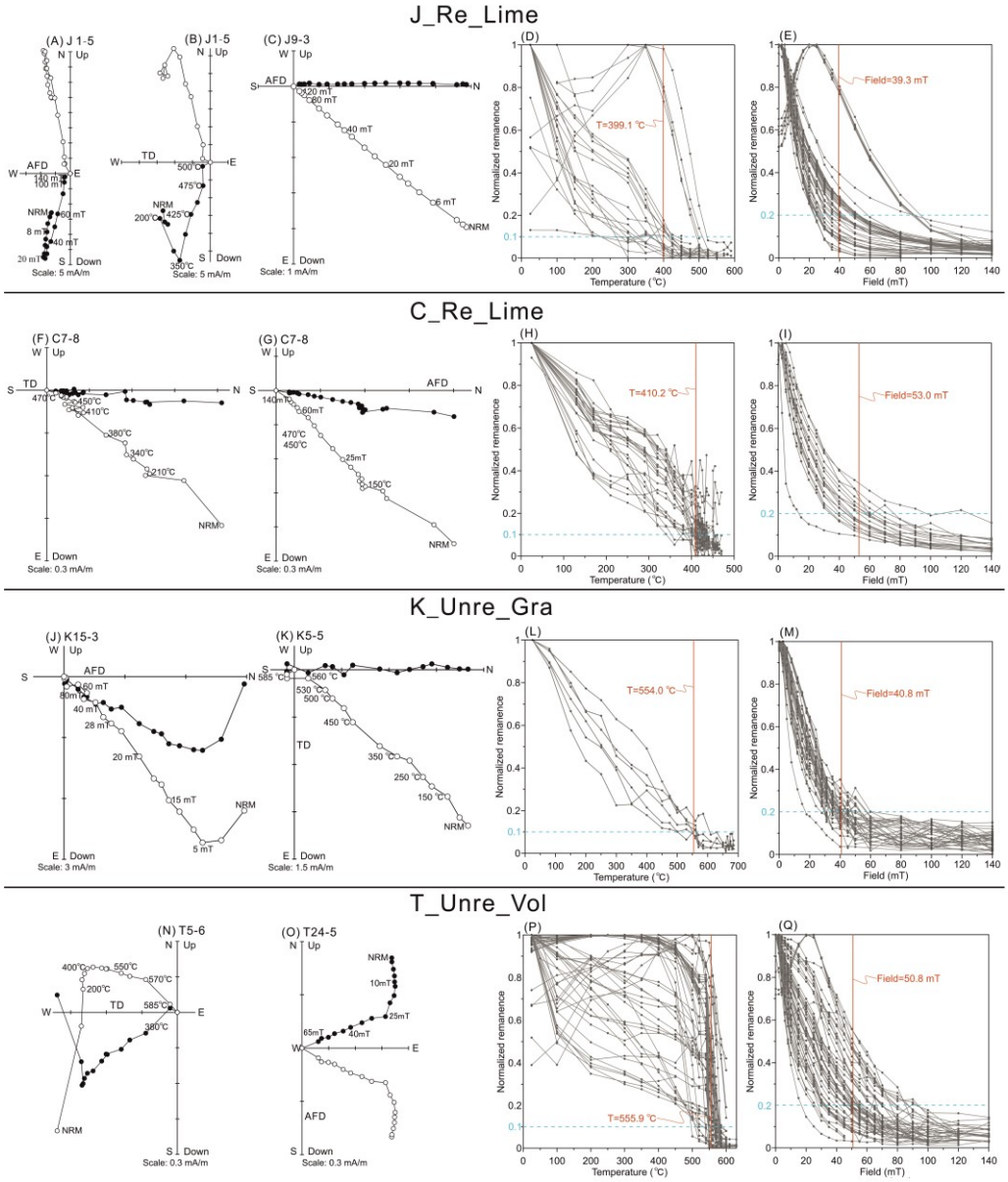
J_Re_Lime
(A) J 1-5
(B) J1-5
(C) J9-3
(D)
(E)
T=399.1 ℃
Field=39.3 mT
C_Re_Lime
(F) C7-8
(G) C7-8
(H)
(I)
T=410.2 ℃
Field=53.0 mT
K_Unre_Gra
(J) K15-3
(K) K5-5
(L)
(M)
T=554.0 ℃
Field=40.8 mT
T_Unre_Vol
(N) T5-6
(O) T24-5
(P)
(Q)
T=555.9 ℃
Field=50.8 mT
Normalized remanence
Temperature (℃)
Field (mT)

Figure 5.2 (previous page). Demagnetization *trajectories of representative samples in geographic coordinates and corresponding normalized remanence decay curves of the (A-E) Jurassic limestones, the (F-I) Carboniferous limestones, the (J-M) Cretaceous granites and the (N-Q) Permo-Triassic tuff and rhyolite samples. In the Zijderveld diagrams (Zijderveld, 1967), solid (open) symbols represent positive (negative) inclination. In the thermal demagnetization decay curves, the vertical red solid lines represent the average temperatures at which 10% of the remanence is remaining in these samples. In the alternating field demagnetization decay curves, the vertical red solid lines represent the average field at which 20% of the remanence is remaining in these samples. J_Re_Lime: remagnetized Jurassic limestones; C_Re_Lime: remagnetized Carboniferous limestones; K_Unre_Gra: unremagnetized Cretaceous granites; T_Unre_Vol: unremagnetized Permo-Triassic volcanic (tuff and rhyolite) samples. The limestones are remagnetized (Fu et al., 2022a (chapter 2); Yu et al., 2022b); the volcanic samples are unremagnetized (Guan et al., 2021; Fu et al., 2022b (chapter 1)).*

The unremagnetized Cretaceous volcanic samples are classified into two types: Type one samples with stable magnetization behavior, and Type two samples which show gyro-remanent magnetization (GRM) (Fu et al., 2022b (chapter 1)). Thus, we mainly focus on the Type one samples that have a single component of normal polarity up to 585 °C or ~40-60 mT. Most of the Gadikao Formation volcanic specimens have two components: a low-field (temperature) viscous overprint demagnetized up to 150-200 °C or 6-20 mT, and a high-temperature (field) component that is decaying linearly towards the origin isolated from ~200-450 °C to 580 °C or from ~8 to 60 mT. The high-temperature (field) component is dual polarity and passes both fold and reversals tests (Guan et al., 2021).

Typical thermal decay curves of the magnetite-dominated samples lost the majority of their NRM near ~585 °C (Van Velzen & Zijderveld, 1992; Shcherbakova & Shcherbakov, 2000; Dunlop & Özdemir, 2000). The remagnetized limestones show different characteristics in that ~90% of the NRM is lost below ~500 °C (Fig. 5.2D, H). In particular, many Jurassic limestone samples drop to ~20% of the starting value below ~400°C (Fig. 5.2D). The average temperature at which 10% of the remanence is remaining is ~410 °C (Fig. 5.2D, H). Some of the samples drop their magnetization quickly at low temperatures (< ~200°C), leading to slightly concave thermal decay curves (Fig. 5.2D, H). In contrast, the unremagnetized volcanic samples drop their magnetization linearly and the thermal demagnetization curves are slightly linear-convex. The average temperature at which 10% of the remanence is remaining is ~560 °C (Fig. 5.2L, P). In terms of the AF demagnetization, both limestones and volcanic samples show convex decay curves (note: the Carboniferous limestones were thermally demagnetized to 250 °C followed by AF demagnetization to ~140 mT). However, the unremagnetized volcanic samples lost ~80% of their NRM at ~ 30-50 mT, while the remagnetized limestones lost a similar proportion of the NRM

between ~ 30 and 100 mT.

5.4 Rock Magnetism

5.4.1 Thermomagnetic runs

Both low-field thermomagnetic runs (susceptibility versus temperature, i.e., χ-T) and high-field thermomagnetic runs (magnetization versus temperature, i.e., M-T) were carried out on representative samples. The low-field thermomagnetic runs were done on a MFK1-FA Kappabridge instrument and a CS-4 high-temperature furnace (AGICO, Czech Republic); the measurement was performed in an argon atmosphere and with a flow rate of 100 mL/min. Stepwise thermomagnetic runs with maximum temperatures of 250, 350, 400 (for some samples), 450, 550, 620, and 700 °C were applied with intermittent cooling to room temperature. The high-filed thermomagnetic runs were conducted using an in-house-built horizontal translation type Curie balance with a sensitivity of ~5 × 10^{-9} Am^2 (Mullender et al., 1993), following the procedure described in Fu et al. (2022a). The successive heating and cooling steps are 250, 150, 350, 250, 450, 350, 520, 420, 620, 500 and 700 °C.

χ-T curves of the remagnetized limestones show a sharp decrease from ~500 to 580 °C and the heating and corresponding cooling cycles are nearly reversible below ~400 °C, which points to magnetite as the main magnetic mineral. However, both the magnetite formed during heating and pre-existing magnetite can produce such features, and magnetite has a very strong susceptibility which overshadows signals of other magnetic minerals. The sharp increase from ~420 °C shows the oxidation of pyrite to magnetite. It is likely that greigite is not present in these samples, because previous studies have shown that some greigite has a Hopkinson peak at~240 to 250 °C followed by a decrease in susceptibility above 250 °C in χ-T curves (Roberts et al., 2011). The most evident irreversibility between the heating-cooling curves occurs in the cycles of 450 to 620 °C, indicating the transformation of weakly magnetic minerals to strongly magnetic minerals (i.e., pyrite transforms to magnetite).

In the high-field thermomagnetic runs (M-T runs), the magnetization gradually decreases from room temperature to ~410 °C, followed by a sharp increase from ~410 to 450 °C and the subsequent cooling segment. Greigite and pyrrhotite do not show up by their alteration behavior in high-field thermomagnetic runs in argon (Dekkers et al., 2000). But in air, greigite begins to break down to form pyrrhotite and pyrite at temperatures above ~320 °C (Roberts, 1995), while pyrrhotite is largely stable below ~320 °C (Torii et al., 1996). The discontinuity in the final cooling curves at ~320 °C may indicate pyrrhotite formed during the experiment (Fig. 5.3B, D, F and H).

Most of the heating-cooling curves of the unremagnetized samples are quasi-reversible, except for some high temperature cycles (i.e., 620 °C or 700 °C) (Fig. 5.3I-P). An abrupt drop in susceptibility occurs between ~ 550 °C and 580 °C after

increasing moderately from room temperature to ~550 °C, revealing typical magnetite behavior. A similar decline is observed in the high-field thermomagnetic runs (Fig. 5.3J, L, N and P). The difference is that the magnetization continues to decline at temperatures below ~550 °C. The ~620 °C and 700 °C cooling curves end with higher

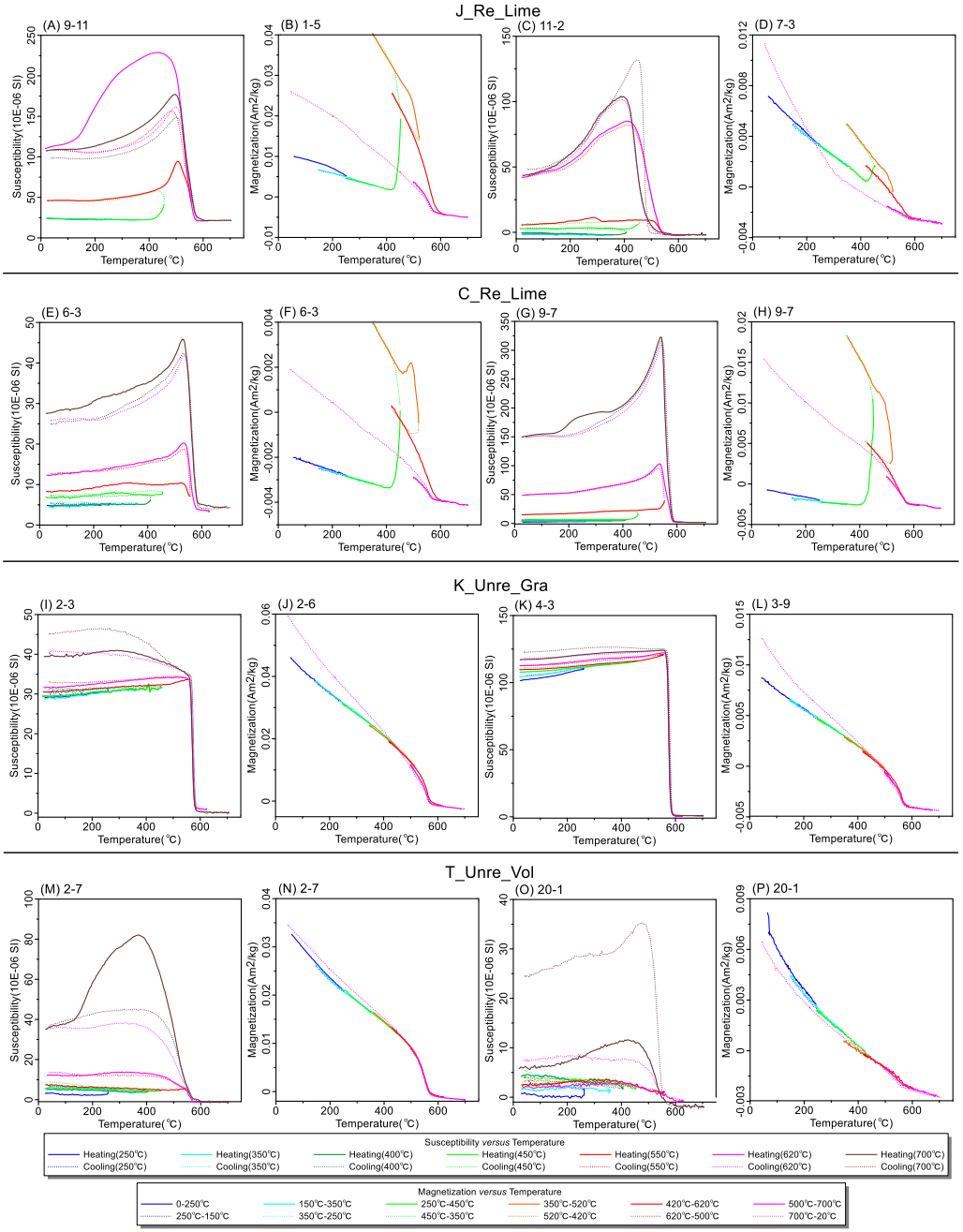

Figure 5.3 (previous page). Multicycle *high-temperature magnetic susceptibility curves (A, C, E, G, I, K, M and O) measured on Kappabridge KLY3-CS and high-field thermomagnetic runs (B, D, F, H, J, L, N and P) measured on a Curie balance for representative samples. Solid (dashed) lines indicate the heating (cooling) curves. J_Re_Lime: remagnetized Jurassic limestones; C_Re_Lime: remagnetized Carboniferous limestones; K_Unre_Gra: unremagnetized Cretaceous granites; T_Unre_Vol: unremagnetized Permo-Triassic volcanic (tuff and rhyolite) samples.*

susceptibility than their heating curves, indicating that some magnetite is formed after 620 °C (Fig. 5.3I) and 700 °C (Fig. 5.3I and J). The remarkable differences between Fig. 5.3M and Fig. 5.3N indicate substantial changes in susceptibility while essentially no changes in magnetization. This points to structural changes within existing (titano)magnetite that are foremost detectable by magnetic susceptibility and much less so with magnetization. The same goes to a lesser extent with Fig. 5.3O and Fig. 5.3P (some magnetite is removed in Fig. 5.3P). Another noteworthy point is that all the samples show a continuous but gradual descent from ~580 °C to 700 °C in the high-field thermomagnetic runs, which is not present in the low-field thermomagnetic runs. We interpret the difference to be associated with the much larger field used in M-T experiments which generates a larger paramagnetic moment above magnetite's Curie temperature, the presence of hematite is unlikely because no discontinuity at ~675 °C is observed.

5.4.2 IRM acquisition curves and coercivity component analysis

A total of over 260 IRM acquisition curves were measured (a large number of data is required for End-member modelling, see section 5.4.6 for more details). The IRM acquisition curves of remagnetized and unremagnetized samples show subtle differences as previous studies have documented (Guan et al., 2021; Fu et al., 2022a (chapter 2), 2022b (chapter 1); Yu et al., 2022b). The IRMs increase rapidly at low fields (below ~100-150 mT) and reach ~80-90% saturation at fields below 200 mT (Fig. 5.4), implying that a soft magnetic phase such as magnetite is the major remanence carrier. However, some IRM acquisition curves of the remagnetized samples show a gentle increase after reaching ~80-90% of the maximum IRM and do not seem to fully saturate at the maximum field of 0.5 or 1.0 Tesla (Fig. 5.4B-D). In contrast, the IRMs of the unremagnetized igneous samples are almost saturated at 300 mT (Fig. 5.4E-H). To semi-quantitatively estimate the contributions of different magnetic minerals to the net magnetization, we applied IRM component analysis to both remagnetized and unremagnetized samples following the cumulative log-Gaussian approach (Kruiver et al. 2001). In general, the acquisition curves can be fit by four IRM components (from magnetically soft to hard): component 1 with $B_{1/2}$ (the field at which half of saturation isothermal remanent magnetization (SIRM) is reached) of a few milli-Tesla and dispersion parameter (DP) of ~0.2-0.3 (log units); component 2 with $B_{1/2}$ of ~10 mT and DP of ~0.2-0.3; component 3 with $B_{1/2}$ of tens of milli-Tesla and DP of ~0.3; and a hard component 4 with $B_{1/2}$ of >300 mT even up to ~800 mT and DP of ~0.2-0.3 (Fig.

5.4 and supporting information Table S5.1).

All four components are needed to fit the measured IRM acquisition curves of remagnetized limestones (Fig. 5.4A-D). Component 1 is magnetically very soft and contributes ~10-20% to the SIRM. It is only required to fit the left-skewed distribution in the software and are generally interpreted to be the result of thermally activated component 3 (Egli, 2004; Heslop et al., 2004; Huang et al., 2015a). Component 2 is likely to stand for slightly larger but still soft quasi-SP particles. Component 3 is the major magnetic carrier and contributes >~80% to the SIRM, representing the magnetite. Component 4 does not saturate in the highest field available and has a ~5% contribution to the SIRM. Because these is no large decay at ~120 °C and ~680 °C (Fig. 5.3), the presence of goethite and hematite can be ruled out. It usually represents very fine-grained magnetite in the samples that do not contain hematite or goethite (Gong et al., 2009).

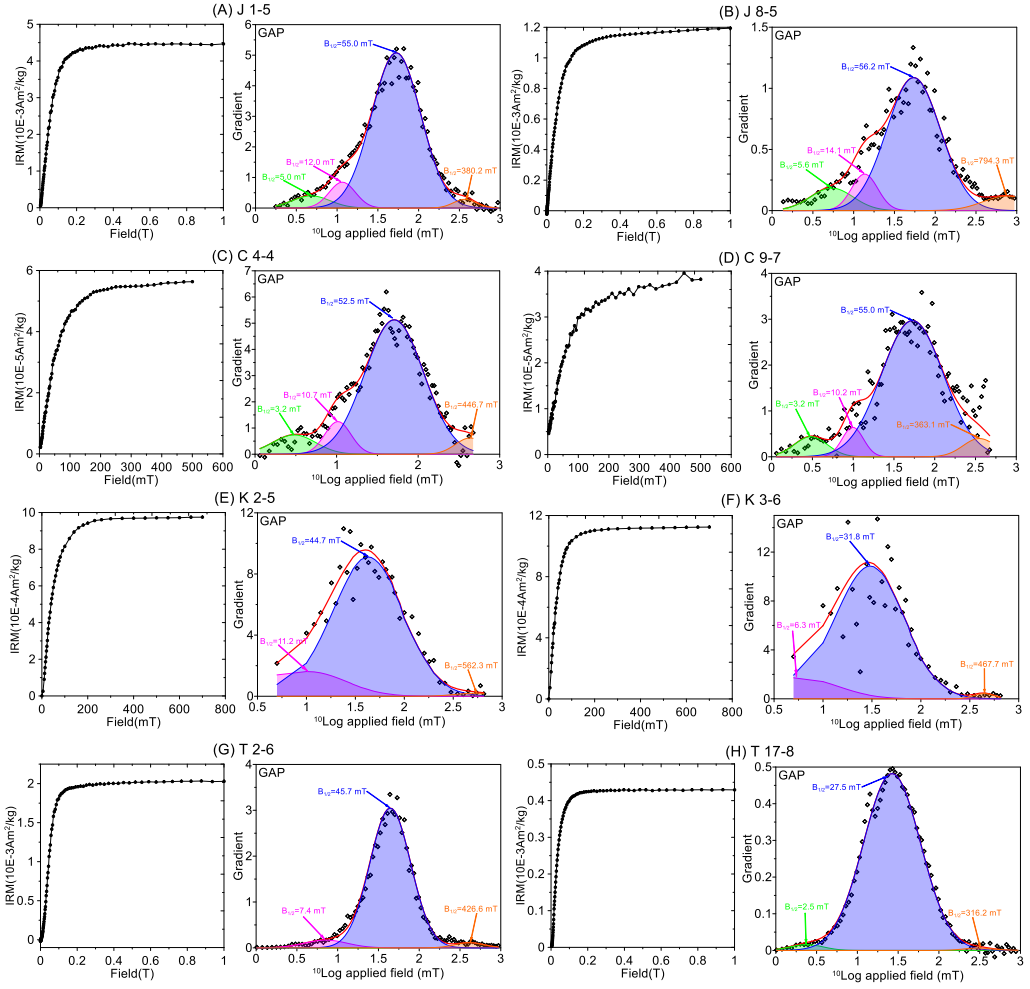

Figure 5.4 (previous page). *IRM acquisition curves and IRM component analysis plots (Kruiver et al. 2001) of representative samples of the (A-B) Jurassic limestones, the (C-D) Carboniferous limestone, the (E-F) Cretaceous granites and the (G-H) Permo-Triassic Tuff and rhyolite samples. The limestones are remagnetized; the volcanic samples are unremagnetized. GAP: gradient acquisition plot.*

The four IRM components are interpreted along the same lines in the unremagnetized volcanic samples. One component is required to fit the left-skewed distributions and component 3 has a higher contribution to the SIRM (Fig. 5.4E-H). The most striking feature is that component 4 has a negligible contribution of only <1% to the SIRM in these unremagnetized volcanic samples, indicating the absence of the very fine-grained magnetite.

Taken together, despite a sharp increase of all the IRM acquisition curves at low field, many remagnetized samples are not fully saturated in high fields. Detailed IRM component analysis reveals a hard component in remagnetized limestones, which generally represents very fine-grained magnetite. However, this component is virtually absent in unremagnetized volcanic samples.

5.4.3 Quantification of hysteresis loop shape and contributions from paramagnetic and ferromagnetic minerals

The overall shape of hysteresis loops results from the aggregate behavior of multiple coercivities. To compare the hysteresis properties of the remagnetized and unremagnetized rocks, approximately 200 hysteresis loops (100 Jurassic limestones, 60 Carboniferous limestones, 20 Cretaceous granites and 20 Permo-Triassic tuff and rhyolite samples) were measured using a Lakeshore 8600 Vibrating Sample Magnetometer (VSM) at the Institute of Tibetan Plateau Research, Chinese Academy of Sciences (ITPCAS, Beijing, China). The measurements were conducted at room temperature in a maximum applied field of 1 T (for the Jurassic limestones) or 0.5 T (for the remaining samples) with an average increment of 5-10 mT and an averaging time of 0.3 s. In addition, 70% automatic slope adjustment was selected for the high-field paramagnetic correction. Hysteresis loops of Jurassic and Carboniferous limestones have similar characteristics: a typical 'wasp-waisted' shape with coercive force (B_c) ranging from ~5-20 mT (Fig. 5.5 A-H). The hysteresis loops of the Cretaceous granites have very small B_c values (<3 mT) and therefore narrow, even linear shapes. For the Permo-Triassic tuff and rhyolite samples, the paramagnetic correction required is higher and narrow hysteresis loops of typical SD/PSD magnetite emerge.

Hysteresis shape 'anomalies', such as 'potbellied' or 'wasp-waisted' shapes, are frequently interpreted as hinting at SP particles or coercivity populations with distinct coercivity spectra (Wasilewski, 1973; Tauxe et al., 1996; Fabian, 2003; Jackson & Swanson-Hysell, 2012). To quantitatively evaluate the hysteresis shape of these

samples, we adopted the method of Fabian (2003) who defined the hysteresis parameters r_{hys} and σ_{hys} as follows:

$$r_{hys} = \frac{E_{hys}}{4M_sB_c}$$

$$\sigma_{hys} = \log\left(\frac{E_{hys}}{4M_sB_c}\right)$$

where E_{hys} is the total area between the two hysteresis branches, M_s and B_c are the saturation magnetization and coercive force, respectively (Fig. 5.6). For a hypothetical ideal loop, r_{hys} = 1 and σ_{hys} = 0. 'Wasp-waisted' loops have $E_{hys} > 4M_sB_c$ and accordingly $r_{hys} > 1$, and $\sigma_{hys} > 0$ and 'potbellied' loops $E_{hys} < 4M_sB_c$, $r_{hys} < 1$, and $\sigma_{hys} < 0$. A total of 63 smooth hysteresis loops were selected randomly from the four formations (22 for the Jurassic, 12 for the Carboniferous, 17 for the Cretaceous and 12 for the Permo-Triassic). As shown in Fig. 5.7 (Table S5.2), all the hysteresis loops of remagnetized samples have $r_{hys} > 1$ and $\sigma_{hys} > 0$, supporting a 'wasp-waisted' shape. In contrast, for the majority of unremagnetized samples, $r_{hys} < 1$ and $\sigma_{hys} < 0$. It is worth noting that the remainder of the unremagnetized samples have $r_{hys} < \sim 1.4$ and $\sigma_{hys} < \sim 0.1$, which is significantly less than those of the remagnetized samples (Fig. 5.7, Table S5.2).

To assess the relative content of the paramagnetic and ferromagnetic fractions of our samples, we analyzed the slope of the hysteresis loops. A hysteresis loop consists of a descending branch $M^+(H)$ and an ascending branch $M^-(H)$ (Fig. 5.6). The 'induced hysteretic' magnetization $M_{ih}(H)$ is defined as

$$M_{ih}(H) = \frac{M^+(H) + M^-(H)}{2}$$

in Fabian & Von Dobeneck (1997). The paramagnetic contribution can be obtained from the high-field slope in $M_{ih}(H)$ before slope-correction. The low-field slope represents the joint contribution of both the paramagnetic and ferromagnetic phases.

A total of 118 hysteresis loops were analyzed, while the remainder were excluded for further analysis due to noisy signal. The paramagnetic content of the 60 Jurassic limestones ranges from 0 to 60.3%, with an average of 12.6% and a median of 10.4%; the 21 Carboniferous limestones range from 0 to 48.4%, with an average of 19.4% and a median of 15.0%; the 20 Permo-Triassic volcanic samples range from 6.5% to 86.1%, with an average of 46.9% and a median of 53.5% and the 17 Cretaceous granites range from 0.8% to 61.5%, with an average of 11.5% and a median of 3.3%. Samples with 0 paramagnetic content are probably due to the paramagnetism and diamagnetism cancelling each other out. The remagnetized limestones have similar contributions from paramagnetic minerals, whereas the unremagnetized rocks have variable paramagnetic contributions (Fig. 5.8, Table S5.3). The granite is classified as S-type

with crustal affinity (QGSI, 2005; QGSI, 2014; Fu et al., 2022b), while the volcanic samples were collected from the rhyolite dacite flows and tuff layers (Guan et al., 2021); magnetic mineral amounts vary and result in correspondingly variable paramagnetic contributions.

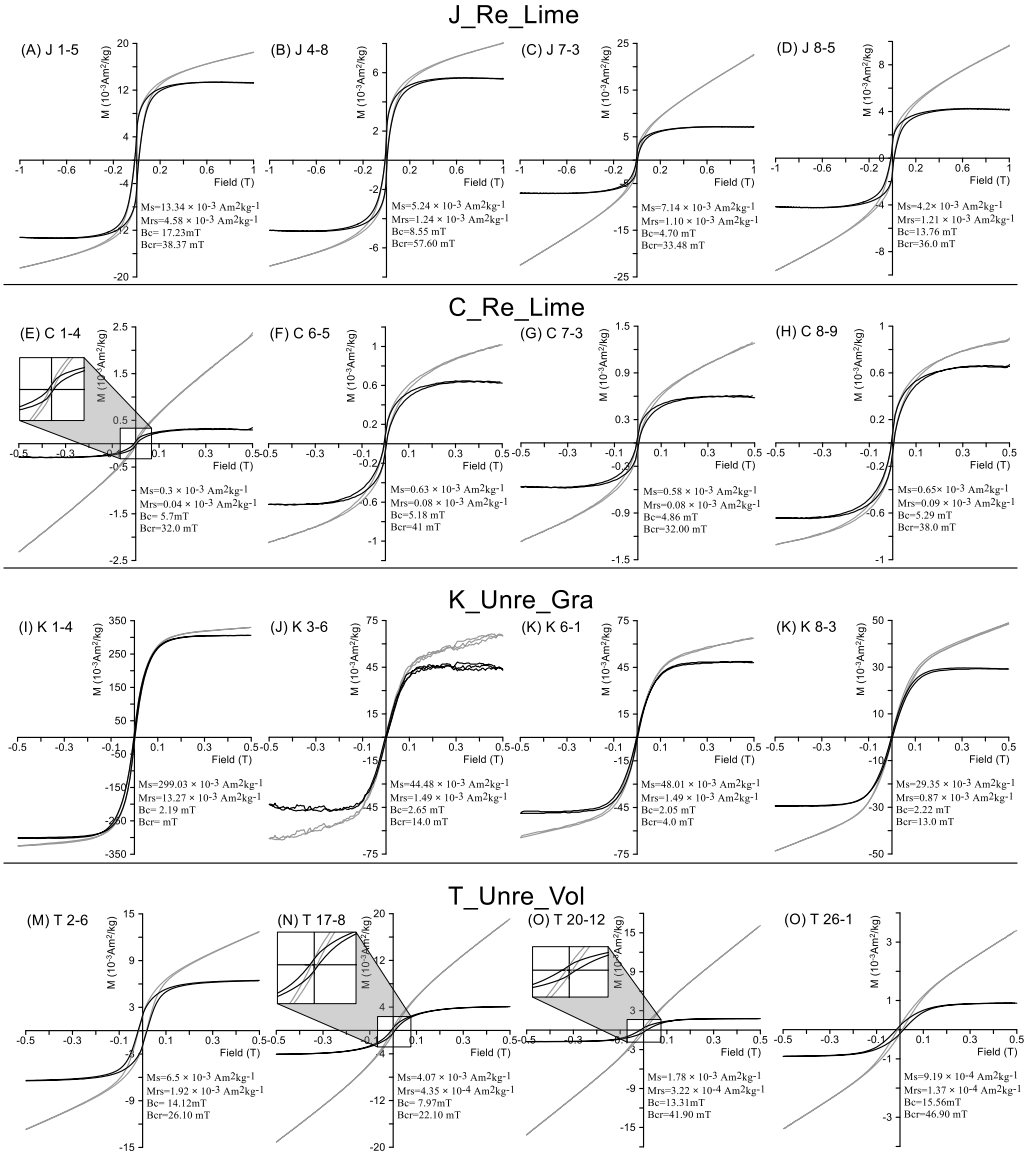

Figure 5.5. *(A-O) Hysteresis loops of representative samples. The grey and black loops are before and after correcting for the paramagnetic contribution; M_s, saturation magnetization; M_{rs}, saturation remanence; B_c, coercive force; B_{cr}, remanent coercive force on each panel (obtained from backfield demagnetization of saturation IRM).*

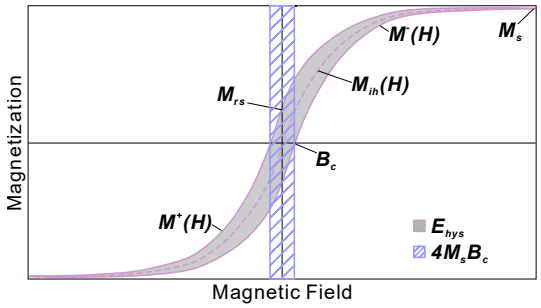

Figure 5.6. *Hysteresis loop of a ferromagnetic substance. $M^+(H)$ represents the descending branch and $M^-(H)$ represents the ascending branch of the hysteresis loop. The induced hysteretic magnetization curve $M_{ih}(H)$ can be calculated by subtracting the two branches. The coercivity parameters B_c, M_s and M_{rs} denote coercive force, saturation magnetization and saturation remanence. E_{hys} represents the total area between the descending and ascending branches. $4M_sB_c$ represents the rectangular area with height $2M_s$ and width $2B_c$.*

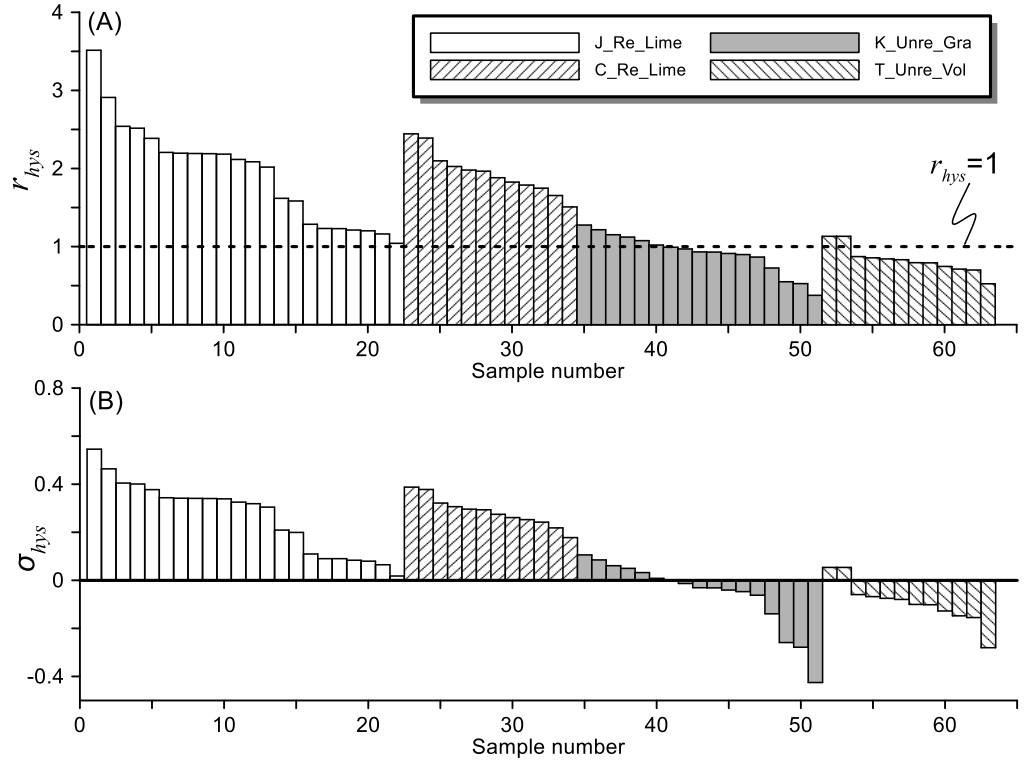

Figure 5.7. Histograms *showing the hysteresis parameters (A) r_{hys} and (B) σ_{hys} in the remagnetized limestones and the unremagnetized volcanic rocks. For a 'wasp-waisted' loop, $r_{hys} > 1$ and $\sigma_{hys} > 0$; for a 'potbellied' loop, $r_{hys} < 1$, and $\sigma_{hys} < 0$; for a hypothetical ideal loop, $r_{hys} = 1$ and $\sigma_{hys} = 0$. Sorted by the value of the r_{hys} and σ_{hys} (from the largest to the smallest).*

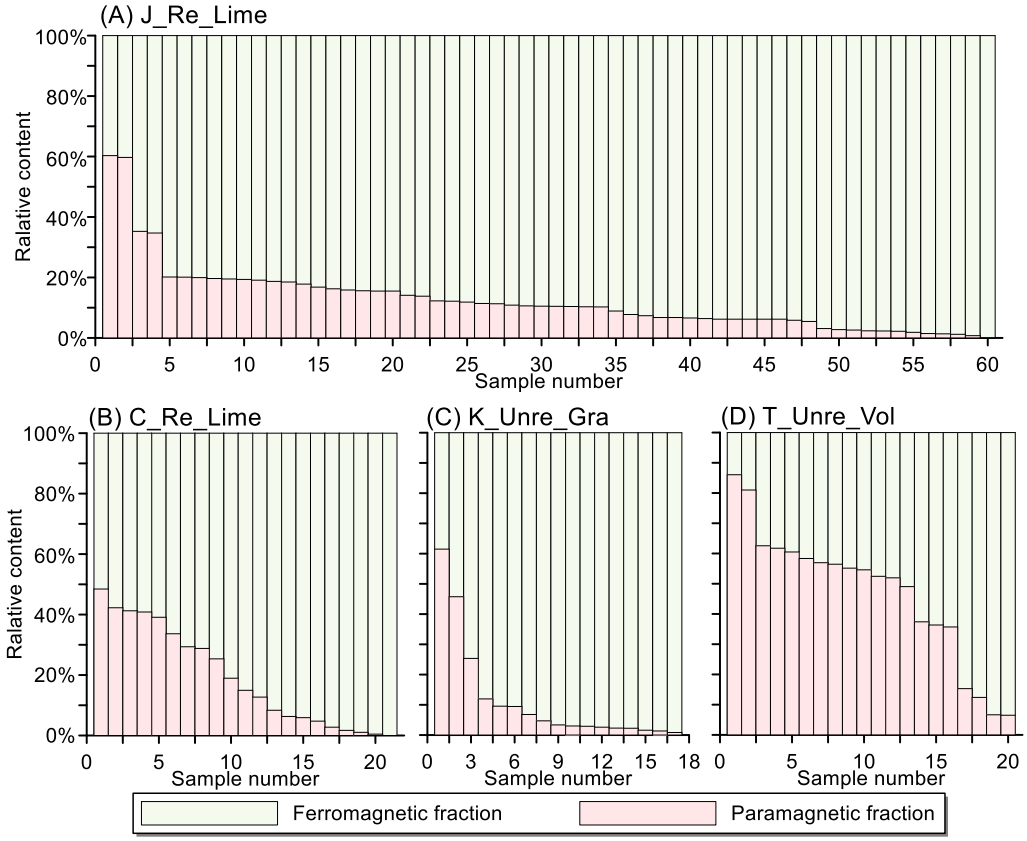

Figure 5.8. *The relative percentage of paramagnetic and ferromagnetic contributions of representative samples of the remagnetized and unremagnetized collection. J_Re_Lime: remagnetized Jurassic limestones; C_Re_Lime: remagnetized Carboniferous limestones; K_Unre_Gra: unremagnetized Cretaceous granites; T_Unre_Vol: unremagnetized Permo-Triassic volcanic (tuff and rhyolite) samples. Sorted by the relative content of the paramagnetic fraction (from the largest to the smallest).*

5.4.4 FORC diagrams

FORC diagrams of at least eight representative samples for each formation were measured with a Lakeshore 8600 Vibrating Sample Magnetometer (VSM) in ITPCAS (Beijing, China). The saturation field is 1 T and the field step size is 4 mT with an averaging time of 0.5 s. Over 100 curves were obtained for each sample at room temperature. The FORC diagrams displaying the magnetic interaction field (B_u) and the coercivity distribution (B_c) of the magnetic mineral assemblages (Roberts et al., 2014), were generated by the FORCinel software (v1.18) with an optimum smoothing factor (SF) (Harrison & Feinberg, 2008).

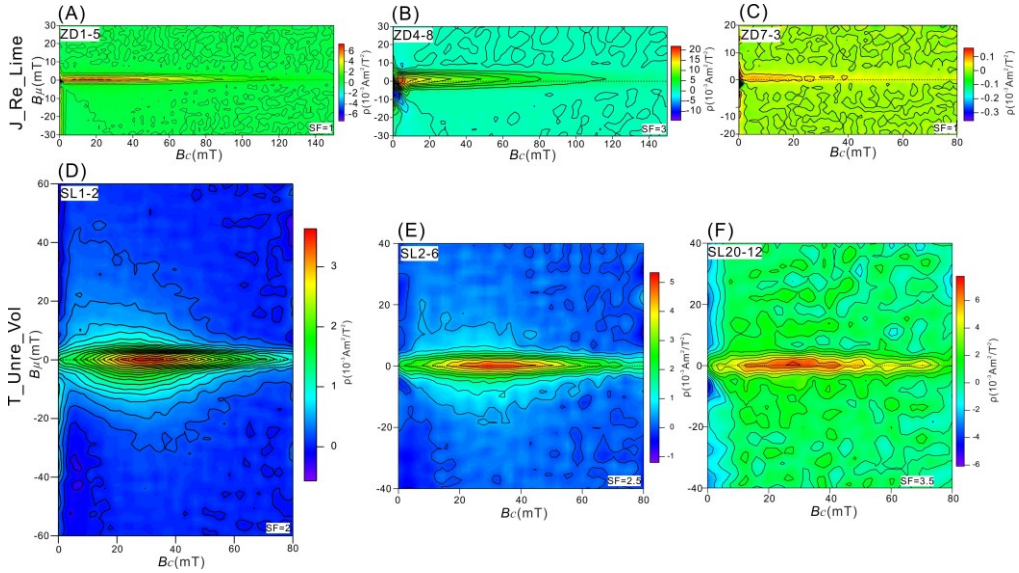

Figure 5.9. *(A-F) FORC diagrams for the representative samples of each formation. The optimum smoothing factor (SF) is calculated by the software FORCinel v1.18 of Harrison & Feinberg (2008). ρ is a mixed second derivative of the magnetization data (Roberts et al., 2014). J_Re_Lime: remagnetized Jurassic* limestones*; T_Unre_Vol: unremagnetized Permo-Triassic volcanic (tuff and rhyolite) samples.*

The FORC diagrams of the remagnetized Jurassic limestones are similar (Fig. 5.9A-C). In general, they exhibit a ρ peak (mixed second derivative of the magnetization data) with closed counters around B_c < 20 mT. The counters are closely spaced along the x-axis of the FORC diagram with a B_c spreading < ~100 mT. In addition, the vertical distribution of the peak is asymmetrical. The center of the distribution is along the trend of B_c = ~0-5 mT with more density in the negative Bu region (~-30 mT) than in the positive Bu region (~5 mT) (Fig. 5.9A-C). These features represent a magnetic population with an appreciable number of particles close to the SD/SP threshold size (Pike et al., 2001; Muxworthy & Dunlop, 2002; Roberts et al., 2006, 2014). The Carboniferous limestones have FORC diagrams similar to the Jurassic limestones. However, the horizontal distribution of the peak shows a minimum value instead of a maximum value for some specimens (Fig. S5.1B, C). The FORC diagrams for the Cretaceous granites are entirely noisy rendering them essentially useless for interpretation (Fig. S5.1D-E). For the unremagnetized Permo-Triassic volcanic samples, the FORC distributions exhibit closed concentric contours about a central peak with a B_c value of ~30 mT, which is in the mean coercivity range of SD (titano-)magnetite (Dunlop & Özdemir, 1997; Roberts et al., 2000). The contours on the FORC diagram are elongated with a slight vertical spread and are like those for non-interacting SD particles (Fig. 5.9D-F). Importantly a SP contribution is non-existent.

5.4.5 Domain state plots

Magnetic properties are controlled by the distribution of magnetic particles with variable magnetic domain states. An accurate portrayal of the domain state is beneficial to appreciate the remanence acquisition mechanism and the reliability of the magnetic recording. Several plots to illustrate the domain state are in use. These include the Day plot (Day et al., 1977), the Néel diagram (Néel, 1955; Tauxe et al., 2002), the Borradaile diagram (Borradaile & Lagroix, 2000; Borradaile & Hamilton, 2003), and the Fabian diagram (Fabian, 2003). We compare those next.

5.4.5.1 The Day plot

The Day plot (Day et al., 1977) is used widely in rock magnetism to identify the domain state despite being criticized recently (Roberts et al., 2018). The majority of the published Day plots of natural samples have data distributions that fall within the PSD field (Qin et al., 2008; Roberts et al., 2019). Even so, it successfully distinguishes remagnetized rocks from unremagnetized rocks, at least for carbonates (Channell & McCabe 1994; Jackson & Swanson-Hysell, 2012; Roberts et al., 2018; Fu et al., 2022a (chapter 2)).

As shown in Fig. 5.10A, the data of the remagnetized rocks and unremagnetized Triassic rocks indeed all fall in the PSD region on Day plot. However, a noticeable grouping is observed: the remagnetized data are close to the SD + SP trend, which is considered as a characteristic feature of CRM, while the unremagnetized Triassic dataset occupies a region closer to the SD + MD mixing trend based on experimental data (Dunlop, 2002). The FORCs of the Triassic rocks show no presence of SP particles, so the deviation to the right of SD-MD mixing line could be associated with some oxidation which rises B_{cr} more than B_c (Roberts et al., 2018). The unremagnetized Cretaceous granites have their data plot away from the other three groups (Fig. 5.10A). These samples have weak magnetic signals that could lead to large measurement uncertainties. Both the coercivity (B_{cr}/B_c) and remanence (M_{rs}/M_s) values are lower than in the other sample groups. In fact, the back field demagnetization curves of the IRM are noisy, which makes B_{cr} determination tedious and the measured B_{cr} values may be too low. Therefore, the unremagnetized Cretaceous granite samples may actually plot more to the right, closer to the SD-MD mixing line.

5.4.5.2 The Néel diagram

The Néel diagram (also called squareness (M_{rs}/M_s) versus coercivity (B_c) diagram in some literature) was first used by Néel (1955); its interpretation was refined by Tauxe et al. (2002). It is a plot of M_{rs}/M_s versus B_c instead of M_{rs}/M_s versus B_{cr}/B_c, which is suggested as a better tool to diagnose the domain state than the Day plot (Tauxe et al., 2002; Roberts et al., 2019). Coercivity increases with the particle axial ratio (length to width ratios) in uniaxial SD (USD) particles. Tauxe et al. (2002) calculated the coercivity of magnetite particles with axial ratios of 1.3:1 and 2:1 which provides an

important interpretive constraint. In general, the typically scattered data distributions in Day diagrams are transformed into simpler near-linear trends in the corresponding Néel diagrams, and most of the data fall in the USD + SP region (Roberts et al., 2019).

Here we compare Néel diagrams for the remagnetized and unremagnetizd samples. The data distributions are in line with what Roberts et al. (2019) observed, that is, trends are near-linear (Fig. 5.10B). The remagnetized samples plot to the left of the USD + SP region, which is occupied by data for samples dominated by SD biogenic magnetite (Fig. 5.10B; Roberts et al., 2019). The difference is that the SD biogenic magnetite has higher values of M_{rs}/M_s. The data for the unremagnetized Cretaceous granite are close to the MD apex, whereas the Triassic volcanic rocks mainly lie in the USD + SP region. Both are distinct from the remagnetized rocks (Fig. 5.10B), and the USD + SP region might be indicative of dominance of uniaxial anisotropies (Roberts et al., 2019). Overall, the Néel diagram also provides a useful representation of hysteresis data for the remagnetized and unremagnetized samples.

5.4.5.3 The Borradaile diagram

The Borradaile Diagram as referred to here, follows the naming that Roberts et al. (2019) used to describe a diagram proposed by Borradaile & Lagroix (2000). It is essentially a three-dimensional display of the Day plot, which is defined by three axes of hysteresis parameters M_{rs}/M_s, B_c, and B_{cr}, all with logarithmic scales. The Borradaile Diagram thus provides an additional dimension for visualizing data variability. Borradaile & Lagroix (2000) and Borradaile & Hamilton (2003) used the diagram to magnetically assess various limestones, including remagnetized limestones. The regression surfaces fitted through the remagnetized data are steeper and displaced upwards above the locus of the SD-PSD-MD trend with lower B_c values (Borradaile & Hamilton, 2003). However, Roberts et al. (2019) suggest that unrealistically low or high B_{cr} and B_c values may occur for SD magnetite because the boundaries indicated for domain state regions are defined by the M_{rs}/M_s and B_{cr}/B_c ratios rather than B_c and B_{cr} values. As shown in Fig. 5.10C-E, most of the data are located within or above the locus of the PSD-MD trend and the remagnetized and unremagnetized data are well distinguished. In addition, some remagnetized data fall on the MD region, while the unremagnetized data fall on PSD region on the B_c-B_{cr} plane.

5.4.5.4 The Fabian diagram

The Fabian diagram, as referred to here, was proposed by Fabian (2003). The vertical and horizontal axes in this diagram are given by σ_{hys} and B_{rh}/B_{cr}, respectively (Fig. 5.10F). σ_{hys} is the shape parameter as described in section 5.4.3; B_{rh} can be defined graphically in two ways: the difference between upper and lower hysteresis branches equals 2 M_{rs} at B = 0, when the difference reduces to half (Option 1), or (Option 2)

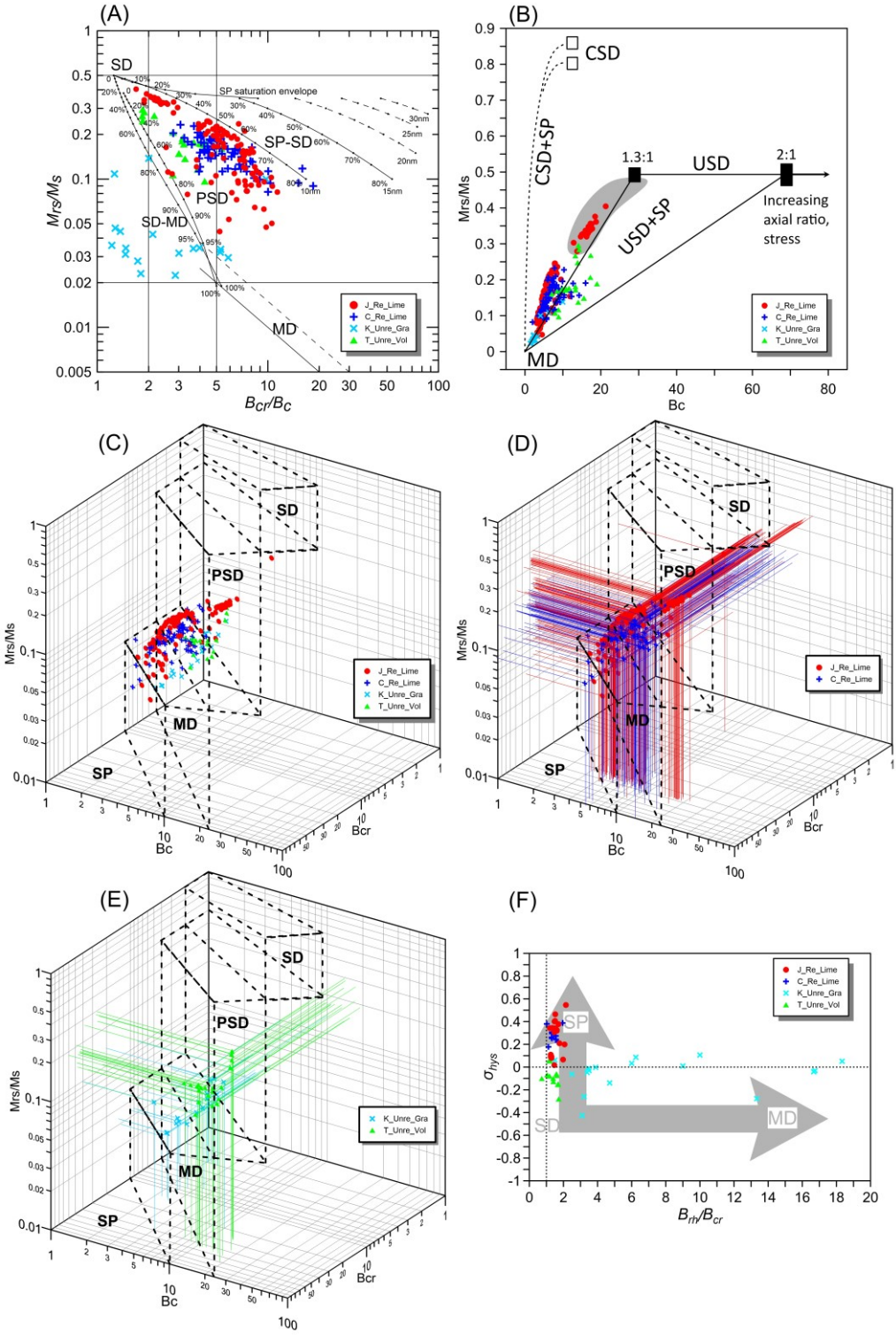
(A)
SD
SP saturation envelope
SP-SD
PSD
SD-MD
MD
30nm
25nm
20nm
15nm
10nm
Mrs/Ms
Bcr/Bc
J_Re_Lime
C_Re_Lime
K_Unre_Gra
T_Unre_Vol
(B)
CSD
CSD+SP
1.3:1
USD
2:1
Increasing axial ratio, stress
USD+SP
MD
Mrs/Ms
Bc
(C)
SD
PSD
MD
SP
Mrs/Ms
Bc
Bcr
(D)
SD
PSD
MD
SP
Mrs/Ms
Bc
Bcr
(E)
SD
PSD
MD
SP
Mrs/Ms
Bc
Bcr
(F)
SP
SD
MD
σ_{hys}
B_{rh}/B_{cr}

Figure 5.10 (previous page). Illustration *of the magnetic domain state using various diagrams as summarized in Roberts et al. (2019). (A) the Day plot (Day et al., 1977; Dunlop, 2002) with regions for SD, PSD, and MD behavior. (B) The Néel diagram (Néel, 1955) with a slightly modified interpretive framework provided by Tauxe et al. (2002), the grey shaded area is occupied by SD biogenic magnetite in Roberts et al. (2019). USD = uniaxial single domain, CSD = cubic single domain. (C) The Borradaile diagram of the remagnetized and unremagnetized samples (Borradaile & Lagroix, 2000; Borradaile & Hamilton, 2003) with regions for SD, PSD, and MD behavior. (D and E) The Borradaile diagram of the remagnetized and unremagnetized samples, respectively; the orthogonal lines portray the three-dimensional projections of each sample. (F) Plot of the shape parameter* σ_{hys} *versus the coercivity ratio* B_{rh}/B_{cr} *(Fabian, 2003) for representative samples, see text for an explanation of the coercivity parameters* σ_{hys} *and* B_{rh}.

move lower hysteresis branch upward by M_{rs}, and it intersects with upper hysteresis branch, the corresponding positive fields in those two potions denotes B_{rh} (Fabian, 2003). From a physical point of view, a transient energy dissipation related ratio is associated with grain size, and thus useful for domain state analysis. B_{rh}/B_{cr} has a linear relationship with the transient energy dissipation ratio and serves as a substitute for the transient energy dissipation ratio for the interpretation of hysteresis loops. High B_{rh}/B_{cr} ratios are indicative of the prevalence of transient irreversible processes and therefore large particle sizes. It is a convenient way to separate SP from MD behavior which is tedious in the three other representations.

Fig. 5.10F shows that most remagnetized samples have shape parameter values $\sigma_{hys} > 0$, while most unremagnetized samples have $\sigma_{hys} < 0$. Yet, there is not a clear separation of the remagnetized limestones from the unremagnetized Triassic volcanic rocks on the horizontal axis. On the other hand, the Cretaceous granite shows markedly high B_{rh}/B_{cr} values, which implies coarse particles.

5.4.6 End member modelling

End-member modelling is an inverse mathematical approach, which allows the measured data to be unmixed with certain so-called end-members. The fundamental of this approach is that the measured data can be treated as a linear mixture of certain invariant constituent components, the endmembers. It is widely used in particle-size distribution analysis (Weltje, 1997; Prins, 1999; Hamann et al., 2008; Toonen et al., 2015), climate reconstructions (Van Dam & Weltje, 1999; Beuscher et al., 2017), and runoff source studies (Brewer et al., 2011). Rock magnetic properties, that is IRM and/or ARM acquisition curves, have been evaluated as well with the end-member modeling approach (Gong et al., 2009; Van Hinsbergen et al, 2010; Meijers et al., 2011; Aben et al., 2014, Huang et al., 2015a, 2015d; Fu et al., 2022b (chapter 1)). However, ARM is biased toward magnetite, which is demonstrated not to be ideal input data

(Gong et al., 2009; Fu et al., 2022b (chapter 1)).

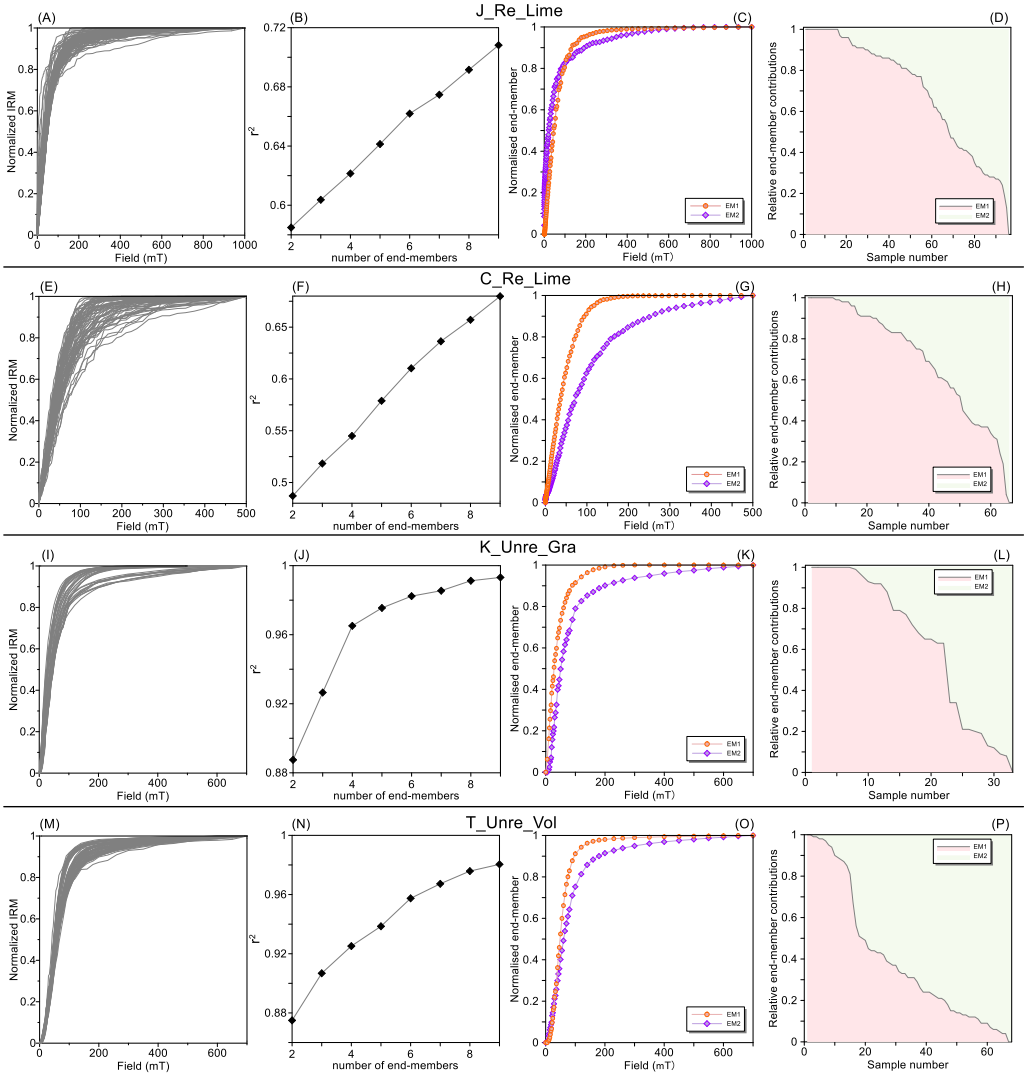

Figure 5.11. *IRM end-member modeling for the representative samples. (A, E, I and M) Normalized IRM acquisition curves; (B, F, J and N) Coefficient of determination versus the number of endmembers, there is a clear break-in-slope at the four end-member model for the unremagnetized Cretaceous granite; (C, G, K and O) Two end-member models of the Normalized IRM acquisition* curves. *(D, H, L and P) Contributions of the two endmembers for individual samples (sorted by the relative contribution of EM1 from the largest to the smallest, see more in supporting information Table S5.4). J_Re_Lime: remagnetized Jurassic limestones; C_Re_Lime: remagnetized Carboniferous limestones; K_Unre_Gra: unremagnetized Cretaceous granites; T_Unre_Vol: unremagnetized Permo-Triassic volcanic (tuff and rhyolite) samples.*

Chemically remagnetized rocks contain abundant fine-grained particles (e.g., Dekkers, 2012). This is because chemical remagnetization frequently adds new magnetic particles to the rock rather than replaces the existing particles. Consequently, it is rather straightforward to appreciate that the magnetic particle distributions in remagnetized and unremagnetized rocks differ due to their distinct NRM acquisition processes. IRM can be faithfully measured on even very weak magnetic samples and depicts the complete magnetic mineralogy. Thus, IRM acquisition curve data sets may mathematically fulfill the requirements to define endmembers.

IRM-acquisition curves of 96 specimens from the remagnetized Jurassic limestones, 66 specimens from the remagnetized Carboniferous limestones, 33 specimens from the unremagnetized Cretaceous granite and 68 specimens from the unremagnetized Permo-Triassic volcanic (tuff and rhyolite) are used here for the end-member modelling. All the IRM-acquisition curves are processed to meet the criterion of monotonic increase. Also, the measured field steps for each IRM acquisition curve are interpolated onto a common grid, yet another requirement of the end-member model algorithm. A break-in-slope on the curve of the r^2 (coefficient of determination) versus the number of end-members diagram is deemed as the optimal number of endmembers. The detailed procedures and end-member modeling algorithm are described in Aben et al. (2014).

5.4.6.1 Remagnetized Jurassic limestones

Normalized IRM acquisition curves of the remagnetized Jurassic limestones show a congregated distribution (Fig. 5.11A). There is no clear break-in-slope in the plot of the coefficient of determination (r^2, ranging from 0 to 1) versus the number of endmembers (Fig. 5.11B), indicating two as the optimal number of end-members model (to avoid over-interpretation). The values of r^2 are rather low since some of the IRM acquisition curves are noticeably noisy; the input signals are not that smooth.

The endmembers in our preferred two end-member solution (called EM1 and EM2) of the remagnetized Jurassic limestones are described as follows. EM1 shows a rapid increase and acquires 90% saturation at low fields (below ~150 mT), and eventually saturates at ~300 mT (Fig. 5.11C, note: the maximum applied field is 1 T). EM2 is a harder component; it consists for 80% of a soft part with a coercivity between 0 and 100 mT while the remaining 20% has a coercivity range up to 600 mT (Fig. 5.11C). The relative contributions of the endmembers to the measured IRM acquisition curves show that approximately two thirds of the samples have EM1 as the major endmember. The remaining one third has EM2 as dominant endmember (Table S5.4). In general, EM1 is the comparatively soft PSD- to SD-style magnetite. EM2 that has a prominent low coercivity part and a high-coercivity tail up to 600 mT, resembles the

remagnetized endmember in the study of Gong et al. (2009). It is interpreted to be a mixture of SD/PSD and SP magnetite instead of magnetite and hematite, as hematite is not detected by other magnetic properties. These small SP particles were formed during the post sedimentary diagenesis, and led to the acquisition of CRM.

5.4.6.2 Remagnetized Carboniferous limestones

The remagnetized Carboniferous limestones have similar magnetic properties as the remagnetized Jurassic limestones (Fig. 5.11E-H, note: the maximum applied field is 500 mT). The absence of a clear break-in-slope in the plot of r^2 versus the number of end-members suggests that the optimal number of end-member model is two. In this model, EM1 represents a soft component that almost reaches its saturation at a fairly low field of ~200 mT. In addition, it contributes over 50% for the majority of the samples, which is generally interpreted to represent soft PSD-style magnetite as in the remagnetized Jurassic limestones (Fig. 5.11G-H). EM2 consists for 60% of a soft component with a coercivity range between 0 and 100 mT while the remaining 40% is characterized by a broad coercivity portion ranging up to ~500 mT (Table S5.4). It is worth noting that this endmember does not saturate at the maximum field of ~500 mT (Fig. 5.11G). It has the same magnetic meaning as EM2 of the remagnetized Jurassic limestones, that is, a mixture of magnetite of (P)SD and SP grain size.

5.4.6.3 Unremagnetized Cretaceous granite

For the Cretaceous granite, the IRM acquisition curves display two clusters visually (Fig. 5.11I). A distinct break-in-slope in the plot of r^2 versus the number of end-members occurs at four end-members, suggesting that as an optimal number (Fig. 5.11J). However, the two end-member solution was preferred after comparing two, three and four end-member models (refer to Fu et al., 2022b (chapter 1) for a detailed description). EM1 represents the typical MD- to PSD- style magnetite while EM2 represents fine-grained magnetite or marginally oxidized magnetite (Fig. 5.11K-L and Table S5.4). Specimens dominated by EM1 show distinct demagnetization behavior compared with those dominated by EM2. However, they are all considered to carry the primary magnetization (Fu et al., 2022b (chapter 1)).

5.4.6.4 Unremagnetized Triassic volcanics

The Triassic volcanics in the Zaduo area show end-member results similar to the Cretaceous granite (Fig. 5.11M-P). Normalized IRM acquisition curves in this unit are more are clustered than the remagnetized limestones but display similarity to the granites (Fig. 5.11A, E, I, M). The curve of the coefficient of determination versus the number of endmembers appears to have a convex shape without clear break-in-slope as with the Jurassic and Carboniferous limestones (Fig. 5.11B, F, N). Like the other three rock units, the two end-member solution was deemed optimal after comparison with three and four end-member models (Fig. 5.11O, P). EM1 has the same meaning as in the other groups, that is, SD/PSD magnetite. EM2 has similar characteristics as in

the remagnetized limestones, however, it has a different meaning: either marginally oxidized magnetite or variable amounts of magmatic titanomagnetite (Huang et al., 2015d).

5.5 Discussion

5.5.1 Remagnetization mechanism of the limestones

Carbonate rocks are vulnerable to secondary magnetizations (Jackson & Swanson-Hysell, 2012; Elmore et al., 2012). CRM acquisition is the currently prevailing mechanism to interpret remagnetization (e.g., McCabe & Elmore, 1989; Font et al., 2006; Elmore et al., 2006; Huang et al., 2017a; Fazzito et al., 2020; Fu et al., 2022a (chapter 2); Yu et al., 2022b), although thermoviscous resetting of the NRM is suggested as explanation in a few cases (Horton et al., 1984; Kent, 1985). Thermal maturities of the rocks under investigation are usually too low for thermoviscous resetting based on relaxation time-blocking temperature relationships (Pullaiah et al., 1975; Jackson, 1990; Dunlop & Özdemir, 2000) to be viable. Chemical remagnetization mechanisms generally involve alteration triggered by a fluid-related agent. These fluids may be produced by different driving mechanisms, including tectonic activity, mere burial, or heat from igneous bodies (Font et al., 2006; Elmore et al., 2006, 2012; Jackson & Swanson-Hysell, 2012; Van der Voo & Torsvik, 2012). The chemical remagnetization mechanisms are divided into two groups: externally derived fluids and internally buffered burial diagenetic processes (Elmore et al., 2012).

Our focus here is on how the chemical remagnetization was acquired, since thermoviscous resetting is deemed unrealistic mainly based on two arguments: 1) nearby outcropping igneous bodies are quite limited, and more importantly, 2) the burial temperature was not at a sufficiently elevated level to invoke thermoviscous resetting as a viable mechanism (Fu et al., 2022a (chapter 2); Yu et al., 2022b). Although it is possible that the limestones were remagnetized by hydrothermal circulation associated with igneous bodies, they were remagnetized at yet another time during the India-Asia collision. If the second remagnetization process is more intense than the first, the first will not be preserved. This rather complex scenario cannot be ruled out, however, the ultimately recorded remagnetization is a CRM associated with the India-Eurasia collision.

The Jurassic and the Carboniferous limestones were both deposited In a littoral and shallow sea carbonate environment (Li et al., 2002; QGSI, 2014; Yan et al., 2016). These conditions are widely perceived as more oxic in comparison with pelagic marine environments. However, in some continental margin settings or deeper water sulfidic basins, the organic carbon fluxes are high, and the oxygen is depleted quickly, leading to anoxic rather than 'suboxic' pore waters (e.g., Murray et al., 1989; Christensen et al., 1989; Canfield et al., 1993; Kuypers et al., 2003; Percy et al., 2008). It is traditionally accepted that with increasing diagenesis, the prevailing conditions become gradually increasingly anoxic (Roberts et al., 2013; Roberts, 2015). Sulfidic conditions may occur

at depths not exceeding tens of centimeters below the sediment–water interface (Roberts, 2015). Iron reduction and sulfate reduction are important processes under such conditions. Detrital magnetite and hematite will dissolve, and iron sulfides such as paramagnetic pyrite or intermediate magnetic iron sulfides like ferrimagnetic greigite will form (Roberts & Turner, 1993; Kao et al., 2004; Fu et al., 2008). Taken together, the primary paleomagnetic record by detrital magnetite/hematite is destroyed during early diagenesis, and sedimentary iron sulfides will occur.

Remagnetized carbonates often contain a large number of SP particles that were produced during burial diagenesis (e.g., Suk et al., 1993; Aubourg & Pozzi, 2010; Kars et al, 2012, 2014). It might be possible to tie the remagnetization to a geological event, particularly orogenesis during which uplift, faulting and/or fluid flow occurred. This is exactly the case of remagnetized limestones in the study area (Fu et al., 2022a (chapter 2); Yu et al., 2022b). The Cenozoic India-Eurasia collision is a most significant geological event that leads to the formation of the Tibetan Plateau. Uplift and denudation may have provided access to meteoric waters that could provide sub-oxic or even oxic conditions, which could drive oxidation reactions of the existing iron sulfides. The high porosity of the limestones contributes to the deep penetration of the fluids.

5.5.2 Hysteresis properties of the magnetite-bearing rocks

'Wasp-waisted' hysteresis signatures induced by the co-occurrence of SP and stable SD particles have been suggested as a fingerprint for carbonate remagnetization (Jackson, 1990; Channell & McCabe, 1994; McCabe & Channell, 1994; Jackson & Swanson-Hysell, 2012; Van der Voo & Torsvik, 2012). The shape of hysteresis loops for both remagnetized and unremagnetized rocks in the Zaduo area was quantitatively assessed to provide additional information. However, what is noteworthy is that the limestones in the Zaduo area are remagnetized, while the volcanics are not. It is still not clear how lithology affects the quantification of the hysteresis shape. In addition, while it is convincing that Day plot is very suited in diagnosing remagnetized limestones (Jackson & Swanson-Hysell, 2012; Roberts et al., 2018), its diagnostic power for other magnetite-bearing lithologies has yet to be examined.

To contribute solving this ambiguity, hysteresis parameters from different lithologies, especially carbonates with a primary NRM and volcanic rocks with a secondary NRM, are reanalyzed, compiled and plotted on a summary Day plot (Fig. 5.12, 5.13; Table S5.5). Typically, pelagic carbonates or carbonates with a biochemical magnetization can preserve a primary NRM (Channell & McCabe, 1994; Belkaaloul & Aïssaoui, 1997; Abrajevitch & Kodama, 2009; Ménabréaz et al., 2010). The dominant magnetic mineral, magnetite in these rocks, yields 'pot-bellied' hysteresis loops, which display hysteresis shape parameters $r_{hys} < 1$ and $\sigma_{hys} < 0$ (Fig. 5.12A, B). This is

similar to the fresh lavas and volcaniclastic sandstones retaining a primary NRM (Fig. 5.12A, B). It also strongly resembles the volcanic rocks with a primary NRM in the Zaduo area (Fig. 5.7). It should be noted that populations with more than one magnetic mineral may also produce strongly contrasting coercivities, which may result in 'wasp-waisted' hysteresis loops. Some limestones with a primary NRM show such 'wasp-waisted' hysteresis loops; thus, their hysteresis shape parameters resemble those of remagnetized rocks, but the combination of magnetite and/or hematite/goethite is the main reason for 'wasp-waisted-ness' in these rocks (Ma et al., 2018; Cao et al., 2019). 'Wasp-waisted' hysteresis loops resulting from mixtures of hematite and magnetite can be distinguished by examining the $\triangle$M curve (the difference between the ascending and descending branches for B > 0 of a hysteresis loop). The $\triangle$M curve of SP/SD magnetite shows a monotonic decrease, whereas a combination of hematite and magnetite shows a 'roller coaster' behavior (Fig. S5.2B, E; Tauxe et al., 1996). The derivative of the $\triangle$M curve presents two distinct humps for a mixture of hematite and magnetite, whereas a single hump for SP/SD magnetite is observed (Fig. S5.2C, F; Tauxe et al., 1996). Remagnetization of volcanic rocks has been infrequently reported in comparison with other lithologies, and some data from the Tibetan Plateau are reanalyzed here. Although tuffs or other volcanic rocks show 'wasp-waisted' hysteresis loops, hence similar hysteresis shape parameters as remagnetized strata, it is attributed to a mixture of two or more minerals (Huang et al., 2015d, 2015e). Remagnetized limestones from the Tibetan Himalaya and Qiangtang Terrane show not only almost the same hysteresis shape parameters, but they also have a remagnetization mechanism similar to that in the Zaduo area (Huang et al., 2017a, 2017b, 2019b). The Cretaceous-Paleogene carbonate specimens of the Tibetan Himalaya are an exception: they show hysteresis shape parameters r_{hys} < 1 and σ_{hys} < 0, but have a primary NRM, which is presumably caused by the amount of detrital magnetite (Huang et al., 2017a; study No. 15 in Fig. 5.12).

The Day plot (Day et al., 1977) has been used extensively in rock magnetism to make inferences about the domain state. Even though ambiguities have long been recognized, the Day plot is successful in identifying remagnetized carbonates from those retaining a primary NRM (Jackson, 1990; Channell & McCabe, 1994; McCabe & Channell, 1994; Jackson & Swanson-Hysell, 2012; Van der Voo & Torsvik, 2012; Roberts et al., 2018, 2019). On a Day plot (Fig. 5.13), hysteresis data of remagnetized rocks compiled from the previous studies plot mainly near the SP + SD mixing envelope according to experimental data (Dunlop, 2002), while those from unremagnetized rocks cluster close to the SD + MD trend line (Fig. 5.13), which is consistent with the Zaduo area limestones (Fig. 5.10A). The underlying reasoning is that a SP-SSD particle-size distribution is geologically rare and basically associated with an *in situ* process of origin (Jackson & Swanson-Hysell, 2012).

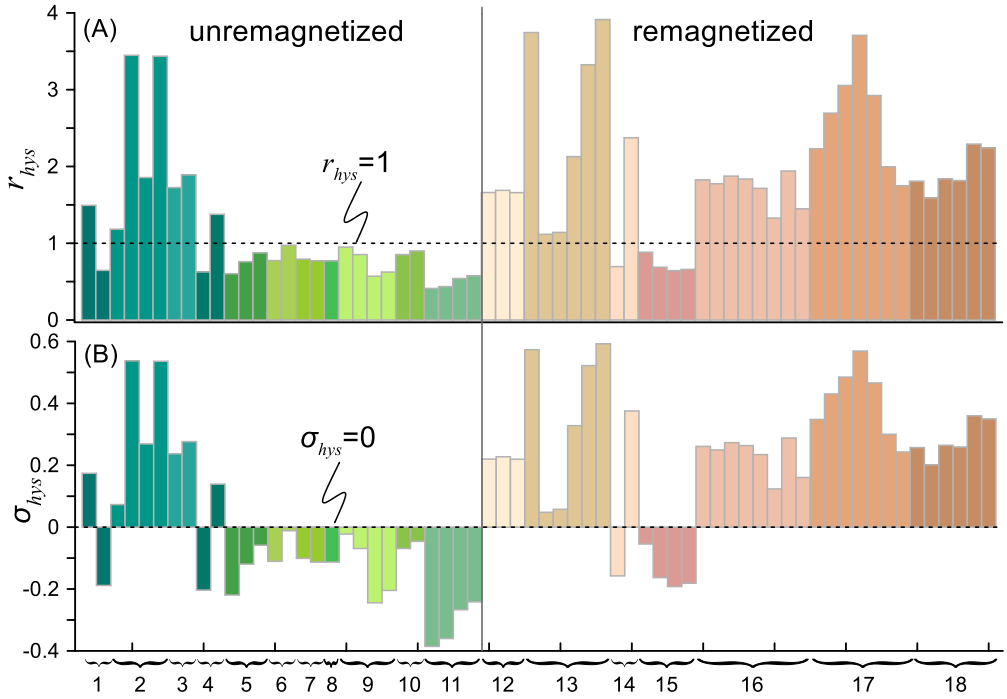

Figure 5.12. *Histogram showing the hysteresis parameters (A) r_{hys} and (B) σ_{hys} (Fabian, 2003) in unremagnetized and remagnetized rocks compiled from literature data (Table S5.5). Numbers below the horizontal axis represent data from previous studies: 1- magnetite and/or hematite in limestones (Yan et al., 2016); 2- magnetite and goethite in limestones (Cao et al., 2019); 3- magnetite and goethite/hematite in limestones (Ma et al., 2018); 4- magnetite and minor goethite/hematite in volcaniclastic sandstones (Huang et al., 2015a); 5-magnetite in chert/sandstones (Huang et al., 2015b); 6- magnetite in marine carbonates (Abrajevitch & Kodama, 2009); 7- titanomagnetite in silty-carbonate (Ménabréaz et al., 2010); 8- magnetite in limestones (Belkaaloul & Aïssaoui, 1997); 9- magnetite in limestones (Channell & McCabe, 1994); 10- titanomagnetite in fresh lava flows (Huang et al., 2015d); 11- magnetite in volcaniclastic sandstones (Huang et al., 2017a); 12- magnetite in limestones (Huang et al., 2015a); 13- magnetite and pigmentary hematite in tuff or siltstones (Huang et al., 2015d); 14- titanomagnetite and secondary hematite in volcanic rocks (Huang et al., 2015e); 15 and 16- magnetite in limestones (Huang et al., 2017a); 17- magnetite in limestones (Huang et al., 2017b); 18- magnetite in limestones (Huang et al., 2019b).*

Figure 5.13 (next page). *Summary Day plot (Dunlop, 2002) of published hysteresis parameters for* different *lithologies.*

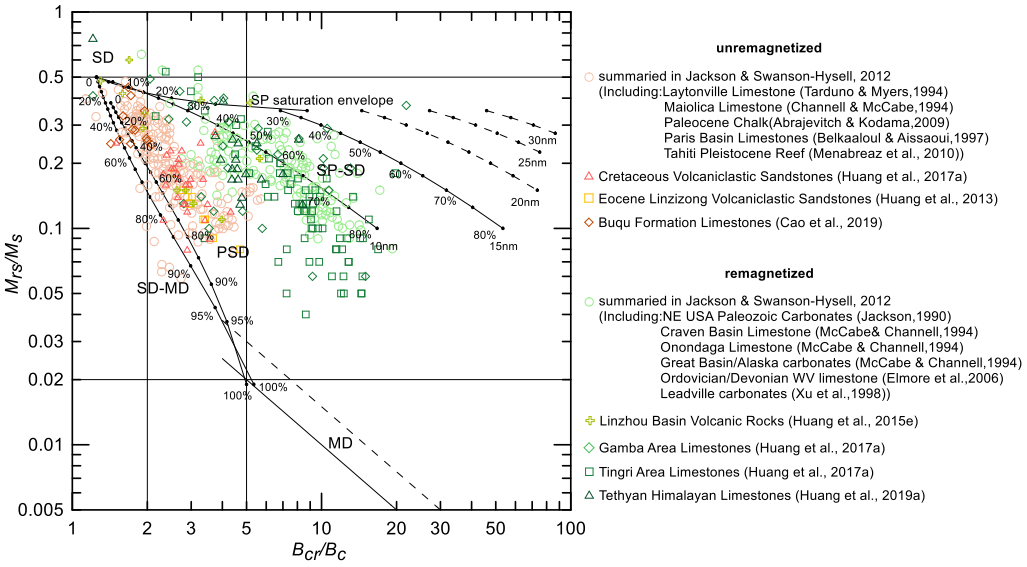

Nevertheless, an exception exists: the volcanic rocks of the Dianzhong Formation in the Linzhou basin are deemed to have been remagnetized, but they exhibit Day plot trends that reflect a primary NRM (Huang et al., 2015e). Magmatic titanomagnetite (partially) reset by a thermoviscous remanent magnetization and secondary hematite with a chemical remanent magnetization are the main magnetic carriers in these rocks, which leads to a shift on the Day plot. In fact, it has been termed a 'false negative' where remagnetized rocks have rock-magnetic properties similar to those of unremagnetized carbonates, and this phenomenon is probably more common than a 'false positive' (Jackson & Swanson-Hysell, 2012). In a review of Day plot interpretation, Roberts et al. (2018) also state that some sedimentary rock hysteresis data falls into the region of remagnetized carbonates on the Day plot, but that there is no carbonate involved in these cases. Significant concentrations of (quasi-)SP particles are the main reason causing the aforementioned data overlap (Rowan et al., 2009; Roberts et al., 2013). Even so, the present dataset involves various lithologies, such as limestones, lavas, tuffs, and volcaniclastic sandstones, providing a more reliable clue to the validity of the Day plot in distinguishing remagnetization.

5.5.3 Characteristics and diagnosis for the remagnetization in carbonates

Both the multiple segment χ-T and magnetization versus temperature curves reveal consistent characteristics in the samples. Mineral transformation occurs between ~410 °C and 450 °C in the remagnetized samples (Fig. 5.2A-I), indicating the presence of pyrite oxidizing (partially) to magnetite. In contrast, no/minor mineral alteration occurs during heating in the unremagnetized samples (Fig. 5.2A-I). In terms of the remanence decay curves of the samples, the maximum unblocking temperature of

the remagnetized samples is lower than that of the unremagnetized samples. Specifically, the remagnetized samples have a low average temperature at which 10% of the remanence are remaining (~410 °C, Fig. 2D, H). That temperature is ~560 °C in the unremagnetized samples (Fig. 5.2L, P). The discrepancy in unblocking temperature spectrum between remagnetized and unremagnetized samples can be attributed to the respective grain size distributions. The low maximum unblocking temperature of the remagnetized samples implies a smaller particle size (O'Reilly, 1984; Dunlop & Özdemir, 2000; Jiang et al., 2015; Huang et al., 2020). AF demagnetization based on coercivity discrimination does not show a remarkable difference between remagnetized and unremagnetized samples (Fig. 5.2E, I, M, Q), so is not recommended for evaluating NRM components.

It has been widely reported that remagnetized carbonates often contain authigenic magnetite grains dominantly in the SP and stable SD size range (McCabe & Elmore, 1989; Jackson & Swanson-Hysell, 2012; Van der Voo & Torsvik, 2012). The SP particles have a high surface area to volume ratio, which contributes to their geochemical instability (Li et al., 2009b). Yet alteration of iron sulfides to magnetite during remagnetization definitely involves the formation of SP grains (Jackson & Swanson-Hysell, 2012). Although SP grains do not contribute to a stable NRM, their presence in abundance in remagnetized carbonates, together with stable SD grains, gives rise to specific magnetic behavior. The hysteresis shape of 'wasp-waisted' loops can be well estimated using the method of Fabian (2003). Accordingly, for the rock units in the Zaduo area, the remagnetized samples generally have hysteresis parameters $r_{hys} > 1$ and $\sigma_{hys} > 0$, whereas the majority of the unremagnetized samples have $r_{hys} < 1$ and $\sigma_{hys} < 0$. Even for the unremagnetized samples with $r_{hys} > 1$, their r_{hys} values are only marginally higher than 1 (Fig. 1.7). When evaluating this criterion on the various lithologies, most of the specimens are consistent with the rocks studied here (Fig. 5.12). At the same time, caution ought to be exercised on whether the hysteresis behavior is caused by a mixture of magnetic minerals in diagnosing remagnetization. Hysteresis parameters become equivocal in a multiple magnetic mineral scenario. It has been certified again in this study that the Day plot is powerful in recognizing of remagnetization (Fig. 5.10). In addition, reanalysis of the data distributions of various lithologies in Day plot demonstrated that it is generally applicable (Fig. 5.13).

On the other hand, M_{rs}/M_s is sensitive to magnetic domain state variations, whereas the B_{cr}/B_c ratio can obscure important coercivity information as both B_{cr} and B_c are sensitive to grain size variations (Néel, 1955; Dunlop & Özdemir, 1997; Tauxe et al., 2002; Roberts et al., 2018, 2019). The Néel diagram is argued to have advantages over the Day plot in domain state diagnosis (Tauxe et al., 2002; Roberts et al., 2018, 2019). Our remagnetized data plot to the left region of the line from the origin to USD particles with an axial ratio of 1.3:1, yet the data of the rocks with a primary NRM occupy the MD and USD + SP regions (Fig. 5.10B). Roberts et al. (2019) plot > 3,100 sedimentary and igneous samples on the Néel diagram, and most data fall within the

USD + SP region as defined by Tauxe et al. (2002). Only those samples containing sufficient SD biogenic magnetite plot to the left of the USD + SP region. In other words, our remagnetized data have some similarity with the SD biogenic magnetite. It is worth noting that biogenic magnetite has axial ratios far exceeding 2:1, and its plotting on the Néel diagram in the region with low axial ratios (Fig. 5.10B) are suggested to be linked to the vortex/supervortex states in collapsed magnetofossil chains (Harrison & Lascu, 2014; Egli & Winklhofer, 2014). However, where the data of the remagnetized samples actually plot (Fig. 5.10B) is likely due to the smaller axial ratios of the authigenic magnetite particles. It is conceivable that the chemical remagnetization allowed magnetic particles to grow evenly and thus with a small axial ratio. Hence, the data approach the CSD + SP region but move away from the USD + SP region. The Borradaile diagram allows plotting B_{cr} and B_c separately and therefore has advantages in data visualization. Remagnetized data fall above the unremagnetized data in three dimensions (Fig. 5.10C), and the distinction between both data types is observable on the B_c-B_{cr} plane (Fig. 5.10D-E). The Fabian diagram shows a distinction essentially via the shape parameter σ_{hys}, as B_{rh}/B_{cr} values are similar for remagnetized limestones and the unremagnetized Triassic volcanic rocks but extremely high for the Cretaceous granite.

End-member modeling of IRM acquisition curves has been demonstrated to be of value in diagnosing remagnetization (Gong et al., 2009; Van Hinsbergen et al., 2010; Meijers et al., 2011; Aben et al., 2014; Huang et al., 2015a; Fu et al., 2022b (chapter 1)). In remagnetized carbonate, an endmember that is close to saturation around 700 mT is typically detected, which is associated with SP magnetite (Gong et al., 2009). In this study, the remagnetized limestones have an endmember that is not saturated at 500-600 mT (Fig. 5.11D-E). The authigenic magnetite in the SP domain can form during the process of remagnetization. The energy barrier for spin reorientation has increased in these particles, leading to higher coercivity (Dekkers, 2012). The hard component in remagnetized limestones is further supported by IRM component analysis (Fig. 5.4A-D), which is virtually absent in unremagnetized volcanic samples (Fig. 5.4E-F). A similar endmember is present in a group of Cretaceous granites with a primary NRM (Fu et al., 2022b). However, these granites are interpreted to have fine-grained magnetite that is responsible for gyroremanent magnetization rather than remagnetization. The presence of this endmember in the Triassic volcanic rocks also has a different interpretation. It stands for marginally oxidized magnetite or magmatic titanomagnetite in variable amounts rather than remagnetization. Another remarkable feature of end-member modeling is that the curve of coefficient of determination shows a convex shape for unremagnetized rocks, but a near-linear shape for remagnetized rocks. This implies for the latter that either the IRM dataset is fully represented by two endmembers (lowest number in the software) or just by a single endmember. Alternatively, it would be underrepresented by nine endmembers (maximum dictated by the software). However, two or more endmembers become essentially identical from four end-member model solutions

onward (Fig. S5.3), indicating that data noise determines the end member configuration, i.e., the data set is over-interpreted. Thus, particle size variations are smaller in remagnetized limestones than in volcanic rocks, which is quite reasonable to be associated with the process when the magnetic particles formed.

5.6 Conclusions

Proper identification of remagnetized rocks is key in classic paleogeographic reconstruction studies. Given the complexity of remagnetization (e.g., the wide variety of possible remagnetization mechanisms, mineral alteration, volume of magnetic carriers, etc.), it is an unrealistic expectation that a single rock-magnetic signature can resolve once and for all. However, comprehensive rock magnetic studies can outline properties of the magnetic particles. Here, as a test case we performed multiple rock magnetic measurements and analyses to a set of magnetite-dominated samples, including both unremagnetized and chemically remagnetized rocks.

The results consistently suggest that magnetic carriers of the CRM are authigenic magnetite of stable SD and superparamagnetic (SP) size. The co-occurrence of stable SD and SP magnetite leads to specific rock magnetic behavior. Both the high-field and low-field thermomagnetic runs reveal the alteration of existing iron sulfides to magnetite. The maximum unblocking temperature of the remagnetized samples is significantly lower than that of the unremagnetized samples. The former drops 90% of the remanence at ~410 °C; the latter reaches that level at ~560 °C. This is because rocks with low unblocking temperature have small particle size, and the lower unblocking temperature spectrum can be regarded as an indicator of CRM. A hard component in remagnetized samples is detected by both the IRM component analysis and the end-member modeling, which is contributed to the SP magnetite. FORC diagrams of the remagnetized Jurassic rocks reveal the presence of SP magnetite while the unremagnetized Triassic rocks have SD-PSD magnetite. The FORC diagrams of the other two groups are too noisy to provide meaningful information. In addition, as in many remagnetized carbonates, 'wasp-waisted' hysteresis loops are also present in our remagnetized samples. In these loops, the ratio of E_{hys} (the total area between the two hysteresis branches) and 4 M_sB_c is > 1, whereas it is < 1 in the unremagnetized samples. This ratio is at the core of Fabian diagram, which is also generally applicable in other rocks when magnetite is the main magnetic carrier (e.g., volcaniclastic sandstones, green chert, sandstone, andesitic tuff as reviewed here). Furthermore, the remagnetized data distributions on the Day plot are consistent with the so-called 'remagnetization trend'. In the Néel diagram, these data approach the CSD + SP region, but plot away from the USD + SP region, yet unremagnetized data occupy the MD and USD + SP regions. The distribution of the remagnetized data implies smalle axial ratios of the authigenic magnetite particles, i.e., more or less equant particles. The Day plot better discriminates remagnetization than the Néel diagram, because B_{cr}/B_c in a Day plot

shows a wider range along the horizontal axis than B_c in the Néel diagram, which increases visibility (Fig. 5.10A and B). The Borradaile diagram is a tridimensional Day plot with its separate B_{cr} and B_c axes, which provides additional information on coercivity-related parameters but complicates visualization. As a novel method, end-member modelling enables IRM acquisition curves to be represented by two endmembers. These endmembers are similar to each other in four groups, however, the remagnetized rocks have a convex curve of the r^2 versus the number of endmembers, whereas the unremagnetized rocks have a near-linear shape. Taken together, the Day plot, Fabian diagram, thermal demagnetization curves, IRM component analysis and end member modeling are the most recommended tools for diagnosing remagnetization in those magnetite-dominated rocks.

5.7 Acknowledgments

This work was co-supported by the Natural Science Foundation of China (Grant 41974080), the Basic Science Center for Tibetan Plateau Earth System (CTPES, Grant 41988101-01), the Natural Science Foundation of China (Grant 42164005), the Second Tibetan Plateau Scientific Expedition Program (Grant 2019QZKK0707), and the Strategic Priority Research Program of Chinese Academy of Sciences (Grant XDA20070201).

E

EPILOGUE

Paleomagnetic, rock magnetic and petrographic studies of the Mid-Late Jurassic limestones and the Early Cretaceous granites in the Eastern Qiangtang Terrane provide new insights into the tectonic evolution of the Qiangtang Terrane since the Early Cretaceous. Identification of the Eocene remagnetization allows us to take a new look at the geological meaning behind it. Integration of paleomagnetic, gravity survey, and magnetic fabric data unveils that the oroclinal bending of the eastern ending of the Qiangtang Terrane encompasses at least a significant portion of its lithosphere. Comparison of the remagnetized and unremagnetized magnetite-bearing rocks helps us to assess potential remagnetization independent of traditional paleomagnetic field tests and paleomagnetic directional information. In addition, the way we assessed the paleomagnetic direction of the Zaduo granite provides a new approach to address situations where the bedding attitude is unknown or equivocal. The main findings of this thesis are as follows:

Lhasa-Qiangtang collision prior to ~126 Ma

Although the Mid-Late Jurassic limestones studied did not deliver meaningful information on the Lhasa-Qiangtang collision itself (or the closure of the Meso-Tethys-Bangong-Nujiang Ocean) because of the remagnetization, the Cretaceous granites provide a constraint on this event. The granites were dated at ~126 Ma by whole-rock and biotite K-Ar geochronology (QGSI 2005, 2014), which form the basis of the paleogeographic reconstruction. Rock magnetic and petrographic studies were carried out to evaluate the reliability of the granite's ChRM, confirming that the granites preserved a primary NRM. However, granites are not that frequently investigated paleomagnetically because their paleohorizontal is generally poorly constrained. Geological boundary conditions inferred from geological map inspection enable different scenarios pertaining to the bedding tilt of strata in contact with the granite. Consequently, the difference between the observed and expected bedding attitudes indicates that the strata of the Yanshiping Group in the Eastern Qiangtang Terrane (at least in the Zaduo area) were tilted during/prior to the intrusion of the Zaduo granite. This is interpreted as a lagged impact of the Lhasa-Qiangtang collision. Given the frequent layer-parallel shortening during early deformation stages, we infer that the Lhasa-Qiangtang collision occurred before ~126

Ma. The way we processed the granite data provides a new avenue for studying tectonic evolution with the help of paleomagnetic information from granites, which was presented in **chapter 1**.

The tectonic evolution of the Eastern Qiangtang Terrane during the Cenozoic

We recognized that the Mid-Late Jurassic limestones were remagnetzied during the Eocene, which was attributed to the changes in diagenetic conditions after the India-Eurasia collision. As shown in **chapter 2**, the secondary remanence reveals that the Zaduo area of the Eastern Qiangtang Terrane has experienced ~15.7° ± 3.2° (~1740 ± 350 km) of latitudinal crustal shortening since the Eocene. In addition, the ~20° clockwise rotation of the Zaduo area relative to Eurasia coincides with the rotation pattern in the eastern part of the Qiangtang Terrane, indicating that the clockwise rotation accommodating the India–Eurasia collision also prevailed in the Zaduo area.

Subsequently, we show that the eastern ending of the Qiangtang Terrane underwent oroclinal bending during the India-Eurasia collision, which was confirmed by an orocline test with paleomagnetic data from the Zaduo, Gongjue and Mangkang areas. To better understand the geodynamic evolution of this region on a lithospheric scale, we analyzed a gravity survey to decipher the deep structures. We used the wavelet multiscale decomposition method and spectral analysis to determine the density differences at various depths. The surface expression and deeper traces of the oroclinal bending appeared to be similar, revealing coupling of the upper and lower crust. The oroclinal bending of the eastern ending of the Qiangtang Terrane resulted from the subduction of the Indian Plate underneath the Eurasian Plate (Yin & Harrison, 2000; Tapponnier et al., 2001; Ding et al., 2017). We concluded that the orocline formation of the eastern ending of the Qiangtang Terrane occurred after the Late Eocene, whereas large-scale crustal flow dominated after the mid-Miocene, resulting in the uplift and outward expansion of the Tibetan Plateau. In addition, we have identified inverse magnetic fabrics in the Jurassic Buqu limestones that were remagnetized in the Eocene. Comparison of the bulk susceptibility (K_m) and two remanences (K_m versus the natural remanent magnetization, K_m versus saturation isothermal remanent magnetization), as well as the relation between K_m and saturation magnetization indicate that susceptibility and remanences were both carried by authigenic magnetite. Together with the AMS data from the Gongjue area, the inverse magnetic fabrics of our study provide a coherent picture of the orocline. This topic was covered in **chapters 3** and **4**.

Distinguishing remagnetization from unremagnetization based on rock magnetic properties

In addition to the rocks studied in some detail in this thesis, Permo-Triassic tuff and rhyolite, and Carboniferous limestones from the same area were investigated as well

(Guan et al., 2021; Yu et al., 2022). The Permo-Triassic lithologies have preserved a primary remanence, while the Carboniferous rocks have not. The remagnetized characteristic remanent magnetization (ChRM) is residing in stable single domain (SD) and cogenetic superparamagnetic (SP) grains of authigenic magnetite, which is absent in the samples with primary remanence. The difference provides a unique opportunity to compare the magnetic properties between remagnetized and unremagnetized rocks, where in all cases magnetite dominates the magnetic carriers. Hence, we performed multiple rock magnetic measurements and subjected them to various analyses, which were presented in the **final chapter** of this thesis. Chemical remanent magnetization (CRM) is the main reason for the Eocene remagnetization. Small authigenic magnetite particles formed during this process. Thermomagnetic runs detect the presence of the oxidation of pyrite to magnetite in remagnetized rocks. Thermal demagnetization decay curves of those samples reveal noticeably lower maximum unblocking temperature compared with unremagnetized samples. The co-occurrence of magnetites in stable SD and SP size in remagnetized rocks results in specific rock magnetic behavior, e.g., 'wasp-waisted' hysteresis loops and the 'remagnetization trend' on the Day plot. Component analysis of acquisition curves of the isothermal remanent magnetization (IRM) enables identification of SP magnetite particles in remagnetized rocks, which are absent in unremagnetized rocks. End-member modeling is used to unmix a collection of IRM acqusition curves. A seperate hard component represents small SP magnetite in remagnetized rocks, which is (largely) non-existent in unremagnetized rocks featuring larger magnetite grains. In addition, in a plot of r^2 *vs* the number of endmembers a convex curve appears in the remagnetized rocks, whereas unremagnetized rocks feature a near-linear shape. The Day plot, Néel diagram, Borradaile diagram, and Fabian diagram were used to illustrate the domain state. We suggeste that the Day plot and Fabian diagram are optimal tools to discriminate remagnetization. In addition, thermal demagnetization curves, IRM component analysis and end member modeling are also recommended.

Outlook

Previous research has shown that the Jurassic Buqu Formation limestones have a different origin of their NRM depending on the sampling location. In the Yanshiping area, the central segment of the Qiangtang Terrane, it is demonstrated that the Buqu Formation has either a primary NRM (Zeng, 2015; Fang et al., 2016; Yan et al., 2016; Song et al., 2016), or a secondary NRM (Ran et al., 2017). In the Shuanghu area, ~300 km west of the Yanshiping area, a primary NRM of the Buqu Formation has been reported (Cao et al., 2019). This thesis presents a secondary NRM more to the east of previous studies. It is interesting to examine the rationale behind this observation. Was it a local or regional remagnetization? Was the mechanism of the remagnetization the same for all locations? Was the remagnetization controlled by the same tectonic event? Therefore, in future research, the well-exposed red beds of the Quemocuo and Xiali formations in the Zaduo area, as well as red beds to the west

are our target lithologies. Given a recently published paper on how to discriminate remagnetization in red beds (Huang et al., 2020), it is doable to conduct a traditional paleomagnetic study coupled with a detailed rock magnetic assessment. On the other hand, the end-member modeling of IRM has been used widely to diagnose remagnetization in this thesis. Given that the NRM decay curves differ in remagnetized and unremagnetized redbeds (Jiang et al., 2015, 2017), it would be tempting to assess NRM decay curves with the end-member modeling approach. Secondary oroclines were also observed and verified across the world, thus integrating paleomagnetism, oroclinal bending, and gravity in other collision zones (e.g., the Arabia-Eurasia convergence zone, or the Mongolian Orocline in Central Asia) would shed light on the occurrence of 'thin *vs* thick skinned' processes.

R

REFERENCES

Aben, F., Dekkers, M., Bakker, R.R., van Hinsbergen, D.J., Zachariasse, W.J., Tate, G.W., McQuarrie, N., Harris, R. and Duffy, B., 2014. Untangling inconsistent magnetic polarity records through an integrated rock magnetic analysis: A case study on Neogene sections in East Timor. Geochemistry, Geophysics, Geosystems, 15(6): 2531-2554.

Abrajevitch, A. and Kodama, K., 2009. Biochemical vs. detrital mechanism of remanence acquisition in marine carbonates: a lesson from the K–T boundary interval. Earth and Planetary Science Letters, 286(1-2): 269-277.

Abrajevitch, A., Pillans, B.J. and Roberts, A.P., 2014. Haematite pigmentation events and palaeomagnetic recording: implications from the Pilbara Print Stone, Western Australia. Geophysical Journal International, 199(2): 658-672.

Allegre, C.o., Courtillot, V., Tapponnier, P., Hirn, A., Mattauer, M., Coulon, C., Jaeger, J., Achache, J., Schärer, U. and Marcoux, J., 1984. Structure and evolution of the Himalaya–Tibet orogenic belt. Nature, 307(5946): 17-22.

Allmendinger, R.W., Cardozo, N. and Fisher, D.M., 2011. Structural geology algorithms: Vectors and tensors. Cambridge University Press.

Andersen, O.B., 2010. The DTU10 Global Gravity field and mean sea surface–improvements in the Arctic, 2nd IGFS meeting.

Antolín-Tomás, B., Román-Berdiel, T., Casas-Sainz, A., Gil-Peña, I., Oliva, B. and Soto, R., 2009. Structural and magnetic fabric study of the Marimanha granite (Axial Zone of the Pyrenees). International Journal of Earth Sciences, 98(2): 427-441.

Appel, E., Crouzet, C. and Schill, E., 2012. Pyrrhotite remagnetizations in the Himalaya: a review. Geological Society, London, Special Publications, 371(1): 163-180.

Aubourg, C. and Pozzi, J.P., 2010. Toward a new< 250 C pyrrhotite–magnetite geothermometer for claystones. Earth and Planetary Science Letters, 294(1-2): 47-57.

Aubourg, C., Rochette, P., Stéphan, J.F., Popoff, M. and Chabert-Pelline, C., 1999. The magnetic fabric of weakly deformed Late Jurassic shales from the southern subalpines chains (French Alps): evidence for SW-directed tectonic transport direction. Tectonophysics, 307(1-2): 15-31.

Bai, D., Unsworth, M.J., Meju, M.A., Ma, X., Teng, J., Kong, X., Sun, Y., Sun, J., Wang, L. and Jiang, C., 2010. Crustal deformation of the eastern Tibetan plateau revealed by magnetotelluric imaging. Nature geoscience, 3(5): 358-362.

Bailey, S.W., 1984. "Structures of layer silicates," in Structures of clayminerals and theirX-ray identification. Editors G. W. Brindley and G. Brown (London: Mineral Society), 1–124.

Balmino, G., Vales, N., Bonvalot, S. and Briais, A., 2012. Spherical harmonic modelling to ultra-high degree of Bouguer and isostatic anomalies. Journal of Geodesy, 86(7): 499-520.

Bao, X., Sun, X., Xu, M., Eaton, D.W., Song, X., Wang, L., Ding, Z., Mi, N., Li, H. and Yu, D., 2015. Two crustal low-velocity channels beneath SE Tibet revealed by joint inversion of Rayleigh wave dispersion and receiver functions. Earth and Planetary Science Letters, 415: 16-24.

Bascou, J., Camps, P. and Dautria, J.M., 2005. Magnetic versus crystallographic fabrics in a basaltic lava flow. Journal of Volcanology and Geothermal Research, 145(1-2): 119-135.

Beaumont, C., Jamieson, R.A., Nguyen, M.H. and Medvedev, S., 2004. Crustal channel flows: 1. Numerical models with applications to the tectonics of the Himalayan-Tibetan orogen. Journal of Geophysical Research: Solid Earth, 109(B6).

Beck, R.A., Burbank, D.W., Sercombe, W.J., Riley, G.W., Barndt, J.K., Berry, J.R., Afzal, J., Khan, A.M., Jurgen, H. and Metje, J., 1995. Stratigraphic evidence for an early collision between northwest India and Asia. Nature, 373(6509): 55-58.

Belkaaloul, N.K. and Aïssaoui, D.M., 1997. Nature and origin of magnetic minerals within the Middle Jurassic shallow-water carbonate rocks of the Paris Basin, France: implications for magnetostratigraphic dating. Geophysical Journal International, 130(2): 411-421.

Besse, J. and Courtillot, V., 2002. Apparent and true polar wander and the geometry of the geomagnetic field over the last 200 Myr. Journal of Geophysical Research: Solid Earth, 107(B11): EPM 6-1-EPM 6-31.

Besse, J. and Courtillot, V., 2003. Correction to "Apparent and true polar wander and the geometry of the geomagnetic field over the last 200 Myr". Journal of Geophysical Research: Solid Earth, 108(B10).

Beuscher, S., Krüger, S., Ehrmann, W., Schmiedl, G., Milker, Y., Arz, H. and Schulz, H., 2017. End-member modelling as a tool for climate reconstruction—an Eastern Mediterranean case study. Plos one, 12(9): e0185136.

Bian, W., Yang, T., Ma, Y., Jin, J., Gao, F., Zhang, S., Wu, H. and Li, H., 2017. New Early Cretaceous palaeomagnetic and geochronological results from the far western Lhasa terrane: Contributions to the Lhasa-Qiangtang collision. Scientific reports, 7(1): 1-14.

Bilardello, D., 2021. Late Paleozoic depositional environments and sediment transport directions of the Itararé Group rocks from the state of São Paulo, Brazil, determined from rock magnetism and magnetic anisotropy. Earth and

Space Science, 8(7): e2021EA001703.
Blakely, R.J., 1996. Potential theory in gravity and magnetic applications. Cambridge university press.
Blumstein, A.M., Elmore, R.D., Engel, M.H., Elliot, C. and Basu, A., 2004. Paleomagnetic dating of burial diagenesis in Mississippian carbonates, Utah. Journal of Geophysical Research: Solid Earth, 109(B4).
Bons, P.D., Elburg, M.A. and Gomez-Rivas, E., 2012. A review of the formation of tectonic veins and their microstructures. Journal of Structural Geology, 43: 33-62.
Bonvalot, S., Balmino, G., Briais, A., Kuhn, M., Peyrefitte, A., Vales, N. and Sarrailh, M., 2012. World Gravity Map. Bureau Gravimetrique International (BGI), map, CGMW-BGI-CNES728, IRD, Paris.
Borradaile, G., 1987. Anisotropy of magnetic susceptibility: rock composition versus strain. Tectonophysics, 138(2-4): 327-329.
Borradaile, G.J., 1988. Magnetic susceptibility, petrofabrics and strain. Tectonophysics, 156(1-2): 1-20.
Borradaile, G.J. and Lagroix, F., 2000. Magnetic characterization using a three-dimensional hysteresis projection, illustrated with a study of limestones. Geophysical Journal International, 141(1): 213-226.
Borradaile, G. and Hamilton, T., 2003. Limestones distinguished by magnetic hysteresis in three-dimensional projections. Geophysical research letters, 30(18).
Borradaile, G.J. and Jackson, M., 2010. Structural geology, petrofabrics and magnetic fabrics (AMS, AARM, AIRM). Journal of Structural Geology, 32(10): 1519-1551.
Brace, W. and Kohlstedt, D., 1980. Limits on lithospheric stress imposed by laboratory experiments. Journal of Geophysical Research: Solid Earth, 85(B11): 6248-6252.
Brewer, M., Tetzlaff, D., Malcolm, I. and Soulsby, C., 2011. Source distribution modelling for end-member mixing in hydrology. Environmetrics, 22(8): 921-932.
Brothers, L., Engel, M. and Elmore, R., 1996. The late diagenetic conversion of pyrite to magnetite by organically complexed ferric iron. Chemical Geology, 130(1-2): 1-14.
Burchfiel, B., Quidong, D., Molnar, P., Royden, L., Yipeng, W., Peizhen, Z. and Weiqi, Z., 1989. Intracrustal detachment within zones of continental deformation. Geology, 17(8): 748-752.
Burnham, K.P. and Anderson, D.R., 2002. A practical information-theoretic approach. Model selection and multimodel inference, 2.
Butler, R.F. and Butler, R.F., 1992. Paleomagnetism: magnetic domains to geologic terranes, 319. Blackwell Scientific Publications Boston.
Calvín Ballester, P., Villalaín Santamaria, J.J. and Casas Sainz, A.M., 2018a. The carriers of AMS in remagnetized carbonates. Insights for remagnetization mechanism and basin evolution. Physics of the Earth and Planetary Interiors.

V. 282, p. 1-20.
Calvín, P., Villalaín, J.J. and Casas-Sainz, A.M., 2018b. Anisotropic magnetite growth in remagnetized limestones: Tectonic constraints and implications for basin history. Geology, 46(9): 751-754.
Canfield, D.E., Thamdrup, B. and Hansen, J.W., 1993. The anaerobic degradation of organic matter in Danish coastal sediments: iron reduction, manganese reduction, and sulfate reduction. Geochimica et Cosmochimica Acta, 57(16): 3867-3883.
Cañón-Tapia, E. and Mendoza-Borunda, R., 2014. Magnetic petrofabric of igneous rocks: Lessons from pyroclastic density current deposits and obsidians. Journal of volcanology and geothermal research, 289: 151-169.
Cao, Y., Sun, Z., Li, H., Pei, J., Liu, D., Zhang, L., Ye, X., Zheng, Y., He, X. and Ge, C., 2019. New paleomagnetic results from Middle Jurassic limestones of the Qiangtang terrane, Tibet: Constraints on the evolution of the Bangong-Nujiang Ocean. Tectonics, 38(1): 215-232.
Cao, Y., Sun, Z., Li, H., Ye, X., Pan, J., Liu, D., Zhang, L., Wu, B., Cao, X. and Liu, C., 2020. Paleomagnetism and U-Pb Geochronology of Early Cretaceous Volcanic Rocks from the Qiangtang Block, Tibetan Plateau: Implications for the Qiangtang-Lhasa Collision. Tectonophysics, 789: 228500.
Cao, X., Sun, Z., Li, H., Cao, Y., Huang, B., Wu, B., Ye, X., Liu, C., Yang, Z. and Berndt, T.A., 2021. Cenozoic deformation in the Tethyan Himalaya, SE Tibet: Insights from magnetic fabrics and structural analysis of Upper Triassic flysch. Tectonophysics, 814: 228967.
Cardozo, N. and Allmendinger, R.W., 2013. Spherical projections with OSXStereonet. Computers & Geosciences, 51: 193-205.
Chadima, M. and Jelinek, V., 2009. Anisoft 4.2: Anisotropy data browser for windows. Agico Inc., Brno.
Channell, J. and McCabe, C., 1994. Comparison of magnetic hysteresis parameters of unremagnetized and remagnetized limestones. Journal of Geophysical Research: Solid Earth, 99(B3): 4613-4623.
Chen, W.P. and Molnar, P., 1983. Focal depths of intracontinental and intraplate earthquakes and their implications for the thermal and mechanical properties of the lithosphere. Journal of Geophysical Research: Solid Earth, 88(B5): 4183-4214.
Chen, L. and Gerya, T.V., 2016. The role of lateral lithospheric strength heterogeneities in orogenic plateau growth: Insights from 3-D thermo-mechanical modeling. Journal of Geophysical Research: Solid Earth, 121(4): 3118-3138.
Chen, Y., Cogné, J., Courtillot, V., Tapponnier, P. and Zhu, X., 1993. Cretaceous paleomagnetic results from western Tibet and tectonic implications. Journal of Geophysical Research: Solid Earth, 98(B10): 17981-17999.
Chen, H., Jon, D., Friedrich, H. and Hao, J., 1995. Paleomagnetic evidence for clockwise rotation of the Simao region since the Cretaceous: a consequence of

India-Asia collision. Earth and Planetary Science Letters, 134(1-2): 203-217.
Chen, Y., Li, W., Yuan, X., Badal, J. and Teng, J., 2015. Tearing of the Indian lithospheric slab beneath southern Tibet revealed by SKS-wave splitting measurements. Earth and Planetary Science Letters, 413: 13-24.
Chen, S.S., Shi, R.D., Fan, W.M., Gong, X.H. and Wu, K., 2017a. Early Permian mafic dikes in the Nagqu area, central Tibet, China, associated with embryonic oceanic crust of the Meso-Tethys Ocean. Journal of Geophysical Research: Solid Earth, 122(6): 4172-4190.
Chen, W., Zhang, S., Ding, J., Zhang, J., Zhao, X., Zhu, L., Yang, W., Yang, T., Li, H. and Wu, H., 2017b. Combined paleomagnetic and geochronological study on Cretaceous strata of the Qiangtang terrane, central Tibet. Gondwana Research, 41: 373-389.
Chen, Y., Ding, L., Li, Z., Laskowski, A.K., Li, J., Baral, U., Qasim, M. and Yue, Y., 2020. Provenance analysis of Cretaceous peripheral foreland basin in central Tibet: Implications to precise timing on the initial Lhasa-Qiangtang collision. Tectonophysics, 775: 228311.
Cheng, X., Wu, H., Diao, Z., Wang, H., Zhang, X., Ma, L., Zhou, Y., Kang, W., Ji, W. and Li, R., 2012. New paleomagnetic result of the Middle-Late Jurassic rocks from northern Qiangtang Block, west China. Chinese Journal of Geophysics, 55(10): 3399-3409.
Christensen, P.B., Nielsen, L.P. and Revsbech, N.P., 1989. Microzonation of denitrification activity in stream sediments as studied with a combined oxygen and nitrous oxide microsensor. Applied and Environmental Microbiology, 55(5): 1234-1241.
Cifelli, F., Mattei, M., Hirt, A. and Günther, A., 2004. The origin of tectonic fabrics in "undeformed" clays: the early stages of deformation in extensional sedimentary basins. Geophysical Research Letters, 31(9).
Cifelli, F., Mattei, M., Chadima, M., Hirt, A. and Hansen, A., 2005. The origin of tectonic lineation in extensional basins: combined neutron texture and magnetic analyses on "undeformed" clays. Earth and Planetary Science Letters, 235(1-2): 62-78.
Cifelli, F., Mattei, M., Chadima, M., Lenser, S. and Hirt, A., 2009. The magnetic fabric in "undeformed clays": AMS and neutron texture analyses from the Rif Chain (Morocco). Tectonophysics, 466(1-2): 79-88.
Clark, M.K. and Royden, L.H., 2000. Topographic ooze: Building the eastern margin of Tibet by lower crustal flow. Geology, 28(8): 703-706.
Clark, M., Schoenbohm, L., Royden, L., Whipple, K., Burchfiel, B., Zhang, X., Tang, W., Wang, E. and Chen, L., 2004. Surface uplift, tectonics, and erosion of eastern Tibet from large-scale drainage patterns. Tectonics, 23(1).
Clark, M.K., House, M., Royden, L., Whipple, K., Burchfiel, B., Zhang, X. and Tang, W., 2005. Late Cenozoic uplift of southeastern Tibet. Geology, 33(6): 525-528.
Cogné, J., Halim, N., Chen, Y. and Courtillot, V., 1999. Resolving the problem of shallow magnetizations of Tertiary age in Asia: Insights from paleomagnetic

data from the Qiangtang, Kunlun, and Qaidam blocks (Tibet, China), and a new hypothesis. Journal of Geophysical Research: Solid Earth, 104(B8): 17715-17734.

Copley, A. and McKenzie, D., 2007. Models of crustal flow in the India-Asia collision zone. Geophysical Journal International, 169(2): 683-698.

Dankers, P. and Zijderveld, J., 1981. Alternating field demagnetization of rocks, and the problem of gyromagnetic remanence. Earth and Planetary Science Letters, 53(1): 89-92.

Day, R., Fuller, M. and Schmidt, V., 1977. Hysteresis properties of titanomagnetites: grain-size and compositional dependence. Physics of the Earth and planetary interiors, 13(4): 260-267.

Deenen, M.H., Langereis, C.G., van Hinsbergen, D.J. and Biggin, A.J., 2011. Geomagnetic secular variation and the statistics of palaeomagnetic directions. Geophysical Journal International, 186(2): 509-520.

Deenen, M.H., Langereis, C.G., van Hinsbergen, D.J. and Biggin, A.J., 2014. Erratum: Geomagnetic secular variation and the statistics of palaeomagnetic directions. Geophysical Journal International, 197(1): 643-643.

Dekkers, M.J., 2012. End-member modelling as an aid to diagnose remagnetization: A brief review. Geological Society, London, Special Publications, 371(1): 253-269.

Dekkers, M. and Pietersen, H.S., 1991. Magnetic properties of low-Ca fly ash: a rapid tool for Fe-assessment and a survey for potentially hazardous elements. MRS Online Proceedings Library, 245(1): 37-47.

Dekkers, M. and Pietersen, H., 1992. Magnetic properties of low-Ca fly ash: a rapid tool for Fe-assesment and a survey for potentially hazardous elements, Mat. Res. Soc. Symp. Proc, pp. 37-47.

Dekkers, M.J., Passier, H.F. and Schoonen, M.A., 2000. Magnetic properties of hydrothermally synthesized greigite (Fe_3S_4)—II. High-and low-temperature characteristics. Geophysical Journal International, 141(3): 809-819.

Dewey, J.F., Shackleton, R.M., Chengfa, C. and Yiyin, S., 1988. The tectonic evolution of the Tibetan Plateau. Philosophical Transactions of the Royal Society of London. Series A, Mathematical and Physical Sciences, 327(1594): 379-413.

Dewey, J., Cande, S. and Pitman, W.C., 1989. Tectonic evolution of the India/Eurasia collision zone. Eclogae Geologicae Helvetiae, 82(3): 717-734.

Ding, L., Kapp, P. and Wan, X., 2005. Paleocene–Eocene record of ophiolite obduction and initial India-Asia collision, south central Tibet. Tectonics, 24(3).

Ding, L., Yang, D., Cai, F., Pullen, A., Kapp, P., Gehrels, G.E., Zhang, L., Zhang, Q., Lai, Q. and Yue, Y., 2013. Provenance analysis of the Mesozoic Hoh-Xil-Songpan-Ganzi turbidites in northern Tibet: Implications for the tectonic evolution of the eastern Paleo-Tethys Ocean. Tectonics, 32(1): 34-48.

Ding, L., Xu, Q., Yue, Y., Wang, H., Cai, F. and Li, S., 2014. The andean-type gangdese mountains: paleoelevation record from the paleocene–eocene linzhou basin.

Earth and Planetary Science Letters, 392: 250-264.
Ding, L., Maksatbek, S., Cai, F., Wang, H., Song, P., Ji, W., Xu, Q., Zhang, L., Muhammad, Q. and Upendra, B., 2017. Processes of initial collision and suturing between India and Asia. Science China Earth Sciences, 60(4): 635-651.
Dong, X., Wang, Z., Tan, C., Yang, H., Cheng, L. and Zhou, Y., 1990. New paleomagnetic results from Yadong-Golmud geoscience transect and a preliminary study on the model of terranes evolution in Qinghai-Xizang Plateau. Chinese Academy of Geological Sciences, 21: 139-148.
Dong, X., Wang, Z., Tan, C., Yang, H., Cheng, L. and Zhou, Y., 1991. New results of paleomagnetic studies of the Qinghai-Tibetan plateau. Geol. Rev, 37: 160-164.
Duan, Z., Liu, Q., Qin, H., Zhao, X. and Gao, X., 2020. Behavior of greigite-bearing marine sediments during AF and thermal demagnetization and its significance. Geochemistry, Geophysics, Geosystems, 21(7): e2019GC008635.
Dunlop, D.J., 2002. Theory and application of the Day plot (Mrs/Ms versus Hcr/Hc) 2. Application to data for rocks, sediments, and soils. Journal of Geophysical Research: Solid Earth, 107(B3): EPM 5-1-EPM 5-15.
Dunlop, D. J., & Özdemir, Ö., 1997. Rock magnetism: Fundamentals and frontiers, (pp. 1–573). Cambridge, U.K.: Cambridge University Press. http://doi.org/10.1017/CBO9780511612794.
Dunlop, D.J. and Özdemir, Ö., 2000. Effect of grain size and domain state on thermal demagnetization tails. Geophysical Research Letters, 27(9): 1311-1314.
Dupont-Nivet, G., Lippert, P.C., Van Hinsbergen, D.J., Meijers, M.J. and Kapp, P., 2010a. Palaeolatitude and age of the Indo–Asia collision: palaeomagnetic constraints. Geophysical Journal International, 182(3): 1189-1198.
Dupont-Nivet, G., Van Hinsbergen, D.J. and Torsvik, T.H., 2010b. Persistently low Asian paleolatitudes: Implications for the India-Asia collision history. Tectonics, 29(5).
Egli, R. and Lowrie, W., 2002. Anhysteretic remanent magnetization of fine magnetic particles. Journal of Geophysical Research: Solid Earth, 107(B10): EPM 2-1-EPM 2-21.
Egli, R., 2004. Characterization of individual rock magnetic components by analysis of remanence curves, 1. Unmixing natural sediments. Studia geophysica et geodaetica, 48(2): 391-446.
Egli, R. and Winklhofer, M., 2014. Recent developments on processing and interpretation aspects of first-order reversal curves (FORC). Ученые записки Казанского университета. Серия Естественные науки, 156(1): 14-53.
Ejembi, J.I., Ferré, E.C., Satolli, S. and Friedman, S.A., 2020. Post-depositional fluid flow in Jurassic sandstones of the Uncompahgre Uplift: Insights from magnetic fabrics. Frontiers in Earth Science, 8: 601415.
Eldredge, S., Bachtadse, V. and Van der Voo, R., 1985. Paleomagnetism and the orocline hypothesis. Tectonophysics, 119(1-4): 153-179.
Elmore Douglas, R., Lee-Egger Foucher, J., Evans, M., Lewchuk, M. and Cox, E., 2006. Remagnetization of the Tonoloway Formation and the Helderberg Group in

the Central Appalachians: testing the origin of syntilting magnetizations. Geophysical Journal International, 166(3): 1062-1076.

Elmore, R.D., Muxworthy, A.R. and Aldana, M., 2012. Remagnetization and chemical alteration of sedimentary rocks. Geological Society, London, Special Publications, 371(1): 1-21.

England, P. and Houseman, G., 1989. Extension during continental convergence, with application to the Tibetan Plateau. Journal of Geophysical Research: Solid Earth, 94(B12): 17561-17579.

Evans, M.A., Lewchuk, M. and Elmore, R., 2003. Strain partitioning of deformation mechanisms in limestones: examining the relationship of strain and anisotropy of magnetic susceptibility (AMS). Journal of Structural Geology, 25(9): 1525-1549.

Fabian, K., 2003. Some additional parameters to estimate domain state from isothermal magnetization measurements. Earth and Planetary Science Letters, 213(3-4): 337-345.

Fabian, K. and Von Dobeneck, T., 1997. Isothermal magnetization of samples with stable Preisach function: A survey of hysteresis, remanence, and rock magnetic parameters. Journal of Geophysical Research: Solid Earth, 102(B8): 17659-17677.

Fan, J., Li, C., Xie, C. and Wang, M., 2014. Petrology, geochemistry, and geochronology of the Zhonggang ocean island, northern Tibet: implications for the evolution of the Banggongco–Nujiang oceanic arm of the Neo-Tethys. International Geology Review, 56(12): 1504-1520.

Fan, J., Li, C., Xie, C., Wang, M. and Chen, J., 2015. The evolution of the Bangong–Nujiang Neo-Tethys ocean: Evidence from zircon U–Pb and Lu–Hf isotopic analyses of Early Cretaceous oceanic islands and ophiolites. Tectonophysics, 655: 27-40.

Fan, J., Li, C., Liu, J., Wang, M., Liu, Y. and Xie, C., 2018a. The Middle Triassic evolution of the Bangong–Nujiang Tethyan Ocean: evidence from analyses of OIB-type basalts and OIB-derived phonolites in northern Tibet. International Journal of Earth Sciences, 107(5): 1755-1775.

Fan, J., Li, C., Wang, M. and Xie, C., 2018b. Reconstructing in space and time the closure of the middle and western segments of the Bangong–Nujiang Tethyan Ocean in the Tibetan Plateau. International Journal of Earth Sciences, 107(1): 231-249.

Fang, X., Song, C., Yan, M., Zan, J., Liu, C., Sha, J., Zhang, W., Zeng, Y., Wu, S. and Zhang, D., 2016. Mesozoic litho-and magneto-stratigraphic evidence from the central Tibetan Plateau for megamonsoon evolution and potential evaporites. Gondwana Research, 37: 110-129.

Fazzito, S.Y., Rapalini, A.E., Geuna, S.E. and Poiré, D.G., 2020. Remagnetized limestones and dolostones from the Upper Cambrian La Flecha Formation, La Rioja province, Argentine Precordillera. Journal of South American Earth Sciences, 104: 102891.

Fedi, M. and Quarta, T., 1998. Wavelet analysis for the regional-residual and local separation of potential field anomalies. Geophysical prospecting, 46(5): 507-525.

Feng, J., Yao, H., Chen, L. and Wang, W., 2022. Massive lithospheric delamination in southeastern Tibet facilitating continental extrusion. National science review, 9(4): nwab174.

Ferré, E.C., 2002. Theoretical models of intermediate and inverse AMS fabrics. Geophysical Research Letters, 29(7): 31-1-31-4.

Fisher, R.A., 1953. Dispersion on a sphere. Proceedings of the Royal Society of London. Series A. Mathematical and Physical Sciences, 217(1130): 295-305.

Flinn, D., 1965. On the symmetry principle and the deformation ellipsoid. Geological magazine, 102(1): 36-45.

Font, E., Trindade, R. and Nédélec, A., 2006. Remagnetization in bituminous limestones of the Neoproterozoic Araras Group (Amazon craton): hydrocarbon maturation, burial diagenesis, or both? Journal of Geophysical Research: Solid Earth, 111(B6).

Froelich, P.N., Klinkhammer, G., Bender, M.L., Luedtke, N., Heath, G.R., Cullen, D., Dauphin, P., Hammond, D., Hartman, B. and Maynard, V., 1979. Early oxidation of organic matter in pelagic sediments of the eastern equatorial Atlantic: suboxic diagenesis. Geochimica et cosmochimica acta, 43(7): 1075-1090.

Fu, Q., Yan, M., Dekkers, M.J., Guan, C., Yu, L., Xu, W., Li, B., Feng, Z., Xu, Z. and Shen, M., 2022a. Remagnetization of the Jurassic limestones in the Zaduo area, Eastern Qiangtang Terrane (Tibetan Plateau, China): Implications for the India-Eurasia collision. Geophysical Journal International.

Fu, Q., Yan, M., Dekkers, M.J., Guan, C., de Boer, R.A., Yu, L., Xu, W., Li, B., Shen, M. and Zhang, J., 2022b. The Early Cretaceous Zaduo Granite, Eastern Qiangtang Terrane (China): An Attempt to Constrain its Paleolatitude and Tectonic Implications. Frontiers in Earth Science, 10: 1-22.

Fu, Y., von Dobeneck, T., Franke, C., Heslop, D. and Kasten, S., 2008. Rock magnetic identification and geochemical process models of greigite formation in Quaternary marine sediments from the Gulf of Mexico (IODP Hole U1319A). Earth and Planetary Science Letters, 275(3-4): 233-245.

Fuller, M.D., 1963. Magnetic anisotropy and paleomagnetism. Journal of Geophysical Research, 68(1): 293-309.

Fuller, M., 1969. Magnetic orientation of borehole cores. Geophysics, 34(5): 772-774.

Gale, J.F., Laubach, S.E., Olson, J.E., Eichhubl, P. and Fall, A., 2014. Natural fractures in shale: A review and new observationsNatural Fractures in Shale: A Review and New Observations. AAPG bulletin, 98(11): 2165-2216.

Gale, A., Mutterlose, J., Batenburg, S., Gradstein, F., Agterberg, F., Ogg, J. and Petrizzo, M., 2020. The Cretaceous Period, Geologic Time Scale 2020. Elsevier, pp. 1023-1086.

Gao, D., Hou, Z. and Tang, J., 2000. Multiscale analysis of gravity anomalies on East

China Sea and adjacent regions. Chinese journal of geophysics, 43(6): 889-896.
Gao, R., Xiong, X., Li, Q. and Lu, Z., 2009. The Moho depth of Qinghai-Tibet Plateau revealed by seismic detection. Acta Geoscientica Sinica, 30(6): 761-773.
Gao, L., Yang, Z., Tong, Y., Wang, H. and An, C., 2015. New paleomagnetic studies of Cretaceous and Miocene rocks from Jinggu, western Yunnan, China: Evidence for internal deformation of the Lanping–Simao Terrane. Journal of Geodynamics, 89: 39-59.
Gao, L., Yang, Z., Han, Z., Tong, Y., Jing, X. and Zhang, S.H., 2018. Remagnetization of the Lower Ordovician Hongshiya Formation of the southwestern Yangtze Block. Tectonophysics, 738: 83-91.
García-Lasanta, C., Oliva-Urcia, B., Román-Berdiel, T., Casas, A., Gil-Peña, I., Sánchez-Moya, Y., Sopeña, A., Hirt, A. and Mattei, M., 2015. Evidence for the Permo-Triassic transtensional rifting in the Iberian Range (NE Spain) according to magnetic fabrics results. Tectonophysics, 651: 216-231.
García-Lasanta, C., Oliva-Urcia, B., Casas-Sainz, A., Román-Berdiel, T., Izquierdo-Llavall, E., Soto, R., Calvín, P., Moussaid, B., El Ouardi, H. and Kullberg, J., 2018. Inversion tectonics and magnetic fabrics in Mesozoic basins of the Western Tethys: A review. Tectonophysics, 745: 1-23.
Garzanti, E., Sciunnach, D., Gaetani, M., Corfield, R., Watts, A. and Searle, M., 2005. Discussion on subsidence history of the north Indian continental margin, Zanskar–Ladakh Himalaya, NW India Journal, Vol. 162, 2005, pp. 135–146. Journal of the Geological Society, 162(5): 889-892.
Ge, K., Liu, Q., Deng, J., Nobes, D., Wang, Y., Wang, Y. and Chen, X., 2017. Rock magnetic investigation and its geological significance for vein-type uranium deposits in southern C hina. Geochemistry, Geophysics, Geosystems, 18(4): 1333-1349.
Gehrels, G., Kapp, P., DeCelles, P., Pullen, A., Blakey, R., Weislogel, A., Ding, L., Guynn, J., Martin, A. and McQuarrie, N., 2011. Detrital zircon geochronology of pre-Tertiary strata in the Tibetan-Himalayan orogen. Tectonics, 30(5).
Geiss, C.E., Umbanhowar, C.E., Camill, P. and Banerjee, S.K., 2003. Sediment magnetic properties reveal Holocene climate change along the Minnesota prairie-forest ecotone. Journal of Paleolimnology, 30(2): 151-166.
Geological Map (1:250000) of the People's Republic of China-Zaduo County Sheet, China (QGSI), 2005. University of Geosciences Press.
Geological Survey Report of the People's Republic of China, Zaduo County Sheet (1:250000), China (QGSI), 2014. University of Geosciences Press.
Geological Survey Report of the People's Republic of China-Zaduo County Sheet (1:200000), China (STRGSQ)., 1988. China Geological Map Press.
Goetze, C. and Evans, B., 1979. Stress and temperature in the bending lithosphere as constrained by experimental rock mechanics. Geophysical Journal International, 59(3): 463-478.
Gong, Z., Dekkers, M., Heslop, D. and Mullender, T., 2009. End-member modelling of isothermal remanent magnetization (IRM) acquisition curves: a novel

approach to diagnose remagnetization. Geophysical Journal International, 178(2): 693-701.

Guan, C., Yan, M., Zhang, W., Zhang, D., Fu, Q., Yu, L., Xu, W., Zan, J., Li, B. and Zhang, T., 2021. Paleomagnetic and Chronologic Data Bearing on the Permian/Triassic Boundary Position of Qamdo in the Eastern Qiantang Terrane: Implications for the Closure of the Paleo-Tethys. Geophysical Research Letters, 48(6): e2020GL092059.

Gustavson, T.C., Hovorka, S.D. and Dutton, A.R., 1994. Origin of satin spar veins in evaporite basins. Journal of Sedimentary Research, 64(1a): 88-94.

Gutiérrez-Alonso, G., Fernández-Suárez, J., Weil, A.B. and Sussman, A., 2004. Orocline triggered lithospheric delamination, Orogenic curvature: Integrating paleomagnetic and structural analyses. Geological Society of America Boulder, CO, USA, pp. 121-130.

Hamann, Y., Ehrmann, W., Schmiedl, G., Krüger, S., Stuut, J.-B. and Kuhnt, T., 2008. Sedimentation processes in the Eastern Mediterranean Sea during the Late Glacial and Holocene revealed by end-member modelling of the terrigenous fraction in marine sediments. Marine Geology, 248(1-2): 97-114.

Hargraves, R.B. and Fischer, A.G., 1959. Remanent magnetism in Jurassic red limestones and radiolarites from the Alps. Geophysical Journal International, 2(1): 34-41.

Harrison, R.J. and Feinberg, J.M., 2008. FORCinel: An improved algorithm for calculating first-order reversal curve distributions using locally weighted regression smoothing. Geochemistry, Geophysics, Geosystems, 9(5).

Harrison, R.J. and Lascu, I., 2014. FORCulator: A micromagnetic tool for simulating first-order reversal curve diagrams. Geochemistry, Geophysics, Geosystems, 15(12): 4671-4691.

Heslop, D. and Dillon, M., 2007. Unmixing magnetic remanence curves without a priori knowledge. Geophysical Journal International, 170(2): 556-566.

Heslop, D., McIntosh, G. and Dekkers, M., 2004. Using time-and temperature-dependent Preisach models to investigate the limitations of modelling isothermal remanent magnetization acquisition curves with cumulative log Gaussian functions. Geophysical Journal International, 157(1): 55-63.

Hinze, W.J., Von Frese, R.R., Von Frese, R. and Saad, A.H., 2013. Gravity and magnetic exploration: Principles, practices, and applications. Cambridge University Press.

Hoke, G.D., Liu-Zeng, J., Hren, M.T., Wissink, G.K. and Garzione, C.N., 2014. Stable isotopes reveal high southeast Tibetan Plateau margin since the Paleogene. Earth and Planetary Science Letters, 394: 270-278.

Horton Jr, R.A., Geissman, J.W. and Tschauder, R.J., 1984. Paleomagnetism and rock magnetism of the Mississippian Leadville (carbonate) formation and implications for the age of sub-regional dolomitization. Geophysical Research Letters, 11(7): 649-652.

Horton, B.K., Yin, A., Spurlin, M.S., Zhou, J. and Wang, J., 2002. Paleocene–Eocene

syncontractional sedimentation in narrow, lacustrine-dominated basins of east-central Tibet. Geological Society of America Bulletin, 114(7): 771-786.

Hou, Z., Zaw, K., Pan, G., Mo, X., Xu, Q., Hu, Y. and Li, X., 2007. Sanjiang Tethyan metallogenesis in SW China: Tectonic setting, metallogenic epochs and deposit types. Ore Geology Reviews, 31(1-4): 48-87.

Hou, Z. and Zhang, H., 2015. Geodynamics and metallogeny of the eastern Tethyan metallogenic domain. Ore Geology Reviews, 70: 346-384.

Hounslow, M., 1985. Magnetic fabric arising from paramagnetic phyllosilicate minerals in mudrocks. Journal of the Geological Society, 142(6): 995-1006.

Hrouda, F., 1982. Magnetic anisotropy of rocks and its application in geology and geophysics. Geophysical surveys, 5(1): 37-82.

Hrouda, F. and Jelinek, V., 1990. Resolution of ferrimagnetic and paramagnetic anisotropies in rocks, using combined low-field and high-field measurements. Geophysical Journal International, 103(1): 75-84.

Hu, S., Appel, E., Hoffmann, V., Schmahl, W.W. and Wang, S., 1998. Gyromagnetic remanence acquired by greigite (Fe3S4) during static three-axis alternating field demagnetization. Geophysical Journal International, 134(3): 831-842.

Hu, S., Stephenson, A. and Appel, E., 2002. A study of gyroremanent magnetisation (GRM) and rotational remanent magnetisation (RRM) carried by greigite from lake sediments. Geophysical Journal International, 151(2): 469-474.

Hu, F., Wu, F.Y., Ducea, M.N., Chapman, J.B. and Yang, L., 2022. Does Large-Scale Crustal Flow Shape the Eastern Margin of the Tibetan Plateau? Insights From Episodic Magmatism of Gongga-Zheduo Granitic Massif. Geophysical research letters, 49(12): e2022GL098756.

Huang, K. and Opdyke, N.D., 2015. Post-folding magnetization of the Triassic rocks from western Guizhou and southern Yunnan provinces: New evidence for large clockwise rotations in the Simao Terrane. Earth and Planetary Science Letters, 423: 155-163.

Huang, K., Opdyke, N.D., Li, J. and Peng, X., 1992. Paleomagnetism of Cretaceous rocks from eastern Qiangtang terrane of Tibet. Journal of Geophysical Research: Solid Earth, 97(B2): 1789-1799.

Huang, W., Van Hinsbergen, D.J., Dekkers, M.J., Garzanti, E., Dupont-Nivet, G., Lippert, P.C., Li, X., Maffione, M., Langereis, C.G. and Hu, X., 2015a. Paleolatitudes of the T ibetan H imalaya from primary and secondary magnetizations of J urassic to L ower Cretaceous sedimentary rocks. Geochemistry, Geophysics, Geosystems, 16(1): 77-100.

Huang, W., van Hinsbergen, D.J., Maffione, M., Orme, D.A., Dupont-Nivet, G., Guilmette, C., Ding, L., Guo, Z. and Kapp, P., 2015b. Lower Cretaceous Xigaze ophiolites formed in the Gangdese forearc: Evidence from paleomagnetism, sediment provenance, and stratigraphy. Earth and Planetary Science Letters, 415: 142-153.

Huang, W., Van Hinsbergen, D.J., Lippert, P.C., Guo, Z. and Dupont-Nivet, G., 2015c. Paleomagnetic tests of tectonic reconstructions of the India-Asia collision

zone. Geophysical Research Letters, 42(8): 2642-2649.
Huang, W., Dupont-Nivet, G., Lippert, P.C., Van Hinsbergen, D.J., Dekkers, M.J., Guo, Z., Waldrip, R., Li, X., Zhang, X. and Liu, D., 2015d. Can a primary remanence be retrieved from partially remagnetized Eocence volcanic rocks in the Nanmulin Basin (southern Tibet) to date the India-Asia collision? Journal of Geophysical Research: Solid Earth, 120(1): 42-66.
Huang, W., Dupont-Nivet, G., Lippert, P.C., Van Hinsbergen, D.J., Dekkers, M.J., Waldrip, R., Ganerød, M., Li, X., Guo, Z. and Kapp, P., 2015e. What was the Paleogene latitude of the Lhasa terrane? A reassessment of the geochronology and paleomagnetism of Linzizong volcanic rocks (Linzhou basin, Tibet). Tectonics, 34(3): 594-622.
Huang, W., Lippert, P.C., Jackson, M.J., Dekkers, M.J., Zhang, Y., Li, J., Guo, Z., Kapp, P. and van Hinsbergen, D.J., 2017a. Remagnetization of the Paleogene Tibetan Himalayan carbonate rocks in the Gamba area: Implications for reconstructing the lower plate in the India-Asia collision. Journal of Geophysical Research: Solid Earth, 122(2): 808-825.
Huang, W., Lippert, P.C., Zhang, Y., Jackson, M.J., Dekkers, M.J., Li, J., Hu, X., Zhang, B., Guo, Z. and van Hinsbergen, D.J., 2017b. Remagnetization of carbonate rocks in southern Tibet: Perspectives from rock magnetic and petrographic investigations. Journal of Geophysical Research: Solid Earth, 122(4): 2434-2456.
Huang, W., Jackson, M.J., Dekkers, M.J., Solheid, P., Zhang, B., Guo, Z. and Ding, L., 2019a. Nanogoethite as a potential indicator of remagnetization in red beds. Geophysical Research Letters, 46(22): 12841-12850.
Huang, W., Jackson, M.J., Dekkers, M.J., Zhang, Y., Zhang, B., Guo, Z. and Dupont-Nivet, G., 2019b. Challenges in isolating primary remanent magnetization from Tethyan carbonate rocks on the Tibetan Plateau: Insight from remagnetized Upper Triassic limestones in the eastern Qiangtang block. Earth and Planetary Science Letters, 523: 115695.
Huang, W., Jackson, M.J., Dekkers, M.J., Solheid, P., Zhang, Y., Li, S., Guo, Z. and Ding, L., 2020. Remagnetization of red beds on the Tibetan Plateau: mechanism and diagnosis. Journal of Geophysical Research: Solid Earth, 125(8): e2020JB020068.
Hunt, C.P., Moskowitz, B.M. and Banerjee, S.K., 1995. Magnetic properties of rocks and minerals. Rock physics and phase relations: A handbook of physical constants, 3: 189-204.
Jackson, M., 1990. Diagenetic sources of stable remanence in remagnetized Paleozoic cratonic carbonates: A rock magnetic study. Journal of Geophysical Research: Solid Earth, 95(B3): 2753-2761.
Jackson, M., 1991. Anisotropy of magnetic remanence: a brief review of mineralogical sources, physical origins, and geological applications, and comparison with susceptibility anisotropy. Pure and Applied Geophysics, 136(1): 1-28.
Jackson, M., Rochette, P., Fillion, G., Banerjee, S. and Marvin, J., 1993. Rock magnetism of remagnetized Paleozoic carbonates: Low-temperature behavior

and susceptibility characteristics. Journal of Geophysical Research: Solid Earth, 98(B4): 6217-6225.

Jackson, M. and Swanson-Hysell, N.L., 2012. Rock magnetism of remagnetized carbonate rocks: Another look. Geological Society, London, Special Publications, 371(1): 229-251.

Jadoon, U.F., Huang, B., Zhao, Q., Shah, S.A. and Rahim, Y., 2021. Remagnetization of Jutal dykes in Gilgit area of the Kohistan Island Arc: Perspectives from the India–Asia collision. Geophysical Journal International, 226(1): 33-46.

Jelínek, V., 1977. The statistical theory of measuring anisotropy of magnetic susceptibility of rocks and its application, 29. Geofyzika Brno, Czech Republic.

Jelínek, V., 1981. Characterization of the magnetic fabric of rocks. Tectonophysics, 79(3-4): T63-T67.

Jelínek, V. and Kropáček, V., 1978. Statistical processing of anisotropy of magnetic susceptibility measured on groups of specimens. Studia geophysica et geodaetica, 22(1): 50-62.

Jia, D., Chen, Z., Luo, L., Hu, Q. and Jia, Q., 2007. Magnetic fabrics in fault-related fold and its relation with finite strain: an example from Mingjiang thrust structures in Western Sichuan. Progress in Natural Science, 17(5): 551-558.

Jian, P., Liu, D., Kröner, A., Zhang, Q., Wang, Y., Sun, X. and Zhang, W., 2009a. Devonian to Permian plate tectonic cycle of the Paleo-Tethys Orogen in southwest China (I): geochemistry of ophiolites, arc/back-arc assemblages and within-plate igneous rocks. Lithos, 113(3-4): 748-766.

Jian, P., Liu, D., Kröner, A., Zhang, Q., Wang, Y., Sun, X. and Zhang, W., 2009b. Devonian to Permian plate tectonic cycle of the Paleo-Tethys Orogen in southwest China (II): insights from zircon ages of ophiolites, arc/back-arc assemblages and within-plate igneous rocks and generation of the Emeishan CFB province. Lithos, 113(3-4): 767-784.

Jiang, Z., Liu, Q., Dekkers, M.J., Tauxe, L., Qin, H., Barrón, V. and Torrent, J., 2015. Acquisition of chemical remanent magnetization during experimental ferrihydrite–hematite conversion in Earth-like magnetic field—implications for paleomagnetic studies of red beds. Earth and Planetary Science Letters, 428: 1-10.

Jiang, Z., Liu, Q., Dekkers, M.J., Zhao, X., Roberts, A.P., Yang, Z., Jin, C. and Liu, J., 2017. Remagnetization mechanisms in Triassic red beds from South China. Earth and Planetary Science Letters, 479: 219-230.

Jiang, K., Liang, W., Wu, G., Liu, C., Zou, X., He, X., Li, J., Wang, X., Zheng, B. and Shen, Q., 2022. Anisotropy of magnetic susceptibility study and its significance in the Late Cretaceous-Cenozoic Sanmenxia Basin in the southeastern Shanxi rift, Central China. Solid Earth Sciences.

Johnston, S.T., Weil, A. and Gutiérrez-Alonso, G., 2013. Oroclines: Thick and thin. Bulletin, 125(5-6): 643-663.

Kanamatsu, T., Herrero-Bervera, E. and Taira, A., 2001. Magnetic fabrics of soft-sediment folded strata within a Neogene accretionary complex, the Miura

group, central Japan. Earth and Planetary Science Letters, 187(3-4): 333-343.
Kao, S., Horng, C., Roberts, A.P. and Liu, K., 2004. Carbon–sulfur–iron relationships in sedimentary rocks from southwestern Taiwan: influence of geochemical environment on greigite and pyrrhotite formation. Chemical Geology, 203(1-2): 153-168.
Kapp, P., Yin, A., Manning, C.E., Murphy, M., Harrison, T.M., Spurlin, M., Ding, L., Deng, X. and Wu, C., 2000. Blueschist-bearing metamorphic core complexes in the Qiangtang block reveal deep crustal structure of northern Tibet. Geology, 28(1): 19-22.
Kapp, P., Murphy, M.A., Yin, A., Harrison, T.M., Ding, L. and Guo, J., 2003a. Mesozoic and Cenozoic tectonic evolution of the Shiquanhe area of western Tibet. Tectonics, 22(4).
Kapp, P., Yin, A., Manning, C.E., Harrison, T.M., Taylor, M.H. and Ding, L., 2003b. Tectonic evolution of the early Mesozoic blueschist-bearing Qiangtang metamorphic belt, central Tibet. Tectonics, 22(4).
Kapp, P., Yin, A., Harrison, T.M. and Ding, L., 2005. Cretaceous-Tertiary shortening, basin development, and volcanism in central Tibet. Geological Society of America Bulletin, 117(7-8): 865-878.
Kapp, P., DeCelles, P.G., Gehrels, G.E., Heizler, M. and Ding, L., 2007. Geological records of the Lhasa-Qiangtang and Indo-Asian collisions in the Nima area of central Tibet. Geological Society of America Bulletin, 119(7-8): 917-933.
Kars, M., Aubourg, C., Pozzi, J.P. and Janots, D., 2012. Continuous production of nanosized magnetite through low grade burial. Geochemistry, Geophysics, Geosystems, 13(8).
Kars, M., Aubourg, C., Labaume, P., Berquó, T.S. and Cavailhes, T., 2014. Burial diagenesis of magnetic minerals: New insights from the Grès d'Annot Transect (SE France). Minerals, 4(3): 667-689.
Kent, D.V., 1985. Thermoviscous remagnetization in some Appalachian limestones. Geophysical Research Letters, 12(12): 805-808.
Kent, D.V. and Opdyke, N.D., 1985. Multicomponent magnetizations from the Mississippian Mauch Chunk Formation of the central Appalachians and their tectonic implications. Journal of Geophysical Research: Solid Earth, 90(B7): 5371-5383.
Kirby, S.H., 1983. Rheology of the lithosphere. Reviews of Geophysics, 21(6): 1458-1487.
Kirschvink, J., 1980. The least-squares line and plane and the analysis of palaeomagnetic data. Geophysical Journal International, 62(3): 699-718.
Koç, A., van Hinsbergen, D.J., Kaymakci, N. and Langereis, C.G., 2016. Late Neogene oroclinal bending in the central Taurides: A record of terminal eastward subduction in southern Turkey? Earth and Planetary Science Letters, 434: 75-90.
Kondo, K., Mu, C., Yamamoto, T., Zaman, H., Miura, D., Yokoyama, M., Ahn, H.-S. and Otofuji, Y.-i., 2012. Oroclinal origin of the Simao Arc in the Shan-Thai

Block inferred from the Cretaceous palaeomagnetic data. Geophysical Journal International, 190(1): 201-216.

Kornfeld, D., Eckert, S., Appel, E., Ratschbacher, L., Pfänder, J., Liu, D. and Ding, L., 2014. Clockwise rotation of the Baoshan Block due to southeastward tectonic escape of Tibetan crust since the Oligocene. Geophysical Journal International, 197(1): 149-163.

Koymans, M.R., Langereis, C.G., Pastor-Galán, D. and van Hinsbergen, D.J.J., 2016. Paleomagnetism.org: An online multi-platform open source environment for paleomagnetic data analysis. Computers & Geosciences, 93: 127-137.

Koymans, M., van Hinsbergen, D., Pastor-Galán, D., Vaes, B. and Langereis, C., 2020. Towards FAIR paleomagnetic data management through Paleomagnetism. org 2.0. Geochemistry, Geophysics, Geosystems, 21(2): e2019GC008838.

Kruiver, P.P. and Passier, H.F., 2001. Coercivity analysis of magnetic phases in sapropel S1 related to variations in redox conditions, including an investigation of the S ratio. Geochemistry, Geophysics, Geosystems, 2(12).

Kruiver, P.P., Dekkers, M.J. and Heslop, D., 2001. Quantification of magnetic coercivity components by the analysis of acquisition curves of isothermal remanent magnetisation. Earth and Planetary Science Letters, 189(3-4): 269-276.

Kruse, S., McNutt, M., Phipps-Morgan, J., Royden, L. and Wernicke, B., 1991. Lithospheric extension near Lake Mead, Nevada: A model for ductile flow in the lower crust. Journal of Geophysical Research: Solid Earth, 96(B3): 4435-4456.

Kuypers, M.M., Sliekers, A.O., Lavik, G., Schmid, M., Jørgensen, B.B., Kuenen, J.G., Sinninghe Damsté, J.S., Strous, M. and Jetten, M.S., 2003. Anaerobic ammonium oxidation by anammox bacteria in the Black Sea. Nature, 422(6932): 608-611.

Larrasoaña, J.C., Pueyo, E.L. and Parés, J.M., 2004. An integrated AMS, structural, palaeo-and rock-magnetic study of Eocene marine marls from the Jaca-Pamplona basin (Pyrenees, N Spain); new insights into the timing of magnetic fabric acquisition in weakly deformed mudrocks. Geological Society, London, Special Publications, 238(1): 127-143.

Larrasoaña, J.C., Roberts, A.P., Musgrave, R.J., Gràcia, E., Piñero, E., Vega, M. and Martínez-Ruiz, F., 2007. Diagenetic formation of greigite and pyrrhotite in gas hydrate marine sedimentary systems. Earth and Planetary Science Letters, 261(3-4): 350-366.

Leloup, P.H., Lacassin, R., Tapponnier, P., Schärer, U., Zhong, D., Liu, X., Zhang, L., Ji, S. and Trinh, P.T., 1995. The Ailao Shan-Red river shear zone (Yunnan, China), tertiary transform boundary of Indochina. Tectonophysics, 251(1-4): 3-84.

Li, C., 1987. The Longmucuo-Shuanghu-Lancangjiang plate suture and the north boundary of distribution of Gondwana facies Permo-Carboniferous system in northern Xizang, China. Journal of Changchun College of Geology, 17(2): 155-

166.
Li, C., 2008. A review on 20 years' study of the Longmu Co-Shuanghu-Lancang River suture zone in Qinghai-Xizang (Tibet) Plateau. Geological Review, 54(1): 105-119.
Li, H. and Zhang, S., 2005. Detection of mineralogical changes in pyrite using measurements of temperature-dependence susceptibilities. Chinese Journal of Geophysics, 48(6): 1454-1461.
Li, H. and Zhang, Y., 2013. Zircon U–Pb geochronology of the Konggar granitoid and migmatite: Constraints on the Oligo-Miocene tectono-thermal evolution of the Xianshuihe fault zone, East Tibet. Tectonophysics, 606: 127-139.
Li, Y., Wang, C. and Yi, H., 2002. Filled sequence and evolution of the Mesozoic Qiangtang composite foreland basin in the Qinghai-Tibet Plateau. Journal of Stratigraphy, 26(1): 62-67.
Li, C., Huang, X. and Zhai, Q., 2006. The Longmu Co-Shuanghu-Jitang plate suture and the northern boundary of Gondwanaland in the Qinghai-Tibet plateau. Earth Science Frontiers, 13(4): 136.
Li, C., Zhai, G., Wang, L., Yin, F. and Mao, X., 2009a. An important window for understanding the Qinghai–Tibet Plateau—a review on research progress in recent years of Qiangtang area, Tibet, China. Geological Bulletin of China, 28(9): 1169-1177.
Li, Y.L., Pfiffner, S.M., Dyar, M., Vali, H., Konhauser, K., Cole, D., Rondinone, A. and Phelps, T., 2009b. Degeneration of biogenic superparamagnetic magnetite. Geobiology, 7(1): 25-34.
Li, J., Qin, K., Li, G., Richards, J.P., Zhao, J. and Cao, M., 2014. Geochronology, geochemistry, and zircon Hf isotopic compositions of Mesozoic intermediate–felsic intrusions in central Tibet: Petrogenetic and tectonic implications. Lithos, 198: 77-91.
Li, Y., Wang, C., Dai, J., Xu, G., Hou, Y. and Li, X., 2015. Propagation of the deformation and growth of the Tibetan–Himalayan orogen: A review. Earth-Science Reviews, 143: 36-61.
Li, Z., Ding, L., Lippert, P.C., Song, P., Yue, Y. and van Hinsbergen, D.J., 2016. Paleomagnetic constraints on the Mesozoic drift of the Lhasa terrane (Tibet) from Gondwana to Eurasia. Geology, 44(9): 727-730.
Li, B., Yan, M., Zhang, W., Fang, X., Meng, Q., Zan, J., Chen, Y., Zhang, D., Yang, Y. and Guan, C., 2017a. New paleomagnetic constraints on middle Miocene strike-slip faulting along the middle Altyn Tagh Fault. Journal of Geophysical Research: Solid Earth, 122(6): 4106-4122.
Li, S., Yang, Z., Deng, C., He, H., Qin, H., Sun, L., Yuan, J., Van Hinsbergen, D.J., Krijgsman, W. and Dekkers, M.J., 2017b. Clockwise rotations recorded in redbeds from the Jinggu Basin of northwestern Indochina. GSA Bulletin, 129(9-10): 1100-1122.
Li, Z., Ding, L., Song, P., Fu, J. and Yue, Y., 2017c. Paleomagnetic constraints on the paleolatitude of the Lhasa block during the Early Cretaceous: implications for

the onset of India–Asia collision and latitudinal shortening estimates across Tibet and stable Asia. Gondwana Research, 41: 352-372.

Li, X., Chen, J., Wang, R. and Li, C., 2018. Temporal and spatial variations of Late Mesozoic granitoids in the SW Qiangtang, Tibet: Implications for crustal architecture, Meso-Tethyan evolution and regional mineralization. Earth-science reviews, 185: 374-396.

Li, S., Yin, C., Guilmette, C., Ding, L. and Zhang, J., 2019a. Birth and demise of the Bangong-Nujiang Tethyan Ocean: A review from the Gerze area of central Tibet. Earth-Science Reviews, 198: 102907.

Li, S., Guilmette, C., Yin, C., Ding, L., Zhang, J., Wang, H. and Baral, U., 2019b. Timing and mechanism of Bangong-Nujiang ophiolite emplacement in the Gerze area of central Tibet. Gondwana Research, 71: 179-193.

Li, L., Fan, M., Davila, N., Jesmok, G., Mitsunaga, B., Tripati, A. and Orme, D., 2019c. Carbonate stable and clumped isotopic evidence for late Eocene moderate to high elevation of the east-central Tibetan Plateau and its geodynamic implications. GSA Bulletin, 131(5-6): 831-844.

Li, B., Yan, M., Zhang, W., Parés, J.M., Fang, X., Yang, Y., Zhang, D., Guan, C. and Bao, J., 2020a. Magnetic fabric constraints on the cenozoic compressional strain changes in the northern qaidam marginal thrust belt and their tectonic implications. Tectonics, 39(6): e2019TC005989.

Li, S., van Hinsbergen, D.J., Najman, Y., Liu-Zeng, J., Deng, C. and Zhu, R., 2020b. Does pulsed Tibetan deformation correlate with Indian plate motion changes? Earth and Planetary Science Letters, 536: 116144.

Li, S., van Hinsbergen, D.J., Shen, Z., Najman, Y., Deng, C. and Zhu, R., 2020c. Anisotropy of magnetic susceptibility (AMS) analysis of the Gonjo Basin as an independent constraint to date Tibetan shortening pulses. Geophysical Research Letters, 47(8): e2020GL087531.

Li, B., Yan, M., Zhang, W., Fang, X., Yang, Y., Zhang, D., Guan, C. and Bao, J., 2021. Two-stage strike-slip faulting of the Altyn Tagh Fault revealed by magnetic fabrics in the Qaidam Basin. Tectonophysics, 821: 229142.

Liang, H., Sun, W., Su, W. and Zartman, R.E., 2009. Porphyry copper-gold mineralization at Yulong, China, promoted by decreasing redox potential during magnetite alteration. Economic Geology, 104(4): 587-596.

Liebke, U., Appel, E., Ding, L. and Zhang, Q., 2013. Age constraints on the India–Asia collision derived from secondary remanences of Tethyan Himalayan sediments from the Tingri area. Journal of Asian Earth Sciences, 62: 329-340.

Lin, J. and Watts, D., 1988. Palaeomagnetic Results from the Tibetan Plateau. Philosophical Transactions of the Royal Society A: Mathematical, Physical and Engineering Sciences, 327(1594): 239-262.

Lippert, P.C., Zhao, X., Coe, R.S. and Lo, C., 2011. Palaeomagnetism and 40Ar/39Ar geochronology of upper Palaeogene volcanic rocks from Central Tibet: implications for the Central Asia inclination anomaly, the palaeolatitude of Tibet and post-50 Ma shortening within Asia. Geophysical Journal

International, 184(1): 131-161.
Liu, C., Ge, K., Zhang, C., Liu, Q., Deng, C. and Zhu, R., 2011. Nature of remagnetization of Lower Triassic red beds in southwestern China. Geophysical Journal International, 187(3): 1237-1249.
Liu, C.Y., Li, S.H., Deng, C.L. and Zhu, R.X., 2013. On the mechanism of remagnetization of Ordovician carbonates from the Yangtze Block, southwestern China. Chinese Journal of Geophysics, 56(2): 579-591.
Liu, D., Huang, Q., Fan, S., Zhang, L., Shi, R. and Ding, L., 2014a. Subduction of the Bangong–Nujiang Ocean: constraints from granites in the Bangong Co area, Tibet. Geological Journal, 49(2): 188-206.
Liu, Q.Y., Van Der Hilst, R.D., Li, Y., Yao, H.J., Chen, J.H., Guo, B., Qi, S.H., Wang, J., Huang, H. and Li, S.C., 2014b. Eastward expansion of the Tibetan Plateau by crustal flow and strain partitioning across faults. Nature Geoscience, 7(5): 361-365.
Liu, D., Shi, R., Ding, L. and Zou, H., 2018. Late Cretaceous transition from subduction to collision along the Bangong-Nujiang Tethys: New volcanic constraints from central Tibet. Lithos, 296: 452-470.
Liu, Y., Tan, J., Wei, J., Zhao, S., Liu, X., Gan, J. and Wang, Z., 2019. Sources and petrogenesis of Late Triassic Zhiduo volcanics in the northeast Tibet: Implications for tectonic evolution of the western Jinsha Paleo-Tethys Ocean. Lithos, 336: 169-182.
Lowrie, W., 1990. Identification of ferromagnetic minerals in a rock by coercivity and unblocking temperature properties. Geophysical research letters, 17(2): 159-162.
Lowrie, W. and Heller, F., 1982. Magnetic properties of marine limestones. Reviews of Geophysics, 20(2): 171-192.
Lüneburg, C.M., Lampert, S.A., Lebit, H.D., Hirt, A.M., Casey, M. and Lowrie, W., 1999. Magnetic anisotropy, rock fabrics and finite strain in deformed sediments of SW Sardinia (Italy). Tectonophysics, 307(1-2): 51-74.
Luo, L., Jia, D., Li, H., Li, Y., Deng, F., Chen, Z., Jia, Q., Sun, S. and Zhang, Y., 2009. Magnetic fabric investigation in the northwestern Sichuan Basin and its regional inference. Physics of the Earth and Planetary Interiors, 173(1-2): 103-114.
Luo, L., Qi, J.F., Jia, D., Wang, K. and Zeng, X., 2013. Magnetic fabric investigation in Tianquan-Leshan section in front of Longmenshan fold-thrust belt and its indicative significance for the Cenozoic deformation. Chinese Journal of Geophysics, 56(2): 558-566.
Ma, Y., Yang, T., Yang, Z., Zhang, S., Wu, H., Li, H., Li, H., Chen, W., Zhang, J. and Ding, J., 2014. Paleomagnetism and U-Pb zircon geochronology of Lower Cretaceous lava flows from the western Lhasa terrane: New constraints on the India-Asia collision process and intracontinental deformation within Asia. Journal of Geophysical Research: Solid Earth, 119(10): 7404-7424.
Ma, A., Hu, X., Garzanti, E., Han, Z. and Lai, W., 2017. Sedimentary and tectonic

evolution of the southern Qiangtang basin: Implications for the Lhasa-Qiangtang collision timing. Journal of Geophysical Research: Solid Earth, 122(7): 4790-4813.

Ma, Y., Yang, T., Bian, W., Jin, J., Wang, Q., Zhang, S., Wu, H., Li, H. and Cao, L., 2018. A stable southern margin of Asia during the Cretaceous: Paleomagnetic constraints on the Lhasa-Qiangtang collision and the maximum width of the Neo-Tethys. Tectonics, 37(10): 3853-3876.

MacCready, T., Snoke, A.W., Wright, J.E. and Howard, K.A., 1997. Mid-crustal flow during Tertiary extension in the Ruby Mountains core complex, Nevada. Geological Society of America Bulletin, 109(12): 1576-1594.

Mallat, S.G., 1989. Multifrequency channel decompositions of images and wavelet models. IEEE Transactions on Acoustics, Speech, and Signal Processing, 37(12): 2091-2110.

Marshak, S., 2004. Salients, recesses, arcs, Oroclines, and SyntaxesA review of ideas concerning the formation of map-view curves in fold-thrust belts. AAPG Special Volumes, 82: 131-156.

Mattei, M., Sagnotti, L., Faccenna, C. and Funiciello, R., 1997. Magnetic fabric of weakly deformed clay-rich sediments in the Italian peninsula: relationship with compressional and extensional tectonics. Tectonophysics, 271(1-2): 107-122.

Mazur, S., Aleksandrowski, P., Gągała, Ł., Krzywiec, P., Żaba, J., Gaidzik, K. and Sikora, R., 2020. Late Palaeozoic strike-slip tectonics versus oroclinal bending at the SW outskirts of Baltica: case of the Variscan belt's eastern end in Poland. International Journal of Earth Sciences, 109(4): 1133-1160.

McCabe, C. and Elmore, R.D., 1989. The occurrence and origin of late Paleozoic remagnetization in the sedimentary rocks of North America. Reviews of Geophysics, 27(4): 471-494.

McCabe, C. and Channell, J., 1994. Late Paleozoic remagnetization in limestones of the Craven Basin (northern England) and the rock magnetic fingerprint of remagnetized sedimentary carbonates. Journal of Geophysical Research: Solid Earth, 99(B3): 4603-4612.

McCarthy, D.J., Meere, P.A. and Petronis, M.S., 2015. A comparison of the effectiveness of clast based finite strain analysis techniques to AMS in sandstones from the Sevier Thrust Belt, Wyoming. Tectonophysics, 639: 68-81.

McFadden, P. and McElhinny, M., 1990. Classification of the reversal test in palaeomagnetism. Geophysical Journal International, 103(3): 725-729.

McKenzie, D., Nimmo, F., Jackson, J.A., Gans, P. and Miller, E., 2000. Characteristics and consequences of flow in the lower crust. Journal of Geophysical Research: Solid Earth, 105(B5): 11029-11046.

Medvedev, S. and Beaumont, C., 2006. Growth of continental plateaus by channel injection: models designed to address constraints and thermomechanical consistency. Geological Society, London, Special Publications, 268(1): 147-164.

Meert, J.G., Pivarunas, A.F., Evans, D.A., Pisarevsky, S.A., Pesonen, L.J., Li, Z.X., Elming, S.Å., Miller, S.R., Zhang, S. and Salminen, J.M., 2020. The magnificent seven: a proposal for modest revision of the quality index. Tectonophysics, 790: 228549.

Meijers, M.J.M., Kaymakci, N., van Hinsbergen, D.J.J., Langereis, C.G., Stephenson, R.A. and Hippolyte, J.C., 2010. Late Cretaceous to Paleocene oroclinal bending in the central Pontides (Turkey). Tectonics, 29(4): n/a-n/a.

Meijers, M.J., Van Hinsbergen, D.J., Dekkers, M.J., Altıner, D., Kaymakcı, N. and Langereis, C.G., 2011. Pervasive Palaeogene remagnetization of the central Taurides fold-and-thrust belt (southern Turkey) and implications for rotations in the Isparta Angle. Geophysical Journal International, 184(3): 1090-1112.

Meijers, M.J.M., Smith, B., Pastor-Galán, D., Degenaar, R., Sadradze, N., Adamia, S., Sahakyan, L., Avagyan, A., Sosson, M., Rolland, Y., Langereis, C.G. and Müller, C., 2017. Progressive orocline formation in the Eastern Pontides–Lesser Caucasus. Geological Society, London, Special Publications, 428(1): 117-143.

Ménabréaz, L., Thouveny, N., Camoin, G. and Lund, S.P., 2010. Paleomagnetic record of the late Pleistocene reef sequence of Tahiti (French Polynesia): A contribution to the chronology of the deposits. Earth and Planetary Science Letters, 294(1-2): 58-68.

Meng, J., Zhao, X., Wang, C., Liu, H., Li, Y., Han, Z., Liu, T. and Wang, M., 2018. Palaeomagnetism and detrital zircon U–Pb geochronology of Cretaceous redbeds from central Tibet and tectonic implications. Geological Journal, 53(5): 2315-2333.

Meng, J., Gilder, S.A., Li, Y., Chen, Y., Zhang, C., Zhou, Z., Liu, T., Zhao, Y., Wang, Z. and Wang, C., 2022. Remagnetization age and mechanism of Cretaceous sediments in relation to dyke intrusion, Hainan Island: Tectonic implications for South China and the Red River Fault. Journal of Geophysical Research: Solid Earth, 127(1): e2021JB023474.

Metcalfe, I., 2006. Palaeozoic and Mesozoic tectonic evolution and palaeogeography of East Asian crustal fragments: the Korean Peninsula in context. Gondwana Research, 9(1-2): 24-46.

Metcalfe, I., 2011. Tectonic framework and Phanerozoic evolution of Sundaland. Gondwana Research, 19(1): 3-21.

Metcalfe, I., 2013. Gondwana dispersion and Asian accretion: Tectonic and palaeogeographic evolution of eastern Tethys. Journal of Asian Earth Sciences, 66: 1-33.

Molnar, P. and Tapponnier, P., 1975. Cenozoic Tectonics of Asia: Effects of a Continental Collision: Features of recent continental tectonics in Asia can be interpreted as results of the India-Eurasia collision. Science, 189(4201): 419-426.

Molnar, P. and Dayem, K.E., 2010. Major intracontinental strike-slip faults and contrasts in lithospheric strength. Geosphere, 6(4): 444-467.

Molnar, P., England, P. and Martinod, J., 1993. Mantle dynamics, uplift of the Tibetan

Plateau, and the Indian monsoon. Reviews of Geophysics, 31(4): 357-396.
Moreau, F., Gibert, D., Holschneider, M. and Saracco, G., 1997. Wavelet analysis of potential fields. Inverse problems, 13(1): 165.
Moreau, F., Gibert, D., Holschneider, M. and Saracco, G., 1999. Identification of sources of potential fields with the continuous wavelet transform: Basic theory. Journal of Geophysical Research: Solid Earth, 104(B3): 5003-5013.
Morris, A. and Robertson, A., 1993. Miocene remagnetisation of carbonate platform and Antalya Complex units within the Isparta Angle, SW Turkey. Tectonophysics, 220(1-4): 243-266.
Mullender, T., Van Velzen, A. and Dekkers, M., 1993. Continuous drift correction and separate identification of ferrimagnetic and paramagnetic contributions in thermomagnetic runs. Geophysical Journal International, 114(3): 663-672.
Mullender, T.A., Frederichs, T., Hilgenfeldt, C., de Groot, L.V., Fabian, K. and Dekkers, M.J., 2016. Automated paleomagnetic and rock magnetic data acquisition with an in-line horizontal "2 G" system. Geochemistry, Geophysics, Geosystems, 17(9): 3546-3559.
Murray, J., Jannasch, H., Honjo, S., Anderson, R., Reeburgh, W., Top, Z., Friederich, G., Codispoti, L. and Izdar, E., 1989. Unexpected changes in the oxic/anoxic interface in the Black Sea. Nature, 338(6214): 411-413.
Muxworthy, A.R. and Dunlop, D.J., 2002. First-order reversal curve (FORC) diagrams for pseudo-single-domain magnetites at high temperature. Earth and Planetary Science Letters, 203(1): 369-382.
Nábělek, J., Hetényi, G., Vergne, J., Sapkota, S., Kafle, B., Jiang, M., Su, H., Chen, J. and Huang, B.S., 2009. Underplating in the Himalaya-Tibet collision zone revealed by the Hi-CLIMB experiment. Science, 325(5946): 1371-1374.
Nédélec, A., Trindade, R., Peschler, A., Archanjo, C., Macouin, M., Poitrasson, F. and Bouchez, J.L., 2015. Hydrothermally-induced changes in mineralogy and magnetic properties of oxidized A-type granites. Lithos, 212: 145-157.
Néel, L., 1955. Some theoretical aspects of rock-magnetism. Advances in physics, 4(14): 191-243.
O'Reilly, W., 1984. Magnetic minerals in rocks, Rock and Mineral Magnetism. Springer, pp. 7-29.
Oliva-Urcia, B., Larrasoaña, J., Pueyo, E., Gil, A., Mata, P., Parés, J., Schleicher, A.M. and Pueyo, O., 2009. Disentangling magnetic subfabrics and their link to deformation processes in cleaved sedimentary rocks from the Internal Sierras (west central Pyrenees, Spain). Journal of Structural Geology, 31(2): 163-176.
Oliva-Urcia, B., Rahl, J.M., Schleicher, A.M. and Parés, J.M., 2010. Correlation between the anisotropy of the magnetic susceptibility, strain and X-ray Texture Goniometry in phyllites from Crete, Greece. Tectonophysics, 486(1-4): 120-131.
Oliva-Urcia, B., Casas, A., Soto, R., Villalaín, J. and Kodama, K., 2011. A transtensional basin model for the Organyà basin (central southern Pyrenees) based on magnetic fabric and brittle structures. Geophysical Journal International,

184(1): 111-130.
Oliva-Urcia, B., Román-Berdiel, T., Casas, A.M., Bógalo, M.F., Osácar, M.C. and García-Lasanta, C., 2013. Transition from extensional to compressional magnetic fabrics in the Cretaceous Cabuérniga basin (North Spain). Journal of Structural Geology, 46: 220-234.
Otofuji, Y., Inoue, Y., Funahara, S., Murata, F. and Zheng, X., 1990. Palaeomagnetic study of eastern Tibet-deformation of the Three Rivers region. Geophysical Journal International, 103(1): 85-94.
Özdemir, Ö. and Dunlop, D.J., 1997. Effect of crystal defects and internal stress on the domain structure and magnetic properties of magnetite. Journal of Geophysical Research: Solid Earth, 102(B9): 20211-20224.
Özkaptan, M., 2019. Crustal disequilibrium of the central Pontides (northern Turkey) due to oroclinal bending revealed by gravity modelling. Journal of Asian Earth Sciences, 186: 104058.
Pan, G., 2004a. Thoughts on some important scientific problems in regional survey of the Qinghai-Tibet plateau. Geological Bulletin of China, 22: 12-19.
Pan, G., Zhu, D. and Wang, L., 2004b. Bangong Lake-Nu River suture zone-the northern boundary of Gondwanaland: Evidence from geology and geophysics. Earth Science Frontiers, 11: 371-382.
Pan, G., Ding, J., Yao, D. and Wang, L., 2004c. Guidebook of 1: 1,500,000 geologic map of the Qinghai–Xizang (Tibet) plateau and adjacent areas. Chengdu, China: Chengdu Cartographic Publishing House, 48.
Pandit, M.K., Manish, K. and Koh, L.P., 2014. Dancing on the roof of the world: ecological transformation of the Himalayan landscape. BioScience, 64(11): 980-992.
Parés, J.M., 2004. How deformed are weakly deformed mudrocks? Insights from magnetic anisotropy. Geological Society, London, Special Publications, 238(1): 191-203.
Parés, J.M., 2015. Sixty years of anisotropy of magnetic susceptibility in deformed sedimentary rocks. Frontiers in Earth Science, 3: 4.
Parés, J.M., van der Pluijm, B.A. and Dinarès-Turell, J., 1999. Evolution of magnetic fabrics during incipient deformation of mudrocks (Pyrenees, northern Spain). Tectonophysics, 307(1-2): 1-14.
Parnell, J., Baron, M., Davidson, M., Elmore, D. and Engel, M., 2000. Dolomitic breccia veins as evidence for extension and fluid flow in the Dalradian of Argyll. Geological Magazine, 137(4): 447-462.
Passier, H.F., de Lange, G.J. and Dekkers, M.J., 2001. Magnetic properties and geochemistry of the active oxidation front and the youngest sapropel in the eastern Mediterranean Sea. Geophysical Journal International, 145(3): 604-614.
Pasteka, R., Mikuska, J. and Meurers, B., 2017. Understanding the Bouguer Anomaly: A Gravimetry Puzzle. Elsevier.
Pastor-Galán, D., Gutiérrez-Alonso, G. and Weil, A.B., 2011. Orocline timing through joint analysis: Insights from the Ibero-Armorican Arc. Tectonophysics, 507(1-

4): 31-46.
Pastor-Galán, D., Gutiérrez-Alonso, G., Mulchrone, K.F. and Huerta, P., 2012. Conical folding in the core of an orocline. A geometric analysis from the Cantabrian Arc (Variscan Belt of NW Iberia). Journal of Structural Geology, 39: 210-223.
Pastor-Galán, D., Groenewegen, T., Brouwer, D., Krijgsman, W. and Dekkers, M.J., 2015. One or two oroclines in the Variscan orogen of Iberia? Implications for Pangea amalgamation. Geology, 43(6): 527-530.
Pastor-Galán, D., Mulchrone, K.F., Koymans, M.R., van Hinsbergen, D.J. and Langereis, C.G., 2017. Bootstrapped total least squares orocline test: A robust method to quantify vertical-axis rotation patterns in orogens, with examples from the Cantabrian and Aegean oroclines. Lithosphere, 9(3): 499-511.
Pastor-Galán, D., Gutiérrez-Alonso, G. and Weil, A.B., 2020. The enigmatic curvature of Central Iberia and its puzzling kinematics. Solid Earth, 11(4): 1247-1273.
Pavlis, N., Holmes, S., Kenyon, S. and Factor, J., 2008. An earth gravitational model to degree 2160: Egm2008. presentation given at the 2008 european geosciences union general assembly held in vienna, austria, 13–18 apr 2008. Available in: http://earth-info. nga. mil/GandG/wgs84/gravitymod/egm2008.
Peltzer, G. and Tapponnier, P., 1988. Formation and evolution of strike-slip faults, rifts, and basins during the India-Asia collision: An experimental approach. Journal of Geophysical Research: Solid Earth, 93(B12): 15085-15117.
Percy, D., Li, X., Taylor, G.T., Astor, Y. and Scranton, M.I., 2008. Controls on iron, manganese and intermediate oxidation state sulfur compounds in the Cariaco Basin. Marine Chemistry, 111(1-2): 47-62.
Perroud, H. and Van der Voo, R., 1984. Secondary magnetizations from the Clinton-type iron ores of the Silurian Red Mountain Formation, Alabama. Earth and planetary science letters, 67(3): 391-399.
Philipp, S.L., 2008. Geometry and formation of gypsum veins in mudstones at Watchet, Somerset, SW England. Geological Magazine, 145(6): 831-844.
Pike, C.R., Roberts, A.P. and Verosub, K.L., 2001. First order reversal curve diagrams and thermal relaxation effects in magnetic particles. Geophysical Journal International, 145(3): 721-730.
Pinto, M.L. and Vidotti, R.M., 2019. Tectonic framework of the Paraná basin unveiled from gravity and magnetic data. Journal of South American Earth Sciences, 90: 216-232.
Potter, D.K. and Stephenson, A., 1988. Single-domain particles in rocks and magnetic fabric analysis. Geophysical Research Letters, 15(10): 1097-1100.
Prins, M., 1999. Pelagic, hemigelagic and turbidite deposition in the Arabian Sea during the Late Quaternary. Geologica Ultraiectina(168): 192.
Pueyo-Morer, E., Millán-Garrido, H., Pocoví-Juan, A. and Parés, J., 1997. Determination of the folding mechanism by AMS data. Study of the relation between shortening and magnetic anisotropy in the Pico del Aguila anticline (southern Pyrenees). Physics and Chemistry of the Earth, 22(1-2): 195-201.
Pueyo Anchuela, Ó., Ramajo Cordero, J., Gil Imaz, A. and Meléndez Hevia, G., 2013.

Analysis of anisotropy of magnetic susceptibility in iron-oolitic beds: a potential tool for paleocurrent identification. International Journal of Earth Sciences, 102(4): 1131-1149.

Pullaiah, G., Irving, E., Buchan, K. and Dunlop, D., 1975. Magnetization changes caused by burial and uplift. Earth and Planetary Science Letters, 28(2): 133-143.

Pullen, A., Kapp, P., Gehrels, G.E., Vervoort, J.D. and Ding, L., 2008. Triassic continental subduction in central Tibet and Mediterranean-style closure of the Paleo-Tethys Ocean. Geology, 36(5): 351-354.

Pullen, A., Kapp, P., Gehrels, G.E., Ding, L. and Zhang, Q., 2011. Metamorphic rocks in central Tibet: Lateral variations and implications for crustal structure. Bulletin, 123(3-4): 585-600.

Pusok, A.E. and Stegman, D.R., 2020. The convergence history of India-Eurasia records multiple subduction dynamics processes. Science advances, 6(19): eaaz8681.

Qin, H., Liu, Q. and Pan, Y., 2008. The first-order reversal curve (FORC) diagram: Theory and case study. Chinese Journal of Geophysics, 51(3): 743-751.

Qiu, J., 2008. China: The third pole. Nature, 454(7203): 393-397.

Ran, B., Deng, B., Wang, C., Zhao, X., Li, Y., Zhang, Y., Meng, J., He, M., Zhu, L. and Xiao, C., 2017. Kinematics of the crust around the Tanggula Shan in North–Central Tibet: Constraints from paleomagnetic data. Gondwana Research, 48: 124-133.

Rashid, H., Cifelli, F. and Mattei, M., 2015. Late folding-related magnetic foliation in the active Ferdows (northeastern Iran) thrust–fold system. Journal of Asian Earth Sciences, 108: 48-57.

Raymo, M.E. and Ruddiman, W.F., 1992. Tectonic forcing of late Cenozoic climate. nature, 359(6391): 117-122.

Ren, H., Yan, M., Meng, Q., Song, C. and Fang, X., 2013. " E/I" corrected paleomagnetic inclination indicates 1 000 km NS shortening of the Qiangtang terrane since the Middle Jurassic. Chinese Journal of Geology, 48(2): 543-556.

Replumaz, A. and Tapponnier, P., 2003. Reconstruction of the deformed collision zone between India and Asia by backward motion of lithospheric blocks. Journal of Geophysical Research: Solid Earth, 108(B6).

Reynolds, R.L., 1990. A polished view of remagnetization. Nature, 345(6276): 579-580.

Roberts, A.P., 1995. Magnetic properties of sedimentary greigite (Fe3S4). Earth and Planetary Science Letters, 134(3-4): 227-236.

Roberts, A.P., 2015. Magnetic mineral diagenesis. Earth-Science Reviews, 151: 1-47.

Roberts, A.P. and Turner, G.M., 1993. Diagenetic formation of ferrimagnetic iron sulphide minerals in rapidly deposited marine sediments, South Island, New Zealand. Earth and Planetary Science Letters, 115(1-4): 257-273.

Roberts, A.P. and Weaver, R., 2005. Multiple mechanisms of remagnetization involving sedimentary greigite (Fe3S4). Earth and Planetary Science Letters, 231(3-4): 263-277.

Roberts, A.P., Cui, Y. and Verosub, K.L., 1995. Wasp-waisted hysteresis loops: Mineral magnetic characteristics and discrimination of components in mixed magnetic systems. Journal of Geophysical Research: Solid Earth, 100(B9): 17909-17924.

Roberts, A.P., Pike, C.R. and Verosub, K.L., 2000. First-order reversal curve diagrams: A new tool for characterizing the magnetic properties of natural samples. Journal of Geophysical Research: Solid Earth, 105(B12): 28461-28475.

Roberts, A.P., Liu, Q., Rowan, C.J., Chang, L., Carvallo, C., Torrent, J. and Horng, C.S., 2006. Characterization of hematite (α-Fe2O3), goethite (α-FeOOH), greigite (Fe3S4), and pyrrhotite (Fe7S8) using first-order reversal curve diagrams. Journal of Geophysical Research: Solid Earth, 111(B12).

Roberts, A.P., Chang, L., Rowan, C.J., Horng, C.S. and Florindo, F., 2011. Magnetic properties of sedimentary greigite (Fe3S4): An update. Reviews of Geophysics, 49(1).

Roberts, A.P., Florindo, F., Chang, L., Heslop, D., Jovane, L. and Larrasoana, J.C., 2013. Magnetic properties of pelagic marine carbonates. Earth-science reviews, 127: 111-139.

Roberts, A.P., Heslop, D., Zhao, X. and Pike, C.R., 2014. Understanding fine magnetic particle systems through use of first-order reversal curve diagrams. Reviews of Geophysics, 52(4): 557-602.

Roberts, A.P., Tauxe, L., Heslop, D., Zhao, X. and Jiang, Z., 2018. A critical appraisal of the "Day" diagram. Journal of Geophysical Research: Solid Earth, 123(4): 2618-2644.

Roberts, A.P., Hu, P., Harrison, R.J., Heslop, D., Muxworthy, A.R., Oda, H., Sato, T., Tauxe, L. and Zhao, X., 2019. Domain state diagnosis in rock magnetism: Evaluation of potential alternatives to the Day diagram. Journal of Geophysical Research: Solid Earth, 124(6): 5286-5314.

Rochette, P., 1987a. Metamorphic control of the magnetic mineralogy of black shales in the Swiss Alps: toward the use of "magnetic isograde". Earth and Planetary Science Letters, 84(4): 446-456.

Rochette, P., 1987b. Magnetic susceptibility of the rock matrix related to magnetic fabric studies. Journal of Structural Geology, 9(8): 1015-1020.

Rochette, P., 1988. Inverse magnetic fabric in carbonate-bearing rocks. Earth and Planetary Science Letters, 90(2): 229-237.

Rochette, P., Jackson, M. and Aubourg, C., 1992. Rock magnetism and the interpretation of anisotropy of magnetic susceptibility. Reviews of Geophysics, 30(3): 209-226.

Roger, F., Jolivet, M. and Malavieille, J., 2010. The tectonic evolution of the Songpan-Garzê (North Tibet) and adjacent areas from Proterozoic to Present: A synthesis. Journal of Asian Earth Sciences, 39(4): 254-269.

Roperch, P. and Taylor, G., 1986. The importance of gyromagnetic remanence in alternating field demagnetization. Some new data and experiments on GRM and RRM. Geophysical Journal International, 87(3): 949-965.

Roperch, P., Dupont-Nivet, G., Guillot, S., Goussin, F., Huang, W., Replumaz, A., Yang, Z., Guo, Z. and Song, B., 2017. Paleomagnetic constraints on early collisional deformation along the eastern margin of the Qiantang terrane (Tibetan plateau) at 50 and 37 Ma, EGU general assembly conference abstracts, pp. 9476.

Rowan, C.J., Roberts, A.P. and Broadbent, T., 2009. Reductive diagenesis, magnetite dissolution, greigite growth and paleomagnetic smoothing in marine sediments: A new view. Earth and Planetary Science Letters, 277(1-2): 223-235.

Roy, M. and Royden, L.H., 2000. Crustal rheology and faulting at strike-slip plate boundaries: 2. Effects of lower crustal flow. Journal of Geophysical Research: Solid Earth, 105(B3): 5599-5613.

Royden, L., 1996. Coupling and decoupling of crust and mantle in convergent orogens: Implications for strain partitioning in the crust. Journal of Geophysical Research: Solid Earth, 101(B8): 17679-17705.

Royden, L.H., Burchfiel, B.C., King, R.W., Wang, E., Chen, Z., Shen, F. and Liu, Y., 1997. Surface deformation and lower crustal flow in eastern Tibet. science, 276(5313): 788-790.

Royden, L.H., Burchfiel, B.C. and van der Hilst, R.D., 2008. The geological evolution of the Tibetan Plateau. science, 321(5892): 1054-1058.

Ruddiman, W.F. and Kutzbach, J.E., 1989. Forcing of late Cenozoic northern hemisphere climate by plateau uplift in southern Asia and the American West. Journal of Geophysical Research: Atmospheres, 94(D15): 18409-18427.

Sagnotti, L. and Winkler, A., 1999. Rock magnetism and palaeomagnetism of greigite-bearing mudstones in the Italian peninsula. Earth and Planetary Science Letters, 165(1): 67-80.

Saint-Bezar, B., Hebert, R., Aubourg, C., Robion, P., Swennen, R. and De Lamotte, D.F., 2002. Magnetic fabric and petrographic investigation of hematite-bearing sandstones within ramp-related folds: examples from the South Atlas Front (Morocco). Journal of Structural Geology, 24(9): 1507-1520.

Sato, K., Liu, Y., Wang, Y., Yokoyama, M., Yoshioka, S.y., Yang, Z. and Otofuji, Y.-i., 2007. Paleomagnetic study of Cretaceous rocks from Pu'er, western Yunnan, China: Evidence of internal deformation of the Indochina block. Earth and Planetary Science Letters, 258(1-2): 1-15.

Schoenbohm, L.M., Burchfiel, B.C. and Liangzhong, C., 2006. Propagation of surface uplift, lower crustal flow, and Cenozoic tectonics of the southeast margin of the Tibetan Plateau. Geology, 34(10): 813-816.

Schwartz, S.Y. and Van der Voo, R., 1983. Paleomagnetic evaluation of the orocline hypothesis in the central and southern Appalachians. Geophysical Research Letters, 10(7): 505-508.

Searle, M.P., Roberts, N.M., Chung, S.L., Lee, Y.H., Cook, K.L., Elliott, J.R., Weller, O.M., St-Onge, M.R., Xu, X.W. and Tan, X.B., 2016. Age and anatomy of the Gongga Shan batholith, eastern Tibetan Plateau, and its relationship to the active Xianshui-he fault. Geosphere, 12(3): 948-970.

Sha, J. and Fursich, F., 1999. Palaeotethys Ocean closed before Capitanian times in Hohxil area (W China): New data on the temporal extent of the Palaeotethys.

Shaw, J., Johnston, S.T. and Rosenbaum, G., 2012a. The Carpathian-Balkan bends: An oroclinal record of ongoing Arabian–Eurasian collision. J. Virtual Explor, 43(4).

Shaw, J., Johnston, S.T., Gutiérrez-Alonso, G. and Weil, A.B., 2012b. Oroclines of the Variscan orogen of Iberia: Paleocurrent analysis and paleogeographic implications. Earth and Planetary Science Letters, 329: 60-70.

Shcherbakova, V., Shcherbakov, V. and Heider, F., 2000. Properties of partial thermoremanent magnetization in pseudosingle domain and multidomain magnetite grains. Journal of Geophysical Research: Solid Earth, 105(B1): 767-781.

Shen, Z.K., Lü, J., Wang, M. and Bürgmann, R., 2005. Contemporary crustal deformation around the southeast borderland of the Tibetan Plateau. Journal of Geophysical Research: Solid Earth, 110(B11).

Shen, M., Zan, J., Yan, M., Zhang, W., Fang, X., Zhang, D. and Zhang, T., 2020. Comparative rock magnetic study of Eocene volcanogenic and sedimentary rocks from Yunnan, southeastern Tibetan Plateau, and its geological implications. Journal of Geophysical Research: Solid Earth, 125(2): e2019JB017946.

Snowball, I.F., 1997a. The detection of single-domain greigite (Fe3S4) using rotational remanent magnetization (RRM) and the effective gyro field (Bg): mineral magnetic and palaeomagnetic applications. Geophysical Journal International, 130(3): 704-716.

Snowball, I.F., 1997b. Gyroremanent magnetization and the magnetic properties of greigite-bearing clays in southern Sweden. Geophysical Journal International, 129(3): 624-636.

Song, C., Wang, J., Fu, X., Feng, X., Chen, M. and He, L., 2012. Late Triassic paleomagnetic data from the Qiangtang terrane of Tibetan Plateau and their tectonic significances. Journal of Jilin University (Earth Science Edition), 42(2): 241-250.

Song, P., Ding, L., Li, Z., Lippert, P.C., Yang, T., Zhao, X., Fu, J. and Yue, Y., 2015. Late Triassic paleolatitude of the Qiangtang block: Implications for the closure of the Paleo-Tethys Ocean. Earth and Planetary Science Letters, 424: 69-83.

Song, C., Zeng, Y., Yan, M., Wu, S., Fang, X., Bao, J., Zan, J. and Liu, X., 2016. Magnetostratigraphy of the middle-upper Jurassic sedimentary sequences at Yanshiping, Qiangtang Basin, China. Geophysical Journal International, 206(3): 1847-1863.

Song, P., Ding, L., Li, Z., Lippert, P.C. and Yue, Y., 2017. An early bird from Gondwana: Paleomagnetism of Lower Permian lavas from northern Qiangtang (Tibet) and the geography of the Paleo-Tethys. Earth and Planetary Science Letters, 475: 119-133.

Song, P., Ding, L., Lippert, P.C., Li, Z., Zhang, L. and Xie, J., 2020. Paleomagnetism of Middle Triassic lavas from northern Qiangtang (Tibet): Constraints on the

closure of the Paleo-Tethys Ocean. Journal of Geophysical Research: Solid Earth, 125(2): e2019JB017804.
Spector, A. and Grant, F., 1970. Statistical models for interpreting aeromagnetic data. Geophysics, 35(2): 293-302.
Stearns, C. and Van der Voo, R., 1987. A paleomagnetic reinvestigation of the Upper Devonian Perry Formation: evidence for Late Paleozoic remagnetization. Earth and planetary science letters, 86(1): 27-38.
Stephenson, A., 1980a. Gyromagnetism and the remanence acquired by a rotating rock in an alternating field. Nature, 284(5751): 48-49.
Stephenson, A., 1980b. A gyroremanent magnetisation in anisotropic magnetic material. Nature, 284(5751): 49-51.
Stephenson, A., 1993. Three-axis static alternating field demagnetization of rocks and the identification of natural remanent magnetization, gyroremanent magnetization, and anisotropy. Journal of Geophysical Research: Solid Earth, 98(B1): 373-381.
Stephenson, A. and Snowball, I.F., 2001. A large gyromagnetic effect in greigite. Geophysical Journal International, 145(2): 570-575.
Su, T., Spicer, R.A., Li, S., Xu, H., Huang, J., Sherlock, S., Huang, Y., Li, S., Wang, L. and Jia, L., 2019. Uplift, climate and biotic changes at the Eocene–Oligocene transition in south-eastern Tibet. National Science Review, 6(3): 495-504.
Suk, D., Peacor, D. and Van der Voo, R., 1990a. Replacement of pyrite framboids by magnetite in limestone and implications for palaeomagnetism. Nature, 345(6276): 611-613.
Suk, D., Van Der Voo, R. and Peacor, D.R., 1990b. Scanning and transmission electron microscope observations of magnetite and other iron phases in Ordovician carbonates from east Tennessee. Journal of Geophysical Research: Solid Earth, 95(B8): 12327-12336.
Suk, D., Van Der Voo, R. and Peacor, D.R., 1993. Origin of magnetite responsible for remagnetization of early Paleozoic limestones of New York State. Journal of Geophysical Research: Solid Earth, 98(B1): 419-434.
Sun, W., Jackson, M. and Craddock, J.P., 1993. Relationship between remagnetization, magnetic fabric and deformation in Paleozoic carbonates. Tectonophysics, 221(3-4): 361-366.
Sun, W., Chen, M., Wan, Y., He, J., Lan, Y., Wei, H. and Chen, H., 2020. Closed-system dolomitization process and the significance for petroleum geology——An example from dolostone in the Middle Jurassic Buqu Formation in southern Qiangtang Depression. GEOLOGICAL REVIEW, 66(5): 1217-1229.
Tan, X., Kodama, K.P., Chen, H., Fang, D., Sun, D. and Li, Y., 2003. Paleomagnetism and magnetic anisotropy of Cretaceous red beds from the Tarim basin, northwest China: Evidence for a rock magnetic cause of anomalously shallow paleomagnetic inclinations from central Asia. Journal of Geophysical Research: Solid Earth, 108(B2).
Tan, F., Wang, J., Li, Y., Du, B. and Zhu, Z., 2004. Late Jurassic–Early Cretaceous

strata and their sedimentary characteristics in the Qiangtang basin, northern Tibet. Geology in China, 31(4): 20-27.

Tan, J., Wei, J., Zhao, S., Li, Y., Liu, Y., Liu, X., Zhang, F., Gan, J. and Wang, Z., 2020. Petrogenesis of Late Triassic high-Mg diorites and associated granitoids with implications for Paleo-Tethys evolution in the northeast Tibetan Plateau. Bulletin, 132(5-6): 955-976.

Tanaka, K., Mu, C., Sato, K., Takemoto, K., Miura, D., Liu, Y., Zaman, H., Yang, Z., Yokoyama, M., Iwamoto, H., Uno, K. and Otofuji, Y.-i., 2008. Tectonic deformation around the eastern Himalayan syntaxis: constraints from the Cretaceous palaeomagnetic data of the Shan-Thai Block. Geophysical Journal International, 175(2): 713-728.

Tang, X., Huang, B., Yang, L., Yi, Z., Qiao, Q. and Chen, L., 2013. Paleomagnetism and Ar-Ar geochronology of Cretaceous volcanic rocks in the middle Lhasa terrane, China and tectonic implications. Chinese Journal of Geophysics, 56(1): 136-149.

Tang, Z., Dong, X., Wang, X. and Ding, Z., 2015. Oligocene-M iocene magnetostratigraphy and magnetic anisotropy of the B axbulak section from the P amir-T ian S han convergence zone. Geochemistry, Geophysics, Geosystems, 16(10): 3575-3592.

Tang, M., Liu, Z.J., Hoke, G.D., Xu, Q., Wang, W., Li, Z., Zhang, J. and Wang, W., 2017. Paleoelevation reconstruction of the Paleocene-Eocene Gonjo basin, SE-central Tibet. Tectonophysics, 712-713: 170-181.

Tapponnier, P., Peltzer, G., Le Dain, A., Armijo, R. and Cobbold, P., 1982. Propagating extrusion tectonics in Asia: New insights from simple experiments with plasticine. Geology, 10(12): 611-616.

Tapponnier, P., Lacassin, R., Leloup, P.H., Schärer, U., Dalai, Z., Haiwei, W., Xiaohan, L., Shaocheng, J., Lianshang, Z. and Jiayou, Z., 1990. The Ailao Shan/Red River metamorphic belt: tertiary left-lateral shear between Indochina and South China. Nature, 343(6257): 431-437.

Tapponnier, P., Zhiqin, X., Roger, F., Meyer, B., Arnaud, N., Wittlinger, G. and Jingsui, Y., 2001. Oblique stepwise rise and growth of the Tibet Plateau. science, 294(5547): 1671-1677.

Tarling, D. and Hrouda, F., 1993. Magnetic anisotropy of rocks. Springer Science & Business Media.

Tauxe, L. and Kent, D.V., 2004. A simplified statistical model for the geomagnetic field and the detection of shallow bias in paleomagnetic inclinations: was the ancient magnetic field dipolar?

Tauxe, L., Bertram, H.N. and Seberino, C., 2002. Physical interpretation of hysteresis loops: Micromagnetic modeling of fine particle magnetite. Geochemistry, Geophysics, Geosystems, 3(10): 1-22.

Tauxe, L., Mullender, T. and Pick, T., 1996. Potbellies, wasp-waists, and superparamagnetism in magnetic hysteresis. Journal of Geophysical Research: Solid Earth, 101(B1): 571-583.

Todrani, A., Speranza, F., D'Agostino, N. and Zhang, B., 2022. Post-50 Ma Evolution

of India-Asia Collision Zone From Paleomagnetic and GPS Data: Greater India Indentation to Eastward Tibet Flow. Geophysical Research Letters, 49(1): e2021GL096623.

Tong, Y., Yang, Z., Zheng, L., Xu, Y., Wang, H., Gao, L. and Hu, X., 2013. Internal crustal deformation in the northern part of Shan-Thai Block: New evidence from paleomagnetic results of Cretaceous and Paleogene redbeds. Tectonophysics, 608: 1138-1158.

Tong, Y.B., Yang, Z., Gao, L., Wang, H., Zhang, X.D., An, C.Z., Xu, Y.C. and Han, Z.R., 2015. Paleomagnetism of Upper Cretaceous red-beds from the eastern Qiangtang Block: Clockwise rotations and latitudinal translation during the India–Asia collision. Journal of Asian Earth Sciences, 114: 732-749.

Tong, Y., Yang, Z., Mao, C., Pei, J., Pu, Z. and Xu, Y., 2017. Paleomagnetism of Eocene red-beds in the eastern part of the Qiangtang Terrane and its implications for uplift and southward crustal extrusion in the southeastern edge of the Tibetan Plateau. Earth and Planetary Science Letters, 475: 1-14.

Tong, Y., Yang, Z., Pei, J., Wang, H., Wu, Z. and Li, J., 2022. Upper Crustal Collapse Reconstructed the Topography and Remodeled the Fault System of the Chuandian Fragment in the Southeastern Edge of the Tibetan Plateau, Evidenced by Anisotropy of Magnetic Susceptibility Data Sets. Tectonics, 41(4): e2021TC007126.

Toonen, W., Winkels, T., Cohen, K., Prins, M. and Middelkoop, H., 2015. Lower Rhine historical flood magnitudes of the last 450 years reproduced from grain-size measurements of flood deposits using End Member Modelling. Catena, 130: 69-81.

Torii, M., Fukuma, K., Horng, C.-S. and Lee, T.-Q., 1996. Magnetic discrimination of pyrrhotite- and greigite-bearing sediment samples. Geophysical Research Letters, 23(14): 1813-1816.

Van Dam, J.A. and Weltje, G.J., 1999. Reconstruction of the Late Miocene climate of Spain using rodent palaeocommunity successions: an application of end-member modelling. Palaeogeography, Palaeoclimatology, Palaeoecology, 151(4): 267-305.

Van der Voo, R., 1990. The reliability of paleomagnetic data. Tectonophysics, 184(1): 1-9.

Van der Voo, R. and Torsvik, T.H., 2012. The history of remagnetization of sedimentary rocks: deceptions, developments and discoveries. Geological Society, London, Special Publications, 371(1): 23-53.

Van Hinsbergen, D.J., Kaymakci, N., Spakman, W. and Torsvik, T.H., 2010. Reconciling the geological history of western Turkey with plate circuits and mantle tomography. Earth and Planetary Science Letters, 297(3-4): 674-686.

Van Hinsbergen, D.J., Steinberger, B., Doubrovine, P.V. and Gassmöller, R., 2011. Acceleration and deceleration of India-Asia convergence since the Cretaceous: Roles of mantle plumes and continental collision. Journal of Geophysical Research: Solid Earth, 116(B6).

Van Hinsbergen, D.J., Lippert, P.C., Dupont-Nivet, G., McQuarrie, N., Doubrovine, P.V., Spakman, W. and Torsvik, T.H., 2012. Greater India Basin hypothesis and a two-stage Cenozoic collision between India and Asia. Proceedings of the National Academy of Sciences, 109(20): 7659-7664.

Van Velzen, A. and Zijderveld, J., 1992. A method to study alterations of magnetic minerals during thermal demagnetization applied to a fine-grained marine marl (Trubi formation, Sicily). Geophysical Journal International, 110(1): 79-90.

Wang, E. and Burchfiel, B.C., 2000. Late Cenozoic to Holocene deformation in southwestern Sichuan and adjacent Yunnan, China, and its role in formation of the southeastern part of the Tibetan Plateau. Geological Society of America Bulletin, 112(3): 413-423.

Wang, M. and Shen, Z.K., 2020. Present-day crustal deformation of continental China derived from GPS and its tectonic implications. Journal of Geophysical Research: Solid Earth, 125(2): e2019JB018774.

Wang, C.Y., Han, W.B., Wu, J.P., Lou, H. and Chan, W.W., 2007. Crustal structure beneath the eastern margin of the Tibetan Plateau and its tectonic implications. Journal of Geophysical Research: Solid Earth, 112(B7).

Wang, L., Pan, Y., Li, J. and Qin, H., 2008. Magnetic properties related to thermal treatment of pyrite. Science in China Series D: Earth Sciences, 51(8): 1144-1153.

Wang, E., Kirby, E., Furlong, K.P., Van Soest, M., Xu, G., Shi, X., Kamp, P.J. and Hodges, K., 2012. Two-phase growth of high topography in eastern Tibet during the Cenozoic. Nature Geoscience, 5(9): 640-645.

Wang, C., Dai, J., Zhao, X., Li, Y., Graham, S.A., He, D., Ran, B. and Meng, J., 2014. Outward-growth of the Tibetan Plateau during the Cenozoic: A review. Tectonophysics, 621: 1-43.

Wang, K., Jia, D., Luo, L. and Dong, S., 2017. Magnetic fabric and structural deformation. Chinese Journal of Geophysics, 60(3): 1007-1026.

Wang, W., Qiao, X. and Ding, K., 2021. Present-day kinematics in southeastern Tibet inferred from GPS measurements. Journal of Geophysical Research: Solid Earth, 126(1): e2020JB021305.

Wasilewski, P.J., 1973. Magnetic hysteresis in natural materials. Earth and Planetary Science Letters, 20(1): 67-72.

Weaver, R., Roberts, A.P. and Barker, A.J., 2002. A late diagenetic (syn-folding) magnetization carried by pyrrhotite: implications for paleomagnetic studies from magnetic iron sulphide-bearing sediments. Earth and Planetary Science Letters, 200(3-4): 371-386.

Weil, A.B. and Sussman, A.J., 2004. Classifying curved orogens based on timing relationships between structural development and vertical-axis rotations, Orogenic curvature: integrating paleomagnetic and structural analyses. Geological Society of America, pp. 1-15.

Weil, A.B. and Yonkee, A., 2009. Anisotropy of magnetic susceptibility in weakly deformed red beds from the Wyoming salient, Sevier thrust belt: Relations to layer-parallel shortening and orogenic curvature. Lithosphere, 1(4): 235-256.

Weil, A.B., Yonkee, A. and Sussman, A., 2010. Reconstructing the kinematic evolution of curved mountain belts: A paleomagnetic study of Triassic red beds from the Wyoming salient, Sevier thrust belt, USA. Bulletin, 122(1-2): 3-23.

Weltje, G.J., 1997. End-member modeling of compositional data: Numerical-statistical algorithms for solving the explicit mixing problem. Mathematical Geology, 29(4): 503-549.

Whittington, A.G., Hofmeister, A.M. and Nabelek, P.I., 2009. Temperature-dependent thermal diffusivity of the Earth's crust and implications for magmatism. Nature, 458(7236): 319-321.

Winklhofer, M., Fabian, K. and Heider, F., 1997. Magnetic blocking temperatures of magnetite calculated with a three-dimensional micromagnetic model. Journal of Geophysical Research: Solid Earth, 102(B10): 22695-22709.

Wu, Y. and Gao, Y., 2019. Gravity pattern in southeast margin of Tibetan Plateau and its implications to tectonics and large earthquakes. Earth and Planetary Physics, 3(5): 425-434.

Wu, Z., Ji, C., Zhao, Z. & Chen, C., 2020. Buried depth evolution and hydrocarbon generation history of the Jurassic System in central Qiangtang Basin. Acta Geol. Sin., 94, 102 823–102 833.

Xizang Geological Survey (XGS)., Geological map (1:250000) of the People's Republic of China-Mangkang Country sheet, 2007. Wuhan: China University of Geosciences Press.

Xiao, F. and Wang, Z., 2017. Geological interpretation of Bouguer gravity and aeromagnetic data from the Gobi-desert covered area, Eastern Tianshan, China: Implications for porphyry Cu-Mo polymetallic deposits exploration. Ore Geology Reviews, 80: 1042-1055.

Xiao, R., Zheng, Y., Liu, X., Yang, Q., Liu, G., Xia, L., Bian, Z., Guan, J., Feng, P. and Xu, H., 2021. Synchronous Sedimentation in Gonjo Basin, Southeast Tibet in Response to India-Asia Collision Constrained by Magnetostratigraphy. Geochemistry, Geophysics, Geosystems, 22(3): e2020GC009411.

Xiong, Z., Ding, L., Spicer, R.A., Farnsworth, A., Wang, X., Valdes, P.J., Su, T., Zhang, Q., Zhang, L. and Cai, F., 2020. The early Eocene rise of the Gonjo Basin, SE Tibet: From low desert to high forest. Earth and Planetary Science Letters, 543: 116312.

Xu, R., Schärer, U. and Allègre, C.J., 1985. Magmatism and metamorphism in the Lhasa block (Tibet): a geochronological study. The Journal of Geology, 93(1): 41-57.

Xu, Z., Yang, J., Li, H., Wang, R. and Cai, Z., 2012. Indosinian collision-orogenic system of Chinese continent and its orogenic mechanism. ACTA PETROLOGICA SINICA, 28(6): 1697-1709.

Xu, Q., Ding, L., Zhang, L., Cai, F., Lai, Q., Yang, D. and Liu, Z., 2013. Paleogene high elevations in the Qiangtang Terrane, central Tibetan Plateau. Earth and Planetary Science Letters, 362: 31-42.

Xu, Y., Yang, Z., Tong, Y., Wang, H., Gao, L. and An, C., 2015. Further paleomagnetic results for lower Permian basalts of the Baoshan Terrane, southwestern China, and paleogeographic implications. Journal of Asian Earth Sciences, 104: 99-114.

Xu, C., Liu, Z., Luo, Z., Wu, Y. and Wang, H., 2017. Moho topography of the Tibetan Plateau using multi-scale gravity analysis and its tectonic implications. Journal of Asian Earth Sciences, 138: 378-386.

Xu, C., Luo, Z., Sun, R., Zhou, H. and Wu, Y., 2018. Multilayer densities using a wavelet-based gravity method and their tectonic implications beneath the Tibetan Plateau. Geophysical Journal International, 213(3): 2085-2095.

Xu, W., Yan, M., van Hinsbergen, D.J.J., Li, B., Guan, C., Fu, Q., Yu, L., Xu, Z., Zhang, D., Shen, M., Feng, Z., Niu, Z., and Vaes, B., submitted, Paleomagnetic Evidence of 50º post-Eocene Clockwise Rotation of Mangkang and its Implications on the Tectonic Evolution of the Southeastern Tibetan Plateau, submitted to Gondwana Research.

Yan, M., Van der Voo, R., Tauxe, L., Fang, X. and M Parés, J., 2005. Shallow bias in Neogene palaeomagnetic directions from the Guide Basin, NE Tibet, caused by inclination error. Geophysical Journal International, 163(3): 944-948.

Yan, M., Zhang, D., Fang, X., Ren, H., Zhang, W., Zan, J., Song, C. and Zhang, T., 2016. Paleomagnetic data bearing on the Mesozoic deformation of the Qiangtang Block: Implications for the evolution of the Paleo-and Meso-Tethys. Gondwana Research, 39: 292-316.

Yan, Y., Chen, L., Huang, B., Yi, Z. and Zhao, J., 2019. Magnetic fabric constraint on tectonic setting of Paleoproterozoic dyke swarms in the North China Craton, China. Precambrian Research, 329: 247-261.

Yang, Z. and Besse, J., 1993. Paleomagnetic study of Permian and Mesozoic sedimentary rocks from Northern Thailand supports the extrusion model for Indochina. Earth and Planetary Science Letters, 117(3-4): 525-552.

Yang, W., Shi, Z. and Hou, Z., 2001a. Discrete wavelet transform for multiple decomposition of gravity anomalies. Chinese journal of geophysics, 44(4): 529-537.

Yang, Z., Yin, J., Sun, Z., Otofuji, Y.i. and Sato, K., 2001b. Discrepant Cretaceous paleomagnetic poles between Eastern China and Indochina: a consequence of the extrusion of Indochina. Tectonophysics, 334(2): 101-113.

Yang, W., Sun, Y., Hou, Z. and Yu, C., 2015. A Multi-Scale Scratch Analysis Method for Quantitative Interpretation of Regional Gravity Fields. Chinese Journal of Geophysics, 58(1): 41-53.

Yao, T., Thompson, L.G., Mosbrugger, V., Zhang, F., Ma, Y., Luo, T., Xu, B., Yang, X., Joswiak, D.R. and Wang, W., 2012. Third pole environment (TPE). Environmental Development, 3: 52-64.

Yao, T., Wu, G., Xu, B., Wang, W., Gao, J. and An, B., 2019. Asian water tower change and its impacts. Bulletin of Chinese Academy of Sciences (Chinese Version), 34(11): 1203-1209.

Yin, A. and Harrison, T.M., 2000. Geologic evolution of the Himalayan-Tibetan

orogen. Annual review of earth and planetary sciences, 28(1): 211-280.
Yonkee, A. and Weil, A.B., 2010. Quantifying vertical axis rotation in curved orogens: Correlating multiple data sets with a refined weighted least squares strike test. Tectonics, 29(3).
Yu, X., Huang, B., Guan, S., Fu, S., Cheng, F., Cheng, X., Zhang, T. and Guo, Z., 2014. Anisotropy of magnetic susceptibility of Eocene and Miocene sediments in the Qaidam Basin, Northwest China: Implication for Cenozoic tectonic transition and depocenter migration. Geochemistry, Geophysics, Geosystems, 15(6): 2095-2108.
Yu, L., Yan, M., Domeier, M., Guan, C., Shen, M., Fu, Q., Xu, W., Xu, Z., Niu, Z. and Yang, L., 2022a. New Paleomagnetic and Chronological Constraints on the Late Triassic Position of the Eastern Qiangtang Terrane: Implications for the Closure of the Paleo - Jinshajiang Ocean. Geophysical Research Letters, 49(2): e2021GL096902.
Yu, L., Yan, M., Guan, C., Li, B., Fu, Q., Xu, W., Feng, Z., Zhang, D., Shen, M. and Xu, Z., 2022b. Remagnetization of Carboniferous Limestone in the Zaduo Area, Eastern Qiangtang Terrane, and Its Tectonic Implications. Frontiers in Earth Science, 10: 1-18.
Yuan, X., Jiao, R., Dupont-Nivet, G. and Shen, X., 2022. Southeastern Tibetan Plateau growth revealed by inverse analysis of landscape evolution model. Geophysical Research Letters: e2021GL097623.
Zegers, T., Dekkers, M. and Bailly, S., 2003. Late Carboniferous to Permian remagnetization of Devonian limestones in the Ardennes: role of temperature, fluids, and deformation. Journal of Geophysical Research: Solid Earth, 108(B7).
Zhai, Q., Jahn, B., Zhang, R., Wang, J. and Su, L., 2011. Triassic subduction of the Paleo-Tethys in northern Tibet, China: evidence from the geochemical and isotopic characteristics of eclogites and blueschists of the Qiangtang Block. Journal of Asian Earth Sciences, 42(6): 1356-1370.
Zhang, K., Xia, B., Wang, G., Li, Y. and Ye, H., 2004. Early Cretaceous stratigraphy, depositional environments, sandstone provenance, and tectonic setting of central Tibet, western China. GSA Bulletin, 116(9-10): 1202-1222.
Zhang, K.J., Zhang, Y.X., Tang, X.C. and Xia, B., 2012. Late Mesozoic tectonic evolution and growth of the Tibetan plateau prior to the Indo-Asian collision. Earth-Science Reviews, 114(3-4): 236-249.
Zhang, L., Ding, L., Pullen, A., Xu, Q., Liu, D., Cai, F., Yue, Y., Lai, Q., Shi, R. and Ducea, M.N., 2014. Age and geochemistry of western Hoh-Xil–Songpan-Ganzi granitoids, northern Tibet: Implications for the Mesozoic closure of the Paleo-Tethys ocean. Lithos, 190: 328-348.
Zhang, H., Oskin, M.E., Liu, Z., Zhang, P., Reiners, P.W. and Xiao, P., 2016a. Pulsed exhumation of interior eastern Tibet: Implications for relief generation mechanisms and the origin of high-elevation planation surfaces. Earth and Planetary Science Letters, 449: 176-185.
Zhang, Y., Li, Z., Zhu, L., Zhang, K., Yang, W. and Jin, X., 2016b. Newly discovered

eclogites from the Bangong Meso–Tethyan suture zone (Gaize, central Tibet, western China): Mineralogy, geochemistry, geochronology, and tectonic implications. International Geology Review, 58(5): 574-587.

Zhang, Y., Replumaz, A., Leloup, P.H., Wang, G., Bernet, M., van der Beek, P., Paquette, J.L. and Chevalier, M.L., 2017. Cooling history of the Gongga batholith: Implications for the Xianshuihe Fault and Miocene kinematics of SE Tibet. Earth and Planetary Science Letters, 465: 1-15.

Zhang, Y., Huang, W., Huang, B., van Hinsbergen, D.J., Yang, T., Dupont-Nivet, G. and Guo, Z., 2018. 53–43 Ma deformation of eastern Tibet revealed by three stages of tectonic rotation in the Gongjue basin. Journal of Geophysical Research: Solid Earth, 123(5): 3320-3338.

Zhang, W., Fang, X., Zhang, T., Song, C. and Yan, M., 2020a. Eocene rotation of the northeastern central Tibetan Plateau indicating stepwise compressions and eastward extrusions. Geophysical Research Letters, 47(17): e2020GL088989.

Zhang, Y., Jia, D., Muxworthy, A.R., Zhang, Y., Li, Y., Yin, H., Chen, Z., Brzozowski, M.J., Li, W. and Wang, M., 2020b. Fluid migration and widespread remagnetization in the Dabashan fold and thrust belt, China. Journal of Geophysical Research: Solid Earth, 125(11): e2020JB019989.

Zhang, D., Yan, M., Song, C., Zhang, W., Fang, X. and Li, B., 2021. Frequent Polarity Reversals in the Cretaceous Normal Superchron. Geophysical Research Letters, 48(5): e2020GL091501.

Zhang, W., Li, B. and Yan, M., 2022a. Anisotropy of Magnetic Susceptibility Reveals Late Miocene Tectonic Activity in the Western Qaidam Basin. FRONTIERS IN EARTH SCIENCE, 10.

Zhang, X., Wang, Q., Wyman, D., Ou, Q., Qi, Y., Gou, G.N., Dan, W. and Yang, Y.N., 2022b. Tibetan Plateau growth linked to crustal thermal transitions since the Miocene. Geology, 50(5): 610-614.

Zhao, Z., Bons, P.D., Wang, G., Liu, Y. and Zheng, Y., 2014. Origin and pre-Cenozoic evolution of the south Qiangtang basement, Central Tibet. Tectonophysics, 623: 52-66.

Zhao, G., Wang, Y., Huang, B., Dong, Y., Li, S., Zhang, G. and Yu, S., 2018. Geological reconstructions of the East Asian blocks: From the breakup of Rodinia to the assembly of Pangea. Earth-Science Reviews, 186: 262-286.

Zheng, M., Zhang, Y., Qi, W. and Liu, X., 2011. Thought and suggestions on regional analysis of potash and its prospecting evaluation in China. Acta Geologica Sinica, 85(1): 17-50.

Zhou, Y., Cheng, X., Wu, Y., Kravchinsky, V., Shao, R., Zhang, W., Wei, B., Zhang, R., Lu, F. and Wu, H., 2019. The northern Qiangtang Block rapid drift during the Triassic Period: Paleomagnetic evidence. Geoscience Frontiers, 10(6): 2313-2327.

Zhu, D., Pan, G., Mo, X., Wang, L., Zhao, Z., Liao, Z., Geng, Q. and Dong, G., 2006. Identification for the Mesozoic OIB-type basalts in central Qinghai-Tibetan Plateau: Geochronology, geochemistry and their tectonic setting. Acta

Geologica Sinica, 80(9): 1312-1328.

Zhu, D., Zhao, Z., Niu, Y., Mo, X., Chung, S., Hou, Z., Wang, L. and Wu, F., 2011. The Lhasa Terrane: record of a microcontinent and its histories of drift and growth. Earth and Planetary Science Letters, 301(1-2): 241-255.

Zhu, D., Zhao, Z., Niu, Y., Dilek, Y., Wang, Q., Ji, W., Dong, G., Sui, Q., Liu, Y. and Yuan, H., 2012. Cambrian bimodal volcanism in the Lhasa Terrane, southern Tibet: record of an early Paleozoic Andean-type magmatic arc in the Australian proto-Tethyan margin. Chemical Geology, 328: 290-308.

Zhu, D.C., Zhao, Z.D., Niu, Y.l., Dilek, Y., Hou, Z.Q. and Mo, X.X., 2013. The origin and pre-Cenozoic evolution of the Tibetan Plateau. Gondwana Research, 23(4): 1429-1454.

Zhu, D., Li, S., Cawood, P.A., Wang, Q., Zhao, Z., Liu, S. and Wang, L., 2016. Assembly of the Lhasa and Qiangtang terranes in central Tibet by divergent double subduction. Lithos, 245: 7-17.

Zi, J., Cawood, P.A., Fan, W., Tohver, E., Wang, Y. and McCuaig, T.C., 2012. Generation of Early Indosinian enriched mantle-derived granitoid pluton in the Sanjiang Orogen (SW China) in response to closure of the Paleo-Tethys. Lithos, 140: 166-182.

Zijderveld, J., 1967. AC demagnetization of rocks: Analysis of results, Methods in Paleomagnetism DW Collinson, KM Creer, SK Runcorn, 254–286. Elsevier, New York.

Zwing, A., Clauer, N., Liewig, N. and Bachtadse, V., 2009. Identification of remagnetization processes in Paleozoic sedimentary rocks of the northeast Rhenish Massif in Germany by K-Ar dating and REE tracing of authigenic illite and Fe oxides. Journal of Geophysical Research: Solid Earth, 114(B6).


Universiteit Utrecht

S

SUPPLEMENTARY INFORMATION TO CHAPTERS

Chapter S1

Supplementary tables

Table S1.1. *Isothermal remanence acquisition (IRM) for individual specimens at room temperature.*

	1-1	1-5	1-6	1-7	1-8	2-1	2-4	2-5	3-1	3-2	3-6
0	0	0	0	0	0	0	0	0	0	0	0
5	65.17	34.57	111.67	203.39	111.95	145.3	40.64	25.22	79.18	126.65	73.13
10	232.76	128.42	344.42	597.98	352.73	396.69	147.87	90.1	189.53	291.65	177.03
12	317.22	175.21	456.06	787.09	472.01	511.99	201.94	122.81	253.76	387.7	237.3
14	388.96	216.85	545.58	940.82	568.81	599.34	248.94	154.28	311.3	452.57	284.14
16	459.59	258.17	633.86	1089.35	664.61	683.85	295.39	185.94	376.53	523.95	336.5
18	519.84	292.94	706.76	1210.52	744.95	750.75	335.07	211.15	401.54	564.22	362.44
20	598.12	337.01	799.23	1366.03	847.6	837.04	383.81	245.08	474.3	663.54	428.55
22	653.81	369.3	864.88	1478.29	921.29	895.29	420.05	270.19	514.26	717.28	465.63
24	718.36	408.04	939.19	1596.91	999.82	956.63	460.97	302.11	539.12	750.48	488.7
26	784.98	448.56	1015.35	1708.8	1074.45	1016.94	502.52	340.22	548.73	761.81	496.37
28	840.16	479.83	1077.12	1808.97	1143.52	1067.86	534.18	366.31	618.51	856.87	561.63
30	910.09	521.6	1153.11	1929.54	1225.22	1129.12	577.3	398.59	654.93	902.89	594.66
33	967.76	557.21	1215.21	2027.62	1295.53	1176	613.21	424.8	691.66	951.13	629.01
36	1036.09	597.95	1287.26	2142.19	1375.07	1231.36	654.56	456.43	723.82	992.62	658.76
40	1133.27	654.96	1384.38	2298.32	1482.73	1304.73	710.33	501.83	798.59	1087.73	726.04
43	1191.8	689.76	1443.06	2391.51	1548.71	1347.5	743.16	530.37	832.27	1128.39	756.11
46	1246.1	721.15	1495.97	2474.1	1606.57	1383.91	772.89	555.98	858.27	1158.9	778.41
50	1324.09	766.22	1569.94	2591.11	1689.97	1434.46	814.04	591.32	911.68	1221.32	823.45
55	1395.19	807.37	1635.48	2691.75	1765.1	1478.8	850	625.17	967.14	1283.96	870.66

60	**1459.64**	**842.56**	**1692.04**	**2779.67**	**1827.43**	**1515.03**	**880.48**	**654.58**	**1001.63**	**1322**	**898.41**
65	1524.64	878.37	1748.23	2865.75	1891.26	1550.39	909.47	685.15	1041.26	1364.99	930
70	1582.36	909.13	1797.25	2940.55	1948.39	1579.75	933.58	711.81	1072.15	1394.1	952.73
75	1632.95	935.3	1839.42	3002.97	1992.22	1603.1	952.74	735.1	1103.85	1426.89	976.89
80	1677.73	958.73	1874.63	3055.09	2032.85	1622.1	969.1	756.96	1120.82	1445.79	989.24
90	1752.26	995.45	1931.12	3137.32	2102.94	1650.97	993.17	791.6	1164.64	1484.73	1018.18
100	1807.19	1020.94	1970.01	3193.9	2145.72	1669.92	1008.87	814.93	1191.1	1505.1	1034.89
120	1899.41	1062.57	2034.12	3279.93	2220.31	1698.04	1030.1	858.22	1237.09	1538.59	1060.85
140	1974.21	1094.85	2083.28	3348.84	2276.8	1714.49	1042.52	893.02	1272.53	1559.21	1078.53
160	2033.5	1124.72	2126.43	3400.47	2318.78	1728.37	1050.74	916.76	1294.36	1569.56	1088.59
180	2069.18	1137.62	2146.73	3428.73	2345.31	1734.44	1053.31	931.17	1311.95	1575.55	1096.38
200	2100.43	1149.4	2166.5	3453.19	2366.37	1739.3	1056.54	941.58	1324.72	1580.92	1102.35
230	2128.03	1161.62	2183.57	3474.34	2384.54	1745.44	1059.95	955.84	1335.41	1584.37	1105.71
260	2143.56	1168.5	2193.28	3484.62	2396.25	1749.75	1062.3	960.69	1341.97	1586.24	1111.01
300	2153.53	1173.75	2200.99	3493.09	2405.72	1752.52	1065.05	966.01	1345.4	1587.89	1113.11
350	2155.25	1174.91	2201.35	3493.19	2406.57	1754.76	1067.31	967.8	1347.3	1588.97	1115.84
400	2157.51	1178.73	2204.78	3495.05	2407.58	1757.29	1070.65	968.75	1348.3	1589.72	1117.45
450	2157.51	1178.73	2204.78	3495.05	2407.58	1757.72	1071.51	969.28	1348.56	1590.24	1118.26
500	2157.51	1178.73	2204.78	3495.05	2407.58	1758.72	1073.54	970.83	1349.15	1591.27	1119.69
550	2157.51	1178.73	2204.78	3495.05	2407.58	1759.29	1075.24	970.97	1349.4	1591.82	1120.86
600	2157.51	1178.73	2204.78	3495.05	2407.58	1760.55	1077.17	971.81	1349.45	1592.55	1122.55
650	2157.51	1178.73	2204.78	3495.05	2407.58	1760.97	1077.89	974.21	1350.19	1594.1	1123.51
700	2157.51	1178.73	2204.78	3495.05	2407.58	1763.53	1078.87	974.72	1350.26	1594.11	1124.34

Table S1.1. *continued below.*

	4-2	**4-5**	**4-6**	**4-7**	**4-8**	**4-10**	**5-1**	**5-2**	**5-3**	**5-4**	**5-6**
0	0	0	0	0	0	0	0	0	0	0	0
5	137.2	254.76	151.45	223.79	164.42	42.65	1.53	0.95	1.52	0.12	1.19
10	313.32	561.47	344.7	486.8	354.89	171.56	12.61	8.56	9.47	9.3	8.27
12	415.44	736.45	459.55	636.3	467.94	233.92	18.75	13.19	14.21	14.1	12.71
14	479.35	845.09	536.61	732	541.93	292.89	24.72	18.1	19.24	19.61	17.42
16	548.41	961.36	620.12	835.36	622.74	341.25	29.42	22.1	23.29	23.75	21.07
18	591.16	1032.19	669.31	894.48	670.73	363.55	32.36	24.65	25.56	26.54	23.29
20	697.59	1206.79	793.17	1041.34	789.17	438.53	41.8	32.52	33.39	35.31	30.97
22	753.03	1298.2	858.58	1117.92	851.95	493.82	49.61	39.16	39.7	42.45	37.19
24	788.46	1356.36	899.91	1167.63	891.75	539.82	55.5	44.45	44.92	48.61	42.27
26	799.25	1375.81	912.98	1183.29	904.74	563.25	59.37	47.79	47.99	52.53	45.47

28	900.73	1538.02	1031.71	1315.77	1016.93	596.16	63.54	51.99	51.7	56.16	48.95
30	949.34	1618.05	1091.37	1385.75	1073.36	659.9	73.45	60.85	60.1	65.66	57.31
33	999.48	1693.61	1148.47	1447.66	1127.6	685.69	77.39	64.64	63.64	69.43	60.59
36	1044.7	1763.4	1201.46	1506.92	1177.77	735.27	85.2	71.96	70.41	77.56	67.42
40	1145.25	1913.42	1314.44	1630.27	1284.13	827.28	99.98	86.75	83.79	93.11	81.03
43	1189.08	1978.51	1364.11	1682	1330.86	855.16	103.8	90.57	87.42	96.86	84.41
46	1222.12	2027.28	1402.01	1723.84	1366.49	886.22	108.95	96.26	92.35	103.31	89.38
50	1289.61	2127.99	1479.89	1806.95	1438.96	939.57	118.2	105.4	100.71	112.2	97.91
55	1359.73	2229.27	1559.42	1890.32	1513.02	1000.65	127.86	115.74	109.93	122.1	107.15
60	1402.46	2290.12	1608.57	1943.67	1557.67	1042.99	134	122.25	115.87	128.97	113.21
65	1450.18	2359.5	1663.29	2001.23	1608.97	1083.95	139.77	128.56	121.58	135.65	119.06
70	1483.03	2407.55	1702.32	2040.18	1644.28	1117.62	144.25	133.37	125.89	140.09	123.34
75	1520.47	2460.26	1745.5	2085.18	1682.62	1151.72	149.67	138.76	131.01	145.73	128.63
80	1543.26	2492.38	1770.1	2113.52	1705.78	1171.31	152.72	141.21	133.67	148.72	131.18
90	1594.33	2558.23	1828.34	2173.99	1758.4	1229.24	161.94	153.05	141.42	157.83	140.74
100	1618.25	2591.34	1857.5	2204.34	1783.6	1276.59	172.23	170.4	148.11	167.13	152.97
120	1659.71	2649.6	1907.4	2253.94	1829.5	1326.1	178.37	175.44	153.26	172.73	158.64
140	1686.77	2688.76	1942.86	2288.32	1860.34	1364.68	183.27	179.82	157.28	176.87	163.49
160	1704.53	2710.84	1962.55	2310.02	1878.23	1391.48	186.63	182.28	159.91	179.6	166.83
180	1713.48	2724.89	1975.85	2322.52	1889.73	1410.49	189.34	184.51	161.95	181.7	169.5
200	1720.19	2735	1983.9	2328.13	1898.12	1426.12	191.82	185.76	163.94	183.82	171.63
230	1728.33	2746.87	1994.93	2342.2	1907.2	1439.05	194.47	188.13	165.72	185.82	174.08
260	1731.4	2749.54	1998.8	2342.95	1911.48	1448.75	196.7	190.08	167.37	187.57	176.01
300	1735.07	2752.46	2000.52	2345.56	1914.72	1455.88	199.14	191.64	169.07	189.44	177.87
350	1735.63	2752.67	2001.12	2346.59	1916.28	1459.8	201.27	193.13	170.7	191.02	179.51
400	1736.66	2753.19	2001.38	2347.72	1917.32	1462.45	203.7	194.79	172.3	192.67	180.86
450	1736.75	2753.62	2001.43	2347.84	1917.58	1463.71	205.9	196.29	173.43	193.98	182.12
500	1736.83	2754.36	2001.51	2348.32	1917.63	1464.73	207.11	196.89	174.5	194.85	182.92
550	1737.02	2754.56	2001.71	2348.49	1918.51	1465.53	209.01	198.5	175.64	195.97	184.07
600	1738.15	2754.84	2002.37	2348.75	1919.65	1467.31	210.5	199.43	176.55	196.5	185.06
650	1738.9	2755.44	2003.13	2350.23	1921.35	1467.6	211.92	200.05	177.38	196.59	185.47
700	1740.18	2755.57	2003.38	2351.2	1921.9	1468.2	213.35	200.96	178.24	197.17	186.49

Table S1.1. *continued below.*

	5-8	**5-10**	**6-2**	**6-3**	**6-5**	**7-1**	**7-3**	**7-4**	**8-11**	**9-1**	**9-10**
0	0	0	0	0	0	0	0	0	0	0	0
5	1.54	1.43	10.56	18.62	35.59	0.5	2.61	1.65	42.1	6.62	12.77

10	9.84	9.72	40.98	69.19	132.82	3.06	6.82	6.83	137.01	9.75	32.94
12	14.66	14.74	59.03	101.52	195.75	5.94	13.56	11.95	192.2	17.07	39.08
14	19.86	20.2	86.08	149.32	285.28	10.55	20.49	19.64	278.62	26.37	52.36
16	24.11	24.22	101.67	175.01	334.57	12.97	26.38	23.8	325.33	31.4	75.49
18	26.31	26.94	108.25	186.92	355.77	14.14	28.16	25.86	346.97	38.39	96.71
20	34.4	36.55	155.34	274	509.62	23.18	43.61	40.64	514.07	61	148.85
22	40.73	43.51	179.09	316.98	583.55	27.91	51.91	48.53	597.7	74.09	219.55
24	45.54	49.1	196.79	349.78	638.88	31.56	58.6	54.41	661.46	77.75	220.43
26	48.65	52.98	202.19	360.62	655.72	32.72	62.31	56.34	681.99	82.35	239.19
28	52.59	56.79	226.95	405.27	730.18	37.82	69.32	64.44	770.03	94.79	278.37
30	60.97	66.47	250.71	450.8	801.99	43.48	79.56	73.25	860.89	109.44	307.96
33	64.4	70.24	271.91	489.98	862.75	48.59	87.7	81.03	940.87	118.56	335.98
36	70.77	78.35	292.71	530.03	924.56	53.63	97.13	88.95	1022.81	128.73	368.73
40	83.91	93.57	328.94	597.43	1027.11	62.19	112.1	102.44	1161.84	153.69	414
43	87.39	96.95	343.63	624.87	1068.82	65.62	118.35	107.75	1218.57	160.07	437.98
46	92.37	102.94	358.89	654	1111.4	69.48	126.67	113.73	1279.05	169.44	453.45
50	101.21	113.2	390.27	713.05	1197.05	77.12	140.4	125.71	1404.63	184.53	485.82
55	110.13	123.08	411.07	752.19	1252.19	82.1	146.43	133.13	1488.9	197.76	524.74
60	115.93	129.28	436.13	799.18	1317.97	88.17	157.18	142.48	1591.32	214.42	552.7
65	121.73	135.72	454.92	833.41	1364.78	92.41	165.74	149.14	1665.66	225.56	575.28
70	126.16	140.91	468.73	859.12	1400.49	95.64	171.99	153.79	1723.13	229.83	599.21
75	130.93	145.98	485.74	890.85	1443.64	99.66	178.31	159.73	1794.75	243.16	622.62
80	133.49	147.96	495.02	907.66	1466.47	101.9	181.25	162.83	1834.73	248.26	637.8
90	142.6	159.51	520.32	953.95	1526.57	107.47	191.17	171.31	1944.48	262.87	672.15
100	152.73	172.8	535.28	979.04	1559.33	110.84	197.55	176	2006.93	274.23	694.83
120	157.82	178.94	559.21	1017.22	1608.28	116.22	209.55	182.81	2103.96	287.09	731.09
140	162.92	181.83	576.98	1044.43	1643.7	120.27	215.57	188.38	2176.26	294.6	761.36
160	164.62	184.43	589.37	1061.09	1664.53	123.33	217.89	191.99	2218.87	300.7	781.76
180	166.82	187.08	600.34	1072.56	1680.03	126.02	222.75	195.54	2247.99	312.14	795.76
200	168.88	188.82	607.58	1080.17	1689.1	128.29	228.69	197.77	2266.22	312.27	808.13
230	171.76	191.46	613.45	1085.69	1695.74	130.13	230.06	200.3	2278.18	314.91	818.76
260	172.76	194.2	618.8	1089.03	1698.42	131.99	230.8	202.66	2281.8	320.26	824.79
300	174.9	195.48	621.76	1090.83	1699.4	133.97	235.87	204.65	2281.86	322.74	825.97
350	177.39	198.11	623.24	1091.29	1699.99	135.73	236.05	206.48	2282.02	324.04	826.02
400	179.35	200.11	624.24	1091.56	1700.33	137.37	238.67	208.51	2283.03	327.93	826.31
450	180.75	202.66	625.21	1091.61	1700.51	138.64	241.85	209.71	2283.49	328.8	826.64
500	181.5	204.05	625.23	1092	1700.56	139.75	243.06	211.16	2284.06	330.57	827.38
550	183.8	206.83	625.57	1092.1	1700.66	140.81	243.81	212.16	2284.3	332.09	827.92
600	184.67	208.05	626.07	1092.53	1700.77	141.74	244.55	213	2284.56	334.58	828.29

650	185.04	209.38	627.44	1093.52	1701.51	142.51	245.68	213.92	2285.29	337.98	828.54
700	187.28	210.77	628.06	1093.71	1701.89	143.33	246.16	214.86	2285.93	339.2	830.3

Note: *sample ID is shown in the first row, applied field (mT) is shown in the first column.*

Table S1.2. *Results of isothermal remanent magnetization (IRM) component analysis for the representative samples and end-members.*

	Component 1					Component 2					Component 3				
Sample	Con (%)	SIRM (μAm^2)	$\log(B_{1/2})$ (mT)	$B_{1/2}$ (mT)	DP (mT)	Con (%)	SIRM (μAm^2)	$\log(B_{1/2})$ (mT)	$B_{1/2}$ (mT)	DP (mT)	Con (%)	SIRM (μAm^2)	$\log(B_{1/2})$ (mT)	$B_{1/2}$ (mT)	DP (mT)
ZD 2-5	15.27	0.15	1.05	11.2	0.37	83.71	0.82	1.65	44.67	0.36	1.02	0.01	2.75	562.3	0.2
ZD 3-6	14.31	0.16	0.8	6.31	0.37	84.71	0.95	1.5	31.62	0.35	0.98	0.01	2.67	467.74	0.1
ZD 5-4	13.57	0.03	1.28	19.05	0.33	80.4	0.16	1.65	44.67	0.32	6.03	0.01	2.57	371.53	0.17
ZD 7-4	14.61	0.03	1.38	23.99	0.33	76.26	0.17	1.63	42.66	0.33	9.13	0.02	2.6	398.11	0.25
ZD 9-10	18.79	0.16	1.39	24.55	0.26	80.26	0.68	1.68	47.86	0.37	0.95	0.01	2.7	501.19	0.25

	Component C1					Component C2					Component C3				
EM	Con (%)	SIRM ($\mu A/m$)	$\log(B_{1/2})$ (mT)	$B_{1/2}$ (mT)	DP (mT)	Con (%)	SIRM ($\mu A/m$)	$\log(B_{1/2})$ (mT)	$B_{1/2}$ (mT)	DP (mT)	Con (%)	SIRM ($\mu A/m$)	$\log(B_{1/2})$ (mT)	$B_{1/2}$ (mT)	DP (mT)
EM1	13.13	0.13	1.28	19.05	0.33	80.81	0.8	1.72	52.48	0.3	6.06	0.16	2.65	466.68	0.13
EM2	8.91	0.09	0.7	5.01	0.38	91.09	0.92	1.48	30.2	0.38	-	-	-	-	-

Note: *Con- contribution; SIRM- saturation isothermal remanent magnetization; $B_{1/2}$- the field at which half of the SIRM is reached; DP- dispersion parameter (Kruiver et al., 2001); EM: end member.*

Table S1.3. *Anhysteretic remanent magnetization (ARM) for individual specimens at room temperature.*

	0	2.5	5	7.5	10	15	20	25	30	35	40	45	50	60	70	85	100	120	150
1-1	0	1.31	3.1	4.68	6.36	8.99	11.06	13.52	14.89	15.9	17.36	18.81	19.27	20.67	21.37	21.82	22.08	22.79	22.91
1-5	0	0.56	1.53	2.23	3.27	4.94	6.37	7.93	9.54	10.64	11.23	12.41	12.98	13.75	14.32	14.78	14.84	15.32	15.41
1-6	0	2.27	4.21	5.37	6.38	9.46	12.04	13.58	15.1	16.99	17.8	18.24	21.11	22.17	22.32	22.56	23.27	24.26	24.66
1-7	0	4.19	8.23	11.48	13.63	15.95	18.74	21.54	22.49	23.55	26.05	26.06	28.09	29.9	30.44	32.05	32.34	32.38	32.41
1-8	0	2.31	4.54	6.15	7.72	10.05	12.24	14.02	15.94	16.56	17.44	18.42	19.55	19.92	20.91	20.94	21.34	21.36	21.68
2-1	0	3.42	6.34	8.38	9.86	11.14	13.02	14.24	14.57	16.12	16.47	16.78	16.91	16.92	16.94	17.19	17.28	17.59	17.72
2-4	0	0.64	1.65	2.74	3.65	5.61	7.49	9.03	10.36	11.22	12.52	13.57	14.08	14.75	14.81	14.9	14.95	15.13	15.4
2-5	0	0.27	0.88	1.58	2.04	3	4.06	5.07	5.74	6.51	7.25	7.53	8.3	8.81	9.25	9.43	9.43	9.5	9.5
3-1	0	1.08	2.43	3.77	4.64	6.16	7.71	9.17	10.17	11.03	11.98	12.89	13.33	14.24	14.64	14.7	14.81	14.91	15.17
3-2	0	1.75	3.62	5.22	6.85	8.57	10.03	11.49	12.34	13.73	14.13	14.93	15.06	16.16	16.49	18.59	18.63	18.65	18.68
3-6	0	0.96	2.16	3.25	4.27	5.84	7.51	9.19	10.54	11.58	12.79	13.23	14.4	15.12	15.26	16.06	16.15	16.18	16.21
4-2	0	1.94	4.04	5.99	7.3	9.03	11.44	13	14.63	15.91	16.43	17.5	17.95	18.78	19.76	19.94	20.48	20.48	20.51
4-5	0	4.36	7.85	10.21	12.32	14.51	16.38	18.62	20	22.87	24.64	25.26	26.37	27.7	28.05	28.24	28.53	28.87	29.44
4-6	0	2.42	4.55	6.19	7.79	9.92	10.82	12.21	13.27	13.87	15.32	15.71	16.23	16.65	16.76	16.77	16.79	17.04	17.1
4-7	0	3.97	6.93	8.86	10.46	11.77	13.64	15.08	15.81	17.1	18.85	18.86	19.42	20.78	20.92	20.95	20.95	21.02	21.04
4-8	0	2.31	4.42	5.86	7.03	9.33	10.99	12.36	13.36	14.8	15.73	16.43	16.87	17.69	18.53	18.68	18.85	19.02	19.04
4-10	0	0.93	2.26	3.65	5.07	6.99	9.17	11.44	12.88	14.66	15.17	16.29	18.35	18.48	18.63	18.64	20.12	20.2	20.41
5-1	0	0.2	0.63	1.17	1.75	3.01	4.24	5.42	6.38	7.25	7.94	8.55	8.99	9.64	9.93	10.09	10.1	10.14	10.15
5-2	0	0.14	0.48	0.89	1.35	2.29	3.31	4.25	5.07	5.86	6.54	7.06	7.54	8.07	8.38	8.63	8.63	8.65	8.65
5-3	0	0.11	0.44	0.86	1.34	2.29	3.29	4.25	5.03	5.77	6.38	6.92	7.29	7.82	8.09	8.25	8.27	8.27	8.27
5-4	0	0.14	0.47	0.89	1.37	2.43	3.54	4.63	5.58	6.45	7.26	7.86	8.37	9.04	9.41	9.74	9.77	9.77	9.78
5-6	0	0.11	0.41	0.79	1.2	2.1	3.07	4	4.87	5.66	6.34	6.87	7.32	7.93	8.25	8.45	8.51	8.55	8.57
5-8	0	0.11	0.4	0.75	1.18	2.03	2.93	3.78	4.52	5.19	5.76	6.22	6.63	7.12	7.42	7.52	7.58	7.61	7.65
5-10	0	0.13	0.51	0.98	1.51	2.64	3.76	4.84	5.71	6.55	7.24	7.81	8.25	8.84	9.13	9.32	9.38	9.39	9.42
6-2	0	0.39	0.98	1.66	2.23	3.3	4.21	5.35	6.14	7.05	7.98	8.32	8.78	9.53	9.75	9.76	9.98	9.99	10.24
6-3	0	0.47	1.28	2.08	2.86	4.44	6.01	7.6	8.85	9.91	10.74	11.39	11.89	12.7	13.13	13.49	13.57	13.6	13.64
6-5	0	1.11	2.75	3.97	5.4	7.28	9.3	11.13	12.46	13.28	14.45	15.52	16.19	17.18	17.48	18.26	18.32	18.44	18.49
7-1	0	0.09	0.32	0.61	0.91	1.62	2.34	3.07	3.72	4.26	4.74	5.11	5.46	5.84	6.02	6.18	6.2	6.2	6.26
7-3	0	0.17	0.47	0.79	1.26	2.06	2.98	4.01	4.82	5.63	6.22	6.82	7.25	8	8.07	8.48	8.52	8.54	8.54
7-4	0	0.14	0.43	0.77	1.17	1.96	2.8	3.58	4.32	5.06	5.63	6.07	6.47	6.88	7.11	7.23	7.24	7.25	7.26

8-11	0	0.76	1.89	3.07	4.43	6.74	8.97	10.83	12.28	13.4	14.86	15.77	16.16	16.55	16.65	17.12	17.54	17.67	18.15
9-1	0	0.37	0.81	1.49	2.38	3.66	5.29	6.86	8.07	9.35	10.26	10.9	11.36	12.2	12.55	12.62	13.24	13.26	13.3
9-10	0	1.01	2.14	3.41	4.8	6.61	8.97	10.67	12.34	13.97	15.17	15.54	17.24	17.67	18.48	19.7	19.94	20.07	20.16

Note: *sample ID is shown in the first row, applied field (mT) is shown in the first column.*

Table S1.4. *Hysteresis parameters of representative samples of the Early Cretaceous granite in Zaduo area.*

No.	ARM_{120mT} (10^{-6} Am^2/kg)	IRM_{700mT} (10^{-4} Am^2/kg)	IRM_{100mT} (10^{-4} Am^2/kg)	ARM_{120mT}/IRM_{700mT}	ARM_{120mT}/IRM_{100mT}
1-1	22.8	21.6	18.1	0.0106	0.0126
1-5	15.3	11.8	10.2	0.013	0.015
1-6	24.3	22	19.7	0.011	0.0123
1-7	32.2	35	31.9	0.0092	0.0101
1-8	20.9	24.1	21.5	0.0087	0.0097
2-1	17.2	17.6	16.7	0.0097	0.0103
2-4	14.8	10.8	10.1	0.0137	0.0147
2-5	9.3	9.7	8.1	0.0095	0.0114
3-1	14.7	13.5	11.9	0.0109	0.0123
3-2	18.6	15.9	15.1	0.0117	0.0124
3-6	15.8	11.2	10.3	0.014	0.0152
4-2	20.5	17.4	16.2	0.0118	0.0127
4-5	28.2	27.6	25.9	0.0102	0.0109
4-6	17.6	20	18.6	0.0088	0.0095
4-7	21	23.5	22	0.0089	0.0095
4-8	19	19.2	17.8	0.0099	0.0107
4-10	20.2	14.7	12.8	0.0138	0.0158
5-1	10	2.1	1.7	0.047	0.0583
5-2	8.5	2	1.7	0.0423	0.0499
5-3	8.2	1.8	1.5	0.0458	0.0551
5-4	9.6	2	1.7	0.0488	0.0576
5-6	8.4	1.9	1.5	0.0453	0.0552
5-8	7.5	1.9	1.5	0.0401	0.0492
5-10	9.3	2.1	1.7	0.044	0.0536
6-2	9.8	6.3	5.4	0.0156	0.0183
6-3	13.2	10.9	9.8	0.0121	0.0135
6-5	18.4	17	15.6	0.0108	0.0118
7-1	6.1	1.4	1.1	0.0426	0.0551
7-3	8	2.5	2	0.0326	0.0407
7-4	7.1	2.1	1.8	0.0331	0.0404
8-11	17.2	22.9	20.1	0.0075	0.0086
9-1	13.2	3.4	2.7	0.0388	0.048
9-10	20.1	8.3	6.9	0.0242	0.0289

Table S1.5. *Contributions of each EM of IRM end-member modeling for the Cretaceous granite.*

Specimen	two end-member model		three end-member model			four end-member model			
	EM1	EM2	EM1	EM2	EM3	EM1	EM2	EM3	EM4
1-1	0.23	0.77	0	0.81	0.19	0	0.75	0.09	0.16
1-5	0.21	0.79	0	0.74	0.26	0	0.67	0.12	0.21
1-6	0.07	0.93	0	0.55	0.45	0	0.53	0.11	0.36
1-7	0.01	0.99	0	0.46	0.54	0	0.42	0.15	0.43
1-8	0.08	0.92	0	0.56	0.44	0	0.5	0.15	0.35
2-1	0	1	0	0.23	0.77	0	0.26	0.13	0.61
2-4	0.12	0.88	0.05	0.44	0.51	0.03	0.38	0.17	0.42
2-5	0.28	0.72	0	0.83	0.16	0	0.79	0.07	0.14
3-1	0.08	0.92	0.02	0.44	0.54	0	0.07	0.52	0.41
3-2	0	1	0.02	0.23	0.75	0	0	0.48	0.52
3-6	0.04	0.96	0.07	0.27	0.66	0.01	0	0.51	0.48
4-2	0	1	0.02	0.29	0.69	0	0	0.5	0.5
4-5	0	1	0	0.23	0.77	0	0	0.45	0.55
4-6	0	1	0.01	0.31	0.68	0	0	0.51	0.49
4-7	0	1	0.01	0.22	0.77	0	0	0.44	0.56
4-8	0	1	0.02	0.27	0.71	0	0	0.49	0.51
4-10	0.37	0.63	0.2	0.49	0.3	0.14	0.42	0.2	0.24
5-1	0.92	0.08	0.65	0.27	0.08	0.48	0.41	0.06	0.05
5-2	0.88	0.12	0.61	0.32	0.07	0.45	0.41	0.1	0.04
5-3	0.8	0.2	0.55	0.36	0.09	0.4	0.39	0.16	0.06
5-4	0.79	0.21	0.52	0.42	0.06	0.38	0.47	0.12	0.04
5-6	0.87	0.13	0.59	0.4	0.02	0.43	0.48	0.09	0
5-8	0.91	0.09	0.64	0.27	0.09	0.47	0.39	0.08	0.06
5-10	1	0	0.75	0.19	0.06	0.55	0.36	0.06	0.03
6-2	0.37	0.63	0.13	0.67	0.19	0.05	0.23	0.57	0.15
6-3	0.32	0.68	0.1	0.66	0.24	0.02	0.16	0.64	0.18
6-5	0.21	0.79	0.07	0.56	0.38	0.01	0.02	0.69	0.28
7-1	0.79	0.21	0.5	0.5	0	0.33	0.23	0.44	0
7-3	0.66	0.34	0.38	0.61	0.01	0.24	0.28	0.48	0
7-4	0.66	0.34	0.41	0.51	0.09	0.26	0.21	0.48	0.05
8-11	0.35	0.65	0.08	0.77	0.14	0	0.25	0.63	0.11
9-1	0.81	0.19	0.54	0.42	0.04	0.36	0.13	0.5	0.01
9-10	0.35	0.65	0.03	0.91	0.06	0	0.53	0.43	0.05

Table S1.6. *Contributions of each EM of ARM end-member modeling for the Cretaceous granite.*

Specimen	two end-member model		three end-member model		
	EM1	EM2	EM1	EM2	EM3
1-1	0.6	0.4	0.3	0.5	0.2
1-5	0.78	0.22	0.3	0.6	0.1
1-6	0.52	0.48	1	0	0
1-7	0.24	0.76	0	0.4	0.6
1-8	0.48	0.52	0.4	0.3	0.3
2-1	0	1	0.3	0	0.7
2-4	0.69	0.31	0.6	0.4	0
2-5	0.79	0.21	0	0.8	0.2
3-1	0.57	0.43	0.4	0.4	0.2
3-2	0.35	0.65	0	0.5	0.6
3-6	0.66	0.34	0.2	0.6	0.2
4-2	0.5	0.5	0.1	0.5	0.4
4-5	0.26	0.74	0.4	0.1	0.5
4-6	0.23	0.77	0.4	0.1	0.5
4-7	0.14	0.86	0	0.3	0.7
4-8	0.46	0.54	0.1	0.5	0.4
4-10	0.64	0.36	0.8	0.3	0
5-1	0.92	0.08	0.2	0.8	0
5-2	0.96	0.04	0	0.9	0
5-3	0.96	0.04	0.1	0.9	0
5-4	1	0	0	1	0
5-6	1	0	0.1	0.9	0
5-8	0.95	0.05	0.1	0.9	0
5-10	0.94	0.06	0.2	0.8	0
6-2	0.73	0.27	0.5	0.5	0.1
6-3	0.84	0.16	0.1	0.8	0.1
6-5	0.6	0.4	0.2	0.6	0.3
7-1	0.99	0.01	0.1	0.9	0
7-3	1	0	0.1	0.9	0
7-4	0.95	0.05	0.1	0.9	0
8-11	0.63	0.37	0.7	0.3	0
9-1	0.88	0.12	0.2	0.8	0
9-10	0.67	0.33	0.1	0.6	0.2

Table S1.7. *Characteristic remanent magnetization (ChRM) direction of each specimen.*

Samplle ID	Method	n	D_g (°)	I_g (°)	D_{s1} (°)	I_{s1} (°)	D_{s2} (°)	I_{s2} (°)	MAD (°)
ZD1-1	AFD	15	351	44.6	26.9	68.7	4	32.6	3.5
ZD1-2	AFD	14	3.4	38.7	34	58.2	11.9	24	2.8
ZD1-3	AFD	16	14.4	50.9	62.2	60.6	12.2	36.3	3.5
ZD1-4	AFD	4	347.5	23.7	0.3	51.8	353.5	13.8	7.4
ZD1-5	AFD	8	160.4	-21.5	169	-51.6	166.3	-13.8	8.8
ZD1-6	AFD	17	1.4	49.9	49.9	66.9	14.1	35.2	3.2
ZD1-7	AFD	16	6.2	34.9	32.9	53.8	13.1	19.9	6.3
ZD1-8	AFD	14	5.5	37.7	35.2	56.3	13.3	22.6	7
ZD1-9	AFD	13	9.6	42.1	44.9	57.6	17.9	26.1	5.5
ZD1-10	AFD	10	349.3	29.9	6.7	56.9	357.1	19.1	7
ZD2-1	AFD	1	3.3	36.2	31	56.3	11	21.7	5.3
ZD2-2	AFD	13	5	39.8	37.1	58.2	13.5	24.7	5.7
ZD2-3	AFD	9	1.8	35.4	28.3	56.3	9.5	21.2	14.4
ZD2-4	TD	12	358.7	41.5	32.2	62.6	8.9	27.8	5.3
ZD2-4	AFD	14	1.8	44.8	40.8	63.5	12.6	30.2	3.5
ZD2-5	AFD	16	4.9	47.3	48.1	63.5	15.8	32	3.6
ZD2-6	AFD	6	12.8	36.9	41.9	52	19.2	20.4	9.2
ZD2-7	AFD	6	354.7	28.5	13.1	53.6	7.5	22.4	9.8
ZD2-8	AFD	16	357	32.6	19.6	56.2	4.6	19.7	3.1
ZD2-9	AFD	10	8.2	54.6	65.2	65.7	20.9	38.4	6
ZD2-10	AFD	12	358.4	31.1	20	54.3	5.3	17.9	6.5
ZD3-1	AFD	14	5	42.6	40.9	60.3	14.4	27.5	5.1
ZD3-2	AFD	13	356.6	20.5	10.2	45.7	0.6	8.3	5.5
ZD3-3	AFD	16	22.5	44.8	59.6	52.5	28.7	26.7	5.1
ZD3-4	AFD	12	5.8	15.9	18.2	37.7	8	1.4	7.8
ZD3-5	AFD	10	3.4	35.1	29.9	55.3	10.8	20.8	6.1
ZD3-6	AFD	6	5.2	48.4	50.3	64	16.4	33	6.9
ZD3-7	AFD	7	358	54.4	57.8	70.9	13.2	40.1	6
ZD3-8	AFD	11	3.3	46.2	44.7	63.6	14.2	31.2	2.6
ZD3-9	AFD	10	5.9	38	35.9	56.4	13.7	22.8	3.5
ZD3-10	AFD	11	6.3	36.8	35.1	55.2	13.7	21.6	6.7
ZD4-1	AFD	12	4.1	36.3	32	56	11.7	21.6	6.4
ZD4-2	AFD	12	7.5	23.6	24.9	43.8	11.1	8.6	4.1
ZD4-3	AFD	10	10.8	30	33.3	47.6	15.8	14.1	6

ZD4-4	AFD	15	358.8	37.8	27.5	59.7	7.8	24.3	7.7
ZD4-5	AFD	6	7.4	33.1	32.5	51.8	13.6	17.8	9.9
ZD4-6	AFD	10	357.6	55.4	60.3	71.6	13.7	41.1	8.5
ZD4-7	AFD	14	13.8	25.5	32.9	42.4	17.5	9.2	9.7
ZD4-8	AFD	12	1.7	38.4	31.7	58.8	10.3	24.2	3.2
ZD4-9	AFD	14	6.7	33.2	31.8	52.2	13.1	18.1	7.8
ZD4-10	AFD	11	1	33.4	25.3	55.1	8.2	19.5	3.9
ZD5-1	AFD	19	4.4	33.1	29.2	53.2	11.1	18.4	2.2
ZD5-2	AFD	15	0.1	36	27	57.7	8.3	22.2	1.7
ZD5-3	AFD	18	30.6	44.5	65.4	48.1	35	25.5	3.4
ZD5-4	AFD	17	358.5	35.4	24.4	57.9	6.9	22.2	1.1
ZD5-5	TD	13	359.3	40.6	31.6	61.6	9.2	26.7	1.8
ZD5-5	AFD	16	358.1	37.6	26.3	59.9	7.1	24.2	1.7
ZD5-6	AFD	18	21.9	55.7	75.2	59.2	30.9	37.5	2.7
ZD5-7	AFD	14	3.4	37.6	45	64.4	11.5	22.9	4.8
ZD5-8	AFD	13	10.3	39.8	42.8	55.5	17.8	23.7	5.4
ZD5-9	AFD	13	4.1	36.4	32.2	56.1	11.8	21.7	12.3
ZD5-9a	AFD	14	2.4	25.6	20.5	47.8	7.3	11.7	2.1
ZD5-10	AFD	13	3.8	33.3	28.6	53.7	10.6	18.7	10.8
ZD5-11	AFD	10	3.2	39.8	35.2	59.2	12.1	25.2	6.8
ZD6-1	AFD	9	38.7	24.5	55.1	28.6	39.8	5	9.7
ZD6-2	AFD	14	350.5	40	18.9	65.3	1.8	28.3	2.4
ZD6-3	AFD	9	7.2	30.9	30.2	50.1	12.9	15.7	6
ZD6-4	AFD	8	357.9	51.5	50.2	69.7	12.2	37.4	3.5
ZD6-5	AFD	6	5.8	36.7	34.4	55.5	13.3	21.7	5.2
ZD6-6	AFD	14	1.4	39.6	32.8	59.9	10.5	25.3	6
ZD6-7	AFD	9	351.3	52.2	45.4	73.5	7.7	39.6	3
ZD6-8	AFD	7	14.8	14.1	26.6	32.1	16	-2.2	4.1
ZD6-9	AFD	15	348.7	33.6	9	60.5	357.9	22.8	3.8
ZD7-1	AFD	9	10.9	29.8	33.2	47.3	15.8	13.9	7.4
ZD7-3	AFD	19	2.3	39.1	33.2	59	11.1	24.6	1.2
ZD7-5	TD	16	327.5	48.6	338	80.4	347.4	42.8	4.5
ZD7-5	AFD	8	5.9	37.6	35.5	56.1	13.6	22.5	2.6
ZD7-6	AFD	9	5.2	39.7	37.2	58	13.6	24.6	2.3
ZD7-7	AFD	9	20.9	41.3	54.2	51	26.8	23.5	5.7
ZD7-8	AFD	9	18.1	36.2	46.3	48.7	23.4	18.9	7.8
ZD7-9	AFD	11	14.6	28.3	35.9	44.2	18.7	11.7	4.5
ZD7-10	AFD	14	2.9	39.1	34	58.7	11.6	24.5	3.7
ZD7-11	AFD	7	0.6	40.8	33.4	61.2	10.2	26.7	1.5

ZD8-1	AFD	10	346.1	39.8	11.5	66.9	358	29.3	4.1
ZD8-2	AFD	9	350.1	37.9	15.6	63.7	0.6	26.5	2.6
ZD8-3	AFD	9	358	41	30.5	62.6	7.7	26.5	4.3
ZD8-4	AFD	19	1.3	35.1	27.4	56.3	9	21	2.6
ZD8-5	AFD	5	332.8	54.9	25.5	84.3	355.8	46.8	10.3
ZD8-6	AFD	7	1.6	41.5	35.5	61.2	11.2	27.1	1.1
ZD8-7	AFD	12	4.7	30.5	27.1	50.9	10.7	15.8	3.7
ZD8-8	AFD	8	2.6	34.8	28.8	55.5	10	20.5	1.8
ZD8-9	TD	13	37.8	30.1	57.5	32.8	39.3	9.6	7.3
ZD9-1	AFD	8	35.7	49.1	74	48.6	39.5	29.6	5.6
ZD8-10	AFD	8	6.3	33.7	31.8	52.8	12.8	18.6	2.3
ZD8-11	AFD	6	5.7	36.8	34.5	55.6	13.3	21.8	1.2
ZD9-1	AFD	8	359.4	35.5	25.6	57.5	7.6	21.8	1.9
ZD9-2	AFD	8	359.7	37.4	28.2	59	8.5	23.7	2.1
ZD9-3	AFD	8	5.3	39.2	36.7	57.6	13.5	24.1	2.7
ZD9-3a	AFD	9	354.6	49.1	40.8	70	8.6	35.9	3.5
ZD9-4	AFD	5	6.7	47.2	49.8	62.5	17.2	31.6	1.1
ZD9-5	AFD	9	0.5	52.9	55.8	68.9	14.7	38.2	6.8
ZD9-6	AFD	9	10.2	41.7	45	56.9	18.2	25.6	4.6
ZD9-7	AFD	13	6.5	57.2	70.2	67.6	20.7	41.1	3.3
ZD9-8	AFD	8	3.4	29.7	25	50.9	9.3	15.4	2.2
ZD9-9	AFD	6	335	53.2	21.1	82.2	356.2	44.7	3.8
ZD9-10	TD	9	28.3	28.6	49	37.4	30.9	10	3.5
ZD9-10	AFD	8	11	46.8	52.9	60	20.3	30.4	2.3

Notes: *Sample ID, specimen identification; Method, alternating field demagnetization (AFD), thermal demagnetization (TD); n, number of demagnetization steps used to define the ChRM direction; Dg, Ig, declination and inclination before tilt correction;* D_{s1}, I_{s1} (D_{s2}, I_{s2})*, declination and inclination after tilt correction by strike /dip of 54°/32° and 321°/20°, respectively; MAD, maximum angular deviation of the ChRM direction.*

Chapter S2

S2.1 Quality evaluation of the existing paleomagnetic data

Including this study, there are a total of 17 paleomagnetic study papers for the Jurassic-Paleogene Eastern Qiangtang Terrane (EQT) (all the paleolatitudes have been converted into our study site at 32.5°N, 95.2°E). For example, for the early study, Lin & Watts (1988) reported paleopoles of 72.3°N, 24.8°E, (A_{95}=9.1°; Q=4) in the Yanshiping area, but they were not included in further analyses because most rocks are remagnetized. Dong et al. (1990, 1991) obtained paleopoles from the Yanshiping area, but this study did not contain field tests and sufficient samples. Cheng et al. (2012) reported two Middle-Jurassic paleopoles from the same area, although the results from the sandstones fulfill all the seven criteria of Van der Voo (1990), the paleolatitude of ~15 °N is apparently lower than expected, which were interpreted as inclination shallowing. Yan et al. (2016) carried out a paleomagnetic study with vast amounts of sites (samples), the results from the Xueshan formation have 25 samples but only from 1 site, and thus excluded. Ran et al. (2017) reported a Cretaceous remagnetization of Jurassic limestone in the Yanshiping area. A total of 3 Cretaceous paleomagnetic studies have been conducted in the EQT, and are all located in Mangkang county. Otofuji (1990) reported a paleopole of 48.5°N, 75.8°E, A_{95}=9.5°. The results were from only 15 samples, and no field tests were performed. Tong et al. (2015) and Huang et al. (1992) obtained similar paleopoles, corresponding to a paleolatitude of ~30°N. The Mesozoic paleomagnetic studies were mainly focused on the Nangqian and Gongjue areas. Cogné et al. (1999) provided a paleopole of 52.6°N, 351.9°E, (A_{95}=8.0°), with a paleolatitude of ~24°N from 10 sites in the Xialaxiu area. The ChRMs yielded a negative fold test but had a dual polarity. Huang et al. (2019b) argued that this is likely remagnetized. The paleomagnetic data from volcanic rocks in the Wulanwulahu area with the acquisition ages of 38.6 ± 0.5 Ma gave paleolatitudes of ~25°N (Lippert et al., 2011). Roperch et al. (2017) reported a paleopole, but they did not provide any demagnetization details. Zhang et al. (2018) reported Eocene paleopoles of 55.1°N, 216.2°E, (A_{95}=2.2°) and 65.5°N, 237.8°E, (A_{95}=2.4°) from the lower Gongjue to upper Ranmugou formations, in the Gongjue area, with a paleolatitude of 11.1±2.9°N and 12.2±3.1°N, respectively. Although the positive reversals and fold tests demonstrate that the characteristic remanent magnetization has a primary origin, they were excluded from inclination discussion due to the apparently shallower paleolatitudes. All the above paleomagnetic data are shown in supporting information table S1.

S2.2 Supplementary tables

Table S2.1. *Paleomagnetic poles for the Eastern Qiangtang Terrane and Eurasia*

Sampling site			Lithology	Age(Ma)	N(n)	Pole location			At Reference Position (32.5°N, 95.2°E)					Criteria (Q)	References	No.
location	Slat (°N)	Slon (°E)				Plat (°N)	Plon (°E)	A_{95} (°)	Paleolat(°)	Dec(°)	ΔDec(°)	Inc(°)	ΔInc(°)			
Eastern Qiangtang Terrane																
YSP	33.4	92	Purple siltstone	J_2	4(15)	60.6	331.1	6.3	13.6±7.9	-24.7	6.5	25.9	10.8	1□3□5□7(4)	Dong et al. (1991)	1
YSP	33.4	92.1	Purple siltstone	J_2	4(21)	53.6	335.5	4.4	10.6±5.8	-31.6	4.5	20.6	8	1□3□5□7(4)	Dong et al. (1991)	1
YSP	34	92	Silt-fine sandstone	J_2	4(19)	64.5	348.4	5.2	22.3±5.6	-26.5	5.6	39.4	7.3	1□3□5□7(4)	Dong et al. (1990)	2
YSP	33.6	92	Limestone	J_2	10(61)	84.4	119.4	11.6	37.6±9.4	2.9	14.6	57	11	123□5□□(4)	Ran et al. (2017)	3
YSP	33.6	92.1	Clastic	165.5->171.2	25(182)	79.1	306.9	5	23.1±5.3	-6.2	5.4	40.4	6.8	123□5R7(6)	Yan et al. (2016)	4
YSP	33.6	92.1	Limestone	163.3-165.5	27(245)	68.9	313.8	2.8	15.3±3.4	-13.5	2.9	28.7	4.6	123F5R7(7)	Yan et al. (2016)	4
YSP	33.6	92	Limestone	163.3-165.5	30(171)	65.5	335	7.8	18.2±9.1	-22.2	8.2	33.4	12.1	123□5□7(5)	Ren et al. (2013)	5
YSP	33.6	92.1	Sandstone	J_2	10(99)	71.6	262	7.3	14.5±9.1	4.3	7.5	27.4	12.3	123F5R7(7)	Cheng et al. (2012)	6
YSP	33.6	92.1	Limestone	163.3-165.5	5(43)	75.1	308.5	8.9	19.8±10.1	-8.6	9.5	35.7	13.3	1□3 F5□7(5)	Cheng et al. (2012)	6
ZD	32.5	95.2	Limestone	163.3-165.5	12(123)	59.8	202.7	2.8	19.7±2.8	30.6	3	35.6	4.2	123□5R7(6)	This study	7
YSP	33.4	92.1	Sandstone	J_2	4(25)	51.8	347	6.8	15.0±8.4	-37.5	7	28.2	11.3	1□3□5D7(5)	Dong et al. (1990)	2
YSP	33.6	92.1	Sandstone	160.1-163.3	24(224)	66.1	332.1	3.5	17.7±4.1	-20.9	3.7	32.6	5.5	123F5R7(7)	Yan et al. (2016)	4
YSP	33.6	92.1	Shale	157.5-160.1	20(191)	72.4	318.6	4.9	19.1±5.6	-12.7	5.2	34.7	7.4	123F5R7(7)	Yan et al. (2016)	4
YSP	33.6	92.1	Mudstone	<157.5	1(25)	76.9	301.1	10.2	20.6±11.4	-6.1	10.9	36.9	14.9	1□3□5□7(4)	Yan et al. (2016)	4
YSP	33.6	92.1	Limestone	157.5-160.1	6(59)	83.3	268.3	7.6	25.8±7.7	0.9	8.4	44.1	9.7	123 F5□7(6)	Cheng et al. (2012)	6
YSP	33.6	92.1	Clastic	Baj-Kim	18(100)	72.3	18.8	8.7	34.9±7.4	-21.1	10.6	54.4	8.8	123□5□7(5)	Lin and Watts, (1988)	8
YSP	33.6	92.1	Red beds, limestone	Baj-Kim	20(104)	72.3	24.8	9.1	36.7±7.5	-20.9	11.4	56.2	8.8	123□5□□(4)	Lin and Watts, (1988)	8
MK	29.7	98.4	Red beds	Berriasian-Barremian	12(68)	40.6	170.5	11.9	30.8±10.9	58.8	13.9	50	13.3	123F5D7(7)	Huang et al. (1992)	9

MK	29.7	98.6	Red sandstones	Barremian-Albian	5(15)	48.5	175.8	9.5	29.6±8.9	48.6	11	48.7	10.9	1□3□5□7(4)	Otofuji et al. (1990)	10
MK	29.7	98.7	Red beds	Aptian-Turonian	11(79)	56.7	172.7	9.5	33.3±8.3	39.9	11.4	52.7	10	123F5□7(6)	Huang et al. (1992)	9
MK	29.7	98.5	Red beds	K_2	17(186)	47	165.1	7.9	36.2±6.5	52.5	9.8	55.7	7.7	□23F5R7(6)	Tong et al. (2015)	11
GJ	30.9	98.3	Sandstone	55.4-61	-(104)	43.4	181.2	3.8	24.3±3.9	52.7	4.2	42.1	5	123F5R7(7)	Li et al. (2020)	12
GJ	30.9	98.3	Sandstone	53.2-55.4	-(68)	46.6	179.7	4.7	26.5±4.7	49.8	6.3	44.9	5.9	123F5R7(7)	Li et al. (2020)	12
XLX	32.6	96.6	Volcanic rocks	49-51	21(-)	76.4	223.2	7.6	23.9±7.6	11.7	8.3	41.1	10.3	123□5□□(4)	Roperch et al. (2017)	13
XLX	32.6	96.6	Red beds	-	-	58.5	348.6	6.6	19.4±7.5	-32.1	5	35.2	8.7	□□□□5□□(1)	Roperch et al. (2017)	13
GJ	31	98.2	Red beds	43.2-56	43(-)	57.9	192.1	2.9	23.7±3.1	35.2	3.2	41.2	3.9	123F5R7(7)	Tong et al. (2017)	14
GJ	31	98.2	Red beds	43-53	28(150)	55.1	216.2	2.2	11.1±2.9	30	2.2	21.4	4	123F5R7(7)	Zhang et al. (2018)	15
GJ	31	98.2	Red beds	43-53	33(178)	65.5	237.8	2.4	12.2±3.1	14.9	2.5	23.4	4.2	123F5R7(7)	Zhang et al. (2018)	15
NQ	32.2	96.6	Sandstone & Marlite	41-53	-(300)	71.7	190.5	4.5	29.1±4.3	21	5.1	48	5.3	123□5R7(6)	Zhang et al. (2020)	16
GJ	30.9	98.3	Sandstone	45.3-47.1	-(162)	60.8	181.5	2.9	29.7±2.7	34.1	3.3	48.8	3.3	123F5R7(7)	Li et al. (2020)	12
GJ	30.9	98.3	Sandstone	41.5-45.3	-(196)	63.9	186	2.8	28.5±2.7	30	3.2	47.4	3.3	123F5R7(7)	Li et al. (2020)	12
XLX	32.8	96.6	Sandstone	E_2	10(-)	52.6	351.9	8	23.6±8.0	-38.4	8.4	33	12.4	123□5D□(5)	Cogné et al. (1999)	17
WH	34.5	90.2	Volcanic rocks	38.6±0.5	7(53)	82.1	298.4	7.8	25.2±8.0	-3.4	8.6	43.3	10.1	123F5□7(6)	Lippert et al. (2011)	18
NQ	32.2	96.6	Mudstone	35-41	-(267)	83.4	217.9	5.3	28.8±5.0	6.3	6	47.7	6.3	123□5R7(6)	Zhang et al. (2020)	16
Eurasia APWP																
				3.1	30	86.3	172	2.6	33.3±2.3	4.3	3.1	52.7	2.7	-		
				8.3	54	85.4	162.5	2	34.2±1.7	5.1	2.4	53.6	2.1	-		
				18.9	38	84	154.8	2.7	35.4±2.3	6.3	3.3	54.8	2.7	-		
				29.5	23	82.8	158.1	3.8	35.5±3.2	7.9	4.7	55	3.8	-		
				40	24	81.3	162.4	3.3	35.5±2.8	9.9	4.1	55	3.3	-		
				52.2	31	80.9	164.4	3.4	35.3±2.9	10.4	4.2	54.8	3.4	-		
				59.7	45	81.1	190.5	2.9	31.3±2.6	10.4	3.4	50.5	3.2	-		
				67.3	34	80.3	204.3	3.2	28.9±3.0	10.5	3.7	47.8	3.8	-		

77.9	14	81.4	206.1	5.9	29.1±5.6	9.2	6.8	48.1	6.9	-
90	13	82.2	202.1	5.2	29.9±4.8	8.6	6	49	6	-
97.6	12	81.7	180.1	6.7	32.9±5.9	9.9	8	52.3	7.1	-
113.6	17	80	183.6	4.2	32.2±3.7	11.8	5	51.6	4.5	-
119.1	20	78.2	189.4	2.4	30.9±2.2	13.7	2.8	50.1	2.7	-
126.4	14	75.8	192.9	2.8	29.5±2.6	16.2	3.2	48.6	3.2	-
136.8	7	73.8	197.6	6	27.7±5.8	17.9	6.8	46.4	7.3	-
151.6	10	75	159.9	6.6	37.8±5.3	17.2	8.3	57.2	6.2	-
162.3	15	72.5	144	5	42.8±3.7	18	6.8	61.6	4.2	-
173.4	21	69.7	112.5	6.7	51.6±4.3	9.6	10.8	68.4	4.7	-
178.8	18	65.5	95.9	5.6	57.0±3.4	0.5	10.3	72	3.6	-
189.7	23	65.3	98.4	4.2	57.1±2.5	2.5	7.7	72.1	2.7	-
196.7	19	63.2	106	4.3	58.6±2.6	9.3	8.2	73	2.7	-

Note: *Slat and Slon, latitude and longitude of the sampling site; Age (Ma), age of the rock units; N(n), number of sites (samples) used to calculate Fisherian mean; Plat. and Plon., latitude and longitude of the pole; A95, radius of the 95% confidence circle; Paleolat, paleolatitude calculated in respect to the reference site at 32.5°N, 95.2°E; Dec, ΔDec, Inc and ΔInc, declination and Inclination with their error converted to the reference site at 32.5°N, 95.2°E; No, number of the references in the Figure 2.1; Eurasia APWP refers to Besse & Courtillot, 2002, 2003. Criteria (Q) = data quality criteria (number of criteria met) modified from Van der Voo (1990): 1, well-determined rock age; 2, sufficient number of samples (N≥6 and n≥36); 3, stepwise demagnetization; 4, robust field tests, F means positive fold test; 5, structural control and tectonic coherence with the craton or terrane discussed; 6, presence of reversal, R means positive reversal test and D means dual-polarity ChRM direction; 7, no resemblance to paleopole of younger age (by more than a period); "□" in the criterion column fails to fulfill this criterion; Gray data are those failed to fulfill the criteria mentioned in the text. YSP: Yanshiping; ZD: Zaduo; GJ: Gongjue; XLX: Xialaxiu; NQ: Nangqian; WH: Wulanwula hu.*

Table S2.2. *Characteristic remanent magnetization (ChRM) direction of each specimen.*

Samplle ID	Method	Demagnetization steps(℃/mT)	n	Dg (°)	Ig (°)	Ds (°)	Is (°)	MAD (°)
ZD 0-1	AFD	25-140	10	195.8	-52.4	212.6	-38	1.2
ZD 0-1	TD	400-500	5	196	-43.9	208.9	-30.1	4.8
ZD 0-3	AFD	25-140	10	196.1	-55.8	213.7	-42.6	1.9
ZD 0-4	AFD	25-140	10	201	-47.1	213.1	-33.2	1.6
ZD 0-5	AFD	25-140	10	198.9	-54.2	215.2	-39.7	1.4
ZD 0-6	AFD	25-140	10	203.2	-50.8	215.9	-36	1.1
ZD 0-7	AFD	25-140	10	201.4	-50.3	214.4	-35.9	1.5
ZD 0-8	AFD	25-140	10	202.5	-52.5	215.7	-37.5	2
ZD 0-9	AFD	25-140	10	197.9	-55.5	214.8	-42	3.6
ZD 0-10	AFD	25-140	10	200	-50.4	214	-36.7	1.5
ZD 0-11	AFD	50-140	6	185.4	-51.1	207	-36.1	2.5
ZD 0-12	AFD	25-140	10	189.1	-66.3	215.9	-49.6	1.9
ZD 1-1	AFD	25-140	9	195.5	-52.3	209.8	-37.8	1.4
ZD 1-2	AFD	25-140	10	197.3	-50.9	212.4	-35.3	1.9
ZD 1-3	AFD	25-140	9	195.7	-52.8	211.7	-39.4	1.2
ZD 1-4	AFD	25-140	9	193.6	-53.4	211.7	-40.1	0.7
ZD 1-5	AFD	25-140	10	197.3	-53.7	213.2	-39.9	1.6
ZD 1-5	TD	350-500	6	198.3	-54.8	214.4	-40.7	3.2
ZD 1-6	AFD	25-140	10	199.4	-51.6	213.7	-37.5	1
ZD 1-7	AFD	25-140	10	202.8	-52.4	214.9	-36.5	0.9
ZD 1-8	AFD	25-140	9	199	-52	213.7	-37.9	1.4
ZD 1-9	AFD	25-140	10	196.6	-54.1	213	-40.4	1.8
ZD 1-10	AFD	25-140	10	199	-48.4	212.7	-32.8	2.7
ZD 1-10	TD	400-525	6	272.9	-74	261	-52.7	4.9
ZD 1-11	AFD	25-140	10	192.3	-50.8	209.8	-37.3	1.2
ZD 1-12	AFD	25-140	8	198.8	-67.3	223.8	-47.3	1.2
ZD 2-1	AFD	NRM-140	19	12.5	34.2	23.9	21.3	0.8
ZD 2-2	AFD	NRM-140	15	16.9	35.9	28.1	21.6	4.3
ZD 2-3	AFD	NRM-140	12	18.8	42.2	32.1	26.9	6.4
ZD 2-4	AFD	NRM-140	17	13.1	40.2	26.9	26.7	0.9
ZD 2-5	AFD	NRM-140	15	4.7	39	19.9	28.3	0.9
ZD 2-6	AFD	NRM-140	19	1.7	47.2	24.9	40.1	0.9
ZD 2-7	AFD	NRM-140	19	5.1	47.1	24.4	35.4	0.7
ZD 2-7	TD	200-425	4	8	47.7	26.6	28.2	6.1

ZD 2-8	AFD	NRM-140	19	355.7	46.8	17.5	38.4	0.8
ZD 2-9	AFD	NRM-140	19	359.4	48.3	21	38.4	1
ZD 2-10	AFD	NRM-140	19	27.1	54.5	42.9	36.3	3.3
ZD 2-10	TD	NRM-300	5	353.8	56.1	26.9	35	2.9
ZD 3-1	AFD	NRM-140	18	15.5	45.1	27.9	29.8	1.7
ZD 3-2	AFD	2-140	10	47.9	43	52	22.7	6.5
ZD 3-3	AFD	NRM-140	19	13.5	42	25.5	26.6	2
ZD 3-5	TD	100-500	7	192.2	-27.3	196.4	-7.3	4.1
ZD 3-6	AFD	16-140	12	17.5	47.9	30.4	32	1.9
ZD 3-7	AFD	NRM-140	19	22.9	48.5	30.8	29.4	1.6
ZD 3-8	AFD	NRM-140	19	11.4	45.1	24.8	30.7	1.1
ZD 3-9	AFD	NRM-140	13	9.2	48.5	24.6	34.4	1.1
ZD 4-2	AFD	NRM-140	19	18.2	29.8	30.3	20.2	1.6
ZD 4-3	AFD	NRM-140	12	19.4	35.2	33.9	24.5	3.6
ZD 4-3	TD	100-350	4	346.9	6	351.3	12.9	5
ZD 4-4	AFD	NRM-140	18	347.3	49.8	20.5	49.8	3.1
ZD 4-5	AFD	NRM-140	19	3.9	50.9	37.1	39.6	2
ZD 4-6	AFD	NRM-140	19	38.2	41.9	51.2	24.4	0.9
ZD 4-7	AFD	NRM-140	19	3.3	40.9	25	35.9	0.7
ZD 4-8	AFD	10-140	14	19.5	40.8	36.9	29.4	3.2
ZD 4-9	AFD	NRM-140	19	14.8	45.6	36.3	35.4	1.4
ZD 5-1	AFD	2-140	13	9.8	47.2	35.9	32.6	2.4
ZD 5-2	AFD	NRM-140	18	9.2	54	40.7	37.9	1.9
ZD 5-3	AFD	2-140	13	346.1	50.6	25.2	45.9	2.8
ZD 5-4	AFD	NRM-140	19	13.8	51.6	41.4	34.3	1.7
ZD 5-5	AFD	NRM-50	14	26.7	50.9	48.5	29.1	1.1
ZD 5-6	AFD	NRM-140	19	1.9	55.6	38.4	42	1.1
ZD 5-7	AFD	NRM-140	18	18.4	51.1	43.7	32.2	0.7
ZD 5-8	AFD	NRM-140	19	16.9	49.8	42	31.8	0.9
ZD 5-9	AFD	NRM-140	19	45.8	46.5	57.3	16.3	1.1
ZD 5-9	TD	NRM-350	7	44.6	45.4	56.1	15.6	3.1
ZD 6-1	AFD	NRM-140	19	8.3	46.7	32.6	32.9	1.1
ZD 6-2	AFD	NRM-140	18	5.7	48.7	32.4	35.5	1.4
ZD 6-3	AFD	NRM-140	19	17.4	47.3	38.9	29.8	1.5
ZD 6-4	AFD	NRM-140	19	8.7	49.7	35	35.1	1.4
ZD 6-5	AFD	NRM-140	19	14.4	44.9	35.4	28.9	1.1
ZD 6-6	AFD	NRM-140	19	13.6	44.2	34.5	28.7	1
ZD 6-6	TD	NRM-450	7	359.7	45.6	26.2	35.8	3.3
ZD 6-7	AFD	NRM-35	12	5	49.7	32.7	36.6	1.6

ZD 6-8	AFD	NRM-140	18	14	47.8	37	31.4	1
ZD 6-9	AFD	NRM-140	19	19.6	43	37.8	25.3	1.3
ZD 6-10	AFD	NRM-140	19	15.8	44.3	36	27.8	0.8
ZD 6-10	TD	NRM-400	8	16.6	40.7	34.4	24.5	2.8
ZD 6-11	AFD	NRM-140	19	20.3	36.7	35	19.6	1.7
ZD 6-12	AFD	NRM-140	19	23.9	43.3	40.8	24	2
ZD 7-1	AFD	NRM-100	16	13.9	42.4	34.9	25.4	0.6
ZD 7-2	AFD	NRM-100	16	355.5	56	35.3	43.5	1.4
ZD 7-3	AFD	NRM-100	16	355.7	42.7	23.5	34.2	1.4
ZD 7-4	AFD	NRM-100	13	9.4	41.3	31.3	26.5	1.4
ZD 7-5	AFD	NRM-100	14	355.2	53.1	32.3	41.7	1.5
ZD 7-6	AFD	NRM-100	14	15.5	44.9	37.4	26.8	1.4
ZD 7-7	AFD	NRM-100	14	342.2	40.3	12.8	39.6	2.2
ZD 7-7	TD	NRM-400	5	340	44.1	15.1	43.3	3.5
ZD 7-8	AFD	NRM-100	14	350.3	49.4	26.2	41.6	1.5
ZD 7-10	AFD	NRM-100	16	10.8	49.3	37.6	32.2	0.9
ZD 7-11	AFD	NRM-100	16	6.2	31.1	22.5	19.9	1.8
ZD 8-1	AFD	NRM-140	19	354.7	44.4	21.4	39.9	1.5
ZD 8-2	AFD	NRM-140	19	355.8	52.7	27.8	43	1
ZD 8-3	AFD	NRM-140	19	352.8	48.5	22.7	42.9	0.7
ZD 8-4	AFD	4-140	16	1.6	48	28.1	38.9	1.8
ZD 8-5	AFD	NRM-35	12	6.3	54.7	36.2	42.4	4.3
ZD 8-6	AFD	NRM-140	19	356.6	52.9	28.4	42.9	0.5
ZD 8-7	AFD	NRM-140	19	1.3	48.3	28.1	39.3	0.7
ZD 8-8	AFD	2-35	11	12.2	46.4	34.1	33.5	3.8
ZD 8-9	AFD	NRM-140	19	355.4	52.4	27.8	44.8	1.4
ZD 8-10	AFD	NRM-140	19	1.8	50.8	30.4	41.1	0.8
ZD 8-10	TD	NRM-350	5	348.6	45.9	17.1	42.9	6.1
ZD 8-11	AFD	2-140	17	358.3	50.9	28.3	42.5	2.8
ZD 9-1	AFD	2-35	10	357.6	48.1	25.2	40.2	1.1
ZD 9-2	AFD	4-140	17	350.1	49.8	21.8	44.7	2
ZD 9-3	AFD	NRM-140	19	358.5	50.2	27.5	41.5	0.9
ZD 9-4	AFD	NRM-140	19	358.3	43.6	22.4	36.4	0.6
ZD 9-5	AFD	NRM-140	19	355.4	48.8	24.3	41.7	0.5
ZD 9-5	TD	NRM-475	10	349.3	46.6	18.2	42.6	1.7
ZD 9-6	AFD	NRM-140	18	6	52.3	33.8	40.2	1.9
ZD 9-7	AFD	NRM-140	19	359.1	51.4	28.8	42.2	1.4
ZD 9-8	AFD	NRM-140	19	3.3	49.2	29.8	38.8	1.6
ZD 9-9	AFD	NRM-140	18	356.8	52.7	28.5	44.1	0.8

ZD 9-10	AFD	NRM-140	18	353.3	49.3	23.4	42.9	0.8
ZD 9-11	AFD	NRM-140	19	358.6	46.9	24.9	38.8	0.8
ZD 9-12	AFD	NRM-140	19	354.6	47.8	23.1	41.2	1.9
ZD 9-12	TD	NRM-500	10	340.7	49.5	15.1	48.6	1.8
ZD 10-1	AFD	NRM-140	19	355.6	47.9	24.4	40.3	1.1
ZD 10-2	AFD	NRM-140	19	356.4	50.8	27.3	42.2	1.2
ZD 10-2	TD	NRM-475	10	340.6	47.7	13.8	47	2.1
ZD 10-3	AFD	NRM-140	19	356.8	49.1	26.1	40.8	2.2
ZD 10-4	AFD	NRM-140	19	356.2	49.8	26.4	41.5	0.9
ZD 10-5	AFD	NRM-140	19	352.3	48.9	23.1	42.5	1.3
ZD 10-6	AFD	NRM-140	19	352.4	44.1	19.3	38.9	1.4
ZD 10-7	AFD	NRM-140	19	355.5	45.1	22.1	38.2	1.4
ZD 10-7	TD	NRM-475	10	345.8	43.4	13.7	41.3	3.8
ZD 10-8	AFD	NRM-140	19	354.9	45	21.6	38.4	1.6
ZD 10-9	AFD	NRM-140	19	356.2	48.3	25.1	40.3	1.5
ZD 10-10	AFD	NRM-140	17	358.2	44.2	23.6	38.1	1.7
ZD 10-11	AFD	NRM-140	19	359	37.2	20.4	32.6	0.8
ZD 11-1	AFD	NRM-140	17	356.4	58.6	29.2	43.9	3.3
ZD 11-2	AFD	NRM-140	17	359	50	23.6	36.9	2.6
ZD 11-3	AFD	NRM-140	18	357.9	53.3	25.2	40	2.5
ZD 11-4	AFD	NRM-140	19	9.3	47	28.5	30.8	2.6
ZD 11-4	TD	NRM-425	8	345.7	58.9	23.2	48.7	1.5
ZD 11-5	AFD	NRM-140	19	358.4	57.8	28.2	41.7	3.4
ZD 11-7	AFD	NRM-140	19	358.2	50.3	23.3	37.4	1.8
ZD 11-8	AFD	NRM-140	19	353.4	50.1	20.1	39	1.8
ZD 11-10	AFD	NRM-140	19	14.8	58.7	38.7	39.3	0.9
ZD 11-11	AFD	NRM-140	19	358.1	53	25.2	39.7	1.2
ZD 11-11	TD	NRM-400	7	338.5	56.5	16.5	49.8	1.3
ZD 11-12	AFD	20-140	11	354	49.3	20	38.2	2.9

Notes: *Sample ID, specimen identification; Method, alternating field demagnetization (AFD), thermal demagnetization (TD); demagnetization Steps, demagnetization step range over which the ChRM direction is determined; n, number of demagnetization steps used to define the ChRM direction; Dg, Ig (Ds, Is), declination and inclination before (after) tilt correction; MAD, maximum angular deviation of the ChRM direction.*

Chapter S3

Supplementary table

Table S3.1. *Characteristic remanent magnetization (ChRM) direction of each specimen.*

Site	Bedding		In situ		Tilt-corrected		A_{95}	*n*
	Strike (°)	Dip (°)	Dec (°)	Inc (°)	Dec (°)	Inc (°)		
Zaduo (~Eocene)								
Site 0	164	21	198.1	-52.1	213.8	-37.8	3.4	11
Site 1	161.5	21	197.2	-52.1	212.4	-37.7	1.5	12
Site 2	168	24	9.5	43.9	26.2	31.5	5.7	10
Site 3	156	22	19.4	43.8	29.9	27.3	7.9	7
Site 4	184	28	13.9	42.7	34.4	32.7	8.6	8
Site 5	178	33	10.5	51.9	39.8	35.9	5.5	9
Site 6	175	31	14.2	45.7	35.7	29.7	3	12
Site 7	176	34	1.8	45.6	29.5	33.4	6.4	10
Site 8	177	29	359.7	50.1	28.5	41.1	2.6	11
Site 9	176	29	357.6	49.2	26.1	41.1	2	12
Site 10	177	30	355.8	46.4	23.5	39.5	1.9	11
Site 11	164	28	359.8	53	26.2	38.8	3.4	10
Gongjue (~Paleogene-Eocene)								
1	198.8	15.4	21.6	44.7	36	42	10.2	18
2	165.4	7.7	44.6	47.4	48.2	40.7	8.3	16
3	172	11.1	218.7	-37.6	223.5	-29.2	8.2	22
4	162.5	14	42.6	36.1	46.4	23.7	5	27
5	180	14	43.6	37.4	49.7	27.2	6.4	23
6	181.9	14.4	35.8	36.9	43.1	28.1	6.2	22
7	189.4	15.6	56.5	37.7	62.7	25.7	6.3	24
8	187.6	13.8	47.2	32.5	52.6	23.2	7.9	18
9	182.9	92.9	49	31.8	53.4	22.1	6.7	24
10	175.8	21.8	41.8	37.1	49.6	20.3	9.1	21
11	173.6	32.1	30.5	49.6	48.4	26	6.7	20
12	173.8	26.4	38.8	41.7	49.3	21.2	7.6	21
13	179.7	22.8	216.6	-32.4	224.7	-17.3	8	17
14	190.1	24	33.7	49	52.4	35.6	5.6	22
15	198.1	22.6	29.8	48.5	50.5	39.8	9.1	21
16	198.7	25.8	20.6	46.2	44.5	32.9	13.1	11
17	181.5	27.7	196.8	-32.2	210.1	-21.6	19.6	11
18	194.9	27.9	213.4	-36.2	228.2	-23.7	20.6	7

19	192.8	36.2	347.4	30.9	13.3	39.2	14.5	8
20	194.6	24.1	34.7	45.1	52.2	33.2	20	8
21	173.1	26.2	39.5	43.3	50.2	22.5	7.4	20
22	183	25.1	209.1	-44.6	225.3	-30.2	12.9	14
24	172.2	31.2	212.4	-41.9	225.3	-18.8	20.7	7
25	170.8	36	216.2	-48.1	231.1	-22.1	10.4	16
26	167.9	31.9	210.9	-36.8	221	-12.7	13.9	17
27	189.8	37.1	202.8	-45.4	228.9	-28.2	11.9	12
28	182.6	24.2	214.7	-52.8	233	-36.5	11.3	15
29	184.3	28.4	215.8	-42.3	230.6	-24.1	8.4	16
30	190.1	34.4	28.7	45.2	51.4	27.3	11.6	16
31	183.1	32.6	222.2	-49.6	239.4	-24.9	11.7	14
32	192.3	30.4	226.8	-50.3	245.4	-28.7	13.1	13
33	176.4	31	211	-43.6	226.3	-22.3	8.4	19
34	178.6	23	223.6	-46.3	234.9	-28.3	11.7	19
35	175.8	27	209.8	-45.1	224.8	-26.9	10.5	19
36	192	33.3	25	50.1	52.9	34.2	10.8	14
37	201.6	27	212.8	-32.8	227	-24.1	16.9	11
38	186.8	27.2	34.8	50.3	54.4	33.2	9.4	18
39	182.8	31.7	220.1	-46.8	236.3	-23.7	7.7	23
40	182.1	31.1	235.9	-50	247.8	-22.8	8.3	18
41	183	26.9	228.4	-50.2	242.2	-28.6	12.1	12
42	171.7	21.6	239.1	-43.8	244.1	-23.5	9.7	15
43	184.6	25.7	224.3	-50.6	239.7	-31.4	11.9	13
44	188.6	30.3	25.6	46.1	47.7	31.3	18.7	11
45	187.2	37.4	20.4	41.3	43.5	24.8	12.4	12
46	183.1	31.7	17.4	43.1	39	29.1	10.6	17
47	188.6	41.1	18.4	49.8	51.2	30.2	10.2	17
48	183.4	40.5	196	-44	222.5	-25.2	11.7	16
49	183.9	39.1	198.3	-41.8	221.9	-23.6	12.8	12
50	175.3	43.2	176.4	-50.2	215.2	-33.5	15.6	11
51	178.1	37.4	171.9	-42	203	-35.5	14.5	11
52	169.7	45.4	2.3	53.5	38.5	28.2	8.2	22
53	172	47.9	350	46.7	29.4	30.4	7	24
54	178.3	43.6	3.3	39.9	31	24.7	6.3	25
55	184.8	48	3.4	41.7	37.7	27.3	8.8	20
56	201.5	52.6	10.5	38.6	49.3	29.8	13	14
57	187.4	40.2	8.4	33.3	31	24.2	11	15
58	185.8	45	4.2	38.5	34.3	27.1	6.5	24

59	185	49.8	356.8	40.1	34.1	29.9	6.4	21
60	190.4	50.4	5.1	34.1	35.3	24.6	8.5	21
61	190.5	55.7	175.9	-29.7	209.3	-27.4	14.2	15
62	176.5	50.2	353.5	37.4	25.5	24.9	6.6	24
63	171.6	53.1	353.2	42.5	28.5	22.9	8.6	21
64	171.8	51	350.4	40	24.3	24.8	9.8	21
65	183.4	57.7	180.4	-45.6	223.3	-24.4	11.1	13
66	189.2	55.5	181.2	-27.5	208.7	-21.3	5.9	10
67	187.2	48.4	190.5	-29	211.6	-16.5	19.4	6
GD10-120	197	15.4	31.4	43.7	44	38.2	13.2	9
GD135-166	182.7	14.8	244.5	-38.7	248.6	-25.4	15.9	6
GD179-360	168.3	19.6	43.3	42.9	50.4	26.1	7	22
GD366-387	161.4	27.1	210.3	-53.9	224.5	-31.1	9.8	9
GD394-432	166	25.1	26.8	39.5	37.2	21.2	7.5	15
GD433-456	165.1	27.1	20.1	41	33	22.8	11.5	15
GD457-483	167.9	21.4	25.4	37.6	34.8	23.1	8	15
GD484-507	183.8	21.2	26.1	42.4	40.3	31.8	10.2	15
GD511-544	181.5	24.8	33.9	40	46.3	24.3	9.7	15
GD545-567	176.5	23.9	26.3	41.2	39.5	26.8	7.9	15
GD573-595	177.1	30	22.8	44.3	40.9	26.7	14.6	9
GD597-618	177.9	30	24.5	44.1	42.2	26.2	7.8	9
GD620-683	160.1	27.1	229.4	-52.6	236.2	-26.6	11.8	13
GD691-711	163.1	10.7	26	32.1	30.1	24.5	7.1	14
GD712-746	156.8	17.9	18.1	38.6	26.1	25.8	9.7	14
GD748-776	166.6	23.4	26.7	38.3	36.4	21.6	24.1	10
GD784-800	167.1	22.3	44.6	34	49.7	14.6	9.4	10
GR3-46	201.8	28.6	207.9	-43.7	230.8	-34.7	9.5	13
GR54-78	187.5	25.7	27.7	46.7	46.9	33.6	7.7	15
GR79-97	187.7	25.5	36.1	42.7	50.9	27.5	9.3	11
GR99-116	185.3	26.8	24.4	52.4	48.2	38.1	14.4	11
GR129-174	187.5	29.6	204.1	-53.2	231	-37.7	18.3	8
GR194-224	160.1	24.1	357.8	52.3	20.3	40.3	19	6
GR234-333	178.5	27.7	196.2	-41.6	214.1	-28.8	17.4	15
GR348-402	179.8	30.3	180.1	-47.9	209.2	-39.7	18	14
GR413-482	175.6	29.1	181.9	-62.8	222	-48.8	13.3	14
GR487-510	168.1	28.4	27.7	55.3	46.4	33.4	13.5	9
GR511-537	178	29.6	193.5	-50.6	218.9	-36	14.1	12
GR538-556	174.1	29.3	38.3	46.1	51.4	23.1	10.7	10
GR570-620	182.9	28.1	213.2	-49.3	231.9	-30.9	8.4	17

GR623-703	178.7	23.8	203	-55.7	225.4	-41.5	10.8	17
GR713-737	180.5	26.9	21.7	48.5	42.3	34	9	15
GR739-787	177	28.2	9.2	41.8	28.9	30.9	11	15
GR793-815	174.6	27.5	17.6	44.9	35.8	29.9	12.7	14
GR816-844	180.7	31.5	220.1	-59.7	242.4	-34.7	10.2	11
GR845-928	180.2	26	214.6	-45.2	229.2	-27.6	13.5	11
GR955.5-1004	184.8	34.7	1.6	40.5	28.6	33.9	14.9	13
GR1005-1044	179.2	37.8	13.3	43.5	37.8	25.8	14.4	12
GR1052-1089	176.4	33.7	212.4	-52.9	232.9	-27.8	8.8	15
GR1090-1119	167.5	46.8	176.7	-53	215	-28.5	12.7	15
GR1123-1171	169.3	50.3	170.5	-59.1	221.7	-32.7	10.3	17
GR1173-1195	168.7	44.8	359.8	56	39	30.8	9.8	14
GR1198-1219	175.4	44.7	345.4	47.5	28.6	37.3	12.5	14
GR1220-1239	171.8	48.4	346.6	52.1	33.9	34.4	10	14
GR1240-1260	182.1	43.1	9	37.7	33.9	22.4	11.3	14
GR1261-1277	183.6	44	357.7	42	32.6	32.3	11.8	14
GR1279-1314	187.6	43.2	6.6	32.1	30.2	23.4	12.2	14
GR1315-1331	173.4	52	4.1	38.4	34.6	32.4	13	14
GR1332-1347	176.6	47.3	353.7	29.8	24.6	27.5	12.9	14
GR1348-1367	189.9	48.6	2.3	34	32.8	26.9	11.7	14
GR1368-1391	191	43.8	3.3	40.9	37.9	32.9	13.4	13
GR1393-1414	184.9	47.6	169.6	-36.5	205.8	-33.9	14	14
GR1415-1439.5	174.7	52.1	344.6	25	9.5	22.6	11.9	14
GR1440-1454	171.9	51.9	334.3	34.3	12.1	33	16	13
GR1460-1486	173.9	50.9	166	-36.5	200.1	-27.4	15.7	12
GR1489-1521	179.3	43.4	180.1	-37.1	207.2	-25.5	9.7	11
Mangkang (Late Cretaceous)								
MK3	140	76	226.5	18.5	224.8	-51.4	8.4	13
MK4	137	68	221.4	15.6	218.2	-51.4	8	12
MK5	138	78	216	29.9	214.6	-38.9	7.4	11
MK6	171	54	75.9	5.5	71.1	59.2	3.8	12
MK7	184	51	87.9	6.6	84.9	56.1	3.9	11
MK8	253	36	107.4	49.9	56.2	55.5	5.8	8
MK9	245	45	104.2	52.3	34.7	57.9	5.6	11
MK10	161	60	62.5	4.6	47.6	62	6	11
MK11	173	45	63.4	19.2	41.8	62.2	11.8	12
MK12	183	45	62	23.4	33.2	56.9	4.8	13

MK13	206	34	64.3	23.4	45.1	40.3	5.2	11
MK14	28	41	1.8	39.1	40.5	44.5	4.9	9
MK15	40	43	350.3	41.2	42.4	59.8	8.5	9
MK16	53	47	348.9	37.6	46.5	69.6	10.1	10
MK17	54	50	25.5	29.7	62.4	39.5	16.1	11
MK18	53	52	10.1	39.6	70.6	53.7	5.9	10
B	174	60	45.7	-9.3	34.8	36.2	5	5
C	130	60	21.5	2.6	3.9	57.5	8	5
D	353	62	298.9	44.2	32.3	57.2	3.9	5
E	30	45	9.8	38.7	49	39.3	3.7	5
F	30	47	337.4	45.2	47.8	63.3	10.7	5
G	56	46	5.5	28.7	43.4	55.1	9.5	5
H	40	50	10.8	36.8	56.6	43.3	8.1	5
I	19	68	151.2	-60.5	242.3	-51	3.2	5
J	21	47	325.2	49.7	44.1	45.8	3.4	5
K	21	47	323.2	52.1	47.6	46.7	3.9	9
M	176	49	44.6	32.1	357.6	55.9	7.6	5
Mangkang (Early Cretaceous)								
A	170	80	268.6	46.6	70.2	52.7	9	4
B	180	84	279.2	42.1	78.6	53	9	4
D	155	120	259.7	5.6	40.9	51.7	11.4	5
E	156	125	265.4	5.8	38.1	45.3	5.4	5
G	150	120	280.6	16.5	14.4	29.3	13.7	5
I	144	120	276.1	23.7	46	31.6	7.9	5
J	171	83	248.2	47.2	94.1	48.3	12.1	5
K	170	85	250.9	55	86.8	39.5	14.1	5
A1	208	115	64.3	-51.6	75.9	41.7	2.6	3
B1	200	115	76.2	-50.1	72.7	53.8	7.8	4
C1	186	107	70.6	-33.9	47.4	61.7	6.2	5
D1	190	113	67.9	-29.4	29.4	60.6	3.3	5

Notes: *n is the number of samples collected and used for paleomagnetic calculation; Dec. and Inc. are declination and inclination, respectively; A_{95} is the radius of the cone at 95% confidence level about the mean direction. In the Zaduo area, the ChRMs are isolated until 140 mT (alternating field demagnetization) or ~500°C (thermal demagnetization) (Fu et al., 2022a); in the Gongjue area, the ChRMs are mostly calculated between 620–680°C (Xiao et al., 2021) or until 690°C (Li et al., 2020b); in the Mangkang area, the ChRMs are isolated until 680-700°C (Huang et al., 1992; Tong et al., 2015).*

Supplementary figures

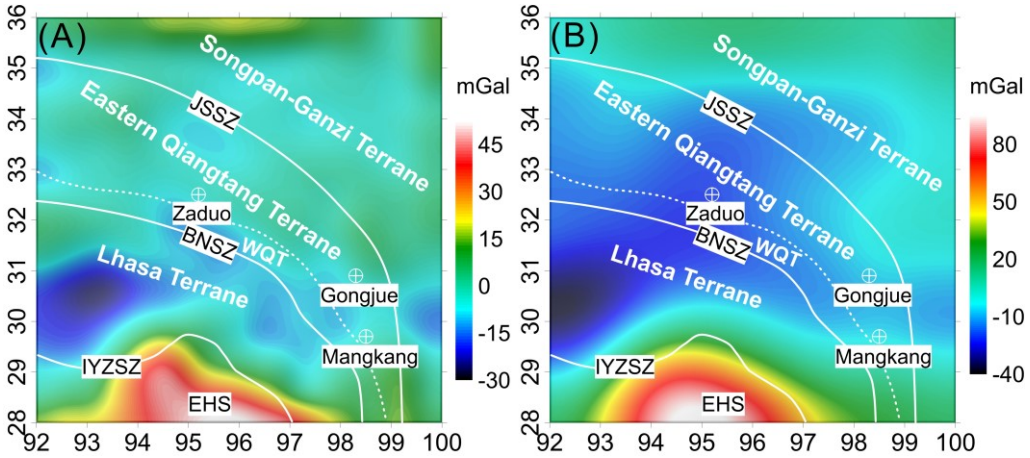

Figure S3.1. *Gravity anomalies and their decomposition of the study area marked with a white rectangle in figure 3.1. The (A) 5th- and (B) 6th-order wavelet detail of the Bouguer gravity anomalies. Refer to figure 3.1 for abbreviations.*

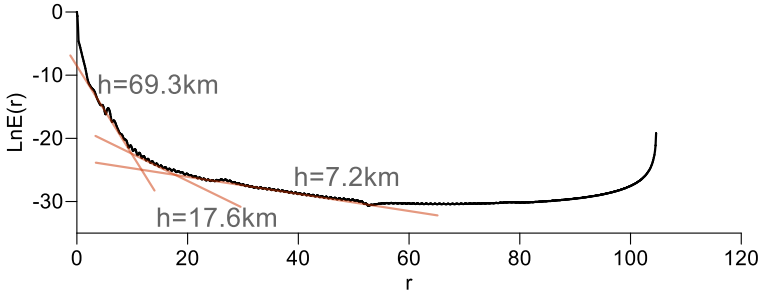

Figure S3.2. *Power spectrum depth estimation of the 5th-order wavelet details the Bouguer gravity anomalies.*

Chapter S4

Supplementary tables

Table S4.1. *Correlation between susceptibility, natural remanent magnetization (NRM), saturation isothermal remanent magnetization (SIRM), and saturation magnetization (M_s) in the remagnetized limestones.*

Sample ID	K_m (10^{-6} SI)	NRM (mA/m)	SIRM (10^{-3} Am²/kg)	M_s (10^{-3} Am²/kg)
1-11	1428.11	12.7	3.5	10.83
1-12	1242.05	16.4	3.1	9.86
2-1	98.15	2.17	0.08	0.54
2-2	991.8	44.4	6.53	16.68
2-3	650.54	17.6	2.91	7.93
2-4	65.11	1.4	0.1	0.39
2-5	70.49	2.06	0.05	0.17
2-6	47.63	0.893	0.06	0.17
2-7	41.99	0.704	0.08	0.7
2-8	37.25	0.786	0.07	1.3
2-9	30.74	0.69	0.08	0.47
2-10	46.23	1.35	0.09	-
3-1	669.27	12.3	0.57	4.25
3-2	783.6	8.69	1.02	5.46
3-3	838.69	25.4	2.24	7.78
3-4	646.87	23.4	1.35	5.98
3-5	747.71	15.9	0.66	3.19
3-6	459.46	7.61	-	1.87
3-7	770.26	14	-	-
3-8	814.25	19.1	1.25	6.21
3-9	839.53	11.1	1.01	5.77
3-10	560.78	11.3	0.56	3.48
4-1	1089.77	28	1.21	5.44
4-2	743.61	22.6	1.29	5.31
4-3	1169.05	26.1	-	-
4-4	664.65	13.7	0.74	3.37
4-5	885.82	25.2	0.63	3.08
4-6	829.92	23.4	1.77	6.44
4-7	776.69	22.3	-	-
4-8	756.59	18.4	3.08	4.01
4-9	772.6	21.8	1.06	4.49

4-10	743.29	19.5	-	-
4-11	877.16	25.3	1.21	-
5-1	923	11.3	1.01	5.4
5-2	566.69	7.76	0.63	3.91
5-3	859.94	10.9	1.04	5.09
5-4	754.82	11.4	0.93	5.14
5-5	782.85	11.2	1.08	5.49
5-6	463.82	9.6	0.58	3.22
5-7	664.98	16.4	0.62	3.31
5-8	855.64	17.8	0.38	3.58
5-9	753.49	13.5	-	-
6-1	440.4	5.69	0.3	-
6-2	438.3	6.4	0.27	2.61
6-3	425.54	7.02	-	-
6-4	402.92	5.6	-	-
6-5	482.01	5.44	-	-
6-6	439.72	6.07	-	-
6-7	535.79	6.06	-	-
6-8	490.43	6.15	-	-
6-9	506.83	6.88	-	-
6-10	449.57	6.06	-	-
6-11	328.26	4.49	0.39	3.46
6-12	370.2	5.62	-	-
7-1	1309.19	22.9	1.34	7.95
7-2	1219.34	14	-	-
7-3	1268.99	13.5	1.09	7.14
7-4	1297.16	12.7	1.17	7.5
7-5	1141.23	11.2	0.95	6.69
7-6	1184	11.4	0.88	6.13
7-7	1336.42	11.4	1	7.71
7-8	1271.56	13.1	1.26	8.17
7-9	1193.38	10.8	1.19	7.46
7-10	1147.64	12.5	-	-
7-11	1080.72	24.1	0.89	6.12
8-1	255.42	6.69	0.57	3.07
8-2	134.77	1.73	0.12	1.63
8-3	114.02	1.46	0.06	1.25
8-4	216	4.56	-	-
8-5	617.98	9.61	1.22	5.21

8-6	140.64	2.59	0.1	1.54
8-7	195.34	4.12	0.74	3.69
8-8	580	5.07	-	4.51
8-9	116.82	2.07	-	-
8-10	135.21	2.46	-	-
8-11	253.54	3.92	-	-
1-1	1526.74	34	-	-
1-2	1142.87	24.6	4.6	13.28
1-3	1205.41	18.6	4.3	12.55
1-4	1101.86	17.8	4.71	13.5
1-5	1479.36	28.7	4.56	13.34
1-6	1159.93	30.4	5.54	16.83
1-7	1182.53	25.7	4.09	13.09
1-9	970.77	15.8	3.51	10.45
1-10	1182.6	14.7	-	13.17
9-1	314.69	4.91	0.14	1.7
9-2	340.05	5.93	-	-
9-3	351.04	6.27	0.21	1.68
9-4	379.82	7.52	-	2.16
9-5	392.12	7.94	0.2	1.77
9-6	366.86	3.15	0.24	2.66
9-7	351.14	3.51	0.24	2.47
9-8	332.21	4.98	0.2	1.85
9-9	278.88	4.48	0.23	2.47
9-10	328.52	5.55	0.23	2.43
9-11	236.13	3.8	0.3	2.98
9-12	262.95	3.86	-	-
10-1	409.94	8.27	0.25	2.59
10-2	409.49	7.82	-	2.74
10-3	374.66	8.16	0.34	3.41
10-4	340.13	6.83	0.23	2.59
10-5	396.09	8.04	-	-
10-6	377.32	7.18	0.29	2.95
10-7	391.24	7.96	0.31	3.35
10-8	395.33	8.24	0.23	2.83
10-9	400.96	8.4	-	-
10-10	366.54	8.41	0.26	3.15
10-11	343.52	8.21	0.35	3.73
11-1	147.35	1.72	0.13	0.95

11-2	143.99	1.49	-	1.16
11-3	133.79	2.15	0.12	0.91
11-4	672.04	14.8	0.35	2.68
11-5	577.81	8.85	-	-
11-6	614.19	8.81	0.53	4.32
11-7	740.69	15.9	0.53	4.37
11-8	746.58	15.1	-	-
11-9	725.1	12.6	0.43	3.9
11-10	724.65	11.8	0.41	4.42
11-11	559.15	9.13	0.25	2.39
11-12	714.87	16.5	0.34	3.14

Supplementary figure

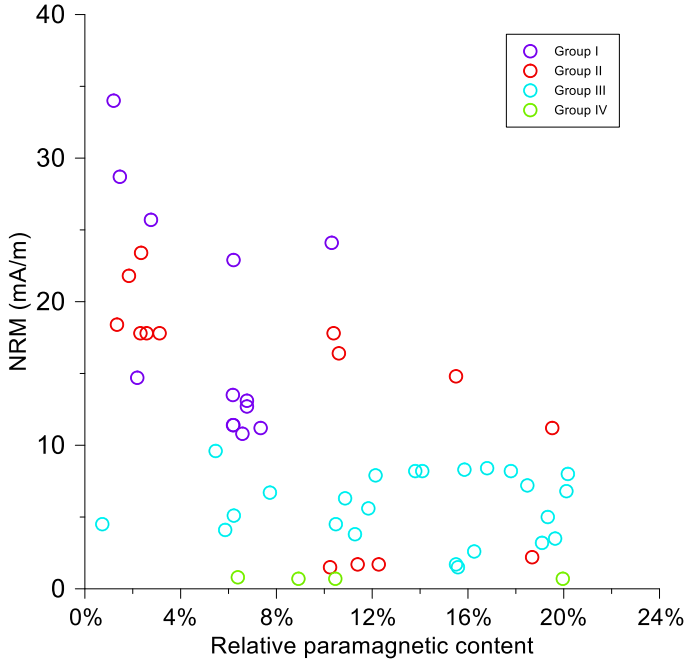

Figure S4.1. *Correlation between NRM and the paramagnetic phase percentage of the Jurassic limestones.*

Chapter S5

Supplementary tables

Table S5.1 *Results of isothermal remanent magnetization (IRM) component analysis for representative samples.*

	Component 1					Component 2					Component 3					Component 4				
Sample	Con	SIRM	log($B_{1/2}$)	$B_{1/2}$	log(DP)	Con	SIRM	log($B_{1/2}$)	$B_{1/2}$	log(DP)	Con	SIRM	log($B_{1/2}$)	$B_{1/2}$	log(DP)	Con	SIRM	log($B_{1/2}$)	$B_{1/2}$	log(DP)
	(%)	(μAm^2)	(mT)	(mT)	(mT)	(%)	(μAm^2)	(mT)	(mT)	(mT)	(%)	(μAm^2)	(mT)	(mT)	(mT)	(%)	(μAm^2)	(mT)	(mT)	(mT)
J 1-5	5.12	0.23	0.7	5.01	0.37	7.57	0.34	1.08	12.02	0.16	85.08	3.82	1.74	55	0.3	2.23	0.1	2.58	380.2	0.14
J 8-5	9.76	0.12	0.75	5.62	0.26	9.76	0.12	1.15	14.13	0.16	73.17	0.9	1.75	56.2	0.33	7.32	0.09	2.9	794.3	0.3
C 4-4	8.15	0.48	0.5	3.16	0.26	8.49	0.5	1.03	10.72	0.16	78.61	4.63	1.72	52.5	0.36	4.75	0.28	2.65	446.7	0.18
C 9-7	6.36	0.22	0.5	3.16	0.2	6.07	0.21	1.01	10.23	0.13	81.79	2.83	1.74	55	0.38	5.78	0.2	2.56	363.1	0.2
K 2-5	-	-	-	-	-	15.27	0.15	1.05	11.2	0.37	83.71	0.82	1.65	44.7	0.36	1.02	0.01	2.75	562.3	0.2
K 3-6	-	-	-	-	-	14.31	0.16	0.8	6.31	0.37	84.71	0.95	1.5	31.6	0.35	0.98	0.01	2.67	467.7	0.1
K 5-4	-	-	-	-	-	13.57	0.03	1.28	19.05	0.33	80.4	0.16	1.65	44.7	0.32	6.03	0.01	2.57	371.5	0.17
K 7-4	-	-	-	-	-	14.61	0.03	1.38	23.99	0.33	76.26	0.17	1.63	42.7	0.33	9.13	0.02	2.6	398.1	0.25
K 9-10	-	-	-	-	-	18.79	0.16	1.39	24.55	0.26	80.26	0.68	1.68	47.9	0.37	0.95	0.01	2.7	501.2	0.25
T 2-6	-	-	-	-	-	5.31	0.11	0.87	7.41	0.26	92.23	1.91	1.66	45.7	0.25	2.46	0.05	2.63	426.6	0.18
T 17-8						1.84	0.01	0.4	2.51	0.2	97.47	0.42	1.44	27.5	0.35	0.69	0	2.5	316.2	0.18

Note: *Con- contribution; SIRM- saturation isothermal remanent magnetization; $B_{1/2}$- the field at which half of the SIRM is reached; DP- dispersion parameter (Kruiver et al., 2001); EM: end member.*

Table S5.2. *Hysteresis parameters of the remagnetized limestones and the unremagnetized volcanic rocks in the Zaduo area.*

Sample ID	Area_E_{hys}	Area_4 M_sB_c	r_{hys}	σ_{hys}
J9-10	0.34	0.1	3.51	0.55
J9-1	0.36	0.12	2.91	0.46
J4-9	0.45	0.18	2.54	0.41
J7-1	0.42	0.17	2.52	0.4
J11-7	0.28	0.12	2.39	0.38
J9-4	0.25	0.11	2.21	0.34
J7-3	0.1	0.05	2.2	0.34
J10-4	0.27	0.12	2.19	0.34
J7-8	0.34	0.15	2.19	0.34
J4-6	0.46	0.21	2.18	0.34
J4-8	0.39	0.19	2.12	0.33
J9-6	0.21	0.1	2.09	0.32
J7-5	0.31	0.15	2.02	0.31
J6-11	0.16	0.1	1.62	0.21
J6-2	0.15	0.1	1.58	0.2
J1-6	0.62	0.48	1.29	0.11
J5-7	0.21	0.17	1.23	0.09
J1-2	0.66	0.54	1.23	0.09
J1-5	0.4	0.33	1.21	0.08
J1-7	0.65	0.54	1.2	0.08
J8-6	0.08	0.07	1.16	0.06
J8-1	0.22	0.21	1.04	0.02
C11-8	0.78	0.32	2.44	0.39
C9-7	0.66	0.28	2.39	0.38
C6-3	0.51	0.24	2.1	0.32
C6-5	0.52	0.26	2.03	0.31
C7-3	0.59	0.3	1.98	0.3
C8-4	0.5	0.25	1.97	0.29
C6-1	0.53	0.28	1.88	0.27
C8-9	0.53	0.29	1.83	0.26
C1-2	0.57	0.32	1.79	0.25
C1-4	0.61	0.35	1.75	0.24
C5-11	0.64	0.39	1.65	0.22
C7-4	0.36	0.24	1.51	0.18
K3-9	0.2	0.16	1.28	0.11

K3-3	0.2	0.16	1.22	0.09
K5-3	0.28	0.24	1.15	0.06
K6-1	0.17	0.15	1.12	0.05
K2-3	0.15	0.14	1.08	0.03
K1-4	0.14	0.14	1.02	0.01
K9-6	0.16	0.16	0.99	0
K1-2	0.14	0.15	0.97	0
K7-1	0.28	0.3	0.93	0
K1-2	0.15	0.16	0.93	0
K4-3-2	0.13	0.14	0.91	0
K8-3	0.16	0.18	0.9	-0.1
K5-1	0.35	0.4	0.87	-0.1
K2-6	0.15	0.2	0.73	-0.1
K3-6	0.08	0.15	0.55	-0.3
K4-3	0.08	0.16	0.53	-0.3
K8-3	0.05	0.13	0.38	-0.4
T-SL9-4	0.74	0.66	1.13	0.05
T-SL4-10	0.87	0.77	1.13	0.05
T-SL3-7	0.82	0.94	0.87	-0.1
T-SL20-4	0.68	0.79	0.86	-0.1
T-SL2-6	1.02	1.21	0.84	-0.1
T-SL20-12	0.7	0.85	0.83	-0.1
T-SL15-10	0.47	0.59	0.79	-0.1
T-SL39-6	0.59	0.75	0.79	-0.1
T-SL26-1	0.67	0.9	0.75	-0.1
T-SL1-2	0.78	1.1	0.71	-0.2
T-SL2-5	0.61	0.87	0.7	-0.2
T-SL17-8	0.28	0.54	0.52	-0.3

Note: *Area_E_{hys} is the total area between the two hysteresis branches; Area_$4M_sB_c$ represents the rectangular area with height $2M_s$ and width $2B_c$;* $r_{hys}=\frac{E_{hys}}{4M_sB_c}$; $\sigma_{hys}=\log\left(\frac{E_{hys}}{4M_sB_c}\right)$.

SUPP. INFO

Table S5.3. *The fractions of the paramagnetic and ferromagnetic contributions of the representative samples in the Zaduo area.*

J_limestones			C_limestones			K_Granites			T_Volcanic rocks		
Sample ID	Para	Ferro	Sample ID	Para	Ferro	Sample ID	Para	Ferro	Sample ID	Para	Ferro
1	0.012	0.988	1	0.484	0.516	1	0.026	0.974	1	0.066	0.934
2	0.015	0.985	2	0.391	0.609	2	0.023	0.977	2	0.065	0.935
3	0.028	0.972	3	0.409	0.591	3	0.008	0.992	3	0.124	0.876
4	0.022	0.978	4	0.127	0.873	4	0.023	0.977	4	0.153	0.847
5	0.353	0.647	5	0	1	5	0.034	0.966	5	0.49	0.51
6	0.089	0.911	6	0.047	0.953	6	0.03	0.97	6	0.564	0.436
7	0.105	0.895	7	0.063	0.937	7	0.096	0.904	7	0.584	0.416
8	0.064	0.936	8	0.294	0.706	8	0.029	0.971	8	0.524	0.476
9	0.2	0.8	9	0.19	0.81	9	0.016	0.984	9	0.626	0.374
10	0.023	0.977	10	0.083	0.917	10	0.013	0.987	10	0.52	0.48
11	0.013	0.987	11	0.004	0.996	11	0.615	0.385	11	0.357	0.643
12	0.018	0.982	12	0.254	0.746	12	0.253	0.747	12	0.374	0.626
13	0.031	0.969	13	0.017	0.983	13	0.047	0.953	13	0.605	0.395
14	0.026	0.974	14	0.412	0.588	14	0.457	0.543	14	0.546	0.454
15	0.023	0.977	15	0.059	0.941	15	0.119	0.881	15	0.552	0.448
16	0	1	16	0.15	0.85	16	0.068	0.932	16	0.617	0.383
17	0.007	0.993	17	0.028	0.972	17	0.094	0.906	17	0.363	0.637
18	0.062	0.938	18	0.288	0.712	-	-	-	18	0.569	0.431
19	0.062	0.938	19	0.011	0.989	-	-	-	19	0.81	0.19
20	0.068	0.932	20	0.423	0.577	-	-	-	20	0.861	0.139
21	0.073	0.927	21	0.336	0.664	-	-	-	-	-	-
22	0.062	0.938	-	-	-	-	-	-	-	-	-
23	0.062	0.938	-	-	-	-	-	-	-	-	-
24	0.068	0.932	-	-	-	-	-	-	-	-	-
25	0.066	0.934	-	-	-	-	-	-	-	-	-
26	0.103	0.897	-	-	-	-	-	-	-	-	-
27	0.077	0.923	-	-	-	-	-	-	-	-	-
28	0.155	0.845	-	-	-	-	-	-	-	-	-
29	0.156	0.844	-	-	-	-	-	-	-	-	-
30	0.055	0.945	-	-	-	-	-	-	-	-	-
31	0.163	0.837	-	-	-	-	-	-	-	-	-
32	0.059	0.941	-	-	-	-	-	-	-	-	-
33	0.062	0.938	-	-	-	-	-	-	-	-	-
34	0.347	0.653	-	-	-	-	-	-	-	-	-
35	0.109	0.891	-	-	-	-	-	-	-	-	-

36	0.121	0.879	-	-	-	-	-	-	-	-	-
37	0.191	0.809	-	-	-	-	-	-	-	-	-
38	0.196	0.804	-	-	-	-	-	-	-	-	-
39	0.193	0.807	-	-	-	-	-	-	-	-	-
40	0.105	0.895	-	-	-	-	-	-	-	-	-
41	0.118	0.882	-	-	-	-	-	-	-	-	-
42	0.113	0.887	-	-	-	-	-	-	-	-	-
43	0.159	0.841	-	-	-	-	-	-	-	-	-
44	0.138	0.862	-	-	-	-	-	-	-	-	-
45	0.201	0.799	-	-	-	-	-	-	-	-	-
46	0.185	0.815	-	-	-	-	-	-	-	-	-
47	0.202	0.798	-	-	-	-	-	-	-	-	-
48	0.141	0.859	-	-	-	-	-	-	-	-	-
49	0.168	0.832	-	-	-	-	-	-	-	-	-
50	0.178	0.822	-	-	-	-	-	-	-	-	-
51	0.603	0.397	-	-	-	-	-	-	-	-	-
52	0.597	0.403	-	-	-	-	-	-	-	-	-
53	0.195	0.805	-	-	-	-	-	-	-	-	-
54	0.106	0.894	-	-	-	-	-	-	-	-	-
55	0.104	0.896	-	-	-	-	-	-	-	-	-
56	0.123	0.877	-	-	-	-	-	-	-	-	-
57	0.114	0.886	-	-	-	-	-	-	-	-	-
58	0.102	0.898	-	-	-	-	-	-	-	-	-
59	0.187	0.813	-	-	-	-	-	-	-	-	-
60	0.155	0.845	-	-	-	-	-	-	-	-	-

Note: *Para respectively Ferro: fraction of the paramagnetic and ferromagnetic contributions in each sample. The paramagnetic contribution is obtained from the high-field slope in $M_{ih}(H)$ (defined as the average of upper and lower branch of a hysteresis loop) before slope-correction. The low-field slope represents the joint contribution of both the paramagnetic and ferromagnetic phases. J_limestones: remagnetized Jurassic limestones; C_limestones: remagnetized Carboniferous limestones; K_Granites: unremagnetized Cretaceous granites; T_Volcanic rocks: unremagnetized Permo-Triassic volcanic (tuff and rhyolite) samples.*

Table S5.4. *The end-member IRM acquisition curves in the two end-member models for the normalized IRM acquisition curves of representative samples.*

J_limesones			C_limesones			K_Granites			T_Volcanic rocks		
Field (mT)	EM1	EM2	Field (mT)	EM1	EM2	Field (mT)	EM1	EM2	Field (mT)	EM1	EM2
0	0	0	0	0	0	0	0	0	0	0	0
0.1	0	0.04	0.1	0.01	0.01	5	0.06	0	5	0	0.01
0.2	0	0.08	0.21	0.01	0.02	10	0.16	0.01	10	0.01	0.03
0.3	0	0.1	0.32	0.01	0.02	12	0.21	0.02	12	0.02	0.04
0.4	0	0.12	0.44	0.02	0.02	14	0.26	0.05	14	0.02	0.06
0.6	0	0.13	0.56	0.02	0.02	16	0.3	0.06	16	0.04	0.07
0.7	0	0.14	0.7	0.02	0.02	18	0.32	0.07	18	0.06	0.09
0.9	0	0.15	0.84	0.02	0.03	20	0.38	0.12	20	0.07	0.1
1	0	0.16	0.99	0.02	0.03	22	0.42	0.16	22	0.1	0.13
1.2	0	0.18	1.15	0.03	0.03	24	0.44	0.18	24	0.12	0.14
1.4	0	0.19	1.31	0.03	0.03	26	0.46	0.2	26	0.16	0.17
1.6	0	0.2	1.49	0.03	0.03	28	0.51	0.22	28	0.17	0.19
1.8	0.01	0.21	1.68	0.03	0.03	30	0.54	0.26	30	0.22	0.21
2	0.01	0.21	1.88	0.04	0.03	33	0.57	0.29	33	0.25	0.23
2.2	0.01	0.22	2.09	0.04	0.03	36	0.6	0.33	36	0.28	0.26
2.5	0.01	0.23	2.32	0.04	0.04	40	0.65	0.4	40	0.36	0.3
2.7	0.02	0.24	2.55	0.04	0.04	43	0.67	0.42	43	0.42	0.33
3	0.02	0.24	2.8	0.05	0.04	46	0.7	0.45	46	0.46	0.36
3.3	0.02	0.25	3.07	0.05	0.04	50	0.73	0.5	50	0.52	0.4
3.7	0.03	0.26	3.35	0.05	0.04	55	0.77	0.54	55	0.6	0.44
4	0.03	0.26	3.65	0.06	0.04	60	0.79	0.58	60	0.66	0.49
4.4	0.03	0.27	3.97	0.06	0.04	65	0.82	0.62	65	0.71	0.54
4.8	0.04	0.28	4.3	0.07	0.04	70	0.84	0.64	70	0.76	0.57
5.2	0.05	0.29	4.65	0.07	0.05	75	0.86	0.67	75	0.8	0.61
5.7	0.05	0.29	5.03	0.07	0.05	80	0.88	0.68	80	0.83	0.64
6.2	0.06	0.31	5.43	0.08	0.05	90	0.9	0.74	90	0.88	0.71
6.7	0.06	0.31	5.85	0.09	0.05	100	0.91	0.79	100	0.91	0.75
7.2	0.07	0.32	6.3	0.09	0.05	120	0.94	0.83	120	0.94	0.81
7.8	0.08	0.33	6.77	0.1	0.05	140	0.96	0.85	140	0.96	0.86
8.5	0.08	0.35	7.27	0.11	0.06	160	0.98	0.87	160	0.97	0.88
9.1	0.09	0.36	7.8	0.11	0.06	180	0.98	0.89	180	0.98	0.9
10	0.1	0.36	8.36	0.12	0.06	200	0.99	0.9	200	0.98	0.91
10.5	0.11	0.38	8.96	0.13	0.07	230	1	0.91	230	0.98	0.93
11	0.12	0.39	9.59	0.14	0.07	260	1	0.93	260	0.99	0.94

12	0.13	0.4	10.25	0.15	0.07	300	1	0.94	300	0.99	0.95
13	0.15	0.41	10.96	0.16	0.08	350	1	0.95	350	0.99	0.96
14	0.16	0.43	11.71	0.17	0.08	400	1	0.96	400	0.99	0.97
15	0.17	0.43	12.5	0.18	0.09	450	1	0.97	450	0.99	0.98
17	0.19	0.44	13.35	0.2	0.09	500	1	0.97	500	1	0.98
18	0.2	0.46	14.23	0.21	0.1	550	1	0.98	550	1	0.99
19	0.22	0.47	15.18	0.23	0.11	600	1	0.99	600	1	0.99
20	0.23	0.48	16.18	0.24	0.11	650	1	0.99	650	1	1
22	0.25	0.5	17.23	0.26	0.12	700	1	1	700	1	1
24	0.27	0.51	18.35	0.27	0.13	-	-	-	-	-	-
25	0.28	0.53	19.54	0.28	0.13	-	-	-	-	-	-
27	0.3	0.55	20.8	0.3	0.14	-	-	-	-	-	-
29	0.33	0.56	22.13	0.32	0.16	-	-	-	-	-	-
31	0.35	0.58	23.54	0.34	0.16	-	-	-	-	-	-
33	0.37	0.6	25.03	0.36	0.18	-	-	-	-	-	-
36	0.4	0.61	26.61	0.38	0.19	-	-	-	-	-	-
38	0.43	0.62	28.29	0.41	0.2	-	-	-	-	-	-
41	0.45	0.65	30.07	0.43	0.22	-	-	-	-	-	-
44	0.49	0.67	31.94	0.45	0.23	-	-	-	-	-	-
47	0.51	0.69	33.94	0.47	0.24	-	-	-	-	-	-
50	0.52	0.71	36.04	0.5	0.26	-	-	-	-	-	-
54	0.56	0.72	38.28	0.52	0.29	-	-	-	-	-	-
57	0.6	0.73	40.64	0.54	0.3	-	-	-	-	-	-
61	0.62	0.75	43.15	0.57	0.32	-	-	-	-	-	-
66	0.65	0.76	45.81	0.61	0.34	-	-	-	-	-	-
70	0.7	0.76	48.62	0.63	0.36	-	-	-	-	-	-
75	0.71	0.78	51.6	0.65	0.37	-	-	-	-	-	-
80	0.73	0.8	54.75	0.68	0.4	-	-	-	-	-	-
86	0.77	0.8	58.09	0.71	0.43	-	-	-	-	-	-
92	0.79	0.82	61.63	0.73	0.45	-	-	-	-	-	-
98	0.8	0.83	65.38	0.75	0.47	-	-	-	-	-	-
105	0.84	0.83	69.35	0.79	0.48	-	-	-	-	-	-
112	0.86	0.84	73.55	0.81	0.52	-	-	-	-	-	-
120	0.86	0.85	78.01	0.83	0.53	-	-	-	-	-	-
128	0.89	0.85	82.73	0.85	0.55	-	-	-	-	-	-
137	0.91	0.85	87.72	0.88	0.57	-	-	-	-	-	-
147	0.92	0.87	93.01	0.9	0.6	-	-	-	-	-	-
157	0.92	0.88	98.62	0.91	0.62	-	-	-	-	-	-
168	0.94	0.88	104.56	0.93	0.64	-	-	-	-	-	-

179	0.95	0.89	110.85	0.94	0.67	-	-	-	-	-	-
191	0.95	0.9	117.51	0.95	0.69	-	-	-	-	-	-
205	0.96	0.91	124.56	0.96	0.71	-	-	-	-	-	-
219	0.96	0.91	132.04	0.97	0.72	-	-	-	-	-	-
234	0.97	0.92	139.95	0.98	0.75	-	-	-	-	-	-
250	0.97	0.92	148.34	0.98	0.77	-	-	-	-	-	-
267	0.98	0.93	157.22	0.99	0.79	-	-	-	-	-	-
285	0.98	0.93	166.62	0.99	0.8	-	-	-	-	-	-
304	0.98	0.94	176.58	0.99	0.82	-	-	-	-	-	-
325	0.98	0.94	187.14	0.99	0.83	-	-	-	-	-	-
348	0.99	0.95	198.31	1	0.85	-	-	-	-	-	-
371	0.99	0.96	210.15	1	0.86	-	-	-	-	-	-
397	0.99	0.96	222.69	1	0.87	-	-	-	-	-	-
424	0.99	0.97	235.97	1	0.88	-	-	-	-	-	-
453	0.99	0.97	250.04	1	0.9	-	-	-	-	-	-
484	0.99	0.98	264.93	1	0.91	-	-	-	-	-	-
517	0.99	0.98	280.72	1	0.92	-	-	-	-	-	-
552	0.99	0.99	297.43	1	0.93	-	-	-	-	-	-
590	0.99	0.99	315.13	1	0.94	-	-	-	-	-	-
630	0.99	0.99	333.89	1	0.95	-	-	-	-	-	-
673	1	1	353.75	1	0.95	-	-	-	-	-	-
719	1	1	374.78	1	0.96	-	-	-	-	-	-
768	1	1	397.06	1	0.97	-	-	-	-	-	-
821	1	1	420.67	1	0.98	-	-	-	-	-	-
877	1	1	445.66	1	0.98	-	-	-	-	-	-
936	1	1	472.14	1	0.99	-	-	-	-	-	-
1000	1	1	500	1	1	-	-	-	-	-	-

Note: *EM1 = Endmember 1; EM2 = Endmember 2.*

Table S5.5. *Hysteresis parameters of different lithologies.*

No.	Area_E_{hys}	Area_4 M_sB_c	r_{hys}	σ_{hys}	Lithology	Note	Reference
1	0.6	0.4	1.49	0.17	limestones	primary	Yan et al. (2016)
2	0.6	0.93	0.65	-0.19	limestones	primary	Yan et al. (2016)
3	0.01	0.01	1.18	0.07	limestones	primary	Cao et al. (2019)
4	0.25	0.07	3.45	0.54	limestones	primary	Cao et al. (2019)
5	0.1	0.05	1.86	0.27	limestones	primary	Cao et al. (2019)
6	0.14	0.04	3.44	0.54	limestones	primary	Cao et al. (2019)
7	0.1	0.06	1.73	0.24	limestones	primary	Ma et al. (2018)
8	0.16	0.09	1.89	0.28	limestones	primary	Ma et al. (2018)
9	0.04	0.07	0.63	-0.2	volcaniclastic sandstones	primary	Huang et al. (2015a)
10	0.24	0.18	1.38	0.14	volcaniclastic sandstones	primary	Huang et al. (2015a)
11	0.02	0.03	0.6	-0.22	green chert	primary	Huang et al. (2015b)
12	0.02	0.03	0.76	-0.12	sandstone	primary	Huang et al. (2015b)
13	0.04	0.04	0.87	-0.06	sandstone	primary	Huang et al. (2015b)
14	0.3	0.39	0.77	-0.11	carbonatites	primary	Abrajevitch & Kodama. (2009)
15	0.15	0.15	0.97	-0.01	carbonatites	primary	Abrajevitch & Kodama. (2009)
16	0.06	0.07	0.79	-0.1	carbonatites	primary	Ménabréaz et al. (2010)
17	0.07	0.09	0.77	-0.11	carbonatites	primary	Ménabréaz et al. (2010)
18	0.09	0.12	0.77	-0.11	carbonatites	primary	Belkaaloul & Aïssaoui. (2010)
19	0.2	0.21	0.95	-0.02	carbonatites	primary	Channell. (1994)
20	0.09	0.11	0.85	-0.07	carbonatites	primary	Channell. (1994)
21	0.03	0.05	0.57	-0.24	carbonatites	primary	Channell. (1994)
22	0.08	0.14	0.62	-0.2	carbonatites	primary	Channell. (1994)

23	0.59	0.69	0.85	-0.07	lava	primary	Huang et al. (2015d)
24	0.48	0.53	0.9	-0.05	lava	primary	Huang et al. (2015d)
25	0.03	0.07	0.41	-0.39	volcaniclastic rock	primary	Huang et al. (2017a)
26	0.03	0.08	0.44	-0.36	volcaniclastic rock	primary	Huang et al. (2017a)
27	0.04	0.07	0.54	-0.27	volcaniclastic rock	primary	Huang et al. (2017a)
28	0.03	0.05	0.57	-0.24	volcaniclastic rock	primary	Huang et al. (2017a)
29	0.09	0.06	1.66	0.22	limestones	remagnetized	Huang et al. (2015a)
30	0.12	0.07	1.69	0.23	limestones	remagnetized	Huang et al. (2015a)
31	0.11	0.07	1.66	0.22	limestones	remagnetized	Huang et al. (2015a)
32	0.83	0.22	3.74	0.57	andesitic tuff	Partially remagnetized	Huang et al. (2015d)
33	1.01	0.9	1.12	0.05	grey dacitic and rhyolitic tuff	Partially remagnetized	Huang et al. (2015d)
34	1.39	1.22	1.14	0.06	andesitic tuff	Partially remagnetized	Huang et al. (2015d)
35	0.51	0.24	2.13	0.33	andesitic tuff	Partially remagnetized	Huang et al. (2015d)
36	0.18	0.06	3.33	0.52	andesitic tuff	Partially remagnetized	Huang et al. (2015d)
37	0.4	0.1	3.91	0.59	andesitic tuff	Partially remagnetized	Huang et al. (2015d)
38	0.05	0.07	0.7	-0.16	volcanic rocks	remagnetized	Huang et al. (2015e)
39	0.75	0.32	2.37	0.38	volcanic rocks	remagnetized	Huang et al. (2015e)
40	0.05	0.06	0.88	-0.05	carbonatites	remagnetized	Huang et al. (2017a)
41	0.03	0.04	0.69	-0.16	carbonatites	remagnetized	Huang et al. (2017a)
42	0.03	0.04	0.64	-0.19	carbonatites	remagnetized	Huang et al. (2017a)
43	0.04	0.05	0.66	-0.18	carbonatites	remagnetized	Huang et al. (2017a)
44	0.04	0.02	1.82	0.26	carbonatites	remagnetized	Huang et al. (2017a)
45	0.08	0.04	1.78	0.25	carbonatites	remagnetized	Huang et al. (2017a)
46	0.06	0.03	1.87	0.27	carbonatites	remagnetized	Huang et al. (2017a)
47	0.07	0.04	1.84	0.26	carbonatites	remagnetized	Huang et al. (2017a)
48	0.03	0.02	1.72	0.23	carbonatites	remagnetized	Huang et al. (2017a)

49	0.03	0.03	1.33	0.12	carbonatites	remagnetized	Huang et al. (2017a)
50	0.07	0.04	1.94	0.29	carbonatites	remagnetized	Huang et al. (2017a)
51	0.08	0.06	1.45	0.16	carbonatites	remagnetized	Huang et al. (2017a)
52	0.08	0.04	2.23	0.35	carbonatites	remagnetized	Huang et al. (2017b)
53	0.12	0.05	2.69	0.43	carbonatites	remagnetized	Huang et al. (2017b)
54	0.16	0.05	3.06	0.49	carbonatites	remagnetized	Huang et al. (2017b)
55	0.09	0.02	3.71	0.57	carbonatites	remagnetized	Huang et al. (2017b)
56	0.19	0.06	2.92	0.47	carbonatites	remagnetized	Huang et al. (2017b)
57	0.14	0.07	2	0.3	carbonatites	remagnetized	Huang et al. (2017b)
58	0.08	0.04	1.75	0.24	carbonatites	remagnetized	Huang et al. (2017b)
59	0.04	0.02	1.81	0.26	carbonatites	remagnetized	Huang et al. (2019b)
60	0.04	0.02	1.59	0.2	carbonatites	remagnetized	Huang et al. (2019b)
61	0.04	0.02	1.84	0.26	carbonatites	remagnetized	Huang et al. (2019b)
62	0.02	0.01	1.82	0.26	carbonatites	remagnetized	Huang et al. (2019b)
63	0.04	0.02	2.29	0.36	carbonatites	remagnetized	Huang et al. (2019b)
64	0.03	0.01	2.24	0.35	carbonatites	remagnetized	Huang et al., (2019b)

Note: *refer to Table S5.2 for the interpretation of the parameters in this table.*

Supplementary figures

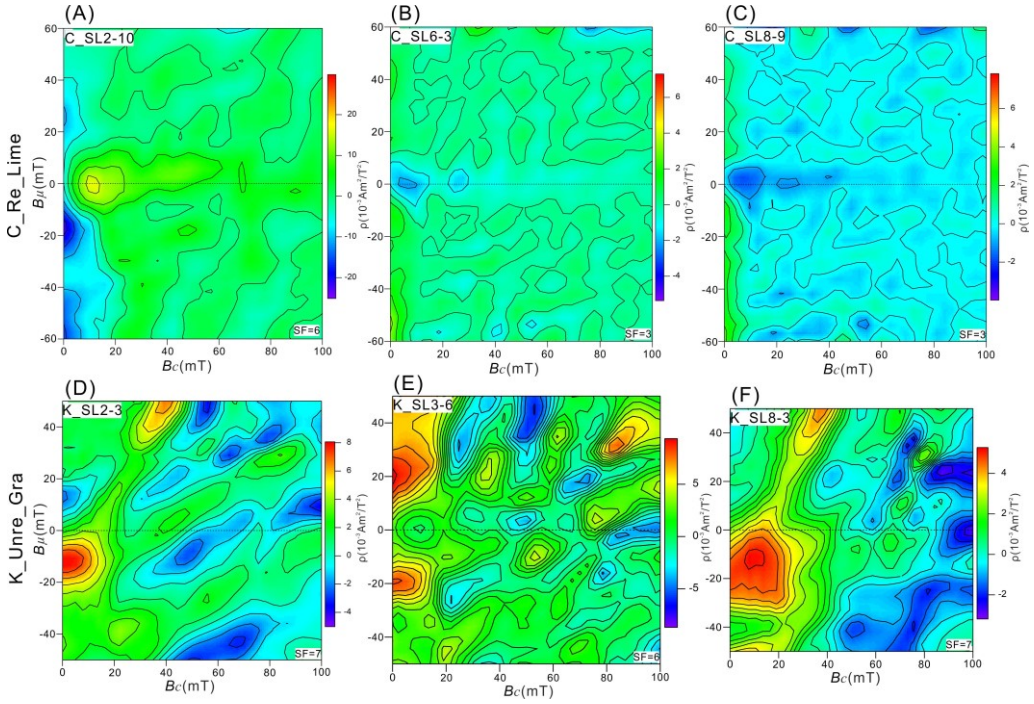

Figure S5.1. *(A-E) FORC diagrams for representative samples of the Carboniferous and Cretaceous formations. The optimum smoothing factor (SF) is calculated by the software FORCinel v1.18 of Harrison and Feinberg (2008). ρ is a mixed second derivative of the magnetization data (Roberts et al., 2014). C_Re_Lime: remagnetized Carboniferous limestones; K_Unre_Gra: unremagnetized Cretaceous granites.*

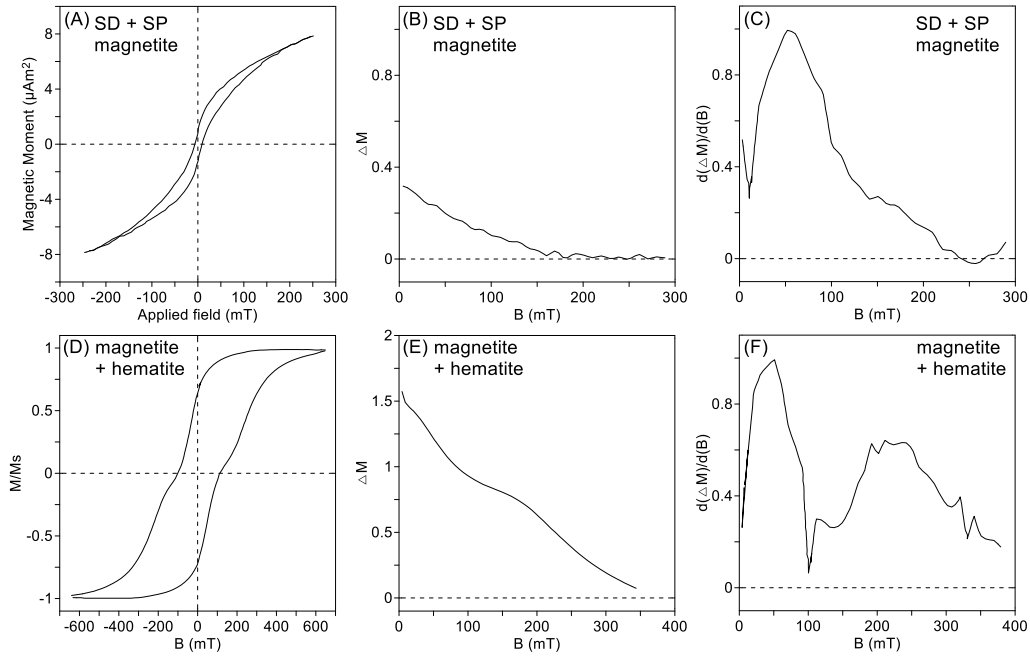

Figure S5.2. *Characteristic hysteresis loops (A), (D); △M curves (B), (E); their derivatives (C), (F) for SD + SP magnetite and magnetite + hematite, respectively, modified from Tauxe et al. (1996).*

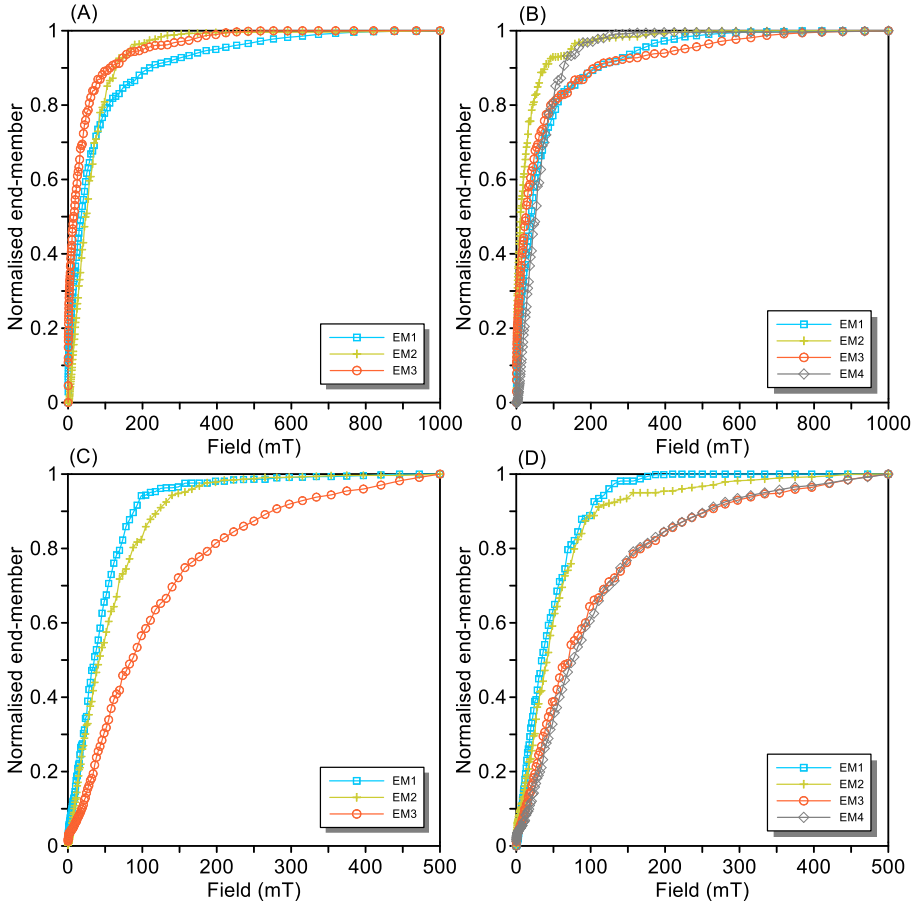

Figure S5.3. *Three and four end-member models of the Normalized IRM acquisition curves for remagnetized Jurassic limestones (A-B) and Carboniferous limestones (C-D). EM: end member.*

Normalized remanence decay curves of the vector difference sum

The remanence decay curves of the vector difference sum show features different from those *curves* in Cartesian coordinates. Most remagnetized limestone samples have a linear curve. However, the linear portion of the Jurassic limestones stretches almost up to ~550 °C, whereas it is restricted to below~400 °C in the Carboniferous limestones (Fig. S5.4A, C). Subsequently, the Jurassic limestones drop their magnetization quickly at temperatures ranging from 550 °C to 580 °C, while the Carboniferous samples decay between ~400 °C to 480 °C (Fig. S5.4A, C). Thus, the average temperatures at which 10% of the remanence is remaining are distinct from each other; it is ~560 °C to 580 °C for the former and ~430 °C to 440 °C for the latter (Fig. S5.4A, C). The unremagnetized granites have two clear discontinuities in their decay curves: ~560 to 580 °C and ~650 to 690 °C (Fig. S5.4E), indicating the unblocking of magnetite and hematite. Note that the rock magnetic measurements do not reveal the existence of hematite. This inconsistency may be attributed to hematite being present in minor amounts but having a strong remanent magnetization. The unremagnetized volcanics have convex decay curves. For those unremagnetized samples, the temperatures at which 10% of the remanence is remaining are ~670 °C and ~580 °C for granites and volcanic samples, respectively (Fig. S5.4E, G). Pertaining to AF demagnetization, the remagntized limestones show characteristics similar to the decay curves calculated from the Cartesian coordinates (Fig. S5.4B, D). The Jurassic rocks lose ~80% of their NRM at ~ 40 mT, while the Carboniferous rocks lose that at ~ 60 mT (Fig. S5.4B, D). In contrast, the unremagnetized samples lose ~80% of their NRM at ~ 80 mT, which is significantly larger than the remagntized samples (Fig. S5.4F, H).

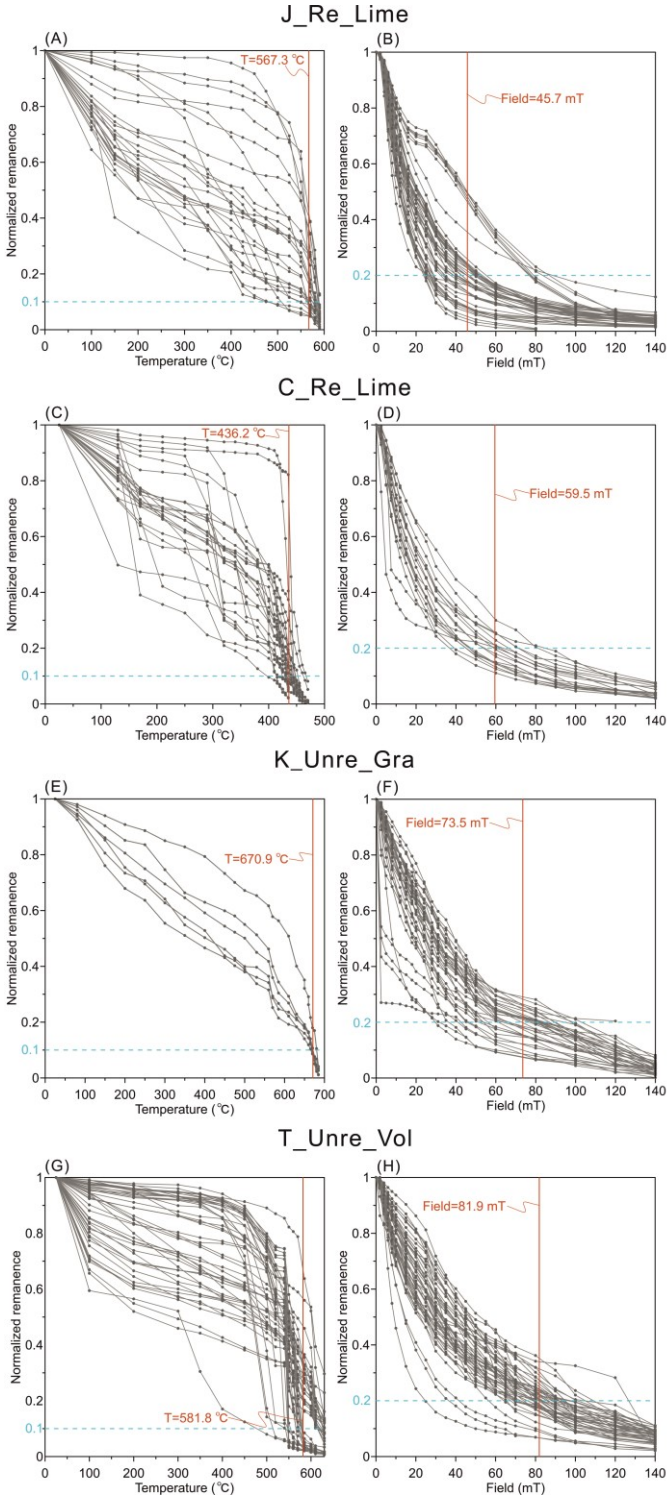

Figure S5.4. *Normalized remanence decay curves (summed vector differences) of the (A-E) Jurassic limestones, the (F-I) Carboniferous limestones, the (J-M) Cretaceous granites and the (N-Q) Permo-Triassic Tuff and rhyolite samples.*

A

ACKNOWLEDGEMENTS

Completing a Ph.D. is a challenging journey that requires hard work, perseverance, and good luck. Throughout this process, I have been fortunate to have the support and encouragement of a network of people who have helped me overcome obstacles, provided guidance, and made significant contributions to my research project. Without their invaluable assistance, this thesis would not have been possible.

First of all, I would like to express my sincere gratitude to my esteemed supervisor, Mark J. Dekkers, for giving me the opportunity to pursue research at Fort Hoofddijk. In July 2018, I attended the short course on Paleo, Rock, and Environmental Magnetism at China University of Geosciences (CUG) (Wuhan), which was taught by Dr. Qingsong Liu and Dr. Mark J. Dekkers. It was during this course that I first met my future supervisor. Later in November 2018, I contacted Mark J. Dekkers via email to inquire about the possibility of conducting research with him, and he promptly provided me with a support letter. My scientific journey at Fort Hoofddijk began in late 2019. Mark J. Dekkers has intellectual rigor, extensive knowledge and passion for research, which inspires me greatly. He is always very kind and patient to teach me how to conduct experiments and analyse data, while also provides me with useful suggestions and constructive feedback throughout my research. I would also like to thank Prof. Wout Krijgsman for his support and help during my Ph.D. The first time I met Wout Krijgsman was in August 2019, when he was invited to give a talk at the 5th Beijing Earth and Planetary Interior Symposium, Beijing, China. I informed him that I would be conducting research at his lab and was warmly welcomed and encouraged by him. Wout Krijgsman often cares about my research progress and life here, and provides me with useful advice on my career future plan. I am always welcome to go and talk with them, even interrupt them without scheduling an appointment.

I would like to extend my sincere appreciation to all the (former) colleagues and students at the 'Fort Hoofddijk': Cor Langereis, Lennart de Groot, Maxim Krasnoperov, Bertwin de Groot, Annemarieke Béguin, Sergei Lazarev, Annika Greve, Federico Andreetto, Martha Kosters, Liz van Grinsven, Frenk Out, Rosa de Boer, Romy Meyer, Jingyu Zhang, David Cortés-Ortuño, Michael Volk, and Dan Palcu. The

‘Fort Hoofddijk’ is a unique study place that is surrounded by a ring of water. The botanical garden outside the windows provides a tranquil atmosphere for study and research. Additionally, I am truly grateful to my (former) roommates in Zeist: Yuntao Ji, Chunning Sun and Xin Li, they share not only the living space with me, but also moments of laughter and happiness.

During my time at the Institute of Tibetan Plateau Research, Chinese Academy of Sciences (ITPCAS), Beijing, China, I would like to acknowledge the pivotal role of my supervisor Prof. Maodu Yan for providing me with the projects, whose creative ideas and insightful suggestions have significantly contributed to the completion of my thesis. He always encourages me to attend conferences & meetings to widen my horizons, and helps me a lot to avoid detours on the research. Without his invaluable guidance, unwavering support, and encouragement throughout my Ph.D. journey, completion of the thesis would not be possible. Prof. Xiaomin Fang, Prof. Jiankun He, Prof. Jinbo Zan, Dr. Weilin Zhang, Dr. Yibo Yang, and Dr. Tao Zhang are also much appreciated for their constructive suggestions and comments.

I would also like to express my gratitude to friends and (former) colleagues at the ITPCAS: Yi Chen, Dawen Zhang, Bingshuai Li, Miaomiao Shen, Chong Guan, Liang Yu, Wanlong Xu, Zunbo Xu, Zhichao Niu, Jian Zhang, Chengcheng Ye, Yahui Fang, Chihao Chen, Shurui Sun, Rongsheng Yang, Xiaobai Ruan, Liye Yang, Ziqiang Mao, Jian Kang, Yudong Liu, Zhantao Feng, Haitao Wang, Fenjun Tang, Tao Li, Xiaojing Li, Zengguang Guo, Yulong Xie, Qinghu Chen, Shuwen Wang, Wenxiao Ning, Maohua Shen, Yanguang Zhang, Xin He, Ahsan Ali Jadoon, Dhan Khatri, Mengqi Tan, Xuezhen Zeng, Guangshuai Cui, Shuai Nan, Yaofei Chen, Jiuyuan Zhang, Shuze Chen, Zhongyu Xiong, Yuwei Zhang, Bin Niu, etc.

Many thanks to the reading committee members for the time and effort they invested in reading and evaluating my work: Prof. dr. D.J.J. van Hinsbergen at Universiteit Utrecht, Prof. dr. Stuart Gilder at Ludwig Maximilians Universitat, Prof. dr. Tilo von Dobeneck at University of Bremen, Prof. dr. Agnes Kontny at Karlsruher Institut fur Technologie, and Dr. Annique van der Boon at University of Oslo.

Finally, my heartfelt gratitude goes out to my family for their encouragement, sacrifices, and unconditional love. My wife has suffered a lot from our long distance relationship, I am forever grateful for her sacrifices and selflessness. My parents and parents-in-law are especially thanked for their understanding and patience, which has been my source of strength and inspiration. My younger brother and brother-in-law have been accompanying our parents and parents-in-law for a long time in China, and provided them with love and care. I am grateful for their constant presence in my life, and I hope to repay their kindness in the future. My kith and kin are also acknowledged a lot for their generosity and kindness all the time.

Following Dan Palcu's idea in his thesis, a random word cloud was generated for fun.

A

ABOUT THE AUTHOR

Qiang Fu, who authored this thesis, was born on 13th, September 1991 in Baoji, Shaanxi, China. He earned his bachelor's degree in geophysics at the School of Geophysics and Geomatics (SGG), China University of Geosciences (CUG) (Wuhan) from September 2009 to June 2013. Subsequently, in September 2013, Qiang commenced his Master's program at SGG, CUG, and obtained his Master's degree in Geological Engineering in June 2015. During his Master's thesis, he concentrated on processing and interpreting magnetic data in the Yangshan iron mining areas, Fujian province.

From 2015 to 2017 Qiang served as an Assistant Engineer at the Northwest Geological Exploration Institute of China Metallurgical Geology Bureau, Xi'an, China. In July 2017, he further continued his study at the Institute of Tibetan Plateau Research, Chinese Academy of Sciences (ITPCAS), Beijing, China, under the supervision of Prof. Maodu Yan. He later initiated his Ph.D. research at Fort Hoofddijk under the guidance of Mark J. Dekkers in December 2019. Throughout his Ph.D. studies, Qiang devoted his enthusiasm to the paleomagnetism of the Qiangtang Terrane, Tibetan Plateau, China, and was involved in several fieldworks within seven months in the Tibetan Plateau, culminating in this thesis.

P

PEER REVIEWED PUBLICATIONS

Xu, W., Yan, M., van Hinsbergen, D.J.J., Li, B., Guan, C., **Fu, Q**., Yu, L., Xu, Z., Zhang, D., Shen, M., Feng, Z., Niu, Z., and Vaes, B., submitted, Paleomagnetic Evidence of 50º post-Eocene Clockwise Rotation of Mangkang and its Implications on the Tectonic Evolution of the Southeastern Tibetan Plateau, submitted to *Gondwana Research*.

Yu, L., Yan, M., Guan, C., Li, B., **Fu, Q**., Xu, W., Feng, Z., Zhang, D., Shen, M. and Xu, Z., Remagnetization of Carboniferous Limestone in the Zaduo Area, Eastern Qiangtang Terrane, and Its Tectonic Implications. *Frontiers in Earth Science*, 2022, 10: 1-18.

Fu, Q., Yan, MD., Dekkers M.J., Guan, C., Boer R.A., Yu, L., Xu, WL., Li, BS., Shen, MM., Zhang, JY., Xu, ZB., The Early Cretaceous Zaduo granite, Eastern Qiangtang Terrane (China) – an attempt to constrain its paleolatitude and tectonic implications[J]. *Frontiers in Earth Science, 2022, 10:829593.*

Yu, L., Yan, M., Domeier, M., Guan, C., Shen, M., **Fu, Q**., Xu, W., Xu, Z., Niu, Z. and Yang, L., New Paleomagnetic and Chronological Constraints on the Late Triassic Position of the Eastern Qiangtang Terrane: Implications for the Closure of the Paleo-Jinshajiang Ocean. *Geophysical Research Letters*, 2022, 49(2): e2021GL096902.

Fu, Q., Yan, MD., Dekkers M.J., Guan, C., Yu, L., Xu, WL., Li, BS., Feng ,ZT., Xu, ZB., Shen, MM., Zhang, DW., Remagnetization of the Jurassic Limestones in the Zaduo area, Eastern Qiangtang Terrane (Tibetan Plateau, China): implications for the India–Eurasia collision[J]. *Geophysical Journal International, 2021, 228, 3, 2073–2091.*

Guan, C., Yan, M., Zhang, W., Zhang, D., **Fu, Q**., Yu, L., Xu, W., Zan, J., Li, B. and Zhang, T., Paleomagnetic and Chronologic Data Bearing on the Permian/Triassic Boundary Position of Qamdo in the Eastern Qiantang Terrane: Implications for the Closure of the Paleo-Tethys. *Geophysical Research Letters*, 2021, 48(6): e2020GL092059.

Meng, JH., Ma, L., Wang, JH., Zhao, LP., Wang, LJ., **Fu, Q.**, Tong, MH., The development and application of gravity data in regional comprehensive interpretation of Delingha region. *Geophysical and Geochemical Exploration* (in Chinese with English abstract), 2021, 45(2): 369-378.

Fu, Q., Yan, MD., Liu, TY., Yang, YS., and Ma, L., Wavelet Transform Analyses of Faults Detection on Isostatic Gravity Anomalies: a Case Study from the Qaidam Basin and Its Adjacent Areas. *Seismology and Geology* (in Chinese with English abstract), 2019, 41(4): 960-978.

Ma, L., Meng, JH., **Fu, Q.**, Shan, ZX., and Li, BL., Application of independent component analysis in gravity and magnetic data processing, *Oil Geophysical Prospecting* (in Chinese with English abstract), 2017, 52(06):1344-1353+1126.

C

CAPTIONS TO CHAPTER PHOTOS

Page	
8	Nature's canvas - Yamzhog Yumco
16	Meili Snow Mountain in Yunnan province
20	Tibetan buddhist prayer flags
26	Autumn in Deqin, Yunnan province
58	A sacred mountain like a turtle, taken in Nangqian, Yushu, Qinghai Province
86	Sunset in Gongjue, Qamdo, Tibet
106	Wildlife of the Tibetan Plateau (Tibetan Rhesus Monkey, Przewalskium albirostris, vulture eating a dead dog/ox, dancing crane, running gazelle, Equus Kiang)
128	A cute marmot